Investigation of the Dzyaloshinskii-Moriya interaction and perpendicular magnetic anisotropy in magnetic thin films and nanowires

Dissertation
zur Erlangung des Grades
Doktor der Naturwissenschaften (Dr. rer. nat.)
am Fachbereich Physik
der Johannes Gutenberg Universität Mainz

von:
Samridh Jaiswal
geboren in Lucknow, India (Indisch)
Mainz 2018

Samridh Jaiswal

Investigation of the Dzyaloshinskii-Moriya interaction and perpendicular magnetic anisotropy in magnetic thin films and nanowires

Johannes Gutenberg Universität Mainz
Institut für Physik
Staudingerweg 7
55128, Mainz

Eidesstattliche Erklärung

Hiermit erkläre ich an Eides statt, dass ich meine Dissertation selbständig und ohne fremde Hilfe verfasst und keine anderen als die von mir angegebenen Quellen und Hilfsmittel zur Erstellung meiner Dissertation verwendet habe. Die Arbeit ist in vorliegender oder ähnlicher Form bei keiner anderen Prüfungsbehörde zur Erlangung eines Doktorgrades eingereicht worden

Mainz, den

Samridh Jaiswal

Statutory Declaration

I hereby declare on oath that I wrote my dissertation independently and without outside help and that I did not use any sources and aids other than the ones I have provided for the preparation of my dissertation. This thesis has not been submitted to any other examining authority in the present or similar form to obtain a doctoral degree

Mainz, den

Samridh Jaiswal

“So my antagonist said, "Is it impossible that there are flying saucers? Can you prove that it's impossible?" "No", I said, "I can't prove it's impossible. It's just very unlikely". At that he said, "You are very unscientific. If you can't prove it impossible then how can you say that it's unlikely?" But that is the way that is scientific. It is scientific only to say what is more likely and what less likely, and not to be proving all the time the possible and impossible.”

— Richard Feynman

Give me the third best technology. The second best won’t be ready in time. The best will never be ready.

— Robert Alexander Watson-Watt

“Incertidubre es la belleza de la vida”

“Uncertainty is the beauty of life”

— Anonymous

Abstract

Material development has led to the advancement of the three different categories of device applications, namely logic, sensors and memory. In recent years, there has been a vast increase in research and development towards ultra-high density and highly energy efficient magnetic memory devices. One of the driving factors of this development has been the uncovering of a multitude of physical phenomena observed at the interface between a Heavy Metal (HM) layer and a Ferromagnetic (FM) material. Here two such interfacial phenomena were probed, namely perpendicular magnetic anisotropy and the interfacial Dzyaloshinskii-Moriya interaction. Both these phenomena have been shown to enhance the storage density and the power efficiency in novel magnetic memory devices. Moreover, in such HM/FM thin films, chiral magnetic spin textures have been shown to be stabilised which are interesting from both a fundamental and a technological perspective for use as a platform for future devices.

In this work material thin films of the form HM/FM/MgO were investigated in which the HMs studied were Ta, W, Pt, Pd and W_xTa_{1-x} and the FM materials were different alloys of CoFeB namely, $Co_{20}Fe_{60}B_{20}$, $Co_{60}Fe_{20}B_{20}$, $Co_{40}Fe_{40}B_{20}$ and Co. The structural symmetry in these heterostructures was broken at the interface between the HM and the FM in order to facilitate the interfacial Dzyaloshinskii-Moriya interaction. Typical thickness of the FM ranged from 0.6 nm – 1 nm. Growth processes using both D.C. and R.F. magnetron sputtering were used to deposit thin films primarily on Si/SiO_2 substrates. It is shown here that the deposition conditions as well as post deposition processes used to deposit the material stack have a dramatic effect on magnetic properties such as domain wall pinning. A higher deposition power of 1500 W was shown to result in smoother domain structures and reduced pinning. The variation of the coercive fields was investigated for different symmetric and non-symmetric structures and found to be much smaller in FM alloys as compared to pure Co-based structures. Post deposition annealing was shown to lead to at least double the coercivity for a range of different heterostructures. Several different means of tuning the magnetic anisotropy were studied. A decrease in the magnetic anisotropy was observed for increasing FM thicknesses. The influence of a seed layer has been shown to affect the underlying domain structure as well as the anisotropy, with Ta and W exhibiting a larger anisotropy than Pd for a given FM. The more conventional out-of-plane magnetised bubble domains are replaced with worm like domains for a Pd seeded multilayer. Also, perpendicular magnetic anisotropy has been shown to be dependent on the composition of the ferromagnetic alloy under consideration. The Dzyaloshinskii-Moriya interaction was studied in optimised thin films of W/$Co_{20}Fe_{60}B_{20}$/MgO using two different magnetic field based methods namely the field driven asymmetric magnetic domain expansion and the magnetic domain strip annihilation. The values for the interfacial DMI were found to be (0.63 ± 0.05) mJm^{-2} and (0.73 ± 0.5) mJm^{-2} respectively. Chiral magnetic spin textures called magnetic skyrmions were studied in thin films of W/$Co_{20}Fe_{60}B_{20}$/MgO and Ta/$Co_{20}Fe_{60}B_{20}$/Ta/MgO structures using synchrotron based Scanning Transmission X-ray Microscopy and the Magneto-optical Kerr microscopy techniques. Charge current induced motion for both the material stacks were demonstrated using current pulses along a nanowire. A very low pinning of the magnetic domains is observed with the insertion of a Ta ultra-thin dusting layer. This thereby, highlights the subtle interfacial effects that govern the magnetic properties in such multi-layered material stacks.

Kurzfassung

Die Materialentwicklung hat zu Fortschritten in drei unterschiedlichen Anwendungsbereichen geführt, nämlich Logikschaltungen, Sensoren und Datenspeichern. In jüngster Zeit kam es zu einem Anstieg an Forschung und Entwicklung im Bereich von hoch effizienten magnetischen Datenspeichern mit ultrahohen Speicherdichten. Ein treibender Faktor dieser Entwicklung war die Entdeckung von mehreren physikalischen Phänomenen an der Grenzschicht zwischen einer Schwermetalllage (HM) und einem ferromagnetischen Material (FM). In dieser Arbeit wurden die senkrechte magnetische Anisotropie und die Dzyaloshinskii-Moriy Wechselwirkung betrachtet. Für beide Phänomene wurde gezeigt, dass sie die Speicherdichte und die Energieeffizienz von neuartigen magnetischen Datenspeichern erhöhen. Darüber hinaus konnte gezeigt werden, dass sich in solchen HM/FM-Dünnschichtsystemen chirale magnetische Spinstrukturen stabilisieren lassen, die sowohl aus Sicht der Grundlagenforschung als auch technischer Sicht einen interessanten Ausgangspunkt für zukünftige Bauelemente darstellen.

In dieser Arbeit wurden Dünnfilme der Form HM/FM/MgO untersucht, bei denen die Schwermetalle Ta, W, Pt, Pd und W_xTa_{1-x} vorkamen und als ferromagnetisches Material unterschiedliche CoFeB-Legierungen, $Co_{20}Fe_{60}B_{20}$, $Co_{60}Fe_{20}B_{20}$, $Co_{40}Fe_{40}B_{20}$ und Co, verwendet wurden. Die Struktursymmetrie dieser Heterostrukturen wurde durch die Grenzschicht zwischen der HM- und der FM-Lage gebrochen, um die Grenzflächen Dzyaloshinskii-Moriya Wechselwirkung zu ermöglichen. Typische Schichtstärken der ferromagnetischen Lage waren zwischen 0.6 und 1 nm. Für das Wachstum der Dünnschichten auf zumeist Si/SiO_2-Substraten wurde sowohl D.C. als auch R.F. Magnetronsputtern verwendet. Es wurde gezeigt, dass sowohl die Depositionsbedingungen als auch die Bedingungen nach der Deposition der Dünnschichten einen dramatischen Effekt auf die magnetischen Eigenschaften, wie das Domänenwand-Pinning, haben. Es wurde gezeigt, dass eine höhere Depositionsenergie von 1500 W zu glatteren Domänenstrukturen und reduziertem Pinning führt. Die Änderung des Koerzitivfeldes wurde für unterschiedliche symmetrische und nicht-symmetrische Strukturen untersucht und es wurde festgestellt, dass sie in FM-Legierungen viel kleiner ist als in rein Co-basierten Strukturen. Es wurde gezeigt, dass nachträgliches Tempern die Koerzitivität verschiedener Heterostrukturen zumindest verdoppelt. Mehrere unterschiedliche Methoden zum Anpassen der magnetischen Anisotropie wurden untersucht. Eine Abnahme der magnetischen Anisotropie wurde bei einer Dickenzunahme der ferromagnetischen Lage

beobachtet. Es konnte gezeigt werden, dass die Saatschicht sowohl die Domänenstruktur als auch die Anisotropie beeinflusst, wobei für Ta und W eine größere Anisotropie als für Pd bei einer gegebenen ferromagnetischen Schicht nachgewiesen wurde. Die konventionelleren aus der Ebene magnetisierten Blasendomänen werden bei einer mehrlagigen Struktur mit Pd Saatschicht durch wurmartige Domänen ersetzt. Ebenso wurde gezeigt, dass die senkrechten magnetischen Anisotropie von der Zusammensetzung der betrachten ferromagnetischen Legierung abhängt. Die Dzyaloshinskii-Moriya Wechselwirkung wurde in optimierten W/$Co_{20}Fe_{60}B_{20}$/MgO Dünnfilmen untersucht unter Ausnutzung zweier magnetischer feldbasierten Methoden, nämlich der feldgetriebenen asymmetrischen Domämenexpansion und der magnetischen Streifendomänenauslöschung. Die Werte für die Grenzschicht Dzyaloshinskii-Moriya Wechselwirkung wurden auf (0.63 ± 0.05) mJm^{-2}, bzw. (0.73 ± 0.5) mJm^{-2} bestimmt. Chirale magnetische Spinstrukturen, magnetische Skyrmionen genannt, wurden in Dünnfilmen mit einem Aufbau von W/$Co_{20}Fe_{60}B_{20}$/MgO und Ta/$Co_{20}Fe_{60}B_{20}$/Ta/MgO mittels synchrotronbasierten Transmissionsrasterröntgenmikroskopie, sowie mit magnetooptischer Kerrmikroskopie untersucht. Die durch elektrischen Strom induzierte Bewegung wurde mittels Strompulsen entlang von Nanodrähte für beide Dünnfilme demonstriert. Ein sehr geringes Pinning der magnetischen Domänen wurde nach dem Einfügen einer sehr dünnen Ta Dusting-Schicht beobachtet. Dies hebt die subtilen Grenzschichteneffekte hervor, die die magnetischen Eigenschaften in solchen mehrlagigen Schichtsystemen bestimmen.

Dedicated to

my parents Sanjay Jaiswal and Manika Jaiswal

and my sister Midushi Jaiswal

Contents

Contents

3 Experimental methods 64

Abbreviations

IoT	Internet of Things
HDDs	Hard Disk Drives
SRAM	Static Random Access Memory
DRAM	Dynamic Random Access Memory
NVM	Non-Volatile Memory
MRAM	Magnetic Random Access Memory
FM	Ferromagnet
STT	Spin Transfer Torque
SOT	Spin-Orbit Torque
MTJ	Magnetic Tunnel Junction
HM	Heavy Metal
PMA	Perpendicular Magnetic Anisotropy
DMI	Dzyaloshinskii-Moriya Interaction
SOI	Spin-Orbit Interaction
LLG	Landau-Lifshitz Gilbert
CMOS	Complementary Metal-Oxide Semiconductor
OOP	Out-Of-Plane
SOC	Spin-Orbit Coupling
TMR	Tunnel Magneto-Resistance
GMR	Giant Magneto-Resistance

PVD	Physical Vapour Deposition
CVD	Chemical Vapour Deposition
DC	Direct Current
RF	Radio Frequency
MOKE	Magneto-Optical Kerr Effect
MO	Magneto-Optical
NM	Non-Magnetic
EM	Electro-Magnetic
GIXR	Grazing Incidence X-ray Reflectometry
LTA	Load Transfer Arm
UHV	Ultra-High Vacuum
TEM	Transmission Electron Microscopy
SQUID	Superconducting Quantum Interference Device
MFM	Magnetic Force Microscopy
XRR	X-Ray Reflectometry
XRD	X-Ray Diffraction
AFM	Atomic Force Microscopy
HR-TEM	High-Resolution Transmission Electron Microscopy
STM	Scanning Tunneling Microscopy
DW	Domain Wall
DFT	Density Functional Theory
STXM	Scanning Transmission X-ray Microscopy
XMCD	X-ray Magnetic Circular Dichroism

|Chapter 1

Introduction

1.1 Introduction

In recent years there has been a tremendous surge in the amount of data generated by connected devices [1][2][3][4]. It has been predicted that the number of Internet of Things (IoT) devices which will be online by 2020 will be more than the current global population at 20 billion devices [5]. With growth of smart devices and sensors, data acquisition and generation has significantly increased. This therefore implores researchers in finding new materials for use in higher density storage devices [6]. Moreover the rise in global trends of wearable devices [7][8] urge the development of ultra-low powered on board storage due to limitations on battery capacity of such devices. The concept of storage of information in devices along with some of the existing storage technologies are briefly explained below.

1.2 Magnetic storage technologies

There exist two basic forms of storage devices; it can be broadly classified as non-volatile and volatile storage. Hard Disk Drives (HDDs) are a form of primitive non-volatile media in which the data is retained even in the absence of power. Volatile storage on the other hand is normally working memory which requires constant power; information is lost when power is switched off. There exists a memory hierarchy which relates relative areal density (amount of information stored per unit area) to the speed of the memory. This is shown in figure 1.

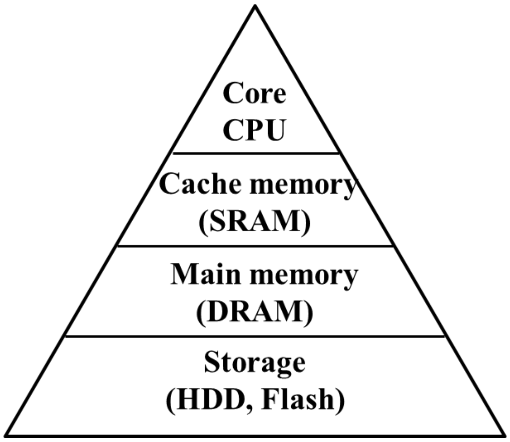

Figure 1: Schematic diagram of the current memory hierarchy.

The closer one gets to the CPU, the speed of the memory increases and the capacity reduces. Hard disk drives are extremely slow and work in the time frame of milliseconds but have extremely large capacities. SRAM or Static Random Access Memory is extremely fast with response time in nanoseconds but very low capacity. Dynamic Random Access Memory (DRAM) is a volatile type of memory which comprises of capacitors which hold charge. The presence or absence of electronic charge is read as a binary ‘1’ or ‘0’ and is used to store information in a particular memory cell. However, due to the limitations placed on the choice of dielectrics used in such capacitors a real capacitor cell loses its ability to hold charge which causes charge leakage. Hence DRAM needs to be constantly refreshed and therefore needs constant power. Typical refresh rates of DRAM cells are 100 ns. Magnetic hard disk drives store information in the form of bits defined by a particular magnetisation state corresponding to a data bit. In HDDs once the magnetic bit is written there is no further requirement for sustained storage via the use of current or magnetic fields. One of the key contenders for Non-Volatile Memory (NVM) technology is Magnetic Random Access Memory (MRAM). MRAM is orders of magnitude faster in its response time as compared to the HDD. This is described briefly in the section below.

1.2.1 MRAM

There exist two fundamental operations in any basic memory element i.e. writing/deleting and reading out of information. Semiconductor based memories such as Dynamic and Static RAM store the charge of an electron and manipulate this charge in a transistor to read or write information. However in an MRAM device information is stored by manipulating the magnetic state of the bit. There are several methods for magnetisation reversal, these form the basis for various different magnetic random access memory. A typical MRAM cell functions on a magnetoresistance effect in which there is a change in the electrical resistance depending on the magnetic configuration of the functional tri-layer. An MRAM cell consists of two ferromagnetic (FM) metals and a non-magnetic material used as a separator. A higher resistance state is obtained with the two magnetic layers magnetisation being anti-parallel and a low resistance is obtained with the layer stack's magnetisation being parallel to each other. This thereby constitutes the binary state used as a '1' and '0' to store information. There are various different kinds of MRAMs in development with the distinguishing feature based on the method used in applying a torque on the ferromagnet to manipulate the resulting magnetic state. Here, the Spin Transfer Torque (STT) MRAM and the Spin-Orbit Torque (SOT) MRAM will be discussed as these are the two products at the forefront of NVM technology and a basic structure of which is utilized in this work to study the interfacial physics phenomena. A brief introduction to these is given below.

Spin Transfer Torque MRAM

In such types of MRAM devices the magnetization reversal occurs via the exchange of angular momentum when a current is injected through the device. A phenomenon first theorised by Berger [9] and Slonczewski [10] in 1996 was brought to use in real devices in the form of Spin transfer torque based MRAMs. Such a device comprises of a tri-layered structure of a reference layer, a free layer and a conducting or insulating spacer layer as is shown in figure 2.

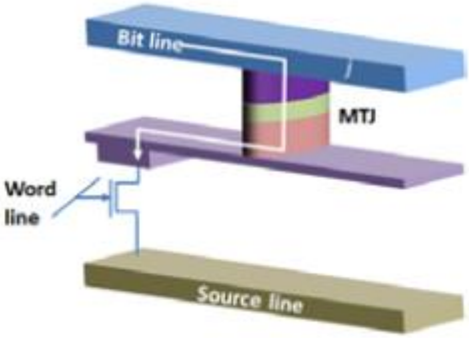

Figure 2 [11]: Schematic diagram of a STT MRAM comprising of an insulating tunnel barrier within the Magnetic Tunnel Junction (MTJ).

When current flows through the device, through the ferromagnetic reference layer, it becomes spin polarised with the fixed magnetisation direction. This spin polarised current on reaching the free layer interacts with the local magnetisation via exchange coupling. This causes a torque to be transferred to the free layer and attempts to rotate the magnetisation along its direction. If the current density is above the threshold switching density the transfer torque is able to reverse the magnetisation of the free layer. By apply a current of opposite polarity the magnetisation of the free layer can be switched parallel and anti-parallel with respect to the reference layer. As the current required to reverse the magnetisation decreases with decreasing device size, scalability is not an issue. However as the device size reduces, the thermal stability of the cells deteriorates. This therefore limits the increase in density of devices utilising STT technology.

Spin-Orbit Torque MRAM

In 2012, Liu *et al* had demonstrated in a prototype the switching of the magnetisation via torque generated from a neighbouring Heavy Metal (HM) layer [12]. The spin-Hall effect, in this case from the Ta layer, creates a spin polarisation. This spin current can then exert a torque on the magnetic layer. The SOT MRAM is a three terminal device [13] as depicted in figure 3.

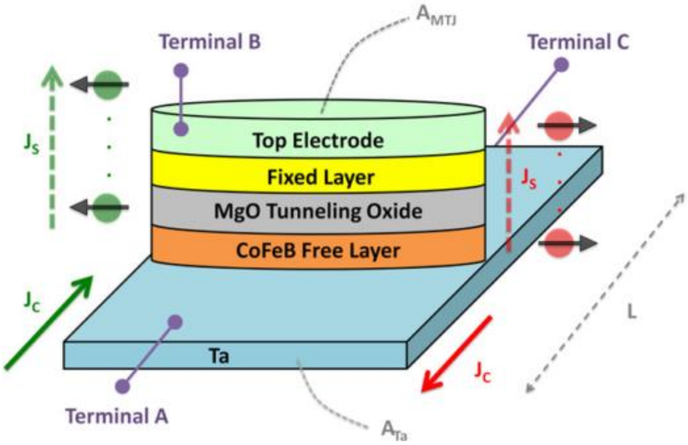

Figure 3 [14]: Schematic representation of a three terminal SOT MRAM device in which the reading occurs via terminals B to A or C and writing occurs separately via terminals A to C. The direction of charge current J_c determines the spin polarisation of the spin current J_s. The Magnetic Tunnel Junction is placed on top of a single Ta wire of length L.

One of the major disadvantages is the scalability to higher densities due to the fact that it is a three terminal device. There are also challenges with respect to the lithographic process in the three terminal device as cell size continues to reduce. SOT MRAM therefore is a suitable candidate for cache memory due to its fast speed and lack of high density [15][16]. However there are significant advantages which address the issues in STT MRAM some of these are outlined below.

Firstly the current density for switching can be tuned by changing the wire width of the heavy metal wire without affecting the thermal stability of the entire stack i.e. not having to change the thickness of the materials in the MTJ. The ratio of the switching current due to spin-Hall to the required current for STT can be approximated by,

$$\frac{\boldsymbol{I}_{SH}}{\boldsymbol{I}_{STT}} \approx \frac{\eta}{\theta_{SH}} \frac{A_{Ta}}{A_{MTJ}}$$

where A_{Ta} and A_{MTJ} are the cross sectional areas of the underlying heavy metal layer and the MTJ stack respectively. η and θ_{SH} are the spin transfer efficiency in an STT MRAM and the spin-Hall angle of the underlying heavy metal layer [14]. Therefore by reducing the thickness of the heavy metal layer it is possible to reduce the switching current. Secondly, due to the fact that the read and write pathways are separated it allows for a disturbance free read operation. Thirdly, since writing occurs via SOT based switching, the switching current does not pass through the MTJ which thereby reduces the degradation of the tunnel barrier and therefore increases the endurance of the SOT-MRAM. The write current passes through a low resistance heavy metal layer which also helps reduce the switching current and brings the switching energy levels on the order of CMOS devices (~ 1 fJ). Another prospective advantage is that spin-orbit torque has been shown to be able to switch the magnetisation state of magnetic insulators which generally have low magnetic damping. This opens up an entire new class of insulator based spintronic devices.

There are innovative approaches in improving MRAM devices which utilise both the properties of STT and SOT MRAM [17]. The intrinsic property of spintronic based devices in utilising magnetic spins for manipulation and storage of information poses them for being a viable candidate for fast, dense and energy efficient non-volatile memory devices [18] .

Since the mechanism for torque generation relies strongly on the material used it is crucial to find new materials with high efficiency for spin polarisation. Moreover, the torque transfer for SOT based MRAMs occurs through the interface between the HM and FM therefore it is essential to find methods to control the quality of the interface. With increases in density and scaling down of device sizes and increasing complexity of the memory stack, it has become more crucial to understand the new physics arising at the interface as well as optimising growth for the development of new memory devices.

1.3 Motivation and aim of the thesis

Magnetic Random Access Memory or MRAM is a class of memory which combines both the non-volatility of the HDDs as well as the speeds of the DRAMs. Instead of electrical charge the magnetic spin is used as a means for storage [18]. Information in an MRAM device is stored by manipulating the magnetic orientation of the bit.

The aim of the thesis is to develop new materials with optimised magnetic properties for use as elements in next generation MRAM devices and to understand the influence of growth on the interfacial properties within a magnetic thin film multi-layered stack. The investigation is focussed on a magnetic heterostructure in which the ferromagnetic thin film is sandwiched between a heavy metal and a non-magnetic oxide.

Since a vast number of phenomena which constitute the building ground for Spin-Orbit Torque MRAMs occur at the interface, interfacial manipulation by varying the quality of the growth through the use of additional seed layers and post deposition processes forms the core of this study. In this project the functional layers of a typical MRAM is studied. Investigation of phenomenon which facilitates the increased storage capacity and higher efficiency for switching in future MRAM devices is performed.

1.4 Thesis outline

This thesis is outlined as follows. Initially a relevant theoretical background to the various phenomena discussed within this work is outlined for the reader in chapter 2. The theoretical aspects required to understand the working of the various techniques used and developed are also discussed in this chapter. Chapter 3 briefly highlights the experimental methods used along with the description of the techniques developed.

Two key ingredients for developing efficient and high capacity MRAMs are Perpendicular Magnetic Anisotropy (PMA) and the Dzyaloshinskii Moriya Interaction (DMI). One of the biggest challenges in storing increased information per unit area is loss of data due to magnetization reversal through the influence of stray fields in highly compacted memory. In order to prevent this, the interfacial perpendicular magnetic anisotropy must be tuned. Perpendicular magnetic anisotropy is the intrinsic ability for the magnetisation of the bit to lie out of the plane of the thin film material allowing more number of bits to be packed together per unit area. Various means are shown to tune and study the PMA in these multi-layered heterostructures. The subtlety of this interfacial property is highlighted in chapter 4 and the interface adjoining the ferromagnetic layer is studied via both structural characterization and magnetic characterization techniques highlighted in chapter 3. It is shown that it is possible to tune interfacial roughness by carefully adjusting the conditions of the growth allowing for a smooth interface. The Dzyaloshinskii-Moriya Interaction which is an anti-symmetric exchange interaction favouring orthogonal alignment of magnetic spins facilitates chiral spin textures and magnetic skyrmions. Magnetic skyrmions have been shown as viable candidates for an alternative memory device with ingenious properties such as edge repulsion and very low threshold currents for motion [19]. Post magnetic and structural characterisation in chapter 4, optimised stacks were patterned and the interfacial DMI of the heterostructure was studied. Tuning the interfacial DMI via material engineering is shown in chapter 5 along with studying magnetic skyrmions in patterned thin films of varying skyrmion diameter. A conclusion and future outlook of the work conducted in this thesis is discussed finally in chapter 6.

1.5 Chapter 1-References

[1] “Data is giving rise to a new economy - Fuel of the future,” *The Economist*, 2017. [Online]. Available: https://www.economist.com/news/briefing/21721634-how-it-shaping-up-data-giving-rise-new-economy. [Accessed: 31-Jan-2018].

[2] A. Adshead, “Data set to grow 10-fold by 2020 as internet of things takes off,” *Computer Weekly*, 2014. [Online]. Available: http://www.computerweekly.com/news/2240217788/Data-set-to-grow-10-fold-by-2020-as-internet-of-things-takes-off. [Accessed: 31-Jan-2018].

[3] Verizon, “State of the Market: The Internet of Things 2016,” pp. 1–24, 2016.

[4] Research and Markets, “Global Industrial IoT (IIoT) Chipsets Market 2017-2021: Increasing Amount of Data Generation Due to IIoT,” *Research and Markets*, 2017. [Online]. Available: https://www.prnewswire.com/news-releases/global-industrial-iot-iiot-chipsets-market-2017-2021-increasing-amount-of-data-generation-due-to-iiot-300483422.html. [Accessed: 31-Jan-2018].

[5] R. Meulen, “Gartner Says 8.4 Billion Connected ‘Things’ Will Be in Use in 2017, Up 31 Percent From 2016,” *Gartner Survey*, 2017. [Online]. Available: https://www.gartner.com/newsroom/id/3598917. [Accessed: 19-Nov-2017].

[6] D. Ravelosona, L. Herrera Diez, W. Zhao, M. Klaui, B. Ocker, R. Mantovan, A. Lamperti, L. Baldi, V. Jacques, R. P. Cowburn, J. P. Adam, G. Agnus, I. Barisik, C. Burrowes, C. Chappert, T. Devolder, A. Digiacomo, S. Eimer, K. Garcia, F. Garcia-Sanchez, M. S. El Hadri, J.-V. Kim, W. Lin, N. Vernier, Y. Zhang, G. Tallarida, M. Fanciulli, L. Lazzarini, L. Nasi, M. Marianni, T. Hingant, and J.-P. Tetienne, “Recent developments in the manipulation of magnetic domain walls in CoFeB–MgO wires for applications to high-density nonvolatile memories,” in *Magnetic Nano- and Microwires*, M. Vázquez, Ed. Woodhead Publishing Series in Electronic and Optical Materials, 2015, pp. 333–378.

[7] J. Wade, “Wearable Technology statistics and trends 2018 | Smart Insights,” *Digital Marketing Toolkits*, 2017. [Online]. Available: https://www.smartinsights.com/digital-marketing-strategy/wearables-statistics-2017/. [Accessed: 31-Jan-2018].

[8] J. Chang, L. Chang, A. Dupret, C. Kim, F. Hamzaoglu, and T. Yoshikawa, “F2: Memory trends: From big data to wearable devices,” in *2015 IEEE International Solid-State Circuits Conference - (ISSCC) Digest of Technical Papers*, 2015, pp. 1–2.

[9] L. Berger, “Emission of spin waves by a magnetic multilayer traversed by a current,” *Phys. Rev. B*, vol. 54, no. 13, pp. 9353–9358, 1996.

[10] J. C. Slonczewski, “Current-driven excitation of magnetic multilayers,” *J. Magn. Magn. Mater.*, vol. 159, pp. L1–L7, 1996.

[11] R. Sbiaa, H. Meng, and S. N. Piramanayagam, “Materials with perpendicular magnetic anisotropy for magnetic random access memory,” *Phys. status solidi - Rapid Res. Lett.*, vol. 5, no. 12, pp. 413–419, 2011.

[12] L. Liu, C.-F. Pai, Y. Li, H. W. Tseng, D. C. Ralph, and R. A. Buhrman, “Spin-torque switching with the giant spin Hall effect of tantalum.,” *Science*, vol. 336, pp. 555–558, May 2012.

[13] S. W. Lee and K. J. Lee, “Emerging three-terminal magnetic memory devices,” *Proc. IEEE*, vol. 104, no. 10, pp. 1831–1843, 2016.

[14] K. L. Wang, J. G. Alzate, and P. K. Amiri, “Low-power non-volatile spintronic memory:STT-RAM and beyond,” *J. Phys. D. Appl. Phys.*, vol. 46, p. 74003, 2013.

[15] G. Prenat, K. Jabeur, P. Vanhauwaert, G. Di Pendina, F. Oboril, R. Bishnoi, M. Ebrahimi, N. Lamard, O. Boulle, M. Miron, K. Garello, J. Langer, B. Ocker, M. Cyrille, P. Gambardella, M. Tahoori, and G. Gaudin, “Ultra-Fast and High-Reliability SOT-MRAM: from Cache Replacement to Normally-off Computing,” *IEEE Trans. Multi-Scale Comput. Syst.*, vol. 2, no. 1, pp. 49–60, 2016.

[16] G. Prenat, K. Jabeur, G. Di Pendina, O. Boulle, and G. Gaudin, “Beyond STT-MRAM, Spin Orbit Torque RAM SOT-MRAM for High Speed and High Reliability Applications,” in *Spintronics-based Computing*, W. Zhao and G. Prenat, Eds. Cham: Springer International Publishing, 2015, pp. 145–157.

[17] Z. Wang, L. Zhang, M. Wang, Z. Wang, D. Zhu, Y. Zhang, and W. Zhao, “High-density NAND-like spin transfer torque memory with spin orbit torque erase operation,” *IEEE Electron Device Lett.*, vol. pp, no. 99, pp. 1–1, 2018.

[18] A. Fert, “Nobel Lecture: Origin, development, and future of spintronics,” *Rev. Mod. Phys.*, vol. 80, no. 4, pp. 1517–1530, Dec. 2008.

[19] A. Fert, V. Cros, and J. Sampaio, “Skyrmions on the track,” *Nat. Nanotechnol.*, vol. 8, no. 3, pp. 152–156, 2013.

|Chapter 2

Theoretical Background

2.1 Introduction

In this chapter the magnetisation processes pertaining to the experimental results discussed further are explained. The chapter outlines the process of formation of magnetic domains and the associated magnetic phenomena at the interface between two magnetic domains are discussed. The theoretical background with respect to domain wall motion is highlighted as well as the underlying theory of the experimental techniques used within this work.

2.2 Magnetic interactions within a ferromagnetic system

Ferromagnetic materials form the basic constituents for magnetic memory devices. Ferromagnetism is a type of magnetic interaction in which materials possess spontaneous magnetisation in the *absence* of an applied field. Examples of ferromagnetic materials include *3d* transition metals such as iron, nickel, cobalt and the rare earth gadolinium as well. In ferromagnetic materials there exists an internal magnetic moment due to the unfilled atomic orbitals. In addition to this there also exists strong coupling between the atomic moments which gives rise to the spontaneous magnetisation. Here, the various interactions between atomic moments are discussed along with their influence on the resulting magnetic structure.

2.2.1 Heisenberg exchange interaction

In magnetic systems there exist different kinds of magnetic ordering which occurs below a certain critical temperature. In ferromagnetic systems, there exists long range magnetic ordering which occurs as a result of the coulombic interaction and Pauli's exclusion principle between two neighbouring spins. The magnetic interaction between two neighbouring spins is known as Heisenberg exchange interaction. The effective magnetic moment in ferromagnets arises from the atomic spin magnetic moment. The direct Heisenberg exchange interaction is defined as the scalar dot product of two spins $\mathbf{S_i}$ and $\mathbf{S_j}$ summed over all spins. It is given as

$$\widehat{\boldsymbol{H}} = \sum_{i<j} -J_{ex}\mathbf{S}_{\mathrm{i}} \cdot \mathbf{S}_{\mathrm{j}} \tag{2.1}$$

Here J_{ex} is the exchange interaction constant that parameterises the type and strength of coupling between the two neighbouring spins. The exchange energy is minimised when the two neighbouring spins are parallel and $J_{ex} > 0$ signifying a ferromagnetic coupling. While anti-parallel spin alignment is parameterised by $J_{ex} < 0$.

2.2.2 Spin-Orbit Interaction (SOI)

The spin-orbit interaction as the name suggests is an interaction between the spin and the orbital angular momentum of an electron. This interaction is the underlying mechanism for a large number of phenomena observed in magnetism. It gives rise to magnetic anisotropy and provides for a mechanism to disperse energy into the atomic lattice via magnetic damping as explained later in section 2.6. In ferromagnetic materials it gives rise to the anomalous Hall effect and the anisotropic magnetoresistance. It also allows for spin dependent scattering of electrons. The SOI gives rise to relativistic fields within a ferromagnet which ultimately results in the Dresselhaus effect and Rashba fields in systems lacking structural inversion symmetry. Semi-classically the SOI can be understood as follows. An atom shown in the figure 1 has an electron orbiting it, while the nucleus remains fixed.

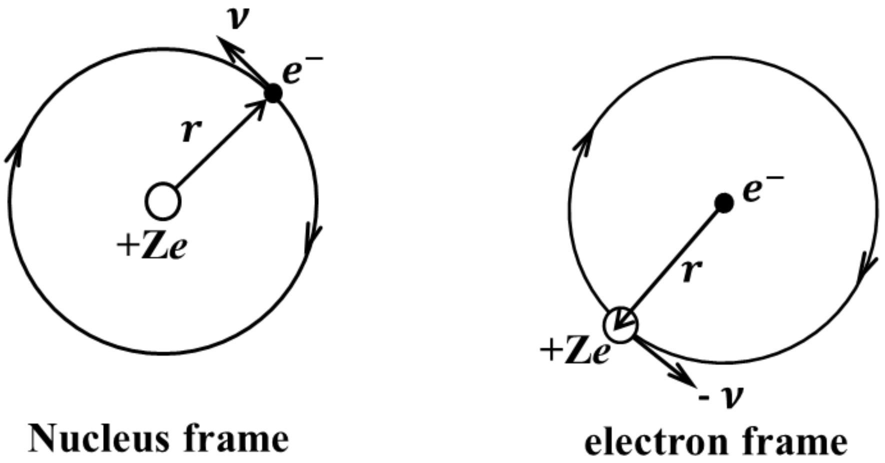

Figure 1: A schematic drawing showing an atom from the frame of reference of its nucleus and the frame of reference of the electron. In the frame of reference of the nucleus the electron orbits it with a velocity v, however, in the electron's frame of reference it observes a positive nucleus of charge +Ze orbiting with velocity $-v$ and forming a closed current loop around it. As a result the electron experiences a magnetic field due to its orbital angular momentum.

Now, consider in the frame of reference of the electron, the electron is stationary and the nucleus is rotating around forming a closed current loop. This orbiting positive charge builds up a magnetic field which then interacts with the spin of the electron. As a result, the spin of the electron is coupled to its orbital motion. For a single electron orbiting the nucleus the SOI energy in *cgs* units can be expressed as

$$\hat{\boldsymbol{H}} = \frac{Ze^2}{2m_e^2c^2r^3}\mathbf{L}\cdot\mathbf{S} \tag{2.2}$$

In the rest frame of the electron a greater current is generated for a larger nuclear charge and a greater spin-orbit interaction. The expectation value here for $< r^{-3} >$ is proportional to Z^3 therefore the SOI scales with the forth power of the atomic number. Hence for heavier elements with larger atomic number the spin-orbit interaction is stronger, such as Pt, Ir, Ta and W etc. For lighter elements the spin-orbit interaction can be considered as a weak interaction and as an addition to the stronger electrostatic interactions. These stronger interactions govern the values of **L** and **S** i.e. the values of the spin and orbital electron momenta are calculated separately. Only after this is done the spin-orbit interaction is introduced as a weak interaction and the total energy is calculated. This regime is known as the Russell-Saunders regime (L-S coupling regime). For heavier elements with larger *Z*, the SOI is dominant compared to the electrostatic interactions and one must couple the spin and orbital momentum for each electron separately. The weaker electrostatic interaction will then couple the total angular momentum *J* for all the electrons. Therefore this regime is called *J-J* coupling regime [1][2].

2.2.3 Dzyaloshinskii-Moriya Interaction

The Heisenberg's exchange interaction allows for direct exchange to occur over very short distances. In a similar manner there exists *indirect exchange interactions* such as the super-exchange interaction in which short ranged exchange interactions are mediated over two non-neighbouring magnetic ions mediated by a non-magnetic ion residing between them. In the same manner, the spin-orbit interaction can play the role of a non-magnetic ion and mediate the interaction between two ferromagnetic spins through the ground and excited states of a heavy metal. Such an interaction is known as the Dzyaloshinskii-Moriya interaction (DMI). This phenomenon was initially proposed by Dzyaloshinskii in 1958 [3] in the attempt of describing "weak ferromagnetism in antiferromagnets". Shortly after in 1960, it was adapted by Moriya [4][5] to understand the "anisotropic super-exchange interaction" in bulk magnetic crystals. The DMI is an antisymmetric exchange interaction since in the corresponding Hamiltonian the two spin vectors are multiplied as a vector product. It can be expressed as a general form

$$\hat{\boldsymbol{H}} = -\mathbf{D_{ij}}\cdot\left[\mathbf{S_i}\times\mathbf{S_j}\right] \tag{2.3}$$

where, $\mathbf{D_{ij}}$ is the Dzyaloshinskii-Moriya interaction vector. This interaction is non-zero only in the presence of inversion asymmetry and acts orthogonal to the plane of $\mathbf{S_i}$ and $\mathbf{S_j}$. This can be seen from figure 2 where, as a result of the interaction between the two neighbouring spins the **D** vector lies in the plane of the interface and points into the page.

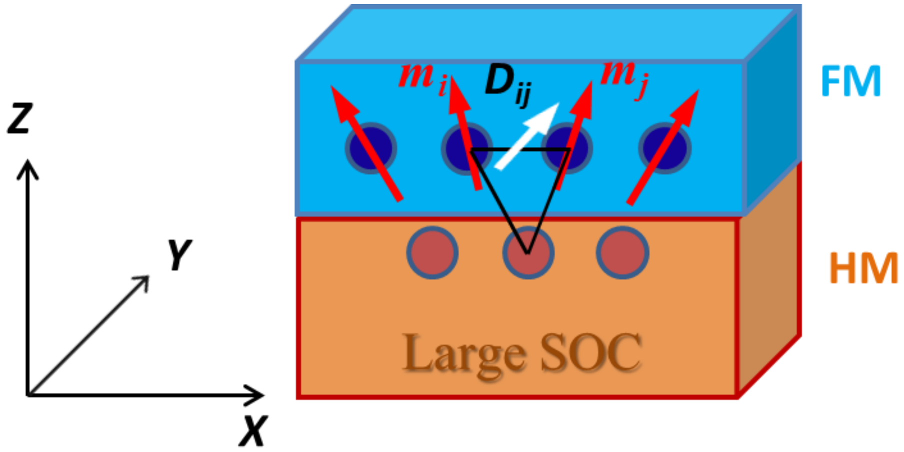

Figure 2: A schematic of a typical stack exhibiting interfacial Dzyaloshinskii-Moriya Interaction between a ferromagnet (FM) and a heavy metal (HM). The magnetic configuration at the ferromagnetic interface is shown. The DM interaction is mediated via the large spin-orbit coupling of the bottom HM atoms to the magnetic atoms located above them. This leads to a canting of the ferromagnetic spins. The DMI vector, $\mathbf{D_{ij}}$ points along the *Y* axis parallel to the plane of the interface. The magnetic moment $\mathbf{m_i}$ and $\mathbf{m_j}$ exhibit this finite canting which leads to the minimization of the DMI energy.

As a result of the orthogonal preference of DMI it competes directly with the Heisenberg exchange interaction and results in weak ferromagnetism in antiferromagnetic materials. DMI can manifest in both bulk and thin film systems. There are two primary requirements for a system to exhibit a sizable DMI. Firstly, there must exist a structural inversion asymmetry in the system under investigation which can occur in the bulk or in thin films at the interface between two materials. Secondly, the strength of the DMI is governed by the spin-orbit coupling in thin films with broken structural symmetry, the spin-spin interaction is mediated via a non-magnetic high spin-orbit interaction centre, i.e. an atomic species with a large spin-orbit coupling through a 3 site indirect exchange interaction. Whilst it has been shown earlier that DMI can occur in bulk systems of the form of B20 compounds in which the symmetry is broken along the crystal lattice. More recently, it has been shown that it is in fact possible to achieve structural inversion asymmetry in thin film multilayers with interfacial DMI as opposed to the bulk DMI studied earlier. The symmetry in this case is broken at the interface by growing ultra-thin thin films using various deposition techniques. Multilayers consisting of heavy metal and ferromagnet are stacked in close proximity. It is at this interface where both the conditions for the existence of interfacial DMI are met. Consider a *3d* ferromagnet and a *5d* heavy metal with large spin-orbit coupling stacked together. There then exists a 3 point interaction between the ferromagnetic spins and the heavy metal. An interfacial DMI is then generated at this interface. It has been shown by Yang *et al.* [6] that this interfacial DMI in fact extends for only the atoms nearest to the interface and there is a sharp decrease in the DMI energy away from the interface of the HM/FM.

In systems with a structure inversion asymmetry and a large spin-orbit coupling mechanism the total Hamiltonian consists of both the exchange energy as well as the contribution from the DMI energy. In certain instances this can cause a change to the ground state of the magnetic system in which the Heisenberg exchange is comparable to the DMI energy. This leads to interesting spin spiral states such as magnetic skyrmions and chiral domain walls. In order to understand the origin of ferromagnetism and its associated phenomena one must understand the filling of the atomic bands near the Fermi surface, this is described in the section below.

2.3 Band theory in ferromagnets-occurrence of magnetism in itinerant electron systems

In single electron systems an electron can be considered as being present in its atomic orbital. However, for larger condensed matter systems one must consider a collection of electrons forming a system consisting of energy bands. Electronic energy bands are formed as a result of overlap between atomic orbitals. Electrons present in the outer shells of atoms are available for bonding with other atoms and are present in the so called *conduction band*, hence the outer electrons are called itinerant electrons. The inner shell electrons remain localized to their respective atoms. The electrons in the system fill up the bands upto the Fermi energy which is located in the conduction band. The valence band configurations for *3d* ferromagnets, Fe, Co and Ni are $3d^6 4s^2$, $3d^7 4s^2$, $3d^8 4s^2$, respectively. The *3d* band has an occupancy of 10 electrons and is a narrow-band therefore naturally it has a high electron density. The *4s* is more spread out in energy. This broad band is occupied by only two electrons. Therefore it has a low electronic density of states. The *3d* band in ferromagnetic transition metals is exchange split which according to the molecular field approach can be explained by the generation of an internal exchange field, $H_{ex} = n_s M$ where n_s is a coefficient which determines the strength of the exchange field and M is the magnetisation. This exchange field lifts the degeneracy of the spin-up and spin-down bands. The exchange splitting implies that the *3d* band is divided in two, parallel (↑) and anti-parallel (↓) spin sub bands. In order to minimize the Zeeman energy the parallel band is filled first followed by the anti-parallel band. Due to the exchange split in the *3d* band, a spin imbalance is created which therefore leads to a net magnetic moment. The energy difference between the two spin states is given by

$$\Delta E_{ex} = 2\mu_o \boldsymbol{\mu}_{\mathbf{e}} \cdot \mathbf{H}_{\mathrm{ex}} \tag{2.4}$$

This band theory was first applied by E.C. Stoner and J.C. Slater in the explanation of non-integer effective Bohr magneton values in transition metal ferromagnets at T = 0 K. The Stoner criterion is an inequality that relates the exchange interaction with the density of states at the Fermi level for a given ferromagnetic material. The criteria is given as,

$$I * N_{\uparrow\downarrow}(E_F) > 1 \tag{2.5}$$

where I is the Stoner exchange parameter and $N_{\uparrow\downarrow}(E_F)$ is the density of state per atom for each spin state (↑ and ↓). It allows for an understanding of the mechanism of electrical conductivity in *3d* ferromagnets

Shown below in figure 3 is the density of states for a non-magnetic metal and an itinerant ferromagnet close to the Fermi energy. It can be seen that the *3d* band in the ferromagnet is spin split giving rise to preferential spin scattering of electrons. The electrical resistivity for example, at room temperature is governed by collisions of the conduction electrons with phonons and the crystal lattice. At a given temperature, an increase in electrical resistivity takes place when the mean free path of the conduction electrons is reduced At the Fermi energy there exist a number of unoccupied states in the split *d* band for the conduction electrons to scatter into. This along with the atomic overlaps between the *s* and the *d* orbital results in a *s-d* hybridization. This therefore allows for the parabolic *s* band to take on some characteristics of the flatter *d* band and allows for the more delocalized *s* electrons which have a lower effective mass to conduct and scatter into the available *d*-band states [7]. As a result of this increased *s-d* scattering the mean free path of the *s* electrons decreases and the electrical resistivity increases.

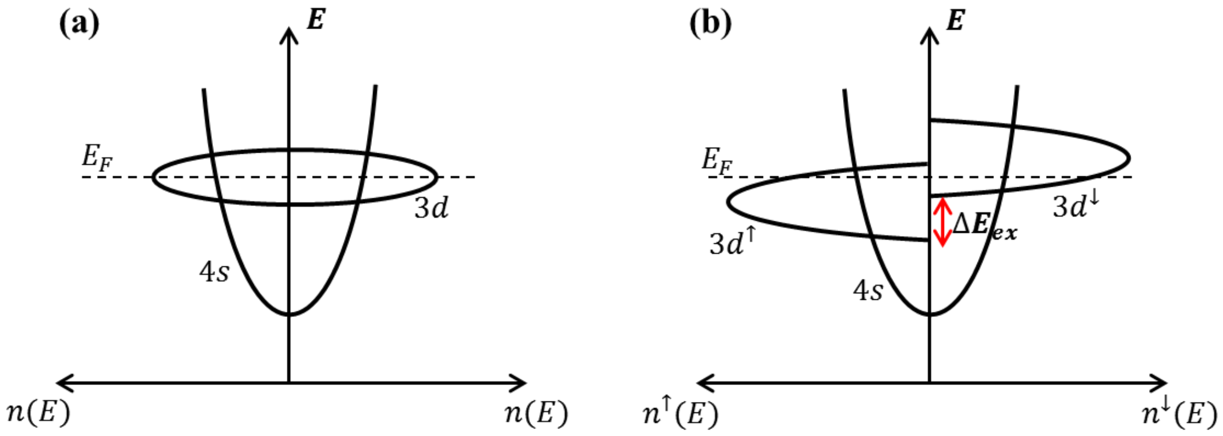

Figure 3: Schematic depiction of the distribution of density of states as a function of energy for the atomic orbitals *4s* and *3d* in (a) a non-magnetic solid and (b) a ferromagnetic solid. Hund's rules in atoms govern the filling of atomic orbitals [1]. The *3d* band is split in the spin-up and spin-down states. The Fermi level is defined as the highest occupied state in the valence band at 0 K and separates filled electronic states from vacant electronic states.

2.4 Energies associated with magnetism

The resultant magnetic state of magnetism in magnetic materials is governed by the contribution of various energy terms associated with the magnetic moment via the spin of the electron.

2.4.1 Zeeman energy

The Zeeman energy is the total energy associated within the magnetic system due to the external magnetic field H_{ext}. The external magnetic field reorients the magnetic moments within a magnetic system along its applied direction. The Zeeman energy is directly proportional to the internal magnetisation of the sample and the external magnetic field as shown in eq. 2.6.

$$E_{Zeeman} = \mu_0 \int \boldsymbol{M_s} \cdot \boldsymbol{H_{ext}} dV \tag{2.6}$$

This energy contribution disappears in the absence of an external field.

2.4.2 Magnetocrystalline anisotropy energy

Magnetic anisotropy implies that the magnetic properties vary depending on the direction along which they are measured. The hysteretic response of a sample can be significantly influenced depending on the contributions of the magnetic anisotropy energy. There exist different kinds of magnetic anisotropies in ferromagnetic systems. These are mentioned below as:

1. Crystal anisotropy
2. Shape anisotropy
3. Stress anisotropy
4. Anisotropy induced by
    a. Magnetic annealing
    b. Plastic deformation
    c. Irradiation
5. Exchange anisotropy

Here the crystalline contributions to the magnetic anisotropy will be discussed. It is defined as the amount of energy required to align the magnetisation from an easy preferred orientation to the hard axis of the crystal structure.

In crystal systems there exists a certain crystallographic direction along which it is relatively easier to align the magnetisation. i.e. a preferred magnetic direction. For example for Fe, it is easier to align the magnetic domains along [100] as compared to the [111] direction. The more favourable direction is referred to as the easy direction, while the least favourable is known as the hard direction. The difference in energy between the easy and hard directions is called the magnetic anisotropy energy [8]. A larger field is required to align the magnetisation along the crystallographic hard axis direction as compared to the easy axis direction. Examples of the hard and easy axis are shown in figure 4.

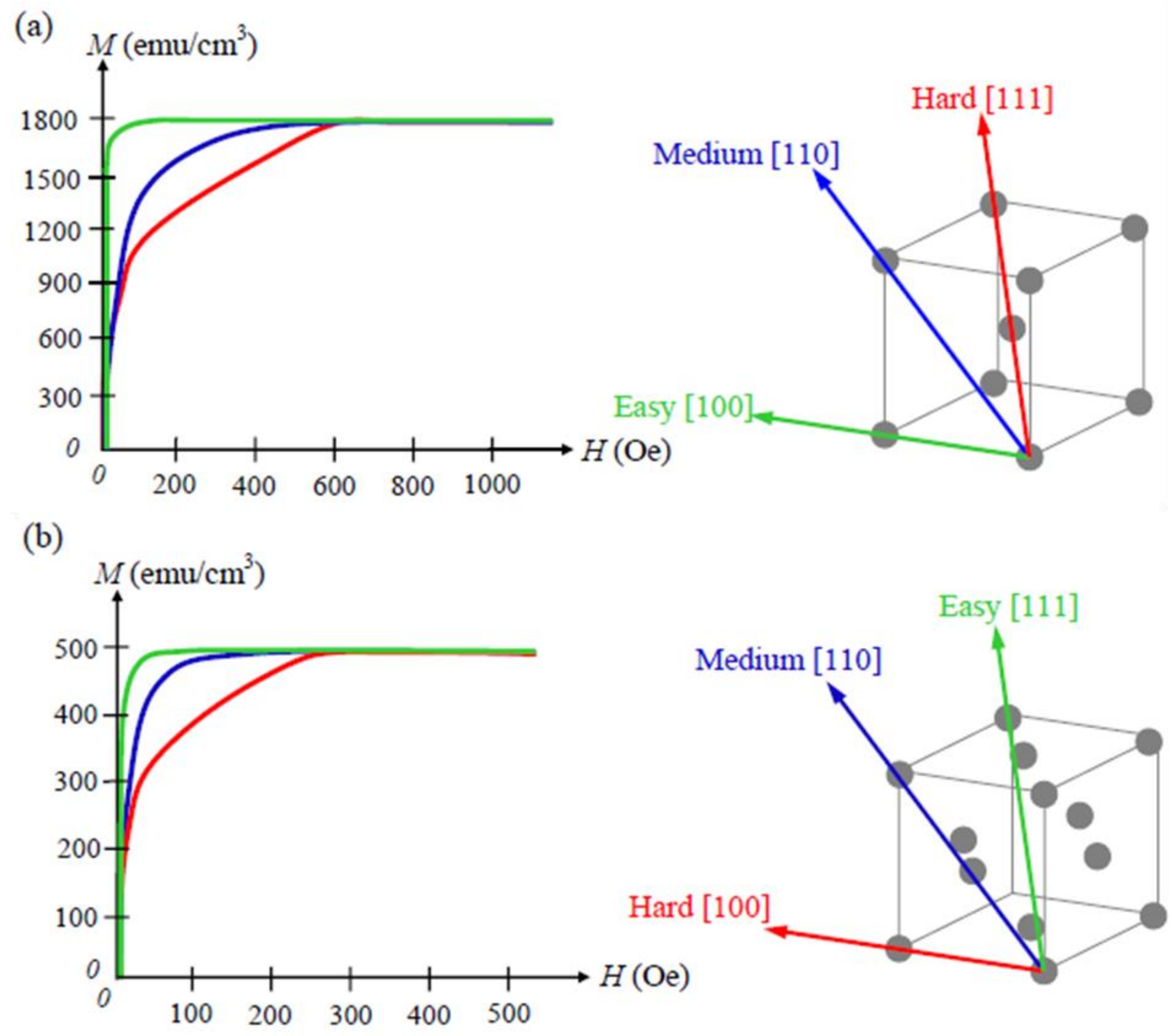

Figure 4: The magnetisation curves of the three principle axis exhibiting easy and hard axis directions for (a) single crystal bcc iron and (b) single crystal fcc nickel. The figure has been adapted from [9][10].

The magnetocrystalline anisotropy dictates to a large extent the magnetic configuration of a material system. For single crystal materials for example there exists a strong preference for the magnetisation to lie along a particular axis. This however is not true for polycrystalline materials with truly random orientations of grains in which there is no predetermined orientation of magnetisation. In reality, however a truly random crystallite may not be possible and the polycrystalline material may exhibit a small magnetocrystalline anisotropy along a particular direction. This is important to note here as some of the materials under investigation here are not single crystalline in nature. For systems with uniaxial crystalline anisotropy the magnetocrystalline anisotropy can be written as

$$E_K = K_0 + K_1 \sin^2(\theta) + K_2 \sin^4(\theta) \tag{2.7}$$

where K_0, K_1 and K_2 are the anisotropy constants for a given material at a given temperature and θ is the angle between the magnetization and the easy axis direction as shown in the figure 5.

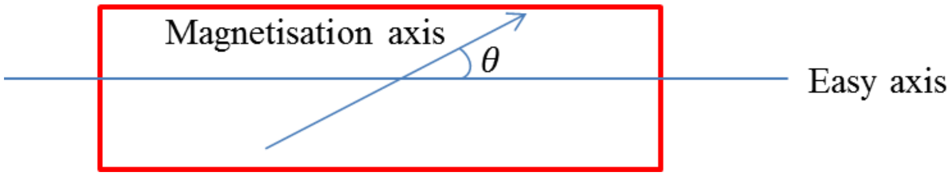

Figure 5: Schematic diagram showing the magnetocrystalline axis within a crystalline material.

Various experiments on the anisotropy constants were originally performed by Bozorth [11] in 1937. He demonstrated that the anisotropy constants are related to the lattice parameter and essentially become zero just before the Curie temperature is reached due to the thermal fluctuations of the lattice.

For complex crystal lattices and lower symmetry structures eq. 2.7 is modified to incorporate higher order terms [10].

2.4.3 Exchange energy

In ferromagnetic systems there exist strong coupling between unpaired atomic magnetic moments, this coupling is known as exchange coupling and the energy associated with their relative alignment to each other is known as the exchange energy. It results from the interaction between Pauli's exclusion principle which forbids two fermions from occupying the same quantum state and the coulombic repulsion between charges [12]. A quantitative description of exchange energy can be explained as following. If two atoms *i* and *j* have a spin angular momentum of $\mathbf{S}_\mathrm{i}$ and $\mathbf{S}_\mathrm{j}$ then $\mathbf{S}_\mathrm{i} = \sum \mathrm{s}_\mathrm{i}$ and $\mathbf{S}_\mathrm{j} = \sum \mathrm{s}_\mathrm{j}$ are the total spin angular momenta associated with the atoms *i* and *j* respectively. The exchange energy experienced between them is then given by

$$E_{exchange} = -2J_{exchange}\mathbf{S}_\mathrm{i} \cdot \mathbf{S}_\mathrm{j} = -2J_{exchange}S^2 \sum_{i>j} \cos\phi_{i,j} = -2J_{exchange}S_iS_j \cos\phi \tag{2.8}$$

where $J_{exchange}$ is the exchange interaction constant and ϕ is the angle between the two interacting spins. Since the exchange interaction decreases rapidly with increasing distance this allows the summation of the total spin angular momentum to be restricted to the nearest-neighbour pairs. Furthermore, if one assumes a small angle between neighbouring atomic spins one can obtain from the above equation a relationship detailing the relative change in exchange energy with respect to the change in the angle ϕ between the spins,

$$\Delta E_{exchange} = J_{exchange} S^2 (\Delta\phi)^2 \tag{2.9}$$

The above simplification is valid provided that all electrons have the same exchange integral J and that the exchange energy between all electrons from the same atom is constant and therefore can be omitted from the summation. The exchange stiffness parameter is related to the exchange constant and can be defined as,

$$A = \frac{J_{exchange} S^2}{a} \tag{2.10}$$

where a is the lattice parameter. It should be noted that the exchange interaction is isotropic and that there is no preferential direction in space for the net alignment of spins. The energy is minimized when all neighbouring spins are aligned parallel to each other.

2.4.4 Magnetostatic energy

Magnetostatic energy can also be referred to as stray field energy, magnetic dipolar energy or demagnetizing energy. Magnetostatic energy is a long range interaction which can influence spatial distribution of magnetization. Similar to how the Zeeman energy is generated due to external magnetic fields the magnetostatic energy is internally generated due to the presence of single magnetic moments within a magnetic sample. A uniformly magnetized sample exhibits a magnetic flux within the sample itself as well as in the vacuum surrounding it. This leads to the formation of magnetic charges located at the surface of the sample shown in figure 6.

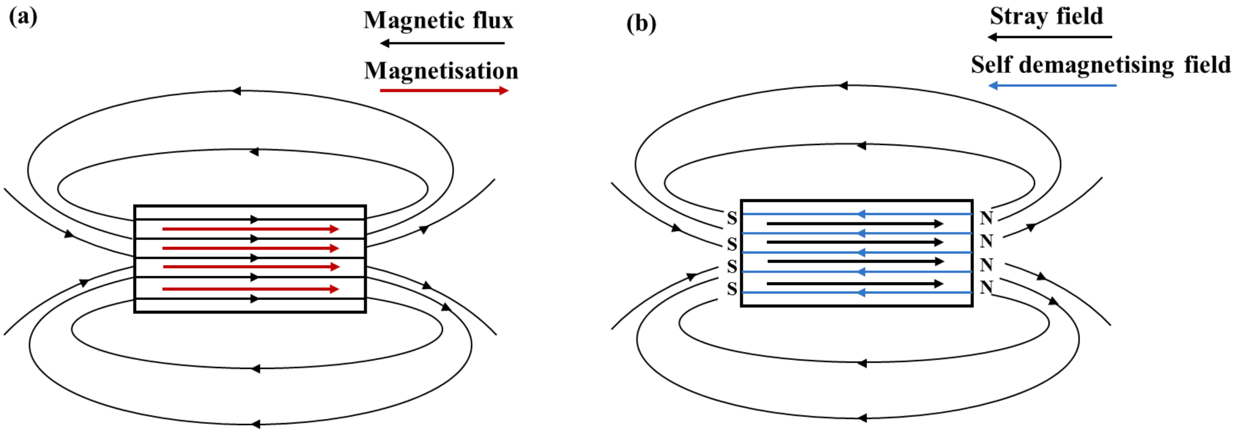

Figure 6: Magnetic field distribution within and around a ferromagnetic material. (a) The magnetic flux from a saturated ferromagnet along with the internal magnetisation direction. (b) The fields produced by the magnetic charges on the surface of the ferromagnet. Note an internal demagnetising field is developed which reduces the total effective field of the ferromagnet.

The magnetic fields associated with these charges follows the flux (which must be continuous) in the vacuum but opposes the magnetization within the sample showing a discontinuity at the ends of the sample. This field opposing the magnetization inside the sample is known as the demagnetizing field. Mathematically, the magnetostatic energy can be expressed as [13]

$$E_{magnetostatic} = \frac{1}{2}\mu_0 \int \mathbf{H}_{dm} \cdot \mathbf{M}\, dV \qquad (2.11)$$

where H_{dm} is the demagnetizing field which varies for ellipsoids linearly with magnetization and a geometrical dependent constant N as

$$H_{dm} = -N\mathbf{M} \qquad (2.12)$$

Calculation of a precise value of H_{dm} for an arbitrary shaped object is non-trivial as it requires the consideration of the dipoles in the entire system and because it is a long range interaction. The magnetostatic energy is minimized when the surface charges, the associated demagnetizing field and hence the stray field within the sample is reduced. One of the methods to do achieve this is by the formation of magnetic domain walls. This is discussed in the following section.

2.5 Domain wall formation in a ferromagnetic material

In an ideal ferromagnet, at low temperatures, exchange energy would dominate and would lead to spontaneously magnetized material. However in reality, the remnant magnetic state of a material is determined by the summation of all the energy terms in eq. 2.13. As with all physical phenomena in order to obtain the equilibrium state the total energy therefore must be minimized and a compromise between the energy costs for the different contributing terms needs to be incorporated. Two key competing energy terms in domain wall magnetism are $E_{exchange}$ and $E_{magnetostatic}$.

$$E_{tot} = E_{magnetostatic} + E_{exchange} + E_K + E_{Zeeman} \tag{2.13}$$

Exchange energy favours parallel alignment of spins. In order to minimize exchange all spins need to be aligned, however this leads to an increase in the magnetostatic energy due to the formation of magnetic charges at the surface. This thereby leads to an increase in the total energy. Hence in order to lower the energy of the system a compromise is reached with the formation of a domain wall. A domain wall is defined as a region separating two neighbouring domains with parallel magnetisation. The magnetisation within a domain wall undergoes continuous reversal.

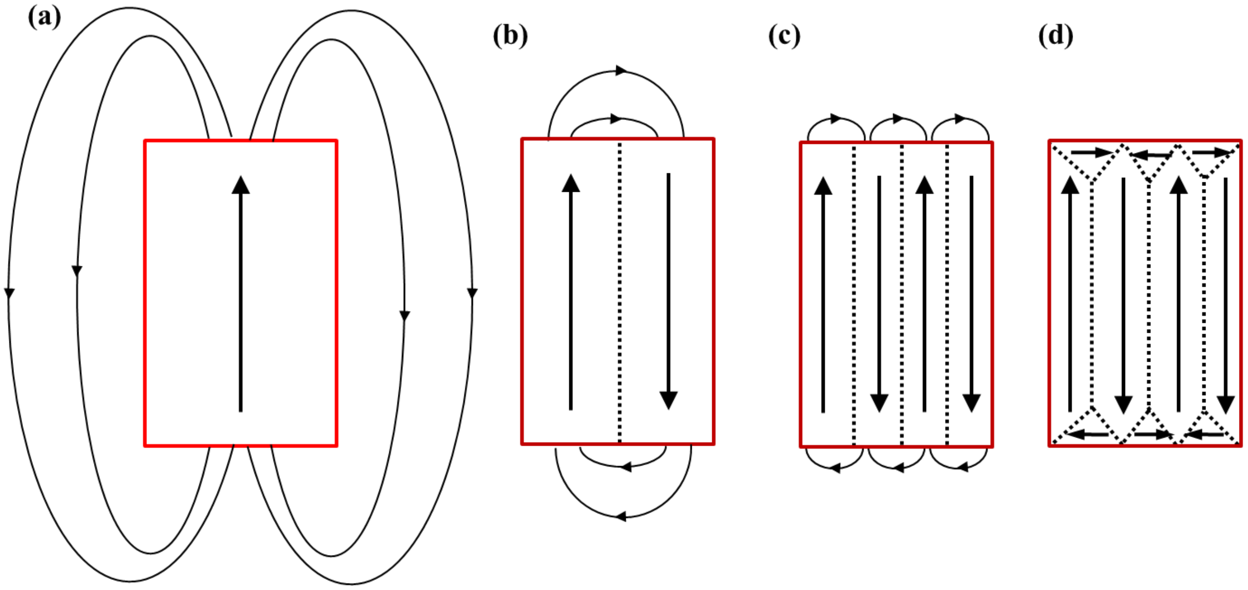

Figure 7: (a-d) Schematics illustrating the process of formation of magnetic domains within a ferromagnet material. Compromise between the exchange energy and the magnetostatic stray field energy gives rise to formation of multiple domains and complete flux closure of the stray fields.

The formation of a domain wall lowers the magnetostatic energy. At magnetic saturation, the exchange energy is low but there is a large magnetostatic energy arising from the stray magnetic fields. The reduction in magnetostatic energy by the introduction of additional domains must be balanced with the increase in energy associated with the introduction of domain walls into the system. The resulting domain formation is a competition between the magnetostatic energy and the exchange energy. A final state in an ideal ferromagnet with complete closure of stray fields is shown in figure 7(d).

In the following section, the different factors affecting the energy of a domain wall are considered and depending on the energetics of the system can give rise to different types and structures of domain walls.

2.5.1 Domain walls in ferromagnetic materials

A domain wall is a region separating two uniformly magnetized domains with opposing spins. It consists of non-uniform spins undergoing a rotation between two saturated domain states. If this spin reversal occurs over a single spin it would result in a significant increase in the exchange energy associated with the domain wall. In order to therefore minimize this, the spin rotation or reversal of the two neighbouring domains must occur over a large number. This minimizes the exchange energy as the angle between two neighbouring spins within a domain wall is smaller and the net rotations occur over a larger number of spins. This therefore results in an increase in the domain wall width. However this state causes the anisotropy energy to increase as now a relatively larger number of spins are not aligned in the direction of the magnetic easy axis. The competition between the two results in the internal structure of the wall.

The dimension of the domain wall is defined by minimizing the sum of the energies $E_{exchange}$ and E_K. The magnetization undergoes a continuous rotation from one domain to another. The energy minimization determines the width of the domain wall which can be expressed as

$$\Delta = Na_0 \approx \sqrt{\frac{A}{K}} \tag{2.14}$$

where A is the exchange stiffness and K is the anisotropy constant, N is the number of spins contained in the domain wall along its width and a_0 is the lattice parameter of the material under investigation.

Bloch and Néel domain walls

Domain walls can be classified into two different categories depending on the method of re-orientation of the spins between the two neighbouring domains into either Bloch walls or Néel domain walls. Here we briefly discuss these two domain types before delving into domain walls in PMA systems and chirality within Néel domain walls.

Both Bloch and Néel domain walls are formed in systems with Perpendicular Magnetic Anisotropy (PMA) i.e. in films where the magnetization lies out of the plane of the sample. The magnetic domains in such a material therefore have their domains either up or down magnetized. In systems with Bloch domain walls the spins within the domain wall undergo a rotation in the direction orthogonal to the plane of the spins in the neighbouring domains. For a Néel domain wall the spin rotation of the domain wall occurs in the plane of the magnetization of neighbouring domains. In typical systems with PMA with relatively large anisotropies the magnetic domain wall width is relatively small as compared to the width of the wire (which is typically 100-1000 nm) and the thickness of the film (< 2 nm). The magnetization rotation therefore between domains would prefer to rotate orthogonal to the wire width as the cost in dipolar energy is lesser compared to if the magnetization would rotate in the plane of the neighbouring domains. Thus a Bloch type domain wall is preferred. However, thin film systems which exhibit a sufficiently large Dzyaloshinskii-Moriya Interaction relative to the magnetic anisotropy energy can exhibit Néel domain walls. This is explained in the section below.

2.5.2 Dzyaloshinskii-Moriya Interaction and chiral Néel domain walls

The effect of the interfacial DMI on magnetic domain structures and its influence on domain walls is discussed here. The DMI interaction favours a tilt of the magnetization of the two neighbouring spins. In order to have an influence on the domain structure, the DMI of a system is required to compete with exchange as well as anisotropy energies. In systems with weak DMI the ferromagnetic order remains intact and the DMI affects only weak points in the system, i.e. the domain walls, where the magnetization is not uniform. In the ferromagnetic domain the DMI must compete energetically with the exchange whereas in the domain walls the DMI must compete with demagnetizing energy which relatively is lower. The DMI therefore can induce a chiral Néel structure.

As explained above magnetostatically in thin films and in commonly investigated nanowires of width w in the range 100-1000 nm a Bloch type domain wall is preferred. However, as shown by Thiaville *et al.* [14] at a HM/FM interface for a system with a large enough DMI, Néel walls maybe the stable state. Increasing the strength of the DMI can allow for a transition from a full Bloch to a full Néel type domain wall. This occurs due to the minimization of the domain wall energy where the magnetostatic energy competes with the DMI giving the resulting Néel like domain state. The transition from a Bloch state to a Néel state is shown in figure 8. It is the favouring of canted neighbouring spins due to DMI which allows for the lowering of the domain wall energy density. As calculated by Thiaville [14] for a system with DMI, D greater than a critical DMI, $D_c = 4\Delta K/\pi$ the system will undergo a transformation and result in all Néel like domain walls. For the case if $D < D_c$ the DMI interaction is not strong enough and the resulting domain state will comprise of Bloch type domain walls.

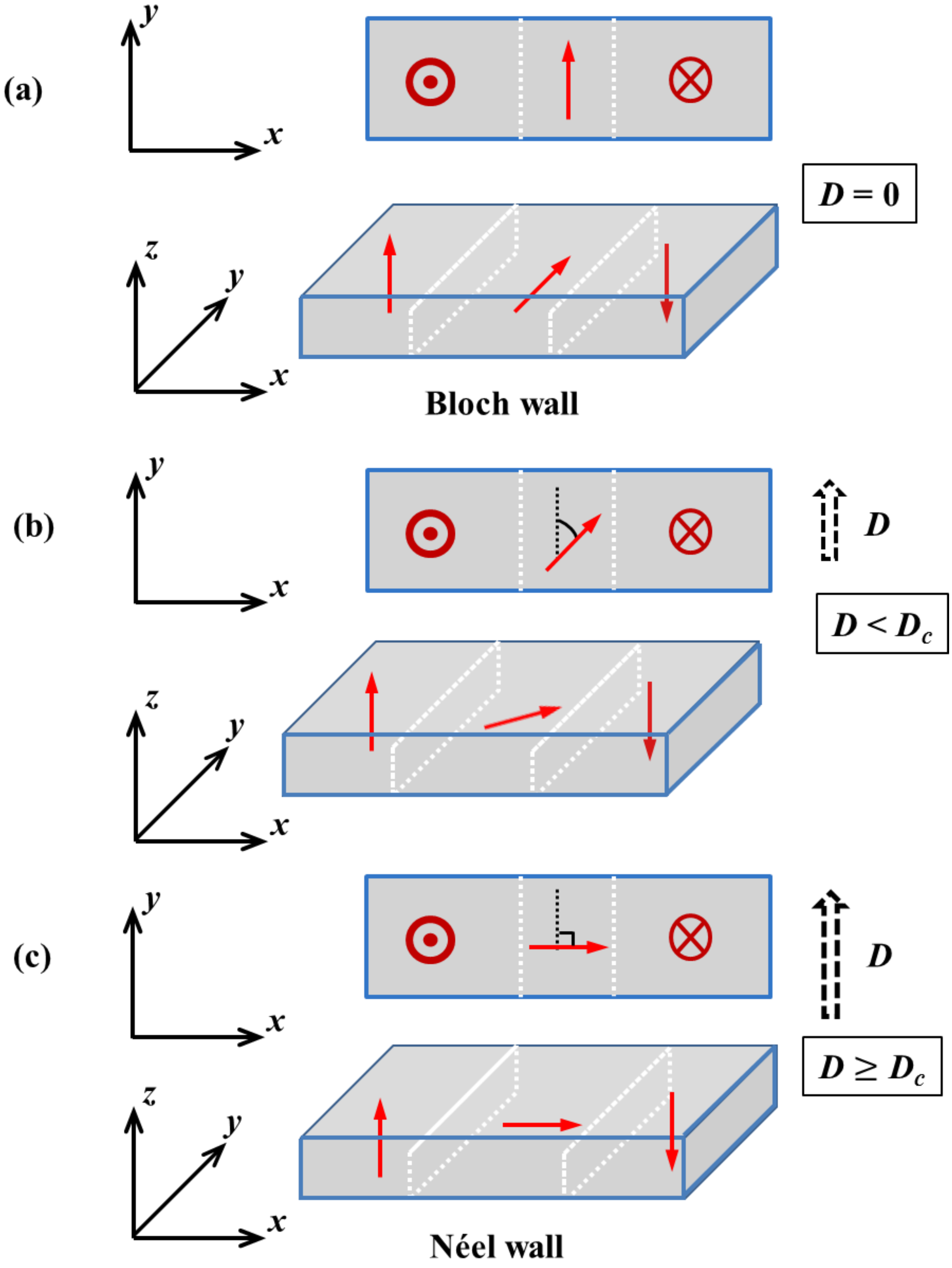

Figure 8: An ↑↓ magnetic domain wall configuration as a function of DMI showing (a) a complete Bloch wall state in the absence of DMI due to strong shape anisotropy of the domain wall with width of the nanowires ≫ domain wall width, and (b) an intermittent wall configuration between a Bloch and a Néel

wall and (c) when the DMI is strong, a full Néel type wall is exhibited. The spin configuration for both cross sectional view and a top view of a magnetic sample is highlighted here.

For perpendicularly magnetised systems the magnetic domains have their magnetisation lying out of the plane of the sample. Therefore there can exist two kinds of domain wall an up-down and a down-up domain wall. As the name suggests in an up-down domain wall the magnetisation rotates between two domains which are magnetised upwards (out-of-the-plane) to downwards (into-the-plane) and vice-versa for a down-up domain wall. The sense of rotation of the core spin of the domain wall can either be towards the left or the right. Depending on the fashion of rotation of the central spin of a domain wall a wall chirality is assigned to the system. In PMA systems lacking DMI the sense of rotation is not fixed. However in systems with DMI present, the DMI can induce chiral Néel walls in the system: i.e. a pair of domain walls in which the core magnetisation of the domain walls are opposed to each other such domain walls are called homochiral that is they each possess the same chirality. In systems with homochiral domain walls when moving from one domain to another the spins within the domain wall will rotate with the same winding around the direction of *D* i.e. either clockwise or anti-clockwise. When this rotation of spins occurs in a clockwise manner the DWs are referred to as possessing right handed chirality and the sign of the DMI is positive whereas if the spin winding occurs anticlockwise it is called left handed chirality and the DMI is negative[15][16][17][18].

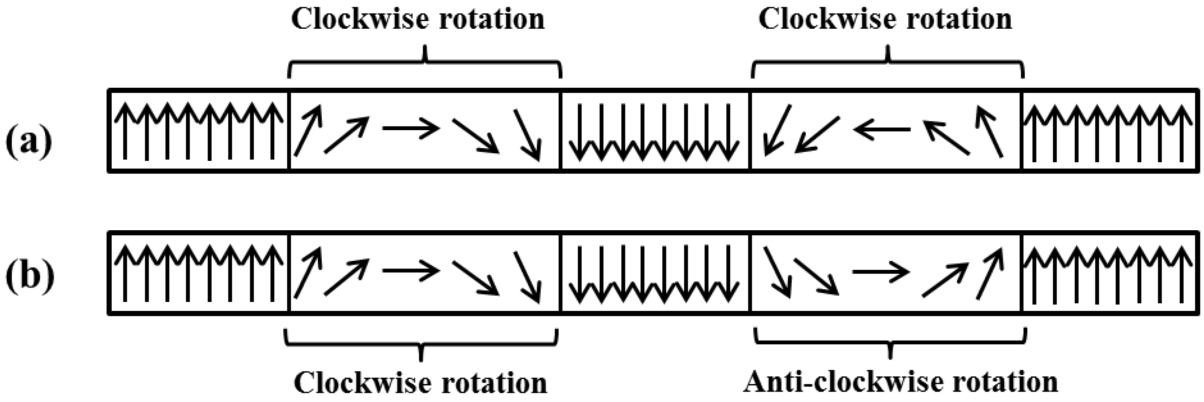

Figure 9: Schematic diagram for rotations of the spins within a magnetic domain wall with the chirality of the two Néel walls are (a) the same exhibiting clockwise rotation and when they are (b) different. For homochiral domain walls the spin texture rotates in the same direction, clockwise whereas the rotation is opposite in the second case. A clockwise rotation of spins across the domain wall is characterised as right handed chirality

Chen *et al.* have used spin-polarised low-energy electron microscopy to image chiral Néel magnetic domain walls in [Co/Ni]$_n$/Pt(111) multilayers and found that one obtains a right handed Néel wall i.e. the magnetisation rotates from out of plane to in-plane with the domain wall core magnetisation pointing to the right. However, when Pt is replaced with Ir(111) the domain wall core magnetisation is reversed and a left handed Néel wall is observed [19].

Phenomenologically the DMI within a sample can be thought of manifesting as an internal effective field localised at the domain wall [14][20][21]. This effective field points along the longitudinal direction and has opposite signs for ↑↓ or ↓↑ domain wall. The expression describing this effective field is [14].

$$H_{DMI} = \frac{D}{\mu_0 M_s \Delta_{DW}} \tag{2.15}$$

Here Δ_{DW} is the width of the Néel like domain wall and H_{DMI} pointing along $+x$-direction ($-x$-direction) when D points along the $+y$-direction ($-y$-direction) as shown in figure 8, for an ↑↓-DW. The same symmetry, but with opposite sign holds for a ↓↑-DW.

2.5.3 Magnetic skyrmions

Magnetic skyrmions are robust topological protected non-collinear quasi-particles which consist of winding spins with a central core. They occur in ferromagnetic systems which favour a magnetic structure with chiral symmetry and can be classified in two categories, Néel and a Bloch type skyrmion as shown in figure 10 depending on the sense of rotation of the spins within it. In a Bloch Skyrmion the spins rotate in the tangential planes i.e. in the plane perpendicular to the radial axis. For a Néel skyrmion the spins rotate along the radial axis from periphery to the core.

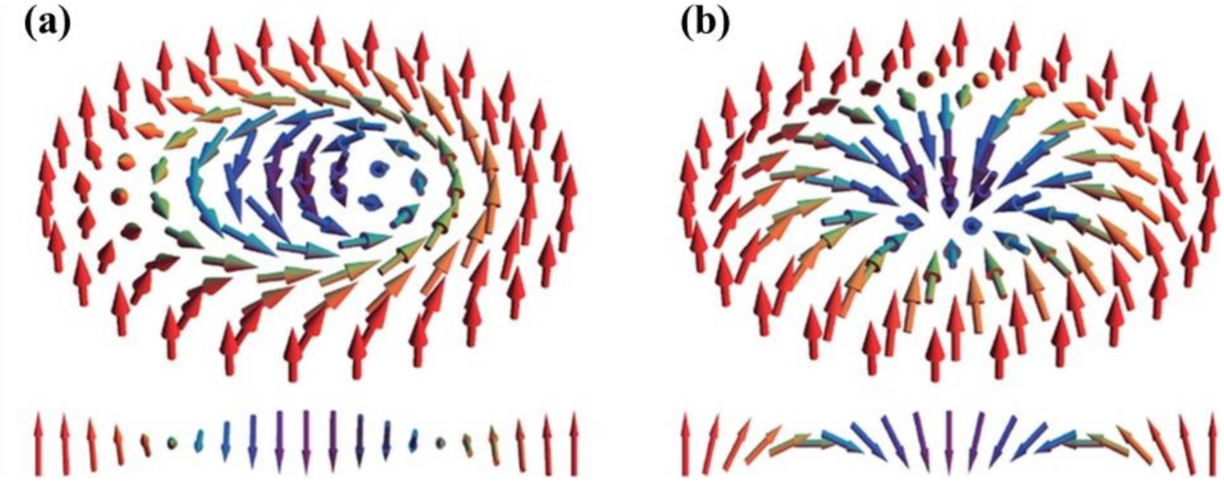

Figure 10: Schematic representation of (a) Bloch type skyrmion and (b) Néel type skyrmion shown along with their cross-sectional representation of the spins along the central diameter. Image has been adapted from [22].

In condensed matter physics such particles were first predicted along with postulations to their shape and size by Bogdanov and Hubert in 1994 [23][24]. These properties govern the response of the particle to external magnetic fields and spin polarised currents. They were first observed in bulk B20 compounds found at low temperature (< 29.5 K) in the experiments conducted by Mühlbauer *et al.* [25] using neutron scattering [26] magnetic skyrmions of 19 nm diameter were found in MnSi. In order to stabilise skyrmions in thin films, multi-layered stacks lacking structural inversion symmetry at the interface between a high spin-orbit coupling material and a ferromagnet were investigated. The first occurrence of skyrmions in such films at room temperatures exhibiting a DMI of 1.9 mJm^{-2} was found in Ir/Co/Pt multilayers by Moreau-Luchaire et al. [27] in 2016. Skyrmions have been theorised to have a distinct advantage over ferromagnetic domain walls via their ultra-low threshold energy for propagation and their negligence towards defects when moved along a track [28]. However it should be noted that recent advances in domain wall based devices such as the synthetic antiferromagnetic racetrack [29] has shown that domain walls can be moved at speeds in excess of 700 m/s there has nevertheless been recent strategies [30][31][32] for the development of different types of skyrmion racetracks in which the presence or absence of a skyrmion is recognised as a binary “1” or “0” and the detection is performed electrically. It is advantageous to move from domain walls to skyrmion based devices strictly from a dimensional point of view as individual skyrmions can be written and confined at will [33]. Moreover their diameters can be controlled by tuning the anisotropy, DMI and external magnetic fields to less than 5 nm [34][35]. Two different materials exhibiting such skyrmions are studied within this work and described in chapter 5. Current in-plane detection as well as creation of skyrmions using homogenous direct currents have led to the possibility of their adoption into the storage industry [36][37][38]. A comprehensive overview comprising of the various detection schemes of skyrmions in magnetic multilayers are outlined beautifully in this recent review by W Jiang *et al.* [39] and G. Finocchio *et al.* [40].

2.6 Domain wall motion

Domain wall motion can occur using both external applied magnetic field or with the application of current. The key difference between the two forms of domain wall motion is that field induced motion is due to the change in the Zeeman energy of the magnetic system as described earlier, while current induced motion occurs as a result of the interaction between conduction electron spins and the intrinsic magnetisation present: spin torque effects. In field driven motion all magnetic domains with spins aligned in the direction of the external field undergo an expansion as it is energetically favourable while the remaining domains with opposite orientation of the spins and field direction contract. This implies a homodirectional expansion of a particular type of domain i.e. the magnetic domain in-line with the applied field will undergo an expansion in all directions equally. For current induced motion this is not the case, current driven motion occurs via the transfer of angular momentum and therefore is uni-directional in its domain expansion. With regard to device application, current driven domain wall motion is preferred as the total magnetic state of the system does not get altered but instead gets shifted in its location thereby allowing for a memory device to be perceived [41][42]. However in PMA systems with DMI it has very recently been shown that a shift register utilising the DMI assisted field driven motion can be used as a functional device [43][44]. The two different mechanisms for domain wall motion are demonstrated in figure 11 shown below.

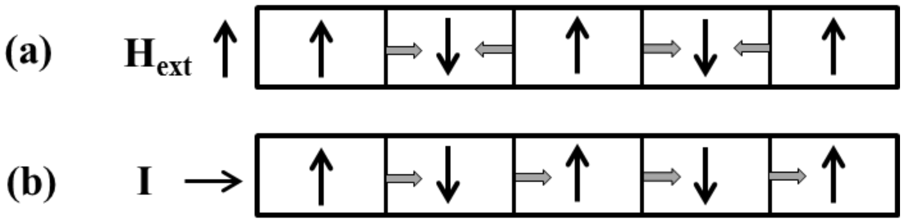

Figure 11: Schematic showing the mechanism of using (a) external magnetic field and (b) via the use of applied current in the manipulation of magnetic domains and domain walls. Field driven mechanism leads to an expansion or contraction of the domains whereas current induced motion leads to the displacement of the domain walls.

Landau-Lifshitz Gilbert equation

All the magnetisation described until now is descriptive of the equilibrium state of the magnetic material. However, it is not explicit how this evolution of magnetisation takes place to result in the equilibrium state. Here the underlying mechanism is elucidated. The time evolution of the magnetisation of a material can be expressed using the Landau-Lifshitz Gilbert (LLG) equation. This primary equation governs the magnetisation dynamics of both the nucleation of the magnetic domain wall as well as the dynamics within a domain wall. It was first derived by Landau and Lifshitz [45] in 1935 and later modified by Gilbert [46][47] in 1955.

When an external field is applied to a ferromagnetic spin it begins to precess in the presence of this applied field shown in figure 12. The torque applied due to the presence of the field is given by the precession term defined as

$$\frac{d\boldsymbol{M}}{dt} = -\gamma \boldsymbol{M} \times \boldsymbol{H}_{eff} \tag{2.16}$$

here γ is the gyromagnetic ratio, $\gamma = ge\mu_0/2m_e$, where g is the Landau g-factor($\approx$ 2). The H_{eff} is the total effective field with contributions from the external applied Zeeman fields, exchange fields, and the magnetocrystalline anisotropy fields etc.

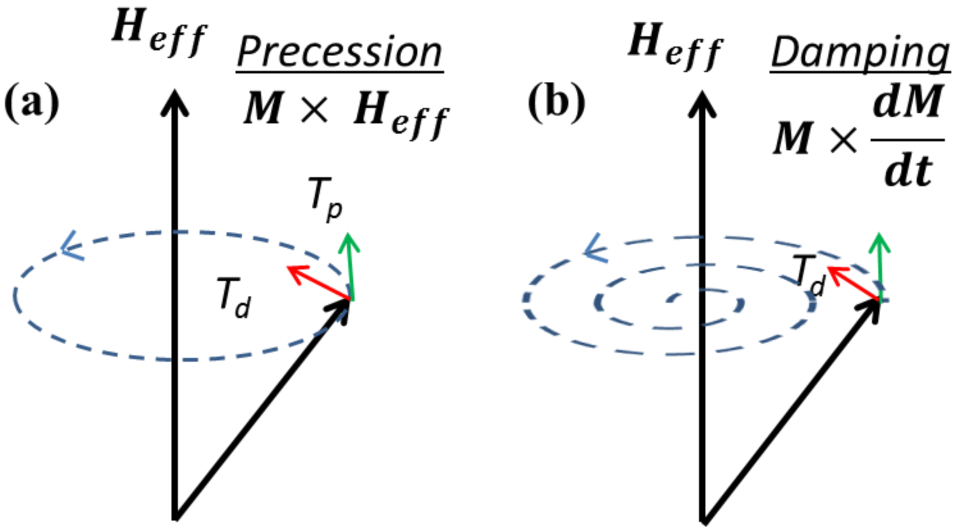

Figure 12: Magnetisation dynamics of a magnetic spin under the presence of an effective magnetic field $\boldsymbol{H}_{eff}$ showcasing (a) precession around the field direction, without any damping the magnetisation describes a perfect circle and (b) damping like torque pulling the magnetisation to align along the direction of the field, $\boldsymbol{H}_{eff}$.

If one considers this as the sole contributing torque then the magnetisation would continue to precess endlessly and not achieve a stable state. However, in reality the magnetisation does indeed attain equilibrium. Hence an additional term which incorporates within it magnetic damping is required to understand the magnetisation dynamics. A damping torque, T_d was therefore introduced and can be expressed as

$$\boldsymbol{T}_d = \alpha \boldsymbol{M} \times \frac{d\boldsymbol{M}}{dt} \tag{2.17}$$

Together, eqs. 2.16 and 2.17 form the LLG equation which can be used to describe the net magnetisation dynamics as the sum of the precession term and the dissipation term,

$$\frac{d\boldsymbol{M}}{dt} = -\gamma \boldsymbol{M} \times \boldsymbol{H}_{eff} + \alpha \boldsymbol{M} \times \frac{d\boldsymbol{M}}{dt} \tag{2.18}$$

2.6.1 Field induced domain wall motion

Magnetic domain wall motion in the presence of a field for a thin film sample can be described by magnetisation reversal process. When the applied external field is greater than the saturation magnetisation of the sample, all domains are saturated and aligned in the direction of the external field. The process of nucleation field driven reversal is shown in figure 13. As the field is reduced and is applied in the opposite direction, magnetic domains of opposite polarity will begin to nucleate. Nucleation occurs at regions where the magnetic anisotropy is partially compromised. Realistic samples have crystal defects which serve as nucleation centres for magnetic domains. There is active research on understanding and manipulating domain nucleation using artificial pinning centres. Shape anisotropy is also exploited to nucleate magnetic domains especially in magnetic domain wall sensors [48].

Once the domains are nucleated they begin to grow in the presence of an increasing magnetic field in order to reduce the total Zeeman energy contribution. New domains can also begin to nucleate on increasing fields. Once the applied field value becomes greater than the H_{sat} the sample is magnetised in the opposite direction from its initial state and a monodomain state is obtained.

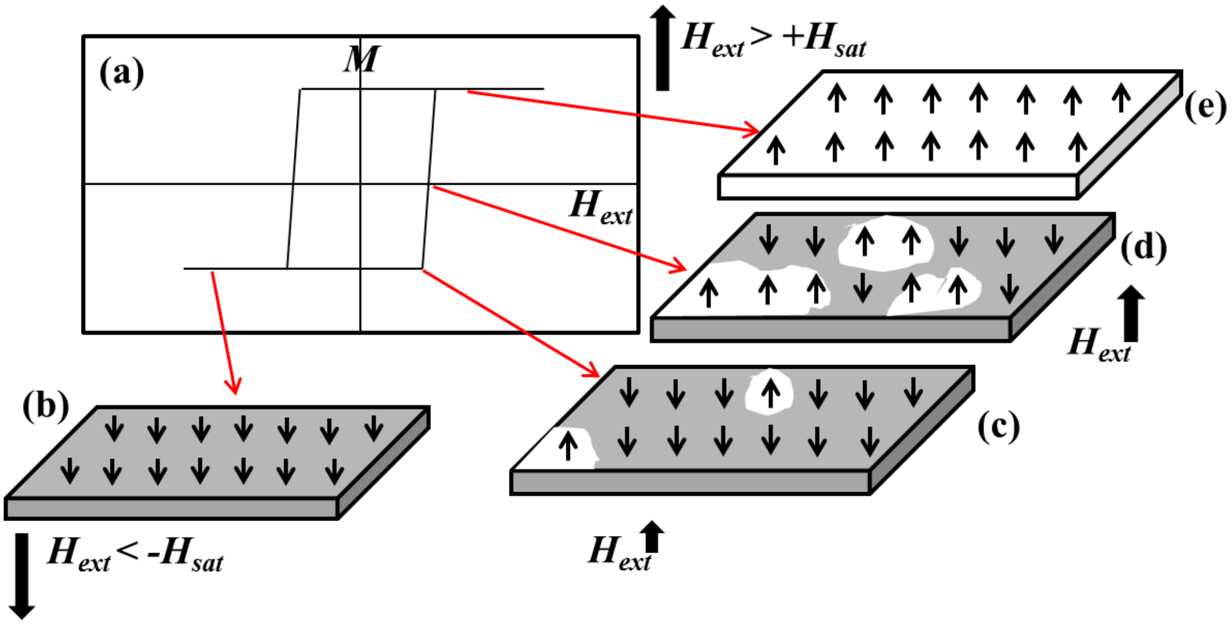

Figure 13: (a-e) Schematic description of the process of field driven domain nucleation and expansion of a ferromagnetic material along different field steps highlighted in a model hysteresis curve. (b) At $H_{ext} < -H_{sat}$ the domain is in saturation along H_{ext}. (c) For a small positive field, reverse domains begin to nucleate. (d) For slightly larger fields the domains grow in size and more nucleation occurs. (e) With the $H_{ext} > H_{sat}$ the magnetisation is fully reversed and saturated up into a single domain state.

The magnetisation dynamics of a domain wall can be understood using simplistic models due to the fact that the energetics of the system is governed by exchange and anisotropy energy which are comparatively much larger than the Zeeman energy contribution due to the external applied field and hence can be considered to be constant.

The only variable within a domain wall is its core magnetisation. The orientation of the core magnetisation can be changed depending on the direction of the applied external field. These changes of domain wall as a function of velocity were first studied by Walker [49].

At the Walker field the internal magnetisation of the domain wall begins to oscillate and the velocity suddenly decreases. On further application of field the velocity gradually increases and the domain wall collectively moves forward together as an entity. Nevertheless, the structure of the domain wall post walker breakdown changes continuously from Néel to Bloch and back to Néel type. It is more turbulent and consists of multiple backwards and forwards motion.

When considering the field induced motion on magnetic domain walls it is essential to understand the total torque which governs the resulting motion. The domain wall undergoes oscillatory and steady state motion as a function of applied fields. These two regimes for motion are determined by analysing the various field dependent torques acting collectively on the domain wall. Here a qualitative description of such torques acting on the domain wall is provided. To obtain a simplistic picture of the wall dynamics only the core magnetisation of a Bloch wall is considered, this is depicted along with the coordinate system under consideration in figure 14.

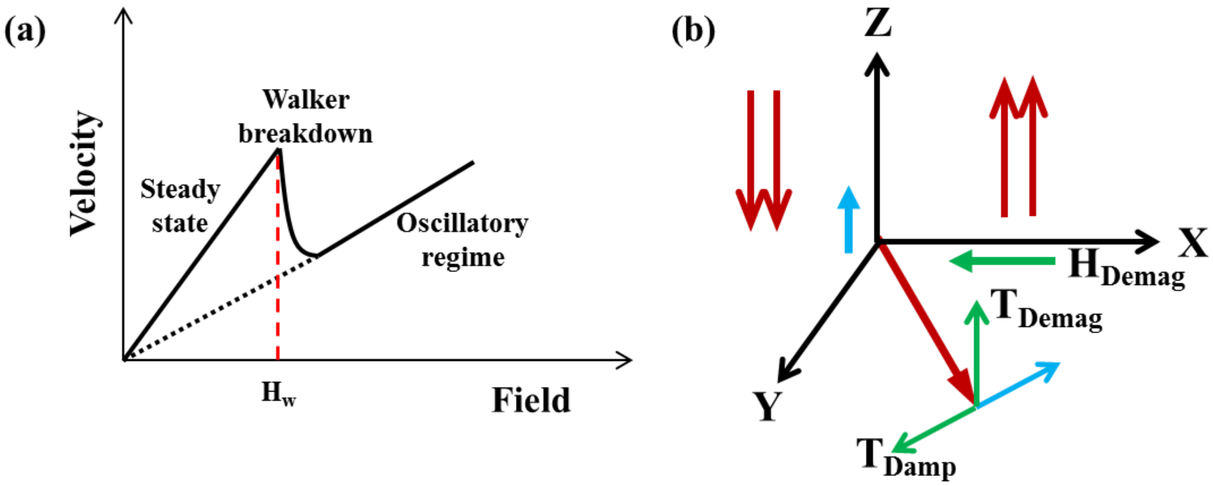

Figure 14 [50]: (a) Schematic diagram showing the velocity of a magnetic domain as a function of applied field amplitude. The domain motion exhibits two separate regimes before and after Walker breakdown at field $\mathrm{H_w}$. (b) Schematic description of the various torques acting on the central magnetisation of a Bloch wall. The applied field (shown in blue) associated with the applied torque rotates the magnetisation in the plane and creates an in-plane dipolar field H_{demag} (shown in green).

The dynamics and torques governing the motion of the domain wall in the presence of a field are given by the LLG equation described above. When an external field is applied it exerts a torque T_{app} on the domain wall. This causes the magnetisation to begin to precess in the XY plane. The rotation of magnetisation causes a build-up of magnetic charges at the edge of the domain wall. This therefore sets-up a demagnetising field H_{demag} in the negative X direction which exerts a torque in the outward direction on the magnetisation of the domain wall. T_{demag}, the demagnetising torque, therefore pulls the magnetisation **M** in the out-of-plane direction. The damping like torque, T_{damp}, associated with this motion then opposes the T_{app} and at equilibrium the two torques cancel each other's contribution and provides for a steady in-plane angle for the magnetisation. The domain wall velocity is then dictated by T_{demag}.

As the field increases the magnetisation continues to rotate causing a continuous increase in T_{demag}. However, the value for T_{demag} achieves saturation for an in-plane angle (XY plane) of θ_{XY} = 45^{o}. For $\theta_{XY} > \pi/4$ the applied field like torque is no longer compensated by the damping like torque and the magnetisation therefore precesses in the XY plane. This therefore leads to the breakdown of the domain wall known as Walker breakdown. On further increase of the field, the domain wall motion becomes turbulent and the domain wall moves forward as a single entity in the turbulent flow regime. Due to the periodic nature of the torque terms the motion of the domain wall is oscillatory. In the case where there is no damping the domain wall will move backwards and forwards about the same initial position. However in the presence of damping the forward displacement is larger than the backward one and therefore results in a net positive displacement in one period with a non-zero average velocity. Since the domain wall undergoes repeated forward and backward motion in this regime the velocity as a function of field is lower post Walker breakdown than in the steady state regime. The analytical expressions of the torques are detailed by A. Mougin [51].

The process described here is not the magnetisation reversal process at the macro-scale for a thin film sample but instead the internal field dependent dynamics of the domain wall itself. The magnetisation of a material will begin its nucleation process above a critical nucleation field governed by defects in the lattice etc. This is explained in the following section along with the theory of domain wall creep motion.

2.6.2 Pinning related phenomenon: Domain wall creep

The influence of field on the magnetic domain motion is governed by the LLG equation as described in the section above. However, this model is only observed in an ideal system. Here the domain motion at room temperature and over large length scales of the sample is explained. The domain wall motion in real samples especially at low fields is governed strongly by crystal imperfections and disorder in the material. As explained earlier these sites of disorder serve as nucleation centres. Apart from that they also act as domain wall pinning sites which modify the domain wall motion. At zero temperature, such centres can completely stop domain wall motion. However, at finite temperatures, there is an interplay between the thermal energy and the energy potential of the pinning site, U_c which defines the resulting domain wall motion. The thermal motion of the domain wall can be assisted by applying a magnetic field. The associated Zeeman energy can then overcome potential barriers of the pinning site and allow for motion. In this respect the domain wall motion can be classified into three different regimes, the creep and thermally assisted flux flow regime, depinning regime and the flow regime. In the creep regime the domain wall motion is thermally driven and, below a certain critical field known as the depinning field H_{dep}, is dominated purely by defects within the landscape of its motion. The velocity of the domain wall is reduced due to these pinning centres and is given by the creep law [52] as,

$$v = v_o \exp\left[-\frac{U_c}{kT}\left(\frac{H_{dep}}{H}\right)^{1/4}\right] \tag{2.19}$$

Here v_o is the characteristic velocity related to the length of wall section that undergoes a forward jump (thermally assisted) in displacement before the avalanche breakdown in which the remaining section of the wall moves forward. The domain wall therefore in this regime can be interpreted as an elastic interface moving in the presence of weak disorder [53]. Increasing the acting force on the wall, in this case the magnetic field, allows for an increase in the total domain wall energy, this along with the thermal energy allows for the wall to overcome local pinning defects. The domain wall is then said to be in the depinning regime and the field above which the wall is no longer pinned by defects is known as the depinning field. The velocity of the wall in this regime undergoes a sudden increase as can be seen from figure 15.

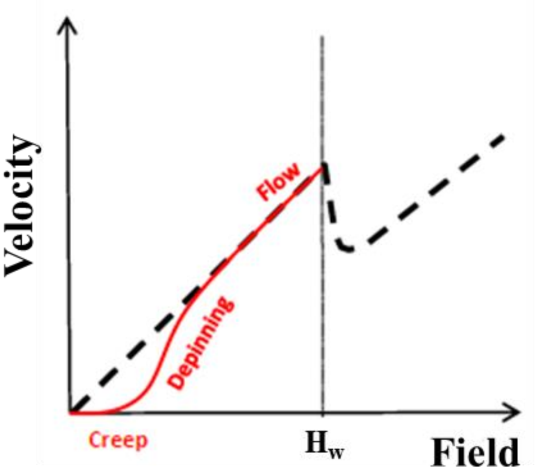

Figure 15 [54]: Schematic diagram of the experimental field induced velocity (shown in red) as compared to the theoretical description of the velocity dependence (shown in dotted black curve). The Walker field occurs at fields larger than creep and de-pinning, the observed linear dependence then corresponds to the steady state flow regime.

As the field value is increased further, the domain wall moves into the flow regime in which it overcomes any defects present due to the intensity of the magnetic field. The velocity in this regime is linear with field as predicted theoretically.

2.6.3 Induced perpendicular magnetic anisotropy

The magnetisation for a large number of samples lies within the plane of the thin film in order to minimize stray field energy. However, by selectively choosing the materials and tuning the growth of a film it is possible for the magnetic anisotropy in certain situations to align in the plane perpendicular to the film growth plane. Thin films which possess such an orientation of the magnetisation are referred to as out-of-plane films or films with perpendicular magnetic anisotropy. The magnetic domains within such a film point either outwards or inwards. There exist multiple methods of achieving out-of-plane magnetised domains. Earlier methods involved the use of strain based anisotropy to orient the domains along a particular axis which was situated in the out of plane direction. These were done using special single crystalline substrates and usually require complex growth measures utilizing high temperatures. PMA in such films arises from the bulk of the crystal with typical thickness in the range of >15 nm. However, recently there have been tremendous efforts to achieve out of plane magnetised complex multi-layered stacks due to the large number of industrial applications as well as rich physics found at the interface [55]. Three prime advantages of using PMA films for storage devices are increased storage capacity per unit area of film, secondly large increase in the read/write speed of the memory devices with PMA and thirdly lower critical switching current, i.e. lower power usage during writing processes (increased efficiency).

Hence, there is a strong industrial focus on achieving films with PMA which have Complementary Metal-Oxide Semiconductor (CMOS) compatibility. Apart from bulk PMA mentioned earlier, interfacial PMA also exists in ultra-thin films. Here the underlying theory giving rise to PMA at an interface between two materials is discussed.

Material films which exhibit interfacial PMA typically consist of the following three functional layers:

- A seed layer, typically HM layer with large spin-orbit coupling relatively thin (approx. 5 nm or less).
- A ferromagnetic layer. This can be a pure elemental FM or an alloy doped with various light materials. The thickness of which is typically less than 2 nm.
- An oxide layer. A light oxide layer typically Si, Mg or Al oxide. This is used as a protective cover as well as a means to induce structural inversion asymmetry to the stack and perpendicular magnetic anisotropy (< 2 nm).

In ultra-thin films the ferromagnetic materials used are polycrystalline in nature with nanometre sized grains and grain boundaries are amorphous in nature. There is therefore no long range structural order within the material to justify crystallographic reasons for PMA as is the case for bulk films. Hence in ultra-thin films there exists a perpendicular magnetic anisotropy developed at the interface. The interfacial origins of PMA arise from both the interfaces the HM/FM and the FM/oxide interface. There exists strong hybridisation between the 5*d*-3*d* orbitals of the HM and FM. Due to SOI the electronic orbitals which have their moments in the out-of-plane direction are energetically favoured and therefore the magnetisation aligns in the Out-Of-Plane (OOP) direction. By first principle calculations [56][57] it has been shown that the atomic orbital overlap between the 3*d* and 2*p* states of the iron and oxygen respectively, also contribute to the PMA in such FM/oxide multilayer stacks. Hence both interfaces are important in the role for providing PMA. More importantly as it will be shown in chapter 4, the interface quality as well as the exact combination of both the HM and FM are required to obtain PMA. It still isn't clear as to how the PMA is brought about in HM with different Spin-Orbit Coupling (SOC) strengths. Therefore a deeper theoretical knowledge of PMA in high SO coupling material interfaces is required. Fine tuning of the FM/oxide interface via annealing has revealed the internal mechanism of interfacial PMA to an extent. Very recent work by Wang *et al.* [58] (shown in figure 16) has revealed that post annealing the crystal structure of the ferromagnet is modified to a pure crystalline form. It is suggested that the changing of the material structure is responsible for an enhancement in the PMA. By tuning the PMA it is possible to obtain an enhancement of the current induced domain wall motion as has been demonstrated micromagnetically by Emori *et al.*[59]. It was shown by Pai *et al.* [60] that one can obtain an enhancement of PMA when a Hf layer is inserted between a W and $Co_{20}Fe_{60}B_{20}$ layers. This is attributed to the high negative formation enthalpy of Hf borides which causes Hf to act as a boron “sink” which in turn leads to a change in the magnetic anisotropy of the ferromagnet. It should be noted here that the role of boron in such ferromagnetic alloys is not restricted only to the tuning of PMA [61] but also impacts the sign of the DMI. Emori *et al.* [62] demonstrated that the DMI is negative for Ta/CoFe/MgO structures whereas when Ta/CoFeB/MgO structures were investigated by Lo Conte *et al.*[63] and Khan *et al.*[64], the observed DMI was greater than zero, thereby highlighting the role of boron [65] in such interfacial phenomenon.

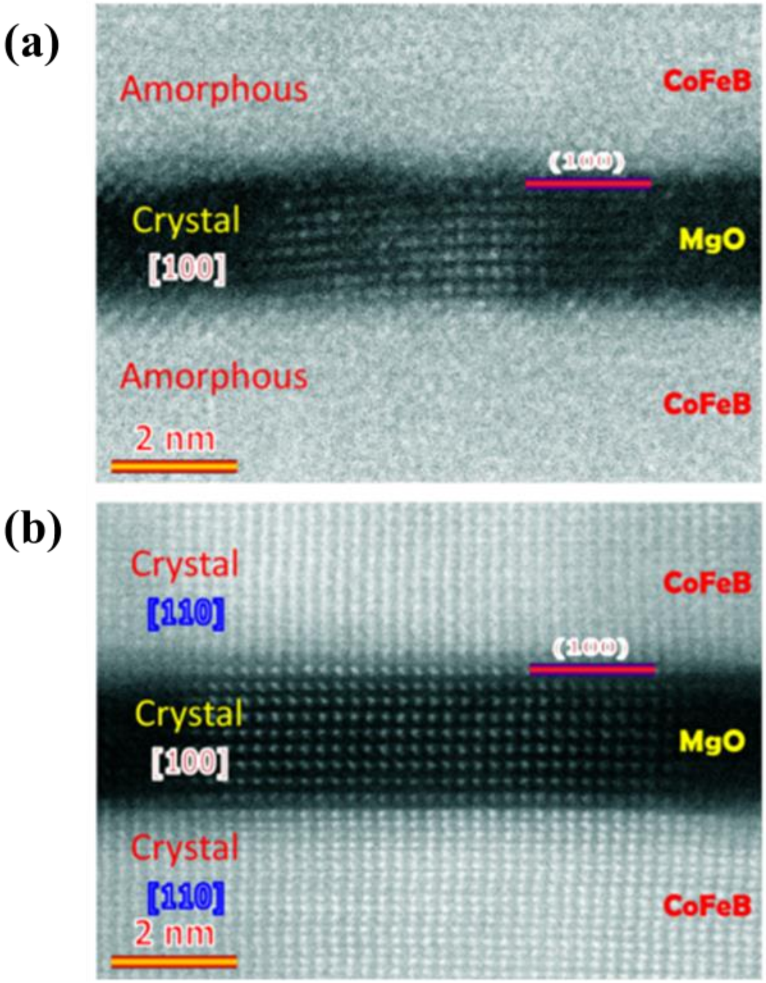

Figure 16: Structural transformation of the CoFeB and increased crystallinity at the interface with MgO by annealing. (a) cross-sectional TEM image of an as deposited trilayer of CoFeB/MgO/CoFeB showing crystallisation of MgO [100] (b) by post deposition annealing the ferromagnetic alloy transforms from amorphous phase into a crystalline phase. The TEM image is extracted from Wang *et al.* [58].

CoFeB which is the preferred ferromagnetic alloy for use in Tunnel Magneto-Resistance (TMR) devices for its high spin polarisation [66], is grown in an amorphous phase. This is capped with MgO which grows in [100] textured orientation [58][67]. The ferromagnet is seeded with a heavy metal. On annealing, the boron due to its low mass and therefore high mobility migrates towards the heavy metal to form metal borides at the bottom HM/FM interface [68]. This occurs as a result of the large negative formation enthalpy of metal borides of the HM [69][70]. The ferromagnet then becomes partially textured due to the stencil growth of the MgO directly above it. The annealing therefore enhances the total TMR as it results in a cleaner interface and hence facilitates electron tunnelling [67][71][72]. Moreover the annealing allows for the 3*d* and 2*p* atomic overlap which thereby enhances the PMA. However, the process of annealing for the modification of an interface needs to be regulated as excessive temperatures or duration of the process can cause an over build-up of boron at the bottom interface. This can interfere with other properties such as spin diffusion across an interface [73], spin mixing conductance [74] and interfacial spin orbit torques [75] all of which may have a derogatory impact on SOT devices ultimately.

2.7 Thin film deposition and lithography

In recent years there has been a strong focus in research at the interface of two materials which have led to many interesting discoveries such as the interfacial spin-orbit torque [75] or the Rashba torque [76], interfacial magnetoresistance [77] and the interfacial Dzyaloshinskii-Moriya interaction [78]. The core requirement of the various phenomena mentioned above and those which are studied in this work require acute control over the interfacial quality during thin film growth. The concept of spin dependent scattering of electrons for example, was laid by Fert and Campbell as early as [79]. However, the technology for its use as a Giant Magneto-Resistance (GMR) spin-valve, had to mature to a certain level of sophistication with respect to thin film growth and the various steps of processing and patterning before it could be implemented into commercial devices. It was only in 2001 when the first GMR read heads were produced commercially for use in hard disk drives. Here I will introduce briefly a few widely used processes for thin film deposition and will delve deeper into the theory of the process used to grow the thin films in this work, i.e. sputter deposition. The theory of nanopatterning is also explained in this section as an overview. Nanoscale lithography is a science in itself and the interested reader is directed towards more comprehensive texts detailing innovative techniques for achieving ultra-fine structures [80][81].

2.7.1 Introduction

Different processes are used to deposit different kinds of materials depending on the ultimate thickness, and the quality desired from the growth process. There exist two broad categories of thin film deposition Physical Vapour Deposition (PVD) and Chemical Vapour Deposition (CVD) [82][83]. Physical processes rely on a certain kind of ejection of atomic species from a target source either due to evaporation or sputtering. Whereas chemical processes rely on changes in the physical properties during chemical reactions. There are essentially two different kinds of CVD processes that are used. One which involves a film that is grown from a medium due to certain chemical formations, typical methods of this kind of growth are electroplating, vapour phase deposition and chemical reduction plating. Another category of CVD processes involve the formation of a film by the use of precursor gases e.g. iodization, gaseous iodization, thermal growth. Methods used for thin film growth in this work employed PVD processes, some of which are briefly highlighted below.

2.7.2 Thermal evaporation

This method of thin film deposition is used for depositing single element materials. In its simplest form the material in question is placed in a crucible enclosed with resistive wire. The crucible is then heated to high temperatures by passing current. This in turn heats the source material which then evaporates and proceeds to be deposited on the substrate material placed in line of sight above the crucible. This however leads to a contamination issue that some material from the crucible may also evaporate which may contaminate the deposited film. Another disadvantage of this method is that not all metals maybe evaporated but only materials with a low melting point. In order to deposit for e.g. W or Mo films this method is not suitable. It is especially difficult to deposit alloys unlike sputter deposition which are crucial in magnetic memory devices. Since each material of an alloy has different vapour pressure therefore the deposition rate during the thermal evaporation for each material in the alloy would be different this in turn results in a film with a different stoichiometry on the substrate than in the crucible. Apart from this a main reason for its lack of use in industrial research is that it is not easily scalable to large wafer sizes as the homogeneity suffers as substrate size is increased. Having mentioned that, it is a quick method to produce relatively thick films 10-100 nm, with not extremely low pressures making the process relatively inexpensive. Moreover, the lack of any precursor gas allows complete unadulterated film depositions. Also due to the fact that a point source is used it results in a poor uniformity as compared to sputter deposition explained below.

2.7.3 Sputter deposition

The growth process that has been adopted for large scale use in industries as well as for research purposes is sputter deposition. This process is a faster growth process compared to thermal evaporation. Sputtering is a molecular mechanical deposition process and is defined as the physical bombardment by ionised atoms onto a target surface which leads to an erosion of the target species and a subsequent deposition of the material onto the substrate. A schematic indicating the processes involved during sputtering is shown in figure 17. This process is dominated by physical momentum exchange between the bombarding ion and the required material for deposition. The material atoms are mechanically ejected from the target surface and deposited onto the substrate. This process is very versatile and can be used to deposit a wide variety of materials. A gaseous species is used as a medium for sputtering. A noble gas such as Argon or Krypton is used as sputtering gases so as to prevent any modification to the chemistry of the target atoms.

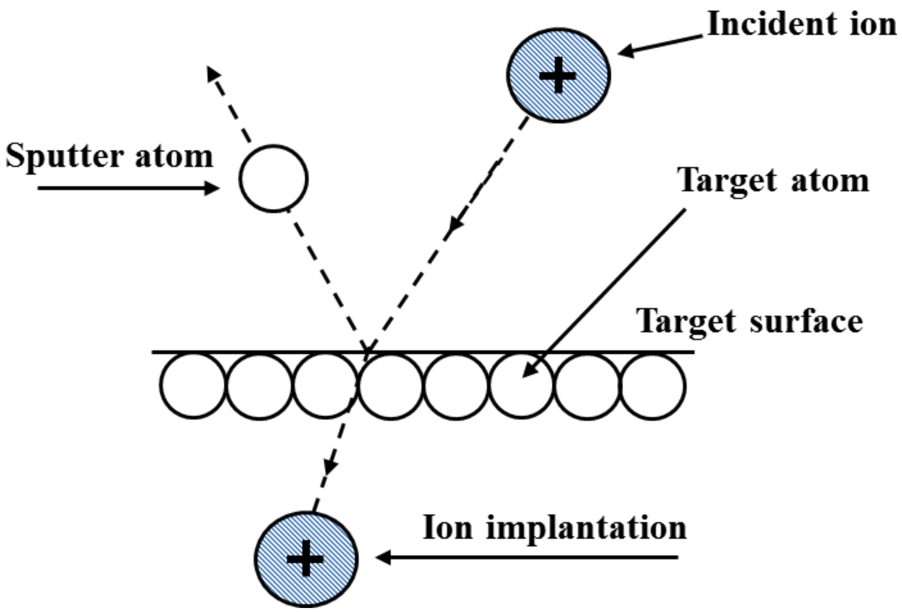

Figure 17: Schematic diagram of the mechanical processes involved during the sputtering of a target surface.

In Direct Current (D.C.) diode sputtering of metals, a potential difference is created between the target cathode and the substrate which causes electrons to emit from the cathode and inelastically collide with the Ar atoms. This causes the Ar atoms to ionise and accelerate towards the target material. The Ar ions mechanically bombard the target and sputter away the target atoms. These target atoms disperse throughout the sputter chamber and subsequently adhere to the substrate. It may be possible that apart from the material to be deposited on the substrate some degree of Argon implantation might also occur. The Ar ions formed can recombine and stop the process of sputtering, therefore in order to have continued sputtering one needs to achieve a self-sustaining plasma. Secondary electrons are produced during the initial bombardment of the target material with the Ar ions. These secondary electrons are then used for continued plasma. In order to obtain a higher sputtering rate the cathode voltage and the working pressure may be increased. However, in conventional D.C. diode sputtering this causes large amount of heat generation, and increased collisions between target species and gas ions due to increased gas flows (as the mean free path reduces for higher gas pressures the chance of Argon implantation also rises). Therefore in order to reduce the voltages while keeping the high sputter rates at the target surface, one must increase the number of bombardments at the target surface. This is done by confining the plasma itself near the target surface using magnets underneath the target in a process called magnetron sputtering. Strong

NdFeB magnets are used for their capability to withstand high temperatures and placed behind the target materials in the N-S-N configuration. This magnet configuration produces closed flux loops through the target surface which leads to the confinement of secondary electrons produced from the ionisation of Ar to near-the-surface of the target. The magnetic pole pieces are oriented such that the magnetic field lines are parallel to the cathode surface. Due to increased plasma density near the surface the entire process can be carried out at a lower pressure. A schematic showing the chamber and the process of sputtering is shown in figure 18.

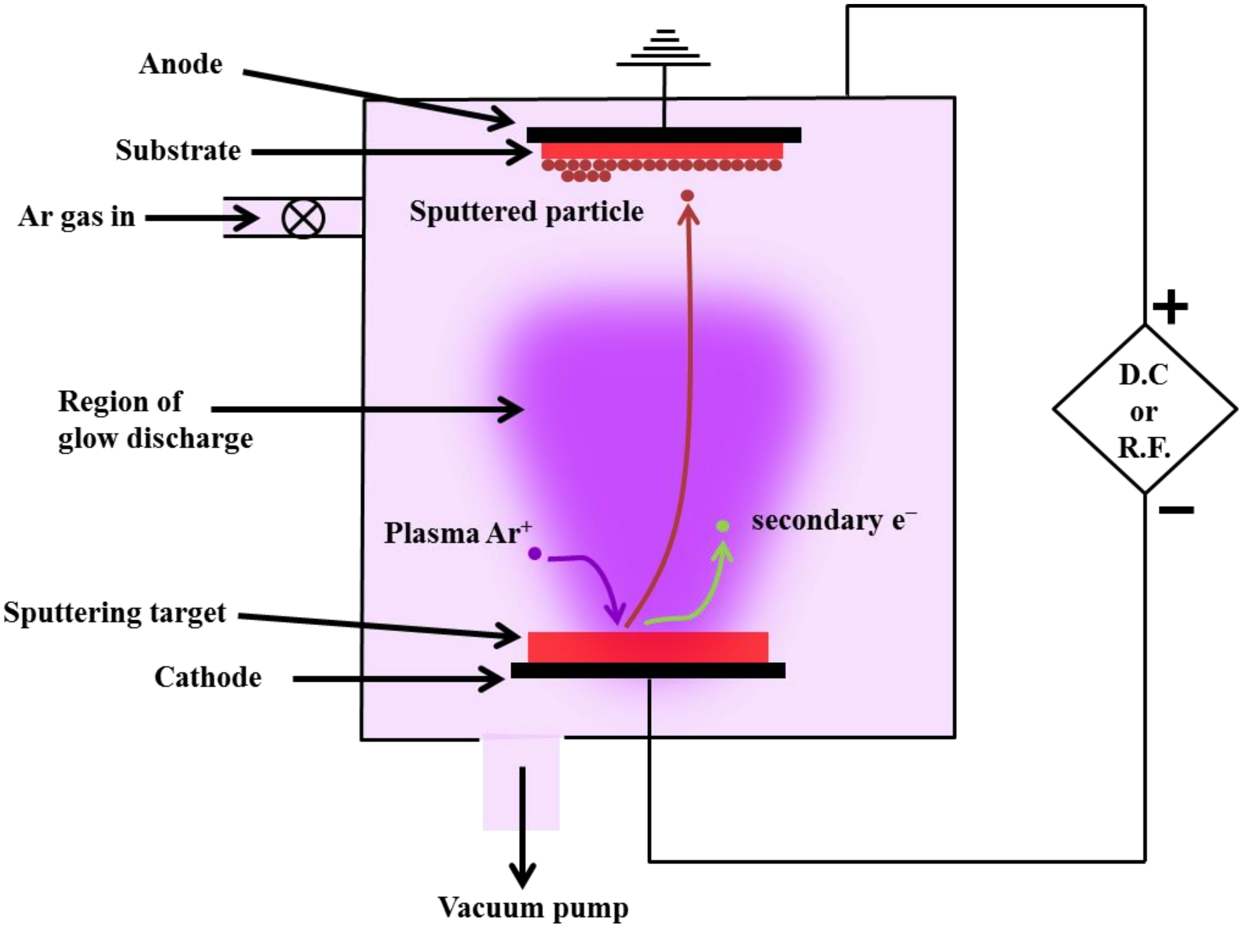

Figure 18: Schematic line diagram of a thin film sputter deposition chamber detailing the basic constituents of a chamber and formation of plasma within it during the process of sputtering.

An advantage of using sputtering as compared to evaporation is that due to its mechanical process of sputtering away target species, the stoichiometry of the metal compounds is preserved during sputtering since all components are sputtered with a similar rate. This is true after presputtering of the composite target. Using D.C. magnetron sputtering allows a large number of metals to be sputtered. However for the deposition of oxides and other insulating materials one cannot use D.C. sputtering. D.C. sputtering causes the build-up of charges on the surface of the electrically insulating materials. This then repels the incoming ion bombardment and therefore stops the process of sputtering. In order to remove these charges an alternating current needs to be applied which will cause these charges to be removed, by a process known as Radio Frequency (R.F.) sputtering. In R.F. sputtering an alternating potential used allows for the prevention of charge build up at the cathode (target). The growth of MRAM devices and GMR or TMR read heads often require a combination of different sputtering processes for different layers used within the stack.

2.7.4 Nanopatterning

For both research and industrial purposes thin films are required to be patterned into nanostructures to study domain wall motion and their interactions in confined spaces or for the production of MRAMs, and GMR sensors. The process of structuring and processing of full continuous films to obtain nanostructures via a controlled lithographic technique is known as patterning of thin films. For PMA based memory, as newer materials are found with higher anisotropies, it allows one to decrease the cell sizes to smaller dimensions in order to pack more information per unit area. Therefore thin films can be structured with smaller feature sizes while remaining within the super paramagnetic limit. Moreover, patterning of thin films allows one to have a greater control over the flow of current within the material along a particular direction. There exist multiple techniques which can be used to obtain structured thin films, depending on the smallest feature size and processing time available.

There exist two general categories of structuring of materials into nanostructures, the top down and the bottom-up approach. The former is more scalable and allows for systematic long range order and coverage, but it usually makes use of sequential writing/patterning through a mask or a pre-defined template to be written on a substrate this is usually a slow process. The bottom up or "self-assembly" approach refers to using short range interactions between two atomic or molecular species to produce large area coverage. Using such a technique, a high spatial resolution can be obtained, however, the repeatability of structures over a large range is poor [7][84]. In this work, electron beam lithography is made use of for the structuring of the thin films. The lithographic processes were conducted in close collaboration with Mr. K. Litzius. The process of electron-beam lithography is highlighted in figure 19 and described below.

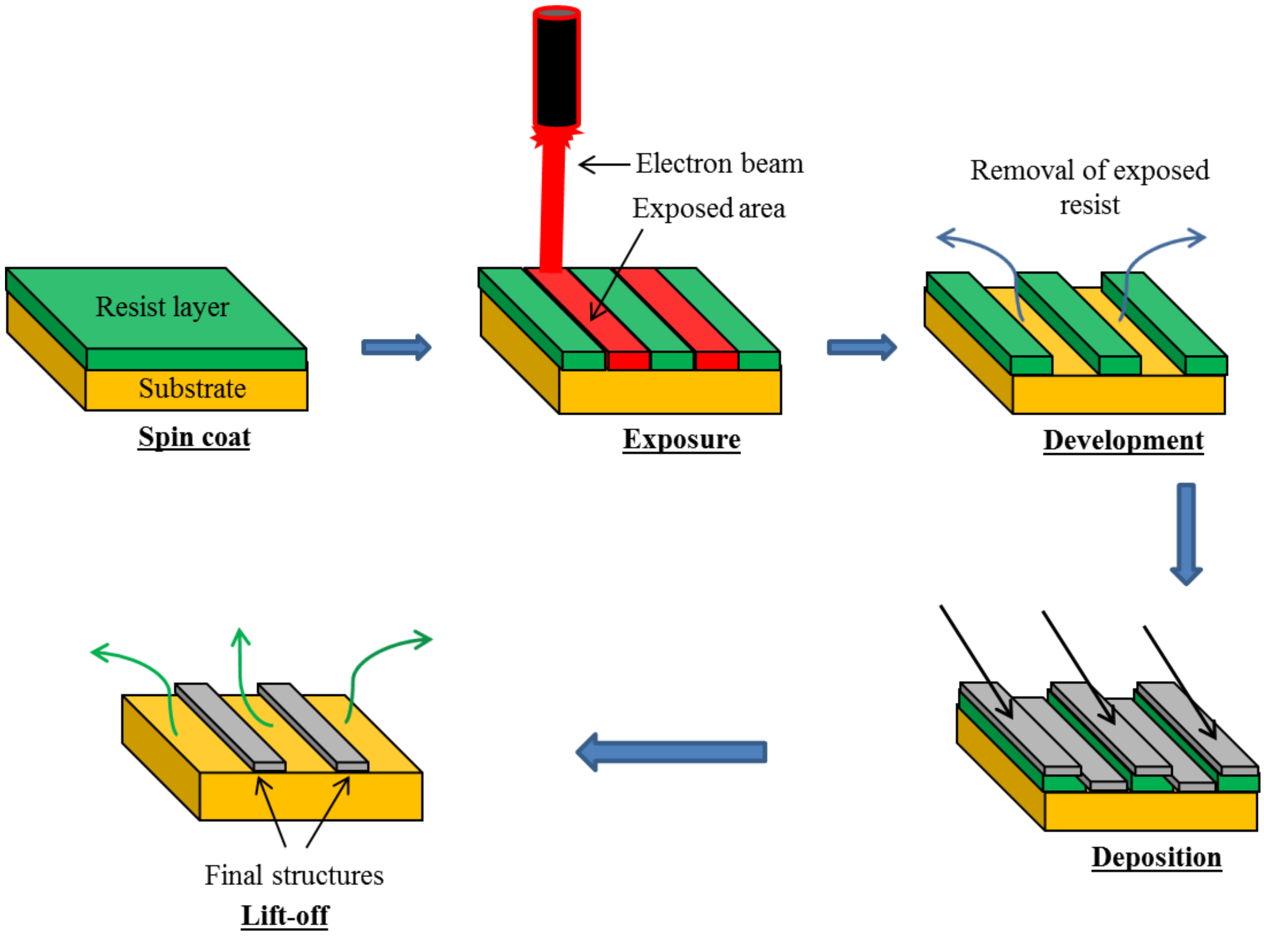

Figure 19: Schematic description of the device fabrication using electron beam lithography illustrating the various steps involved. An electron-beam is used to expose a previously spin coated resist onto a substrate layer. Following which chemical alteration is brought about via the use of a developing solution and subsequent removal of the resist. The film is then metallised and the final structures are obtained via lift off usually done using acetone.

In electron-beam lithography, electrons are used to produce a stencil design on a continuous film from which the nanostructures can be obtained. Initially a substrate is spin coated with a suitable resist. A mask is created in this resist layer by exposing the resist to an electron beam which is traced on the substrate to obtain the desired design. If the dosage of the electron beam is appropriately high it causes the breakage of the bonds of the molecules within the resist layer. The resist is now "exposed". The film along with the resist is then treated chemically via a developer which dissolves the molecules with the broken bonds. This leaves only the un-exposed stencil pattern on the film surface. Following the production of this mask, metallisation of the substrate can be performed in which the desired material is deposited. The remaining resist is then removed via "lift-off" which completes the process of lithography. This leaves only the material deposited in regions with the exposed resist resulting in a patterned thin film. For a more detailed description of electron beam lithography and its effects on edge roughness on magnetisation dynamics in nanowires can be found by D. Atkinson *et al* [85].

2.8 Magneto-Optical Kerr effect (MOKE)

The magnetic response to field is one of the fundamental characteristics of any ferromagnetic material. Therefore studying this hysteretic response is crucial for the development and understanding of the underlying physics for a given material. One method to do this is using the Magneto-optical Kerr effect. Here the underlying theory of the effect is presented the technique of which is employed to study the materials in this work.

It is the interaction between visible light and magnetic material which leads to magneto-optical effects where differently polarised light beams experience different refractive indices when interacting with the magnetic material. The magneto-optical Kerr effect consists of the rotation of the plane of polarisation when polarised light is reflected from a magnetic material. The rotation of the plane of polarisation of light was first reported by Faraday in 1845 [86] for light transmitted through a sample. Later in 1877 a similar effect was observed by John Kerr [87] for light reflected from a magnetic sample. Even though the Faraday effect is stronger it is limited in its usage since the sample is required to be transparent. The MOKE effect therefore can be described as the change in polarisation of reflected light and is directly proportional to the change in the magnetisation of the investigated material [87][88]. A topical overview of magnetic microscopy techniques is detailed by J. McCord in [89].

Depending on the orientation of the magnetisation of a film the MOKE effect can be probed in different configurations. These geometries are outlined below along with the physical origin of the effect in section 2.8.2.

2.8.1 Geometries of the MOKE

There exist three different geometries in which the MOKE effect is commonly observed. They depend on the relative orientation of the magnetisation vector within the sample and the plane of incidence of the incoming light. The three geometries used are termed longitudinal, transversal and polar. These geometries are shown schematically in figure 20.

When the magnetisation lies within the plane of the film and is oriented parallel, or perpendicular to the plane of incident radiation, the configuration is termed as longitudinal or transversal geometry, respectively. When the plane of magnetisation orientation is out of the plane of the sample and parallel to the incident light the geometry used is termed as the polar geometry.

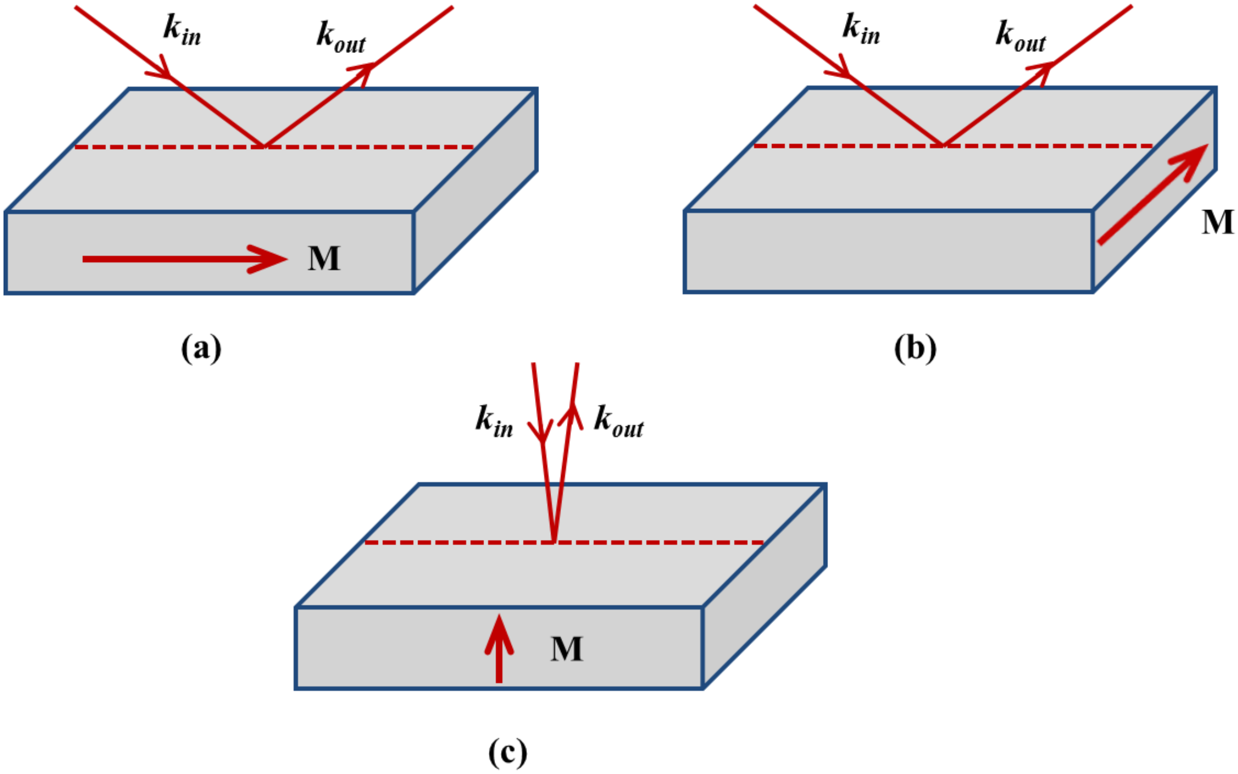

Figure 20: Schematic to show the three different geometries of the MOKE and the relative orientations of the magnetisation (a) longitudinal, (b) transversal, and (c) polar.

Due to the properties of the systems studied here the samples can exhibit both in-plane and out of plane magnetisation. The MO Kerr effect was first used to study magnetic domains by Fowler *et al.* [90] in 1953. He used the Kerr effect to observe domains on a (110) surface of silicon-iron crystal. The origin of the MOKE effect for these geometries is explained in the section below.

2.8.2 Origins of the Magneto-Optical Kerr Effect

In the Kerr effect, when linearly polarised light is reflected from a magnetic material it is no longer linearly polarised. Instead the reflected light is elliptically polarised with the primary polarisation axis off by a certain degree as compared to the initial polarisation. This amount of ellipticity and the degree of rotation is given by ε_K and θ_K, respectively. Together the complex Kerr angle may be defined as $\phi_K = \theta_K + i\varepsilon_K$. In order to obtain a deeper understanding of the MOKE one must consider the quantum mechanical response of the material towards incoming electro-magnetic radiation. The microscopic origin of the Kerr effect can be attributed to spin-orbit interaction present within the ferromagnetic material. The MOKE can be considered as a birefringence effect due to the magnetic properties of the sample, where spin-orbit coupling and exchange interaction act at the same time on the electronic states involved in the absorption/emission processes [91][92]. For a detailed overview of the quantum mechanical origin of the MOKE effect the reader is directed towards references [93][94].

The electric field of an incoming radiation consists of two components, s and p defined as the components perpendicular and parallel to the plane of incidence. When polarised light of a given source is incident on a material the electric field component of the electro-magnetic radiation causes a motion of electrons, this motion of electrons acts as a source and re-radiates the light with equal wavefronts of the same frequency. However, when linearly polarised light is incident on a magnetic material it causes a change in the angle of the plane of polarisation.

Classically the MO Kerr effect can be interpreted via the Lorentz force. Incident beam of light with an electric field $\mathbf{E}^{\mathbf{i}}$ excites electrons within a material which causes them to oscillate with a velocity $\boldsymbol{v_e}$. Due to the non- zero internal magnetic field, $\mathbf{H}_{\text{int}}$ of the material and the oscillating electrons a Lorentz force will influence the motion of the electrons, of the form, $\mathbf{F}_{lor} = -e\mathbf{v}_e \times \mathbf{B}_{int}$. Such oscillations cause re-emission of EM radiation with an added component, $\mathbf{E_k}$ to the total electric field. This is defined as the Kerr component. Due to the additional Kerr component the reflected beam exhibits a different state of polarisation with respect to the incoming beam. The in-phase component of $\mathbf{E_K}$, with respect to $\mathbf{E^r}_{\mathbf{s,p}}$ generates the Kerr rotation θ_K, while the out-of-phase component of $\mathbf{E_K}$, generates the Kerr ellipticity, ε_K .

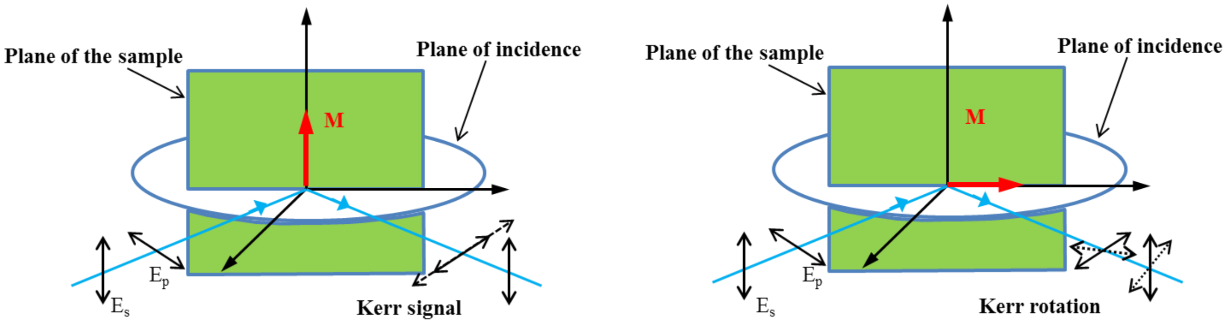

(a) Transverse **(b) Longitudinal**

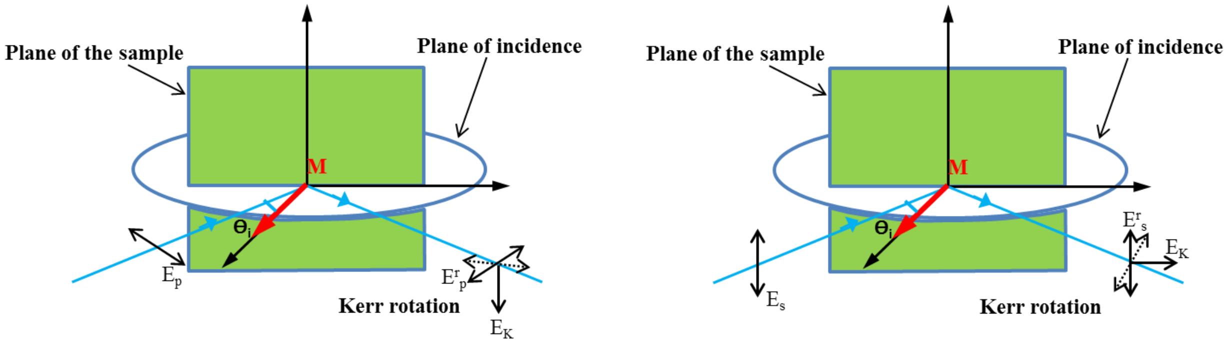

(c) Polar- ***p polarisation*** **(d) Polar-** ***s polarisation***

Figure 21: The MO Kerr effect underlying principle detailing the *s* and *p* polarisation of incoming radiation and its subsequent manipulation for (a) transversal (b) longitudinal and (c-d) polar geometry of the MOKE set-up.

As depicted in figure 21, the polar MOKE configuration sensitive to the out-of-plane magnetisation of a thin film results in both the *s* and *p* components undergoing Kerr rotation. In order to maximise the Kerr signal the orthogonality between the electric field vector and the sample magnetisation is maximised, this implies the angle of incidence, θ_i must be small ($\theta_i \approx 0$). Hence for polar configurations the light is incident normal to sample plane.

For longitudinal and transversal orientations the intrinsic magnetisation of the sample lies in the plane of the material, incident light must be presented at oblique angles to the sample. Since, if electric field and magnetisation are parallel it would result in no Kerr effect. In the transverse geometry the magnetisation is perpendicular to the incoming radiation and therefore provides for the magneto-optical enhancement of the *p* component of the electric field. In longitudinal geometries the magnetisation lies parallel to the plane of incidence of the incoming radiation and therefore results in the rotation of the angle of polarisation.

2.8.3 MOKE depth sensitivity – penetration depth

The MOKE effect is a surface sensitive effect determined by the electromagnetic penetration depth of the thin film under investigation. The penetration depth is a material dependent property that quantifies the drop in light penetration and defines an upper limit for the information depth achieved during a MOKE measurement. It is defined as the depth at which the laser intensity is attenuated to $1/e$ of its initial value due to absorption effects within the material. This depth is known as the skin depth of a given material. For an estimate, the skin depth for NiFe as measured by Bogart *et al* [9] is approximately 10-15 nm depending on the growth texture. The skin depth is defined as

$$\lambda_{MOKE} = \frac{1}{2k\beta} \tag{2.20}$$

where k is the modulus of the wavevector of the incident light and β is related to the absorption within the material. The Kerr response to films thinner than the penetration depth is directly proportional to the amount of magnetic material. The MOKE is one of the fastest and most versatile methods of understanding magnetic responses in thin films for both research and industrial development of devices. Due to the fact that the laser MOKE employs the use of a laser spot ($\sim \mu$m) its sensitivity to magnetisation response is very localised. Therefore the magnetic response of nanowires separated by a few microns can in principle be studied using this technique. While at the same time wide field Kerr microscopy can be used using a lamp source instead of a laser spot and an area of few hundred microns can be investigated at a given instance. Hence the MOKE is a very effective tool for understanding magnetisation dynamics in both thin films and nanowires.

2.9 X-ray reflectivity

In order to obtain an insight to a number of bulk and interfacial effects it is imperative to understand the underlying crystal structure of the material along with other structural properties. There exist a number of techniques which are conducive to the exploration of the surface structure and the bulk structure. A vast number of magnetic properties are influenced by the structure of the materials used for both thin films as well as bulk materials. For example the magnetisation reversal for the GMR tri-layered structure such as FM/NM/FM is strongly influenced by the thickness of the Non-Magnetic (NM) spacer layer which in turn influences the signal obtained from such a read head. The crystal structure too has been shown to have a direct influence on the total TMR percentage for a MTJ stack where a higher crystallinity of the barrier allows for more coherent tunnelling to occur. Hence it is very important to have an understanding of the structural properties. Here the principles behind the mechanism of the X-ray reflectivity are outlined which is used to study the material thickness, roughness and the electron density of the multi-layered thin films studied in the following chapters. The experimental details of this method are outlined in chapter 3.

2.9.1 Theory of X-ray reflectometry and total external reflection

When Electro-Magnetic (EM) radiation is incident on a material the incident photon is absorbed which causes the electron cloud of an atom to undergo oscillations. This oscillation then acts as a source of EM radiation and re-radiates instantly a photon with the same energy in an elastic process known as non-resonant scattering [95]. When the incident photon is incoming with sufficient energy to promote an electron from a current ground state into an unfilled orbital, it causes the atom to move into an excited state in a process known as absorption. The atom can then undergo a change to its relaxed state through a dissipative process and decay in the form of thermal radiation via phonons or the atom can undergo spontaneous emission and release energy radiatively via the emission of photon with the same energy as the energy difference between the ground and excited state. When the incident photon energy matches the transition energy, resonant enhancement of the scattering occurs, where the process of excitation and spontaneous emission is rapidly repeated [95][96].

When the material is illuminated with such EM radiation it gives rise to a number of such scattering events. These can be better described as waves in which the atoms are the sources which cause the emission of the waves. These waves then undergo interference with each other in such a way that one can infer the structure of the material by studying the scattered pattern from a sample [97].

2.9.2 Total external reflection

The scattering of X-rays from a material results in both reflection as well as transmission of the beam as shown in figure 22. When monochromatic X-ray beams are incident on a sample they experience a change in the refractive index [9]. The refractive index of a material is defined as the ratio of the phase velocity of the EM radiation in vacuum to the phase velocity of the EM radiation within a material and is defined as

$$n = \frac{c}{v} \tag{2.21}$$

where c is the speed of radiation in vacuum and v is the speed within the material. If the angle of incidence, is less than a certain critical angle α_c, the scattered X-rays undergo total external reflection and are scattered elastically.

The incident X-rays onto the sample, undergo a certain degree of refraction. X-rays being EM radiation are subject to Snell's laws of refraction which governs the beam path as it moves between two media of different refractive index. Snell's law relates the angle of incidence α_i and the angle of refraction, α_r when a beam of light passes through two media with different refractive indices n_0 and n_1 as [7][9]

$$n_0 \cos \alpha_i = n_1 \cos \alpha_t \tag{2.22}$$

The refractive index of the medium is given by,

$$n = 1 - \delta + i\beta \tag{2.23}$$

where δ and β are the dispersion and the absorption coefficients. For X-rays these coefficients are of the order of 10^{-5} with β much smaller than δ [97][98][99]. Inserting these values in eq. 2.23 gives a refractive index slightly less than unity [n≈1]. Therefore, when X-rays are incident on a material the material appears to be optically less dense and therefore the X-rays refract away from the surface normal as shown in figure 22.

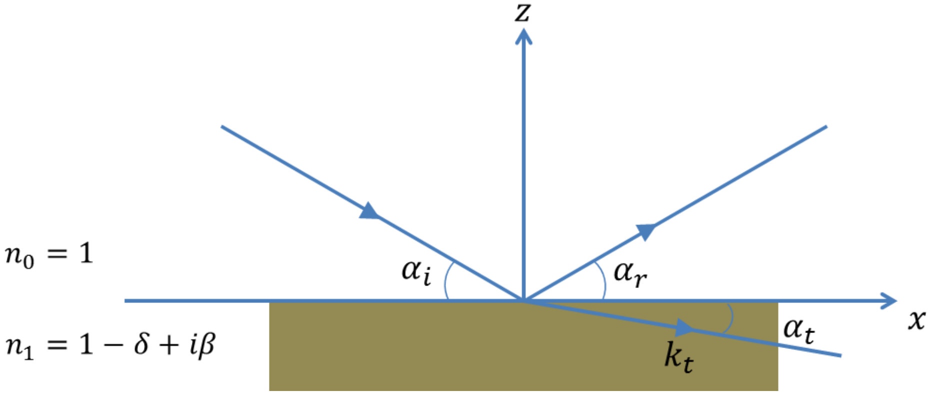

Figure 22: Schematic diagram detailing the path of the X-ray beam incident onto a sample surface. The X-rays are totally externally reflected when the angle of incidence is less than the critical angle. It is assumed that the X-rays undergo elastic scattering.

At a certain incident angle the transmitted X-ray beam will propagate parallel to the sample surface. This angle of incidence, α_i at which the angle of transmittance α_t is 0° is known as the critical angle. Below this critical angle the transmitted wave is complex. At low grazing incidence angles the incident beam experiences total external reflection; there is only an evanescent surface electric field in the sample and the penetration depth is very low. This penetration depth increases rapidly above the critical angle, reaching a maximum value at normal incidence [100]. X-rays are used to study samples with thicknesses up to ≈ 500 μm. From Snell's law if the X-ray moves from air into the material applying the cosine approximation for small angles, $1 - \frac{\alpha_c^2}{2}$ and below critical angle $\alpha_t = 0$ in eq. 2.22 one obtains

$$\cos\alpha_c = n_1 \approx 1 - \frac{\alpha_c^2}{2} + \cdots \tag{2.24}$$

$$2n_1 = 2 - \alpha_c^2$$

$$\alpha_c = \sqrt{2\delta} \tag{2.25}$$

The scattering centre's for the X-rays within the sample are the electrons and therefore δ is a good estimate for the electron density of the material under inspection.

The scattering of X-rays from the surface depends not only on the electron densities which serve as scattering centres but also on the roughness of the film. The X-rays can be diffusely or coherently scattered depending on the roughness of each interface. In a thin film consisting of multiple layers, X-rays are scattered from each of the interfaces within the material and contributions from every layer below the surface are added to give the specular reflection pattern. For a single layer material the interface is between the substrate-material and the material-vacuum/air interfaces which give rise to interference fringes. The scattering off of each interface is shown schematically in figure 23.

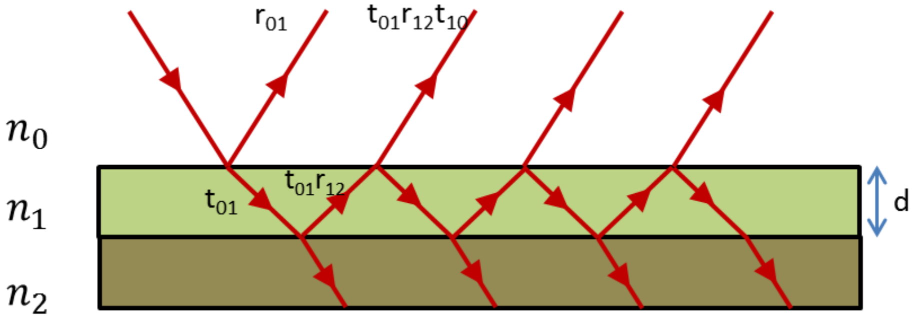

Figure 23: X-ray interaction with a thin film sample with multiple interfaces. X-rays are refracted, transmitted and reflected from each interface. The collective reflected X-ray intensity is analysed to estimate structural parameters. The refractive index of each material (n_1,n_2,…n_i) determines the X-ray refraction from that material.

The total reflection in this situation is the initial reflection r_{01} along with every successive transmittance from each interface. Therefore the total reflection from the film stack can be written as explained in [63] as

$$r_{stack} = r_{01} + t_{01}r_{12}t_{10}p^2 + t_{01}r_{12}r_{10}r_{12}t_{10}p^4 + \cdots \tag{2.26}$$

here p is the phase factor added to the reflectivity term to account for the relative path difference given by:

$$p^2 = \exp(iqd) \tag{2.27}$$

where q contains the incoming wavevector and the angle of incidence, eq. 2.26 forms a geometric series which can be simplified using Fresnel's equation [97] to obtain the net reflectivity as:

$$r_{stack} = r_{01} + \frac{t_{01} r_{12} t_{01} p^2}{1 - r_{10} r_{12} p^2} = \frac{r_{01} + r_{12} p^2}{1 + r_{01} r_{12} p^2} \tag{2.28}$$

These multiple reflections off of each interface in a multi-layered structure give rise to Kiessig fringes, which can be detected and studied as shown in the following chapter. Grazing Incidence X-ray Reflectometry (GIXR) is used to obtain information on the roughness of the sample as well as the thickness. For an extremely rough sample the scattering from the interfacial surface is very diffuse and the specular reflections from the interface deteriorate significantly at small incident angles. Since GIXR is only sensitive to the average change in refractive index across the thickness of the sample it is not possible to distinguish between a topologically sharp interface with large undulations or flat, but a chemically graded interface. The experimental methods used in obtaining the results are described in the following chapter.

2.10 Chapter 2- References

[1] S. Blundell, *Magnetism in condenced matter*. Oxford: Oxford University Press, 2001.

[2] R. Rowan-Robinson, "Spin-orbit phenomena and interfacial proximity effects in magnetic multilayers," PhD theses, Durham University, 2016.

[3] I. Dzyaloshinsky, "A Thermodynamic Theory of 'Weak' Ferromagnetism of Antiferromagnetics," *J Phys. Chem. Solids*, vol. 4, pp. 241–255, 1958.

[4] T. Moriya, "Anisotropic Superexchange Interaction and Weak Ferromagnetism," *Phys. Rev.*, vol. 120, pp. 91–98, 1960.

[5] T. Moriya, "New mechanism of anisotropic superexchange interaction," *Phys. Rev. Lett.*, vol. 4, no. 5, pp. 228–230, 1960.

[6] H. X. Yang, M. Chshiev, B. Dieny, J. H. Lee, A. Manchon, and K. H. Shin, "First-principles investigation of the very large perpendicular magnetic anisotropy at Fe|MgO and Co|MgO interfaces," *Phys. Rev. B*, vol. 84, no. 5, p. 54401, 2011.

[7] S. Jaiswal, "Investigating magnetisation dynamics in magnetic thin films and micro-structures," MSc Theses, Durham University, 2016.

[8] M. A. Omar, "Magnetism and magnetic resonances," in *Elementary Solid State Physics*, Philippines: Addison-Wesley, 1975, pp. 424–479.

[9] L. Bogart, "An Investigation of the Structure, Pinning and Magnetoresistance of Domain Walls in Ni81Fe19 Planar Nanowires," PhD theses, Durham University, 2010.

[10] B. D. Cullity and C. D. Graham, "Magnetic Anisotropy," in *Introduction to Magnetic Materials, Second Edition*, Online edition: John Wiley & Sons, Ltd, 2009, pp. 197–239.

[11] R. M. Bozorth, "Directional ferromagnetic properties of metals," *J. Appl. Phys.*, vol. 8, no. 9, pp. 575–588, 1937.

[12] D. J. Griffiths, *Introduction to Quantum Mechanics*. New Jersey: Prentice Hall, Inc, 1995.

[13] A. Hubert and R. Schäfer, *Magnetic Domains: The Analysis of Magnetic Microstructures*, Illustrate. Berlin: Springer Science & Business Media, 1998.

[14] A. Thiaville, S. Rohart, É. Jué, V. Cros, and A. Fert, "Dynamics of Dzyaloshinskii domain walls in ultrathin magnetic films," *Europhys. Lett.*, vol. 100, no. 5, p. 57002, Dec. 2012.

[15] M. Bode, M. Heide, K. Von Bergmann, P. Ferriani, S. Heinze, G. Bihlmayer, A. Kubetzka, O. Pietzsch, S. Blügel, and R. Wiesendanger, "Chiral magnetic order at surfaces driven by inversion asymmetry," *Nature*, vol. 447, no. 7141, pp. 190–193, 2007.

[16] J. P. Pellegren, "Analyzing Creep Mobility of Dzyaloshinskii Domain Walls with an Effective Elastic Band Model," PhD theses, Carnegie Mellon University, 2017.

[17] V. Kashid, T. Schena, B. Zimmermann, Y. Mokrousov, S. Blügel, V. Shah, and H. G. Salunke, "Dzyaloshinskii-Moriya interaction and chiral magnetism in 3 d − 5 d zigzag chains: Tight-binding model and ab initio calculations," *Phys. Rev. B*, vol. 90, no. 5, p. 54412, Aug. 2014.

[18] E. Martinez, S. Emori, N. Perez, L. Torres, and G. S. D. Beach, "Current-driven dynamics of

Dzyaloshinskii domain walls in the presence of in-plane fields: Full micromagnetic and one-dimensional analysis,” *J. Appl. Phys.*, vol. 115, no. 21, p. 213909, 2014.

[19] G. Chen, T. Ma, A. T. N. Diaye, H. Kwon, C. Won, Y. Wu, and A. K. Schmid, “Tailoring the chirality of magnetic domain walls by interface engineering,” *Nat. Commun.*, vol. 4, p. 2671, 2013.

[20] K. Ryu, L. Thomas, S. Yang, and S. Parkin, “Chiral spin torque at magnetic domain walls,” *Nat. Nanotechnol.*, vol. 8, no. June, pp. 527–533, 2013.

[21] S. Emori, U. Bauer, S. Ahn, E. Martinez, and G. S. D. Beach, “Current-driven dynamics of chiral ferromagnetic domain walls,” *Nat. Mater.*, vol. 12, no. 7, p. 611, 2013.

[22] I. Kezsmarki, S. Bordacs, P. Milde, E. Neuber, L. M. Eng, J. S. White, H. M. Rønnow, C. D. Dewhurst, M. Mochizuki, K. Yanai, H. Nakamura, D. Ehlers, V. Tsurkan, and A. Loidl, “Néel-type skyrmion lattice with confined orientation in the polar magnetic semiconductor GaV4S8,” *Nat. Mater.*, vol. 14, no. 11, pp. 1116–1122, 2015.

[23] A. Bogdanov and A. Hubert, “Thermodynamically stable magnetic vortex states in magnetic crystals,” *J. Magn. Magn. Mater.*, vol. 138, no. 3, pp. 255–269, Dec. 1994.

[24] A. Bogdanov and A. Hubert, “The Properties of Isolated Magnetic Vortices,” *Phys. Status Solidi*, vol. 186, no. 2, pp. 527–543, 1994.

[25] S. Mühlbauer, B. Binz, C. Pfleiderer, A. Rosch, A. Neubauer, and R. Georgii, “Skyrmion Lattice in a Chiral Magnet,” *Science*, vol. 323, no. February, pp. 915–920, 2009.

[26] S. Mühlbauer, B. Binz, F. Jonietz, C. Pfleiderer, A. Rosch, A. Neubauer, R. Georgii, and P. Böni, “[Supplementary online material] Skyrmion lattice in a chiral magnet,” *Science*, vol. 323, no. February, pp. 915–919, 2009.

[27] C. Moreau-Luchaire, C. Moutafis, N. Reyren, J. Sampaio, C. A. F. Vaz, N. Van Horne, K. Bouzehouane, K. Garcia, C. Deranlot, P. Warnicke, P. Wohlhüter, J.-M. George, M. Weigand, J. Raabe, V. Cros, and A. Fert, “Additive interfacial chiral interaction in multilayers for stabilization of small individual skyrmions at room temperature,” *Nat. Nanotechnol.*, vol. 11, no. May, pp. 444–449, 2016.

[28] A. Fert, V. Cros, and J. Sampaio, “Skyrmions on the track,” *Nat. Nanotechnol.*, vol. 8, no. 3, pp. 152–156, 2013.

[29] S.-H. Yang, K.-S. Ryu, and S. Parkin, “Domain-wall velocities of up to 750 m/s driven by exchange-coupling torque in synthetic antiferromagnets.,” *Nat. Nanotechnol.*, vol. 10, no. 3, pp. 221–226, Mar. 2015.

[30] R. Tomasello, E. Martinez, R. Zivieri, L. Torres, M. Carpentieri, and G. Finocchio, “A strategy for the design of skyrmion racetrack memories.,” *Sci. Rep.*, vol. 4, p. 6784, Jan. 2014.

[31] J. Müller, “Magnetic skyrmions on a two-lane racetrack,” *New J. Phys.*, vol. 19, p. 25002, 2017.

[32] W. Kang, C. Zheng, Y. Huang, X. Zhang, Y. Zhou, and W. Lv, “Complementary Skyrmion Racetrack Memory with Voltage Manipulation,” *IEEE Electron Device Lett.*, vol. 37, no. 7, pp. 924–927, 2016.

[33] N. Romming, C. Hanneken, M. Menzel, J. E. Bickel, B. Wolter, K. V Bergmann, A. Kubetzka, and R. Wiesendanger, “Writing and Deleting Single Magnetic Skyrmions,” *Science*, vol. 341, no. August, pp. 636–639, 2013.

[34] N. Romming, A. Kubetzka, C. Hanneken, K. von Bergmann, and R. Wiesendanger, "Field-dependent size and shape of single magnetic skyrmions," *Phys. Rev. Lett.*, vol. 114, no. 17, p. 177203, 2015.

[35] A. Soumyanarayanan, M. Raju, A. L. G. Oyarce, A. K. C. Tan, M. Y. Im, A. P. Petrovic, P. Ho, K. H. Khoo, M. Tran, C. K. Gan, F. Ernult, and C. Panagopoulos, "Tunable room-temperature magnetic skyrmions in Ir/Fe/Co/Pt multilayers," *Nat. Mater.*, vol. 16, no. 9, pp. 898–904, 2017.

[36] K. Zeissler, K. Shahbazi, J. Massey, S. Finizio, J. Raabe, F. Al Ma'Mari, M. C. Rosamond, E. H. Linfield, T. A. Moore, G. Burnell, and C. H. Marrows, "Direct imaging and electrical detection at room temperature of a single skyrmion," *arXiv:1706.06024v1*, Jun. 2017.

[37] D. Maccariello, W. Legrand, N. Reyren, K. Garcia, K. Bouzehouane, S. Collin, V. Cros, and A. Fert, "Electrical detection of single magnetic skyrmions in metallic multilayers at room temperature," *Nat. Nanotechnol.*, vol. Not assign, no. 10.1038/s41565-017-0044-4, 2018.

[38] K. Everschor-Sitte, M. Sitte, T. Valet, A. Abanov, and J. Sinova, "Skyrmion production on demand by homogeneous DC currents," *New J. Phys.*, vol. 19, p. 92001, 2017.

[39] W. Jiang, G. Chen, K. Liu, J. Zang, S. G. E. te Velthuis, and A. Hoffmann, "Skyrmions in magnetic multilayers," *Phys. Rep.*, vol. 704, pp. 1–49, 2017.

[40] G. Finocchio, F. Büttner, R. Tomasello, M. Carpentieri, and M. Kläui, "Magnetic skyrmions: from fundamental to applications," *J. Phys. D. Appl. Phys.*, vol. 49, no. 42, p. 423001, 2016.

[41] J. H. Franken, H. J. M. Swagten, and B. Koopmans, "Shift registers based on magnetic domain wall ratchets with perpendicular anisotropy," *Nat. Nanotechnol.*, vol. 7, no. July, pp. 499–503, 2012.

[42] M. Hayashi, L. Thomas, R. Moriya, C. Rettner, and S. S. P. Parkin, "Current-controlled magnetic domain-wall nanowire shift register," *Science*, vol. 320, no. 5873, pp. 209–211, 2008.

[43] F. Ummelen, H. Swagten, and B. Koopmans, "Racetrack memory based on in- plane-field controlled domain-wall pinning," *Sci. Rep.*, vol. 7, no. January, p. 833, 2017.

[44] R. Sbiaa and S. N. Piramanayagam, "Recent developments in spin transfer torque MRAM," *Phys. status solidi - Rapid Res. Lett.*, vol. 11, p. 1700163, 2017.

[45] L. Landau and E. Lifshits, "On the theory of the dispersion of magnetic permeability in ferromagnetic bodies," *Phys. Zeitsch. der Sow.*, vol. 8, p. 153, 1935.

[46] T. L. Gilbert, "A phenomenological theory of damping in ferromagnetic materials," *IEEE Trans. Magn.*, vol. 40, no. 6, pp. 3443–3449, 2004.

[47] T. L. Gilbert, "A lagrangian formulation of the gyromagnetic equation of the magnetization field," *Phys. Rev.*, vol. 100, no. 4, p. 1243, 1955.

[48] B. Borie, A. Kehlberger, J. Wahrhusen, H. Grimm, and M. Kläui, "Geometrical dependence of domain-wall propagation and nucleation fields in magnetic-domain-wall sensors," *Phys. Rev. Appl.*, vol. 8, no. 2, p. 24017, 2017.

[49] N. L. Schryer and L. R. Walker, "The motion of 180° domain walls in uniform dc magnetic fields," *J. Appl. Phys.*, vol. 45, no. 12, pp. 5406–5421, 1974.

[50] P. J. Metaxas, J. P. Jamet, A. Mougin, M. Cormier, J. Ferré, V. Baltz, B. Rodmacq, B. Dieny, and R. L. Stamps, "Creep and Flow Regimes of Magnetic Domain-Wall Motion in Ultrathin Pt/Co/Pt Films

with Perpendicular Anisotropy," *Phys. Rev. Lett.*, vol. 99, no. November, p. 217208, 2007.

[51] A. Mougin, M. Cormier, J. P. Adam, P. J. Metaxas, and J. Ferré, "Domain wall mobility, stability and Walker breakdown in magnetic nanowires," *Europhys. Lett.*, vol. 78, no. 5, p. 57007, 2007.

[52] P. Chauve, T. Giamarchi, and P. Le Doussal, "Creep and depinning in disordered media," *Phys. Rev. B*, vol. 62, no. 10, pp. 6241–6267, 2000.

[53] S. Lemerle, J. Ferré, C. Chappert, V. Mathet, T. Giamarchi, and P. Le Doussal, "Domain wall creep in an Ising ultrathin magnetic film," *Phys. Rev. Lett.*, vol. 80, no. 4, pp. 849–852, 1998.

[54] S. Chenattukuzhiyil, "Study of domain wall dynamics in the presence of large spin-orbit coupling: chiral damping and magnetic origami," PhD theses, L'Université Grenoble Alpes, 2016.

[55] F. Hellman, A. Hoffmann, Y. Tserkovnyak, G. S. D. Beach, E. E. Fullerton, C. Leighton, A. H. Macdonald, D. C. Ralph, D. A. Arena, H. A. Dürr, P. Fischer, and J. Grollier, "Interface-induced phenomena in magnetism," *Rev. Mod. Phys.*, vol. 89, no. June, p. 25006, 2017.

[56] A. Hallal, H. X. Yang, B. Dieny, and M. Chshiev, "Anatomy of perpendicular magnetic anisotropy in Fe/MgO magnetic tunnel junctions: First-principles insight," *Phys. Rev. B*, vol. 88, no. 18, p. 184423, Nov. 2013.

[57] J. Zhang, C. Franz, M. Czerner, and C. Heiliger, "Perpendicular magnetic anisotropy in CoFe/MgO/CoFe magnetic tunnel junctions by first-principles calculations," *Phys. Rev. B*, vol. 90, no. 18, p. 184409, Nov. 2014.

[58] Z. Wang, M. Saito, K. P. McKenna, S. Fukami, H. Sato, S. Ikeda, H. Ohno, and Y. Ikuhara, "Atomic-Scale Structure and Local Chemistry of CoFeB-MgO Magnetic Tunnel Junctions," *Nano Lett.*, vol. 16, no. 3, pp. 1530–1536, 2016.

[59] S. Emori and G. S. D. Beach, "Enhanced current-induced domain wall motion by tuning perpendicular magnetic anisotropy," *Appl. Phys. Lett.*, vol. 98, p. 132508, 2011.

[60] C. Pai, M. Nguyen, C. Belvin, L. H. Vilela-Leão, D. C. Ralph, and R. A. Buhrman, "Enhancement of perpendicular magnetic anisotropy and transmission of spin-Hall- effect-induced spin currents by a Hf spacer layer in W/Hf/CoFeB/MgO layer structures," *Appl. Phys. Lett.*, vol. 104, p. 82407, 2014.

[61] J. Sinha, M. Hayashi, A. J. Kellock, S. Fukami, M. Yamanouchi, H. Sato, S. Ikeda, S. Mitani, S. Yang, S. S. P. Parkin, and H. Ohno, "Enhanced interface perpendicular magnetic anisotropy in Ta|CoFeB|MgO using nitrogen doped Ta underlayers," *Appl. Phys. Lett.*, vol. 102, p. 242405, Jun. 2013.

[62] S. Emori, E. Martinez, K.-J. Lee, H.-W. Lee, U. Bauer, S.-M. Ahn, P. Agrawal, D. C. Bono, and G. S. D. Beach, "Spin Hall torque magnetometry of Dzyaloshinskii domain walls," *Phys. Rev. B*, vol. 90, no. 18, p. 184427, Nov. 2014.

[63] R. Lo Conte, E. Martinez, A. Hrabec, A. Lamperti, T. Schulz, L. Nasi, L. Lazzarini, R. Mantovan, F. Maccherozzi, S. S. Dhesi, B. Ocker, C. H. Marrows, T. A. Moore, and M. Kläui, "Role of B diffusion in the interfacial Dzyaloshinskii-Moriya interaction in Ta/Co20 F e60 B20/MgO nanowires," *Phys. Rev. B*, vol. 91, no. 1, p. 14433, Jan. 2015.

[64] R. A. Khan, P. M. Shepley, A. Hrabec, A. W. J. Wells, B. Ocker, C. H. Marrows, and T. A. Moore, "Effect of annealing on the interfacial Dzyaloshinskii-Moriya interaction in Ta/CoFeB/MgO trilayers," *Appl. Phys. Lett.*, vol. 109, p. 132404, 2016.

[65] S. Ikeda, R. Koizumi, H. Sato, M. Yamanouchi, K. Miura, K. Mizunuma, H. Gan, F. Matsukura,

and H. Ohno, “Boron Composition Dependence of Magnetic Anisotropy and Tunnel Magnetoresistance in MgO/CoFe(B) Based Stack Structures,” *IEEE Trans. Magn.*, vol. 48, no. 11, pp. 3829–3832, Nov. 2012.

[66] S. X. Huang, T. Y. Chen, and C. L. Chien, “Spin polarization of amorphous CoFeB determined by point-contact Andreev reflection Spin polarization of amorphous CoFeB determined by point-contact Andreev reflection,” *Appl. Phys. Lett.*, vol. 92, no. 24, p. 242509, 2008.

[67] Y. M. Lee, J. Hayakawa, S. Ikeda, F. Matsukura, and H. Ohno, “Effect of electrode composition on the tunnel magnetoresistance of pseudo-spin-valve magnetic tunnel junction with a MgO tunnel barrier,” *Appl. Phys. Lett.*, vol. 90, no. 21, p. 212507, 2007.

[68] H. Bouchikhaoui, P. Stender, D. Akemeier, D. Baither, K. Hono, A. Hütten, and G. Schmitz, “On the role of Ta cap in the recrystallization process of CoFeB layers,” *Appl. Phys. Lett.*, vol. 103, no. 14, p. 142412, 2013.

[69] A. K. Niessen and F. R. De Boer, “The enthalpy of formation of solid borides, carbides, nitrides, silicides and phosphides of transition and noble metals,” *J. Less-Common Met.*, vol. 82, pp. 75–80, 1981.

[70] A. T. Hindmarch, V. Harnchana, A. S. Walton, A. P. Brown, R. M. D. Brydson, and C. H. Marrows, “Zirconium as a Boron Sink in Crystalline CoFeB/MgO/CoFeB Magnetic Tunnel Junctions,” *Appl. Phys. Express*, vol. 4, no. 1, p. 13002, Jan. 2011.

[71] J. Hayakawa, S. Ikeda, F. Matsukura, H. Takahashi, and H. Ohno, “Dependence of giant tunnel magnetoresistance of sputtered CoFeB/MgO/CoFeB magnetic tunnel junctions on MgO barrier thickness and annealing temperature,” *Jpn. J. Appl. Phys.*, vol. 44, no. 19, pp. L587–L589, 2005.

[72] H. Kurt, K. Rode, K. Oguz, M. Boese, C. C. Faulkner, and J. M. D. Coey, “Boron diffusion in magnetic tunnel junctions with MgO (001) barriers and CoFeB electrodes,” *Appl. Phys. Lett.*, vol. 96, p. 262501, 2010.

[73] P. Deorani and H. Yang, “Role of spin mixing conductance in spin pumping : Enhancement of spin pumping efficiency in Ta/Cu/Py structures,” *Appl. Phys. Lett.*, vol. 103, p. 232408, 2013.

[74] C. O. Avci, A. Quindeau, M. Mann, C. F. Pai, C. A. Ross, and G. S. D. Beach, “Spin transport in as-grown and annealed thulium iron garnet/platinum bilayers with perpendicular magnetic anisotropy,” *Phys. Rev. B*, vol. 95, no. 11, p. 115428, 2017.

[75] S. Emori, T. Nan, A. M. Belkessam, X. Wang, A. D. Matyushov, C. J. Babroski, Y. Gao, H. Lin, and N. X. Sun, “Interfacial spin-orbit torque without bulk spin-orbit coupling,” *Phys. Rev. B*, vol. 93, no. 18, p. 180402R, 2016.

[76] I. M. Miron, G. Gaudin, S. Auffret, B. Rodmacq, A. Schuhl, S. Pizzini, J. Vogel, and P. Gambardella, “Current-driven spin torque induced by the Rashba effect in a ferromagnetic metal layer,” *Nat. Mater.*, vol. 9, no. 3, pp. 230–234, 2010.

[77] A. Kobs and H. P. Oepen, “Disentangling interface and bulk contributions to the anisotropic magnetoresistance in Pt/Co/Pt sandwiches,” *Phys. Rev. B*, vol. 93, p. 14426, 2016.

[78] J. Cho, N.-H. Kim, S. Lee, J.-S. Kim, R. Lavrijsen, A. Solignac, Y. Yin, D.-S. Han, N. J. J. van Hoof, H. J. M. Swagten, B. Koopmans, and C.-Y. You, “Thickness dependence of the interfacial Dzyaloshinskii–Moriya interaction in inversion symmetry broken systems,” *Nat. Commun.*, vol. 6, no. May, p. 7635, 2015.

[79] A. Fert and I. A. Campbell, “Transport properties of ferromagnetic transition metals,” *J. Phys. Colloq.*, vol. 32, no. C1, pp. C1-46-C1-50, 1971.

[80] N. Vigneswaran, F. Samsuri, B. Ranganathan, and P. Padmapriya, “Recent advances in nano patterning and nano imprint lithography for biological applications,” *Procedia Eng.*, vol. 97, pp. 1387–1398, 2014.

[81] J. A. Rogers and H. H. Lee, *Unconventional nanopatterning techniques and applications*. Online edition: John Wiley & Sons, Inc., 2009.

[82] H. Adachi, T. Hata, T. Matsushima, T. Motohiro, and T. Kikuo, *Handbook of Sputter Deposition Technology: Fundamentals and Applications for Functional Thin Films, Nanomaterials, and MEMS*, Second. Online edition: Elsevier, 2012.

[83] H. Frey and H. R. Khan, *Handbook of Thin-Film Technology*. Berlin: Springer, 2015.

[84] J. V. Barth, G. Costantini, and K. Kern, “Engineering atomic and molecular nanostructures at surfaces,” *Nature*, vol. 437, pp. 671–679, 2005.

[85] D. Atkinson, “Patterning nanostructures to study magnetization processes,” *J. Phys. Conf. Ser.*, vol. 17, no. 1, pp. 33–39, 2005.

[86] M. Faraday, “On the magnetization of light and the illumination of magnetic lines of force,” *Philos. Trans. R. Soc. London*, vol. 136, no. 1, pp. 1–20, 1846.

[87] J. Kerr, “On rotation of the plane of polarization by reflection from the pole of a magnet,” *Philos. Mag.*, vol. 3, no. 19, pp. 321–343, 1877.

[88] J. Kerr, “On reflection of polarized light from the equatorial surface of a magnet,” *Philos. Mag.*, vol. 5, no. 30, pp. 161–177, 1878.

[89] J. McCord, “Progress in magnetic domain observation by advanced magneto-optical microscopy,” *J. Phys. D. Appl. Phys.*, vol. 48, p. 333001, 2015.

[90] C. A. Fowler and M. Fryer, “Magnetic domains by the longitudinal Kerr effect,” *Phys. Rev.*, vol. 94, no. 1, pp. 52–56, 1954.

[91] R. L. Conte, “Magnetic nanostructures with structural inversion asymmetry,” Johannes Gutenberg-Universität Mainz, 2015.

[92] G. Schönhense, “Imaging of magnetic structures by photoemission electron microscopy,” *J. Phys. Condens. Matter*, vol. 11, pp. 9517–9547, 1999.

[93] P. Weinberger, “John Kerr and his effects found in 1877 and 1878,” *Philos. Mag. Lett.*, vol. 88, no. 12, pp. 897–907, 2008.

[94] P. N. Argyres, “Theory of the Faraday and Kerr effects in ferromagnetics,” *Phys. Rev.*, vol. 97, no. 2, pp. 334–345, 1955.

[95] E. Hecht, *Optics*. Reading, Mass.: Addison-Wesley, 2002.

[96] D. M. Burn, “Domain wall behaviour in ferromagnetic nanowires with interfacial and geometrical structuring,” PhD theses, Durham University, 2013.

[97] J. Als-Nielsen and D. McMorrow, *Elements of Modern X-Ray Physics-Second Edition*. West Sussex: John Wiley & Sons, Ltd, 2011.

[98] K. Stoev and K. Sakurai, “Recent theoretical models in grazing incidence X-ray reflectometry,”

Rigaku J., vol. 14, no. 2, 1997.

[99] H. Kiessig, “Interferenz von Röntgenstrahlen an dünnen Schichten (Interference of x-rays in thin layers),” *Ann. Phys.*, vol. 402, no. 6, pp. 715–725 & 769–788, Jan. 1931.

[100] D. S. Eastwood, “Grazing Incidence X-ray Scattering from Magnetic Thin Films and Nanostructures,” PhD theses, Durham University, 2009.

|Chapter 3

Experimental methods

3.1 Introduction

In order to understand the experimental results, we must firstly understand *the methods* used to obtain the given results. This chapter details the various experimental techniques and methods used in understanding material growth, structure, and their resulting magnetic properties both, bulk properties such as anisotropy as well as localised properties such as domain wall pinning in ferromagnetic materials. The chapter is structured from the beginning to end as congruent to the process of experimental investigation; The growth of thin films followed by measurement of magnetic properties and finally to understanding domain wall motion via the MOKE effect.

3.2 Material growth and structural characterisation

Before any material characterisation or device testing is performed, it is required to grow the required material systems in a controlled manner; here we discuss the methods employed in the growth of the thin films for the given study as well as the X-ray analysis experimental setup used for the structural characterisation of these thin films.

3.2.1 Preparation of substrates

In order to grow thin films of high quality, substrates used for their deposition were scribed and cleaned before deposition. The substrates underwent a rigorous cleaning routine which comprised of three minutes sonication each in acetone followed by iso-propan-2-ol and de-ionised water. The substrates were then dried in a clean room using dry N_2. The acetone was used to ensure no residual organic impurities were left on the substrate. Isopropanol and N_2 were used to remove acetone leftover and dry the substrate. Post cleaning the substrate was ready for deposition as highlighted below.

3.2.2 Growth of thin films

All thin films used in this study were grown on an industrial sputtering tool capable of growing samples up to 200 mm diameters. The details of the sputter chamber are highlighted below.

The Rotaris sputtering chamber primarily used for this study comprised of two ultra-high vacuum deposition main chambers, a single transport chamber connecting both main chambers and a load-lock for installation of new substrates. All chambers were pumped using water cooled turbo pumps and the two main chambers were additionally equipped with cryogenic pumps for obtaining lower pressures in a smaller period of time. All substrates were loaded into the load-lock chamber. The purpose of the load-lock is to allow for fast pump down times (due to the smaller size in comparison to the main chambers) to improve sample throughput as well as to avoid the venting of the main chamber in order to load substrates. The load-lock comprised of a single cassette assembly capable of housing up to 25, 200 mm wafers/substrate holders to be pumped in a single pump down cycle. In order to deposit samples of smaller sizes, the substrates were scribed and placed on a substrate holder. The edges of the substrate were held on to the holder using high vacuum compatible Kapton tape. It is important to minimise degassing which might occur due to the Kapton tape. Hence minimal amounts were used to fix the substrate onto the wafer. The load-lock chamber is connected to a central transport chamber housing a robot system which serves as a transport hub for ultra-high vacuum transfer of films and substrates between chambers. This drastically improves not only the throughput of the system but also the capabilities, in terms of for example performing reactive sputtering for a single layer and then using a second chamber to grow single element species. The transport chamber comprised of a two-pronged 3-axis Load Transfer Arm (LTA) used for manipulating sample transfer between the three adjoining chambers. Each chamber was connected to the central transport chamber via a high vacuum gate valve. The two main chambers are used for the deposition of the film. Together they house 12 targets, each of 100 mm in diameter. The target assembly is mounted on the roof of the chamber for ease of access for quick target installation. The target configuration differs depending on the geometry of the deposition system. Each target is individually water cooled to prevent over heating during the sputtering process. Every target comprises of a backing plate with a permanent magnet assembly fitted into it. The magnet assembly can be configured depending on the target requirement. Stronger magnets with up to 0.5 T are used for ferromagnetic materials. Along with each target an individual target shutter is used. These target shutters are used to regulate the deposition onto the substrates as well as to ensure stable plasma prior to deposition. The chamber is capable of co-sputtering up to 3 targets simultaneously with the aid of two D.C. and one R.F. power sources. The targets are angled towards each other to facilitate co-sputtering as shown in the schematic in figure 1. The substrate is loaded on to a wafer stage underneath the targets.

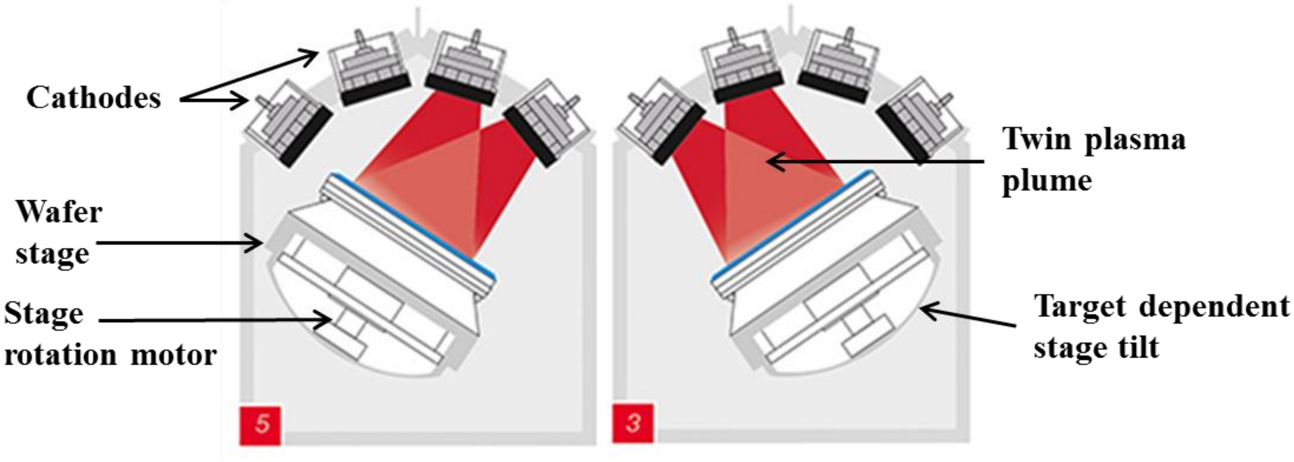

Figure 1: Cross-sectional schematic of the *Singulus Rotaris*® deposition system main chamber interior. The sample stage can be tilted as shown to allow for co-sputtering of targets as well be displaced linearly with respect to the targets to optimize deposition homogeneity. The image is adapted from [1].

Given the geometry of the system the stage is capable of tilting towards either side of the chamber wall to facilitate deposition from the magnetron sources. Two intertwined SiC heaters are installed underneath the wafer stage. These heaters can be heated up to 750°C. The maximum temperature at the substrate surface however is 580°C. This is due to the finite distance between the heater and the substrate and the poor conductivity in vacuum. The main chambers are fitted with nitrogen and oxygen gas inlets to allow for reactive sputtering. All gas injections in the chamber are controlled via mass flow controllers. Prior to film deposition, the target was ignited and a sustainable plasma was formed with the shutter closed. The gas flows were then adjusted to the desired growth pressures from the ignition pressures, once the plasma was stable, the shutter was opened and allowed to deposit on the substrate. The stage onto which the sample and substrate holder were placed is rotated at a fixed rounds per minute (rpm) for a given deposition. This is done so as to ensure homogenous film deposition across the wafer. The rotation speed can be varied between 0 to 60 rpm. The homogeneity of the sample is shown in figure 2.

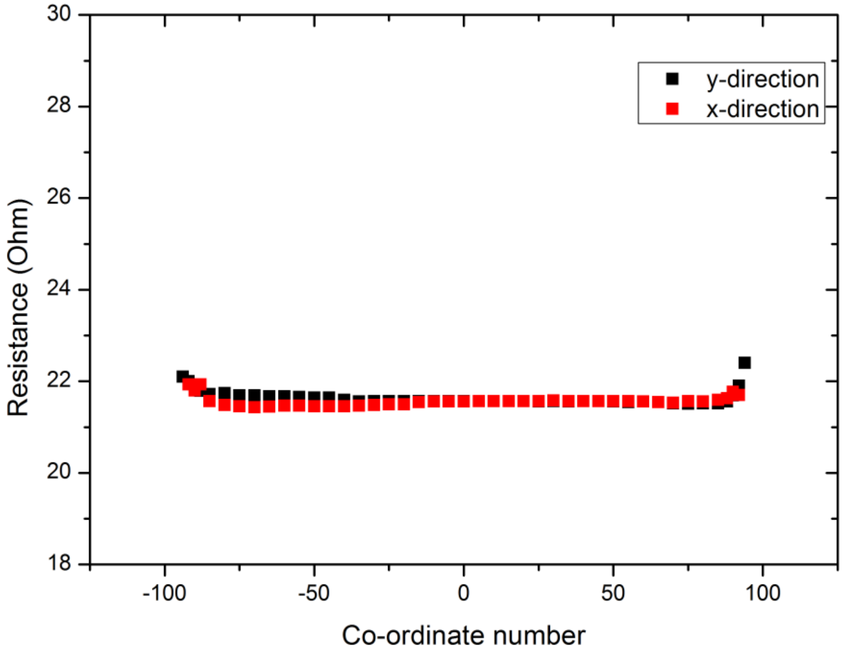

Figure 2: Variation of measured resistance (representative of inverse sample thickness) as a function of wafer length as measured along the 200mm wafer diameter along the horizontal (red) and the vertical direction (black). Small deviations near the edges are accountable due to measurements at clamped areas of the wafer.

This Ultra-High Vacuum (UHV) chamber when baked out is capable of obtaining base pressures of $< 2 \times 10^{-9}$ mbar. The low base pressure along with the high throughput make the system very suitable for the deposition of complex layered structures.

3.2.3 X-ray reflectometry

Given the strong structural dependence of the physical phenomena investigated here it is essential to obtain information of the underlying materials. There exist various different techniques to obtain different structural details about a sample. Transmission Electron Microscopy (TEM) for example obtains information at the atomic scale although the samples need to be prepared on specialised substrates. Reflective high energy electron diffraction provides estimates on the crystallinity of the sample however, it is an in-situ UHV technique and not used for post deposition characterisation. X-ray diffraction provides information of the in-plane and out-of-plane ordering of the materials by studying the diffraction of X-rays via the sample. X-ray Reflectometry essentially is the study of very small incident angle X-rays reflected from a sample. The reflection and the consequent interference of such X-rays off multiple interfaces from a sample allows the estimation of the thickness and roughness of the material. There also exist related methods of X-ray florescence which is used to obtain element specific information relating to depth of a sample.

Here reflectometry and diffraction are employed to obtain structural information pertaining to the multilayers studied. A Bruker D8- horizontal four circle diffractometer was used. The system consists of a Cu-anode used for the production of the X-rays as a source. A schematic of the set-up is shown in figure 3.

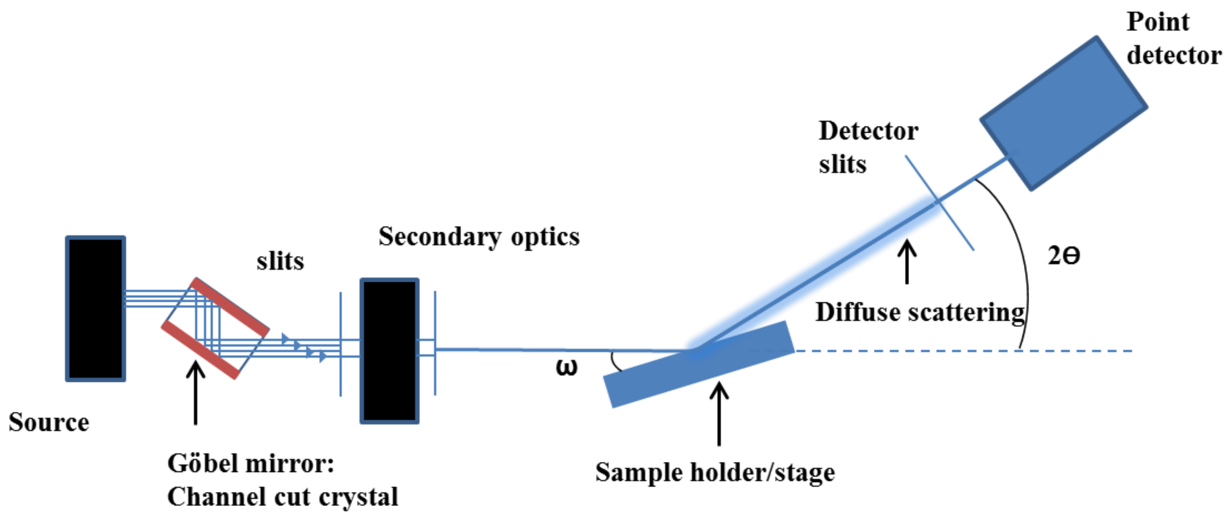

Figure 3: Line diagram of the X-ray beam path taken in a Bruker D8 discover laboratory X-ray diffractometer.

Prior to sample illumination the X-rays are collimated into parallel beams via a channel cut crystal. A monochromator is used to select Cu $K_{\alpha}1$ radiation. Stainless steel slits are used to further obtain a line focus on to the sample. The sample is placed on an Eulerian cradle capable of tilt correction as described in appendix A. Scattered X-rays from the sample are collected using a point count detector for measuring X-ray counts per second. There are additional motorised slits located before the detector for reducing the background intensity. It is important to open these slits wide while studying a new sample as reducing their width will result in a loss of intensity. The sample stage is used to move the sample position via motorised axis controls. This allows for accurate positioning of the sample during alignment scans required prior to measuring reflectometry or X-ray diffraction. This procedure is explained in the appendix A.

3.3 SQUID magnetometry

In order to obtain magnetisation properties and to study temperature dependence of the same, samples were subjected to Superconducting Quantum Interference Device (SQUID) magnetometry to extract their hysteretic responses to magnetic fields. Here the SQUID magnetometer is described. The methods used to obtain corrected magnetisation curves along with the procedure used to align the sample is described in appendix A.

3.3.1 Description of magnetometer

A Superconducting Quantum Interference Device is a very sensitive tool to measure very low magnetic moments. The device used here is a commercially available *QuantumDesign RF SQUID*. In this work it is used to measure the magnetisation of ultra-thin ferromagnetic films. The device consists of detection coils or pick-up coils used to detect the signal, the SQUID device itself and the electronics for the read-out.

The sample is placed in a holder which is moved through detection coils placed at the centre of the magnet shown in figure 4. This movement of the sample and the moment associated with it causes a build-up of current in the detection coil. The current in the detection coils is inductively coupled to the SQUID device itself via superconducting wires. There is a compensating feedback current flowing in the device which undergoes a change due to the changing magnetic field in the detection coils. This is then amplified and output through the SQUIDs electronics. The feedback current variations in the SQUID detector then provide an accurate measurement of the samples magnetisation [2].

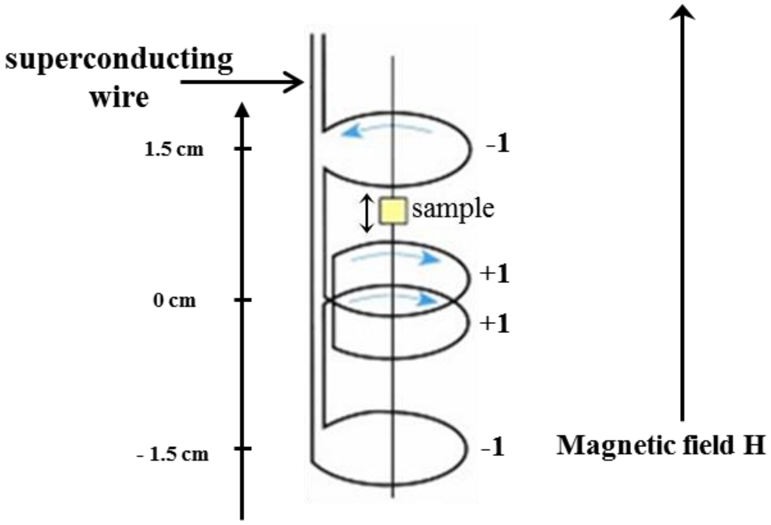

Figure 4: Schematic of the sample space and the detection coils within the SQUID magnetometer. The pick-up coils comprise of a set of three coils which are placed at the centre of the superconducting magnet,

outside the chamber. The sample is coupled inductively to the coil as it is moved through it. The diagram has been adapted from [2].

The SQUID measures the magnetic moment of the entire sample as opposed to the MOKE which can be focussed to obtain localised magnetic properties near the surface of the sample. Given the high sensitivity and the reliance of measurement of changing magnetic flux through the detection coil, the sample alignment in the chamber with respect to the coils is crucial. This is described in appendix A.

3.4 MOKE magnetometry

In order to obtain bulk information on the total magnetic response to structural reconfiguration one can employ the SQUID to measure bulk magnetic properties as described in the section above. However, to understand the local magnetisation variation with respect to studying of domain wall motion and visualisation of the magnetic domains Magneto-Optical Kerr Effect (MOKE) microscopy was used. There exist other means of measuring local magnetisation on the sample such as a Magnetic Force Microscopy (MFM) which essentially is sensitive to the stray fields generated near the surface of the sample that is picked up by a magnetic tip for mapping out the magnetisation over a given area. Other than the fact that MFM is extremely slow in obtaining information it is also difficult to eradicate any influence from the sensing probe to the sample being measured. This is especially important for samples with low coercive fields which exhibit sharp magnetisation reversal. A MOKE measurement performed on the sample is 1. sensitive up to a certain depth of the sample and 2. it is only sensitive to changes in magnetisation and not to the magnetisation itself like the SQUID. Hence the MOKE cannot be used to obtain information on magnetisation of a material but can be used to image magnetic domains and study field driven magnetisation reversal.

The general working of MOKE microscopy along with the protocol used for the measurements are described in the sections below.

3.4.1 Description of the microscope

In order to study magnetisation reversal using the MOKE technique the following 5 basic objects are needed,

A light source, which can be used to illuminate the sample and as a probe for the area over which the magnetisation is to be studied.

A polariser, which is used for polarising an incoming beam of light so as to study changes in the plane of polarisation.

A sample, a thin ferromagnetic sample, in which the ferromagnet is located near the surface of the film**.**

An analyser, to extract information on the degree of rotation of the plane of polarisation, which is sensitive to the magnetisation of the material.

A detector, this can be a photodiode or a camera with a CCD used to capture incoming light for processing the image for changes in grey scale.

A ray diagram of the light path within the MOKE microscope setup is shown in figure 5. A white light source is used to illuminate a wide surface area of the sample. This is focussed onto the sample surface via convex lenses. A centred aperture is used to focus the light at the centre of the polarisation cross. The centred aperture is used to select the MOKE sensitivity for polar or longitudinal configuration via the extinction cross. For polar sensitivity the centre of the polarisation cross is selected i.e. such that the light is incident and reflected at 0°.

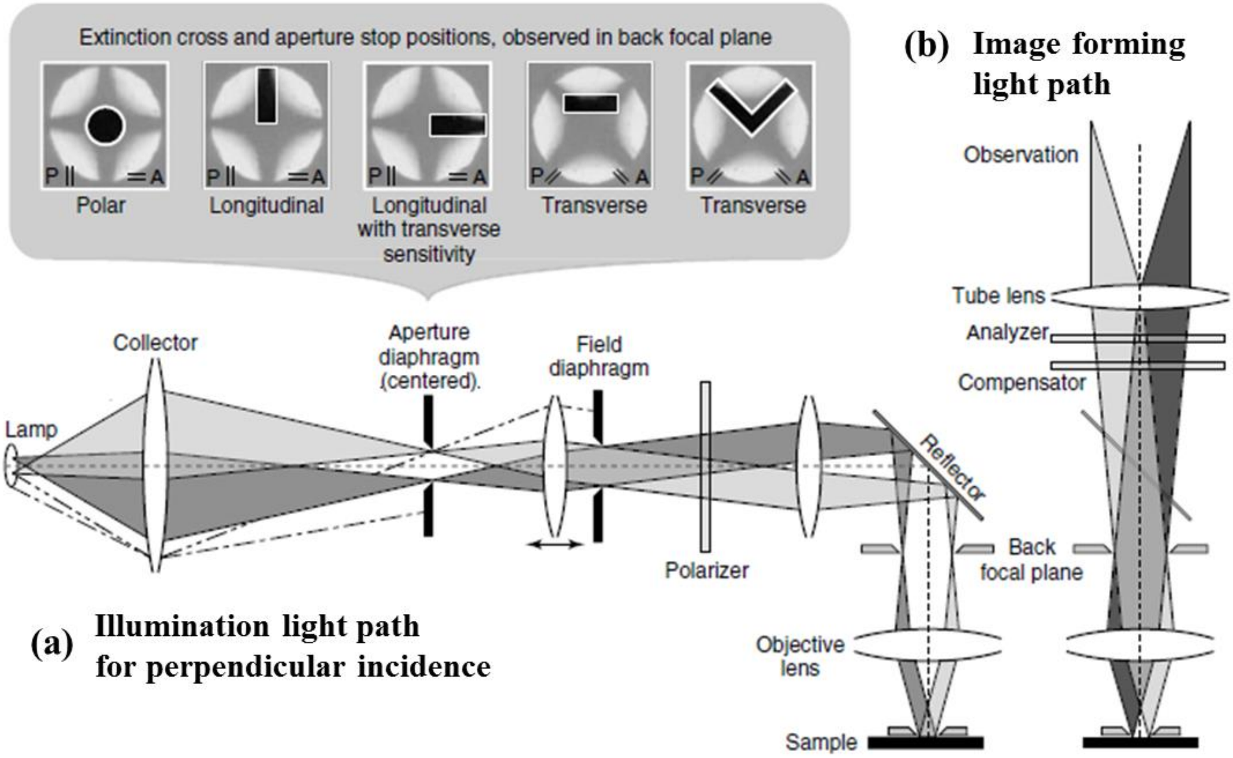

Figure 5: Ray diagram of the light path in the MOKE microscope for (a) sample illumination in the front focal plane set-up for perpendicular incidence and (b) for the image forming path allowing the light to pass through the objective, past the analyser and compensator and into the CCD camera. In the back focal plane the aperture diagram can be viewed and adjusted to select polar (centred slit) or longitudinal and transverse effects (displaced slits from centre). The image is reproduced from [3].

Following this a polariser is used along with the analyser to measure the change in the reflected plane of polarisation. It is connected to the camera. A plane view image of the sample is displayed as one obtained with a microscope detailing the surface defects and superficial structures along with, changes in intensity as obtained by the MO Kerr effect. A hysteresis curve can be obtained via measurement of the changes in grayscale over the entire image as viewed through the camera or of a particular selected region of interest. A magnetic field can be applied via the in-plane or out-of-plane water cooled magnet. The entire microscope along with the magnet assembly is placed on a damped optical table for stabilised imaging. Here a white light source is used which does not incorporate the dependence of the Kerr effect on wavelength [4][5]. Hence if the sample under observation has a high wavelength dependence, a MOKE with a monochromatic laser light source would be required.

3.4.2 Protocol for measuring domain wall motion

The method used for measuring the domain expansion to study the influence of magnetic structures as a function of field is described below.

For the imaging of the magnetic domains an *Olympus MPLFLN20xBD* optical imaging lens with a 20x magnification was used to obtain a wide area field of view of 450 × 450 μm^2. In order to study the asymmetric field driven expansion of magnetic domains, a pulsed out-of-plane field was applied. This was done using an Agilent 33250A arbitrary waveform generator. The line diagram of the set-up is shown in figure 6(a).

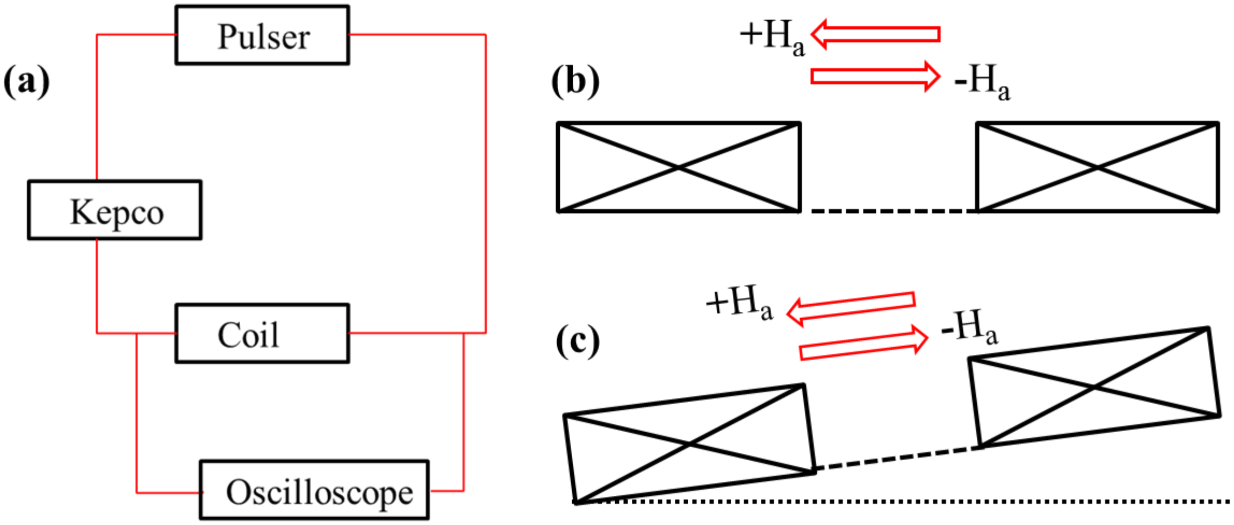

Figure 6: (a) Circuit diagram of the experimental set-up used to apply pulsed fields for studying field driven domain wall motion. (b) Schematic of an in-plane magnet placed on a stage with no tilt present. Here there is no field component in the out of plane direction and (c) the in-plane magnet without tilt

correction, here the applied in-plane has an additional out-of-plane moment with opposite sign in-plane field (±H_a) exhibiting opposite out-of-plane component.

The pulse shape as a function of pulse duration was tested using a DPO7354Tektronics oscilloscope. The minimum duration for which the pulse shape was not distorted from a square waveform was 37 µs, below which the Kepco power supply was not able to amplify the signal without distorting the pulse from the pulse generator. The Kepco was driven by the pulse generator to pulse the OOP coil. The minimum pulse duration used for the experiments was of the order of few 100 µs thereby resulting in a clean square waveform without any ringing or spikes. The sample was placed on a holder between the in-plane magnet which consisted of copper wires wound around an iron core a schematic of this is shown in figure 6(b). The maximum in-plane field the magnet was able to supply was limited to 350 mT. The in-plane magnet was placed on a tilt stage which was used to compensate and remove any out-of-plane component of field provided due to the tilting of the in-plane magnet. An out-of-plane coil is placed underneath the sample such that the field can be applied in both directions simultaneously. High field split pole shoes were used in the in-plane magnet to provide a higher homogeneity of the field. The sample was positioned in the region of minimum variation in the field as measured by the Hall probe prior to the measurement to reduce any error. The magnetic field was calibrated using a *Lakeshore model 475 DSP* magnetic Hall probe.

Once the out-of-plane coil is calibrated, the sample was saturated along the out-of-plane direction and the measurement was performed using difference imaging technique, in which the image prior and post excitation are subtracted, resulting in an enhanced contrast of the magnetic domain structure as shown in figure 7(a).

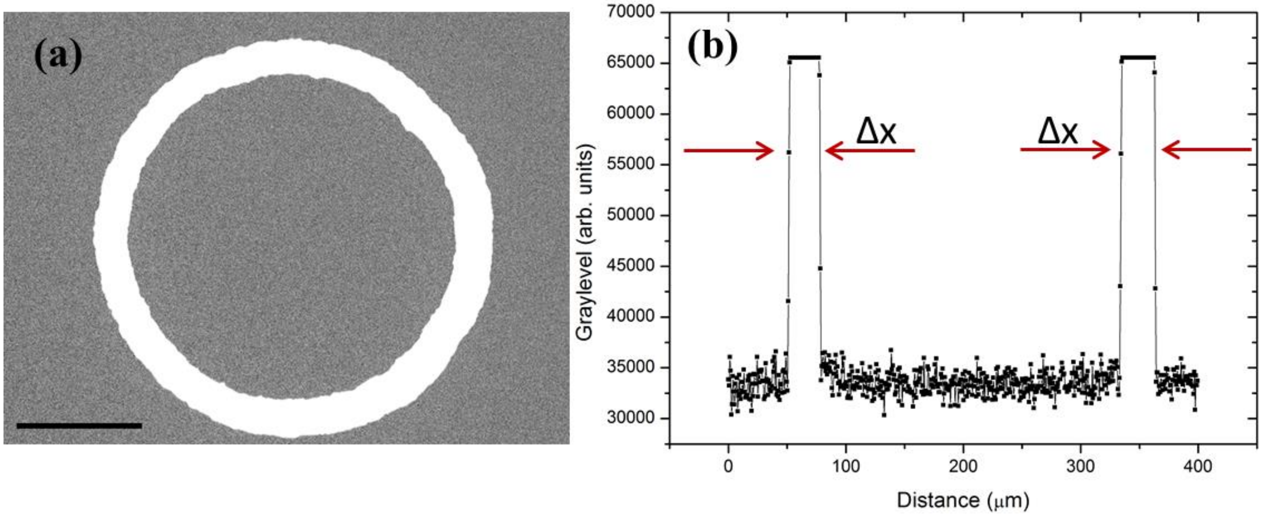

Figure 7: (a) 450 × 450 µm^2 image captured using *evico* Kerr microscope in an out-of-plane magnetised sample with polar Kerr sensitivity. The magnetic domain motion during the field pulse is shown in white contrast. The scale bar is 100 µm. (b) Plot profile of a line scan across (a) obtained using *ImageJ*® for measuring distance travelled by domain during field pulse application.

ImageJ®, an image processing software is then used to calculate the distance moved by the domain during the pulse duration (shown in white figure 7(a)). A line profile across the image obtained from the microscope post differential subtraction results in two square pulse shapes (figure 7(b)). The peaks correspond to the strong change in intensity from grey to white. The width of the peak is measured as the displacement of the domain. Given the known pulse duration from the pulse generator the velocity can be calculated.

Hence the MO Kerr effect is a very versatile tool for studying domain wall motion as well as obtaining quick characterisation of the magnetic properties of the sample. In the following chapter results obtained using the above mentioned techniques are detailed.

3.5 Chapter 3- References

[1] Singulus Technologies, “Rotaris deposition system.” [Online]. Available: http://www.singulus.com/en/innovative-technology/thin-film-deposition/rotaris.html. [Accessed: 10-Jan-2018].

[2] M. McElfresh, “Fundamentals of Magnetism and Magnetic Measurements,” *Quantum Design*, 1994. [Online]. Available: https://www.qdusa.com/sitedocs/appNotes/mpms/FundPrimer.pdf. [Accessed: 10-Jan-2018].

[3] R. Schäfer, “Investigation of Domains and Dynamics of Domain Walls by the Magneto-optical Kerr-effect,” in *Handbook of Magnetism and Advanced Magnetic Materials*, Hoboken, NJ, USA: John Wiley & Sons, Ltd, 2007.

[4] M. Mansuripur, F. Zhou, and J. K. Erwin, “Measuring the wavelength dependence of magnetooptical Kerr (or Faraday) rotation and ellipticity: a technique.,” *Appl. Opt.*, vol. 29, no. 9, pp. 1308–11, 1990.

[5] S. Hashimoto, Y. Ochiai, and K. Aso, “Light Wavelength Dependence of Magneto-Optical Properties in Ultrathin Co/Pt and Co/Pd Multilayered Films,” *Jpn. J. Appl. Phys.*, vol. 28, no. 10A, p. L1824, 1989.

|Chapter 4

Tuning of the perpendicular magnetic anisotropy in ultra-thin films

4.1 Introduction

In this chapter the structural properties as well as the magnetic characterisation of multiple thin film multilayers are discussed which are of prime importance for use as material systems for next generation memory devices. Different methods have been demonstrated and evaluated herein which may be used to modify the Perpendicular Magnetic Anisotropy (PMA) in such Heavy Metal (HM)/Ferromagnet (FM)/oxide multi-layered ultra-thin films. Given that PMA is the *key* ingredient that is required for achieving higher areal density per unit area it is crucial to evaluate novel material systems which exhibit the presence of PMA. Using systematic material engineering one strives to understand the origin of perpendicular magnetic anisotropy in these systems. Finally, magnetic Kerr microscopy at room temperature was utilised to evaluate and screen the magnetic domains in material stacks which may be used for SOT, STT and field induced MRAM as well as to understand if the material system is a plausible candidate for DMI engineering.

4.2 Structural properties

Magnetic thin films studied in this work are in the ultra-thin regime. Films with thicknesses in the order of less than few monolayers are under consideration in this work. Given the novel physics arising within this thickness regime [1], the interface quality as well as a precise control over the thickness of the critical layers is of crucial importance [2][3][4]. Since all thin film samples studied here were grown on a newly installed industrial sputter deposition system, the instrument cluster needed to be initiated and the thin film growth optimised. There was a significant learning curve associated with the mechanisms of the deposition tool.

In order to grow films of defined thickness the deposition rates for each target need to be accurately determined. Given that the Singulus Rotaris deposition system was recently installed and all sputter targets loaded in the chamber were all brand new, it was necessary to calibrate each target before use as well as understand basic conditions for sustained plasma with respect to gas flows and desired power outputs. This involved finding conditions for plasma ignition; deposition of a certain amount of material; using X-ray reflectometry to measure the thickness; finally adjusting the deposition duration to the measured thickness. Example target calibration reflectometry for some targets are shown below (section 4.2.1).

4.2.1 Calibration of sputter targets

X-Ray Reflectometry (XRR) was used to measure the sample thickness. Each sample was subjected to X-rays and the Kiessig fringes were obtained. The Kiessig fringe pattern was then simulated using a recursive algorithm to fit the measured spectra and obtain the film thickness. An open source python based software, GenX® was used to fit the measured spectra[5]. Given that most materials studied in this work undergo a certain degree of oxidation when removed from Ultra-High Vacuum (UHV) environment, the Pt target was the first to be calibrated for thickness which can then be used as a capping layer for the thickness calibration of other targets.

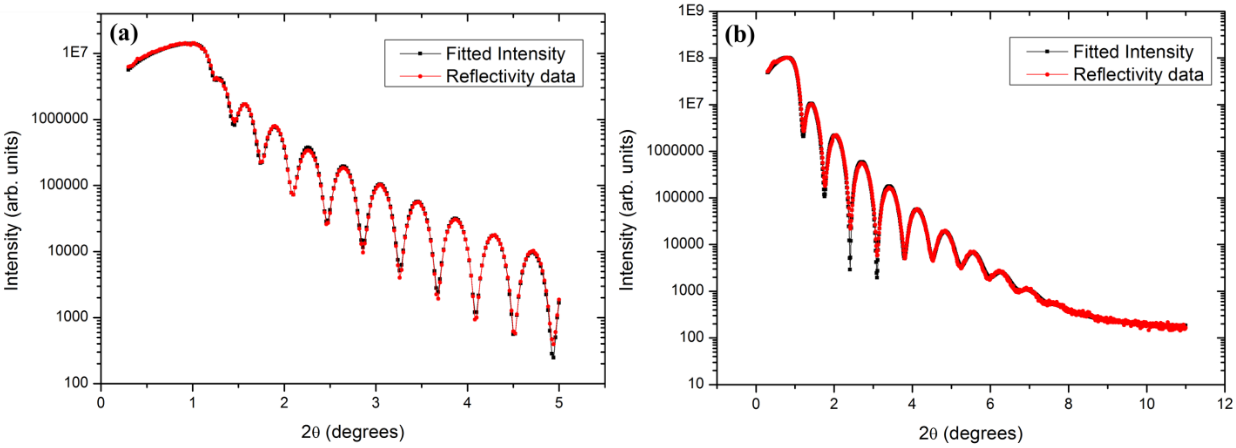

Figure 1: XRR reflectometry curves for Si/SiO_2/Pt(20 nm) (left, (a)) along with fitted curve using GenX (shown in red). XRR curve shown for Si/SiO_2/Pd(20 nm)(right,(b)). Pt film was grown at 0.8 kW and 5×10^{-3} mbar. The Pd film was grown at 0.8 kW and 3.6×10^{-3} mbar. The roughness of Pt and Pd were 0.42 nm and 0.59 nm respectively.

As can be seen from figure 1(a) reflectometry of a single layered Pt thin film, displays a strong fringe pattern. The origin of these Kiessig fringes arises from the interference of the X-ray reflection from multiple interfaces. As mentioned in chapter 3 all films used here were grown on Si substrates (unless stated otherwise) which were covered with thermally oxidised SiO_2 (nominal thickness ≈ 1000 Å). The X-rays therefore interfere from the two interfaces, SiO_2/Pt and the Pt/Air interface. Strong Kiessig fringes up to high angles are observed for such a single layer. The degree to which Kiessig fringes occur indicates the amount of topographical roughness for a given interface. For large roughness the X-rays do not undergo specular reflection and therefore loose intensity at lower angles as compared to samples with excellent interfacial roughness.

Ta is another target which was used extensively not only for seed layer studies but also as a dusting layer for the production of skyrmions.

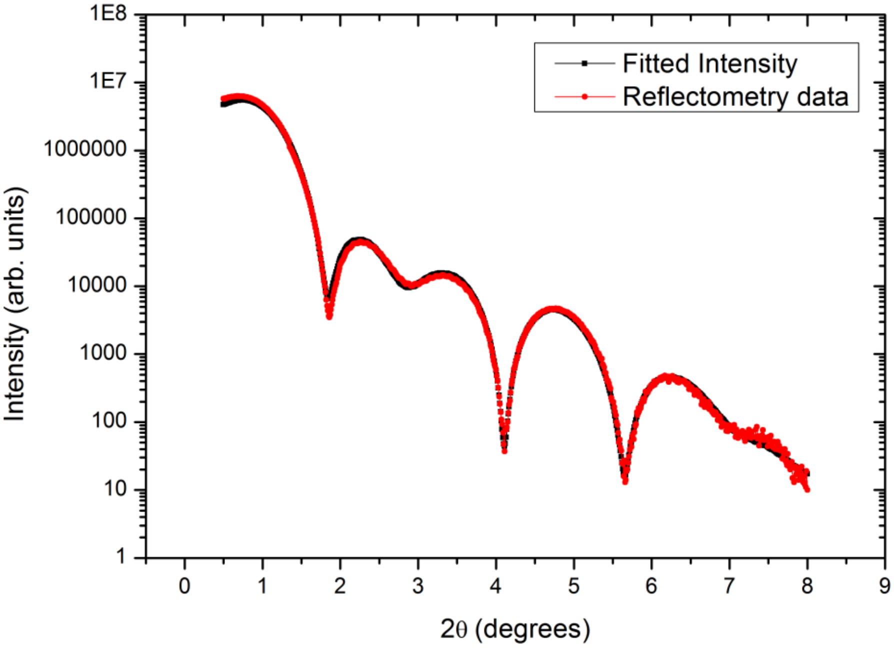

Figure 2: Kiessig fringes (shown in red) obtained via X-ray reflectometry of Si/SiO_2/Ta(5 nm) grown at 0.2 kW and 3.5×10^{-3} mbar. Fitted data simulated using GenX® fitting software shown in black indicating a fitted roughness of ≈0.41 nm for Ta.

A Ta film was deposited for the calibration of Ta target, X-ray reflectivity of which is shown in figure 2. In this case no Pt cap was used as Ta and Pt both materials have similar high densities of 16.6 g/cm^3 and 21.45 g/cm^3 respectively. It is not possible to obtain clear X-ray contrast and differing fringes for two materials with similar densities sharing a common material interface using grazing angle X-ray reflectometry [6]. This therefore adds to complications in fitting the reflectometry. Therefore, the Ta film was not capped with Pt but instead left to naturally oxidise. Ta oxide has a lower density of 8.16 g/cm^3.

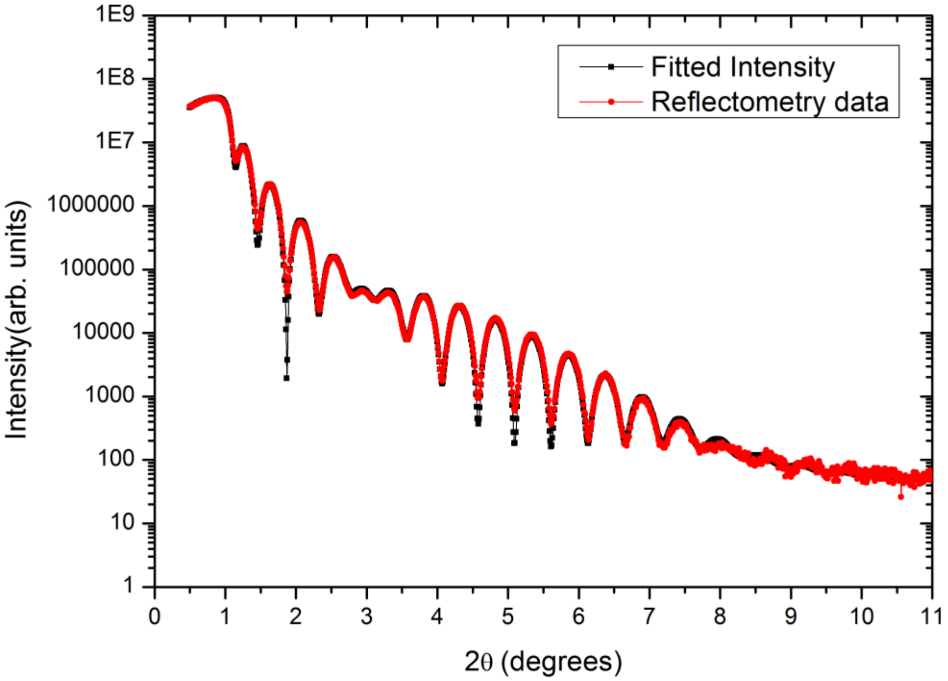

Figure 3: XRR of Si/SiO_2/Ta(20 nm) exhibiting Kiessig fringes upto 10 degrees with a native Ta oxide formation occuring post deposition. The Ta film was grown at 0.2 kW and 3.5 $\times 10^{-3}$ mbar with the Ta roughness ≈ 0.41 nm.

In order to obtain an accurate measure of the material thickness, films were grown for different durations. Shown above in figure 3 is X-ray reflectometry of the same Ta film as shown in figure 2 except the fitted thickness of the film here is 20 nm. It can be seen that for thicker films the number of Kiessig fringes increases, the origin of this is outlined in the theory behind X-ray reflectometry in chapter 2. More importantly it should be noted that the characteristic fringe for a Ta_2O_5 is obtained at approx. 3°. This is visible for both thick and thin films indicating a similar amount of oxide formation (≈1.6 nm) irrespective of initial Ta layer thickness. Similar scans were performed on all sputter targets used in this study.

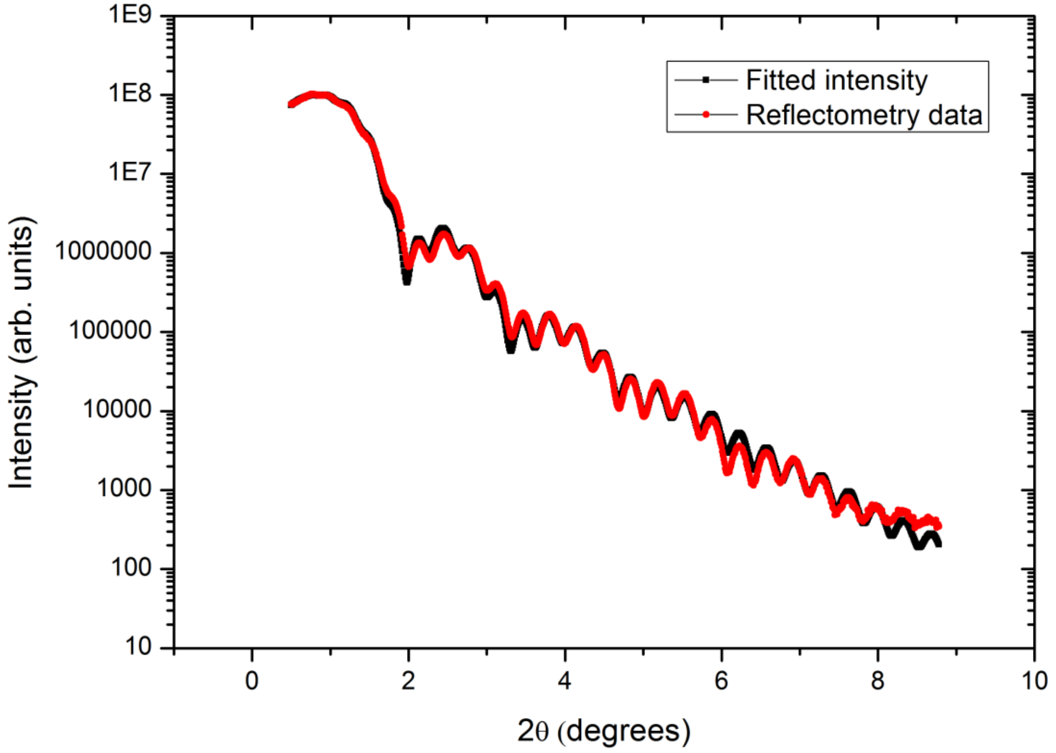

Figure 4: Reflectometry of Si/SiO_2/$Co_{20}Fe_{60}B_{20}$(20 nm)/Pt (5 nm), exhibiting two sets of fringe patterns. Higher frequency from CoFeB and lower frequency from the thinner Pt.

Once the Pt target was calibrated, it was then used as a capping layer for the calibration of other targets prone to oxidation. Shown in figure 4 is an XRR-fitted calibration of $Co_{20}Fe_{60}B_{20}$ film capped with Pt. The FM alloy targets were capped with a Pt capping layer and then subject to X-ray reflectometry for two reasons 1) to prevent oxidation and 2) a combination of Pt and any ferromagnet give good X-ray contrast due to the large difference in their relative densities. It can be seen from the figure above that the XRR spectra is significantly different from a single layered material such as Pt or Ta. There exists an overlaying super structure with periodic oscillation as well as a higher frequency fringe pattern. This is due to the fact that there now exist multiple interfaces i.e. SiO_2/$Co_{20}Fe_{60}B_{20}$; $Co_{20}Fe_{60}B_{20}$/Pt and the Pt/air interface, which collectively contribute to the obtained XRR pattern.

It should also be noted that the substrate or base layer used to grow thin films is critical to the smoothness of subsequent layers. This is evident from figure 5 which highlights the vastly different reflectivity's obtained for different substrates.

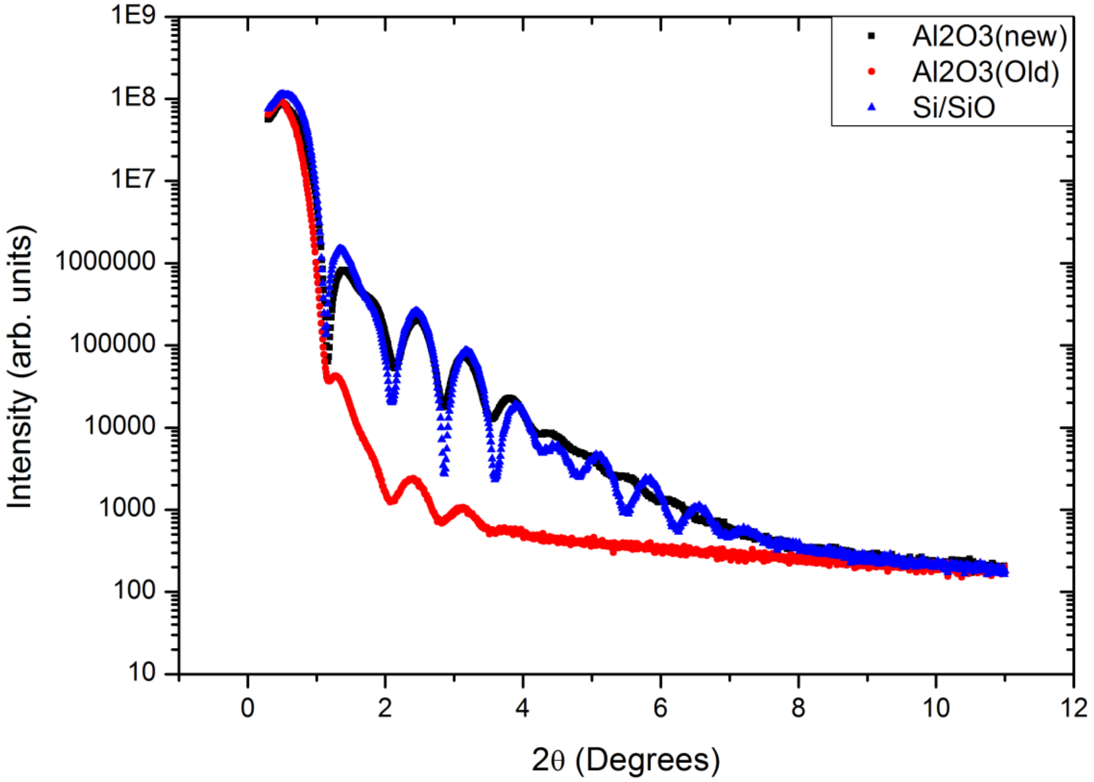

Figure 5: X-ray reflectometry showing the variations of interfacial roughness between three different substrates all with the identical film stack of $Co_{20}Fe_{60}B_{20}$ (10 nm)/AlN(2 nm) grown on them.

Three different substrates namely; Si/SiO_2 single side polished, a recently purchased c-plane sapphire and a c-plane sapphire substrate few years old. A bi-layered film of $Co_{20}Fe_{60}B_{20}$/AlN was deposited on all three substrates in the same deposition run. Therefore, each substrate underwent the exact same deposition. The estimated roughness for each film grown on the three different substrates are shown below in table 4.1.

Substrate used	**Material deposited**	**Nominal thickness(Å)**	**Fitted thickness (Å)**	**Fitted roughness (Å)**
Al_2O_3 New	AlN	20	28.34	7.00
	$Co_{20}Fe_{60}B_{20}$	100	99.65	13.22
Al_2O_3 Old	AlN	20	30.89	14.70
	$Co_{20}Fe_{60}B_{20}$	100	96.29	12.82
silicon	AlN	20	27.87	6.16
	$Co_{20}Fe_{60}B_{20}$	100	97.99	7.08

Table 4.1: Detailing thicknesses and roughness of films of CoFeB/AlN deposited on various different

substrates show casing silicon to have the lowest roughness and therefore the most number of Kiessig fringes.

It can be seen from figure 5 that the film deposited on the Si/SiO$_2$ substrate exhibits Kiessig fringes up to the highest angle as compared to the two other substrates. They were all also measured identically. This indicates that the film grown on the Si/SiO$_2$ substrate is far superior in terms of smoothness compared to the other substrates this is validated as observed from the roughness of the films shown in table 4.1. The roughness for both the AlN as well as the ferromagnet is < 1 nm as shown in table 4.1 when comparing to the Al$_2$O$_3$ (old) substrates both the AlN and the CoFeB are very rough. This implies that the mechanically polished Si/SiO$_2$ substrates are ideal for growing ultra-thin films especially given that these substrates are commercially available at relatively lower in price and already used for CMOS device development. Thereby allowing a faster integration of the materials developed in this work into the storage industry.

Interfacial roughness for a ferromagnet deposited on Al$_2$O$_3$ and Si substrates was studied by Khaydukov *et al*. [7] using X-ray and neutron reflectometry in which they showed that the interfacial roughness and vertical correlation of the roughness of different interfaces are lower for structures deposited on Al$_2$O$_3$ than those deposited on silicon. Using the program VESTA® [8] both the silicon and the sapphire substrates were analysed and the packing density of atoms on silicon was found to be two times that of sapphire.

The substrate roughness correlation for films deposited via magnetron sputtering is governed by the spreading of the atomic species on the substrate surface. This spreading is facilitated by the presence of vacancies on the substrate surface. Atoms deposited on a sapphire substrate have more time to spread as compared to those deposited on silicon due to the higher packing density and therefore the interfacial roughness at the substrate is larger for sapphire than silicon substrates. However it should be noted that the effect of substrate on interfacial roughness is less dominant than the post deposition annealing if performed on such heterostructures. This was demonstrated in a study by Acharya *et al.* [9] in which strontium ferrite films were grown on three different substrates namely silicon, saphhire and Gd$_3$Ga$_5$O$_{12}$ and they found that annealing plays a more major role in the government of the film microstructure as compared to various deposition conditions.

4.2.2 Structural characterisation of ultra-thin films and multilayers

Thin films of W(5 nm)/Co$_{20}$Fe$_{60}$B$_{20}$(0.6 nm)/MgO(2 nm)/Ta(5 nm) were grown on Si/SiO$_2$ substrates. All thicknesses given in parenthesis are in nanometres. In order to study the influence of sputter deposition conditions on the growth of the films, different deposition powers were used to grow the W layer while maintaining the same gas flow. The X-ray reflectometry of these films is shown in figure 6. The sputter power and gas flow was kept the same for all other layers in the material stack.

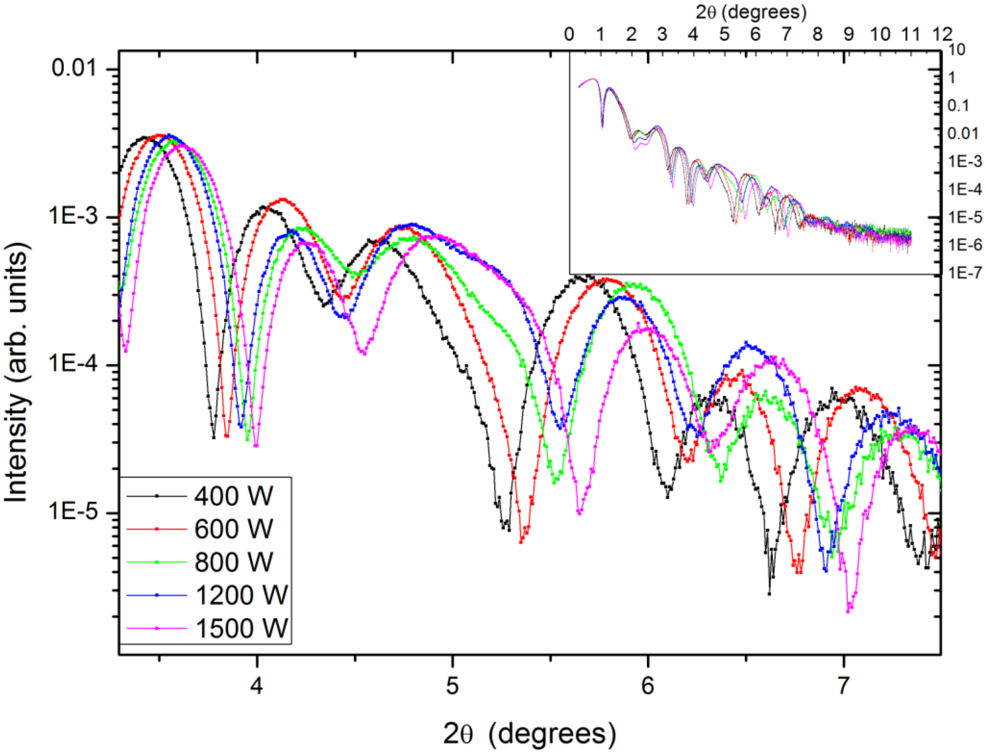

Figure 6: X-ray reflectometry of W(5)/$Co_{20}Fe_{60}B_{20}$(0.6)/MgO(2)/Ta(5) with Si/SiO_2 as the substrate layer and varying deposition power of the W seed layer from 400 W (low power) to 1500 W (high power). All thicknesses given in parenthesis are in nanometres. Inset showing complete XRR spectrum.

As can be seen that the film deposited at higher W power of 1500 W (pink trace) is positively leading i.e. it is leading in angle compared with the lower deposition 400 W (black trace). The 1500 W grown tungsten film exhibits fringes up to a slightly higher degree, thereby implying that the film with the 1500 W tungsten has a better interface quality. Depending on the sputter deposition power applied during growth, the rate of target species arriving at the substrate vary. During the process of sputtering this increase in the target atom species leads to a higher supersaturation of the atomic cloud at the substrate surface. This therefore provides for a higher nucleation rate and one expects a more uniform surface for subsequent layer deposition.

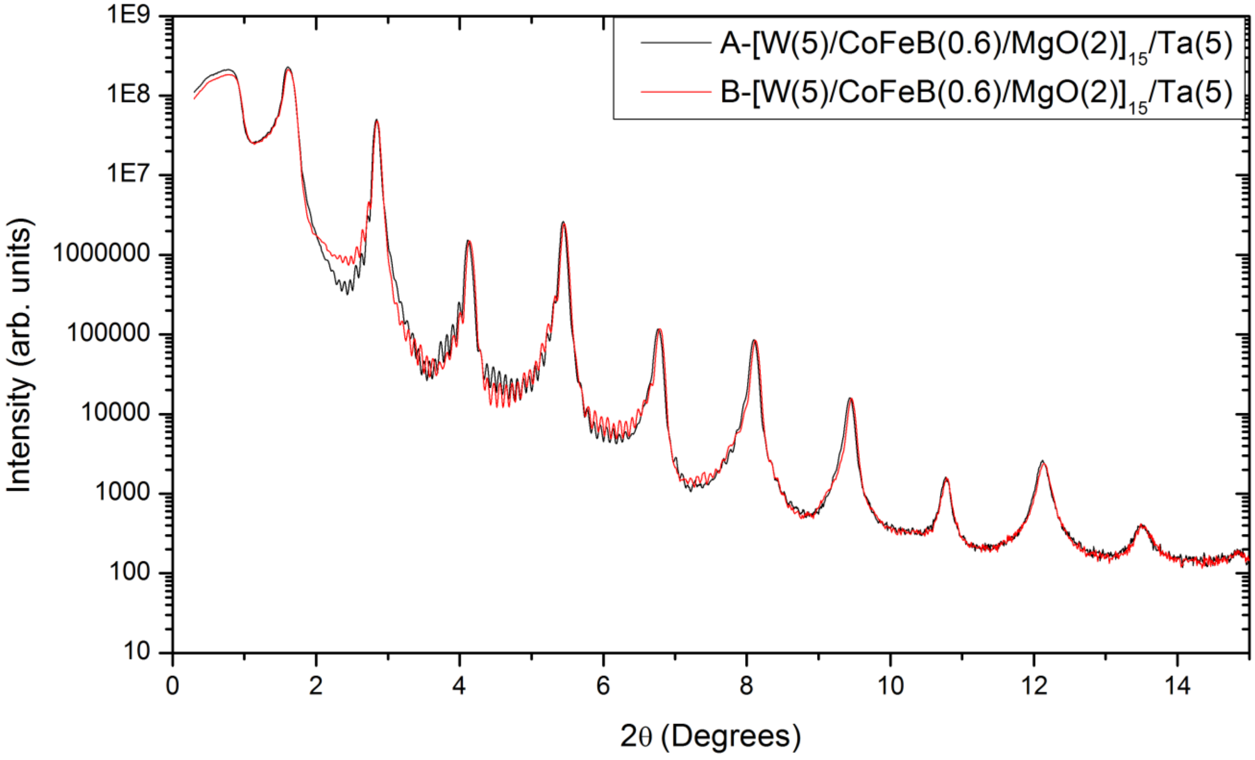

Figure 7: X-ray reflectometry performed on identical multilayers of W/$Co_{20}Fe_{60}B_{20}$/MgO grown on Si/SiO_2 substrates with a time difference of 3 months. Indicative towards reproducibility of the film growth.

Multilayer films with the trilayered stack of [W(5 nm)/$Co_{20}Fe_{60}B_{20}$(0.6 nm)/MgO(2 nm)]$_n$ were grown with varying the trilayer repetition number, n. This was done in order to understand the influence of the magnetic properties on the variation of stack repetition number (discussed in section 4.3.2) as well as interface reproducibility. X-ray reflectometry was performed on n = 5, 10 and 15 repetition stacks, all stacks exhibit similar fringe patterns. An example XRR is shown in figure 7. It can be seen here that there is a distinct difference between the reflectometry of a multi-layered stack and a single repetition trilayer stack with the same individual thicknesses of the materials as shown in figure 6. The two sets of Kiessig fringe patterns shown in figure 7 are for two, nominally similar samples grown on two separate substrates with a 3 month time difference between the individual growths. This is done to check for sample reproducibility which is especially important for industrial development of devices which require very strong reproducibility at all stages from material development to device lithography. One of the factors which may affect the reproducibility apart from statistical variations is sputter target usage. As the target material is sputtered away it will cause a change in the width and depth of the racetrack which can affect the sputter yield of the system. Also if the cathodes were not water cooled during a particular deposition run this could cause heating of the magnets which can affect the stray fields above the cathode and thereby influence the ultimate film growth. Therefore it is important to conduct checks to ensure the system for thin film growth is reproducible and take corrective measures for the same, especially when working on an interfacial physical phenomenon that is strongly influenced by thickness and structure of the underlying material. The two samples A and B show strong reproducibility over 15 repetition layers. The number of peaks for a 15 repetition sample is much greater than the trilayered sample. Also, the periodicity of the stack can be clearly seen from the peaks in the reflectometry data. In order to determine the structure of the film growth, X-Ray Diffraction (XRD) was performed on the three multi-layered samples.

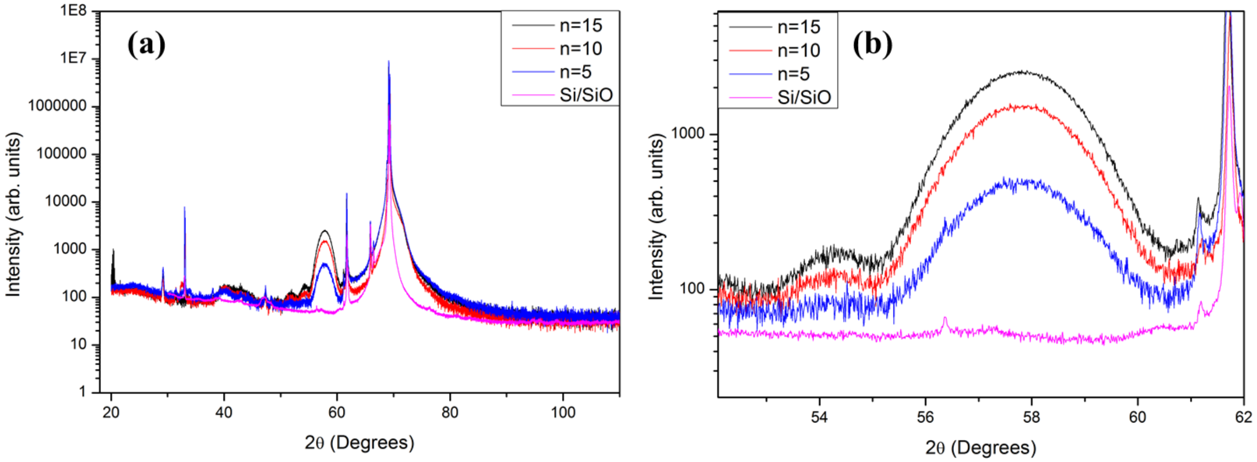

Figure 8: (a) Full range X-ray diffraction of [W(5 nm)/$Co_{20}Fe_{60}B_{20}$(0.6 nm)/MgO(2 nm)$]_n$/Ta(5 nm) for n= 5, 10, 15 repetitions as well as bare substrate scans for comparison. Sharp peaks arise from the strong crystallinity of the substrate while the broader peaks have their origin in the deposited film. All scans were performed using a 0.6 mm slit width at the detector side. (b) Zoomed in section from 2ϴ=52°- 62° of the scan shown in (a) this highlights the texturing arising from the W layers obtained for the multi-layered stack as compared to the substrate which does not show any visible peaks.

Figure 8 shows XRD pattern for $[W/CoFeB/MgO]_n$ for n = 5,10,15. All films were capped with Ta(5 nm) for protection against oxidation. As can be seen the diffraction pattern is rich with a number of peaks. However, overlaying the substrate diffraction pattern allows one to distinguish between the peaks arising from the substrate vis-à-vis the overlaying material. The primary substrate peak occurs at 2ϴ = 69.135° the Si(400) peak. A linear increase in the peak height (intensity) post background subtraction with number of repetitions can be observed for 2ϴ = 57.7° with a peak width of Δ=3.42° assigned to a cubic α W(200) reflection. The Scherrer formula is given as, $d = \kappa\lambda/\Delta\cos\theta$ where λ is the wavelength of the incident radiation and κ is a dimensionless constant relating to the line shape of the diffraction peak. The peak width corresponds to a coherent scattering crystallite size, d of 2.6 nm, i.e. the crystallites in the tungsten layers are smaller than the layer thickness. The intensity increase occurs as with increasing repetitions of the stack, the total amount of material under-going diffraction also increases. For thicker samples therefore the diffraction peaks are more clearly visible. It is difficult to obtain peaks for materials with thicknesses less than 10 nm. Therefore, tri-layered thin films of W(*t*)/CoFeB/MgO were grown on Si/SiO$_2$ substrates with *t* in the range from 6 to 20 nm. XRD of these films is shown in figure 9.

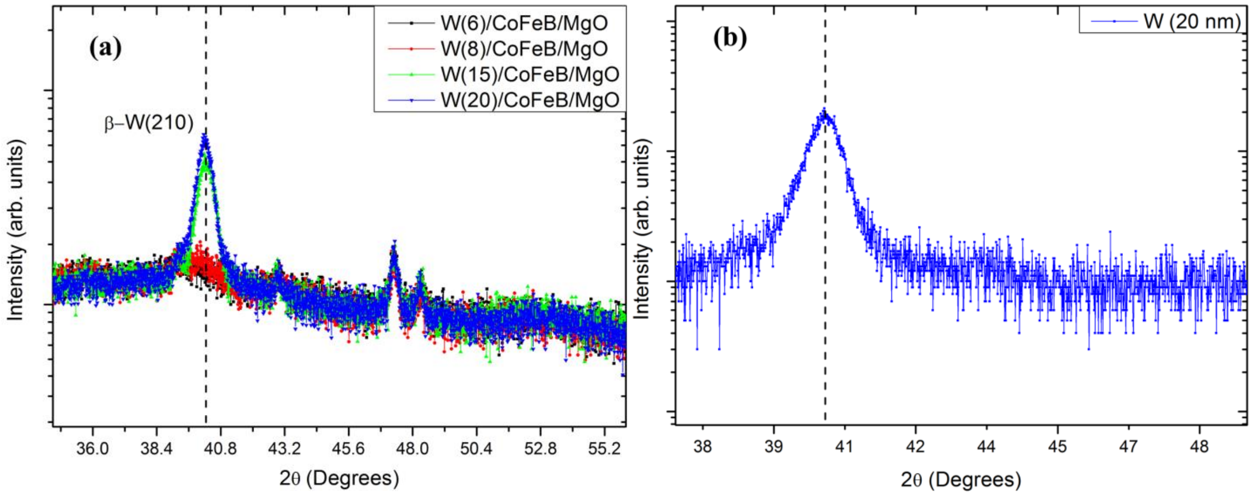

Figure 9: (Left,(a)) X-ray diffraction for thin films of Si/SiO$_2$/W(*t*)/Co$_{20}$Fe$_{60}$B$_{20}$(0.6 nm)/MgO(2 nm)/Ta(5 nm) with *t*= 6 nm,8 nm,15 nm,20 nm. (Right,(b)) XRD of single layered Si/SiO$_2$/W(20 nm) with the (210) peak of the β-tungsten phase indicated.

It can be seen from figure 9 that strong diffraction peaks are obtained for thicker W thickness samples. This peak at 40° corresponds to the W(210), beta-phase[10]. There is slight texturing in the W growth. It has been shown that the beta-W has a much larger spin-Hall conductivity compared to its alpha phase which therefore is suitable for SOT devices[11]. However, in order to confirm that the peak at 40.14^{o} does indeed occur from the W layer and to understand its structural properties, single layer thin film of W was grown on identical substrates and subjected to X-ray diffraction. This is shown in the figure 9(b). Indeed the W film exhibits the (210) peak underlining that the peak arises from the W layer itself. It should be noted however that there might exist a thickness dependence to the structure of the tungsten[10] and further evaluation via cross sectional Transmission Electron Microscopy (TEM) would reveal insights into the same.

In order to evaluate the viability of these HM/FM/oxide layers as materials to be used for storage devices as well as to understand the interfacial physics we need to understand their response to magnetic field. In the next section, thin films and the growth techniques required to achieve PMA are evaluated.

4.3 Magnetic properties and evaluation of perpendicular magnetic anisotropy

There is a need for a thorough study for the evaluation of thin films with respect to PMA. The reasons for which are three fold. Firstly, given the vast number of interfacially dependent phenomena and the slight changes of material structure depending on growth methods, it has become increasingly important for comparative studies that the entire range of the study is performed in a single laboratory using a single deposition chamber. Globally, various groups have studied different interfacial phenomena and reported conflicting results, possibly due to small variations in thicknesses and roughness of the interface. Hence it is important to understand the perpendicular magnetic anisotropy, which is crucial for storage devices, in a range of different materials produced in the same laboratory. Secondly, one needs to find new materials which give rise to PMA as well as interesting domain structures such as skyrmions which when used in devices are more efficient than SOT MRAM and other domain wall based devices. Thirdly, new ways need to be found in which the PMA can be tuned given the limitations imposed by the processing of CMOS devices (temperature limitations).

In this section, the magnetic properties of the ultra-thin films poised to be used as next generation memory elements are highlighted. Details of manipulating the coercive fields, anisotropy, and magnetic saturation via multiple different techniques are discussed herein. Moreover, the domain configurations and structures are evaluated for the selection of the optimal material stack for use as a memory element in next generation spin-electronic device.

4.3.1 Achieving perpendicular magnetic anisotropy

Thin films of W(5 nm)/$Co_{20}Fe_{60}B_{20}$(t)/MgO(2 nm)/Ta(5 nm), were grown and their magnetic properties studied using magneto-optical Kerr effect and Superconducting Quantum Interference Device magnetometry. A composite target was used as an alloy and deposited via D.C. magnetron sputtering of a single target. Post target deposition rate calibration and growth optimization, CoFeB thin films with a composition of 20-60-20 by atomic % were grown in the thickness range of t = 0.6 nm – 1.0 nm. A tungsten layer was used as a seed due to the large spin-orbit coupling. The entire system was capped with a Ta layer to prevent oxidation. The magnetic response as a function of out-of-plane applied magnetic field for W/$Co_{20}Fe_{60}B_{20}$(t)/MgO is shown below.

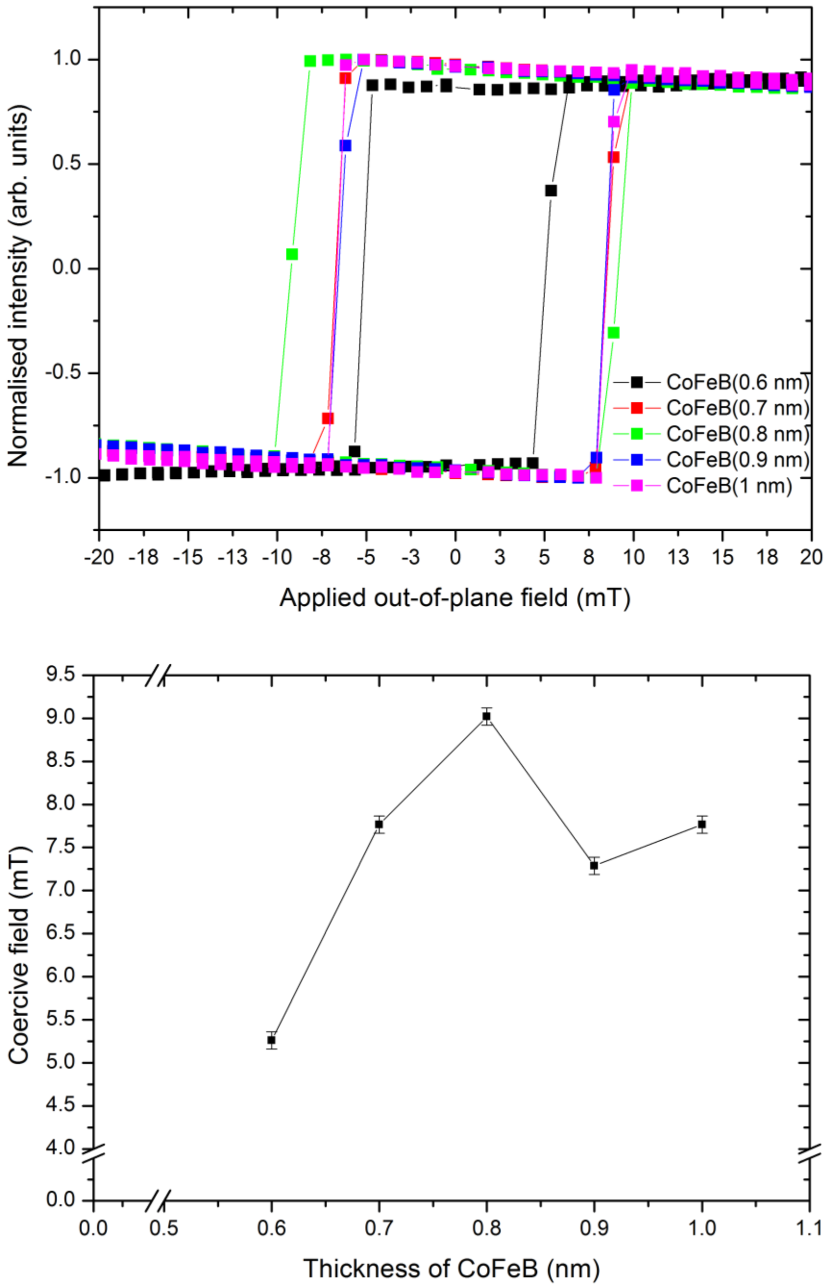

Figure 10: (top) Out-of-plane hysteresis loops using the MO Kerr effect for continuous as-deposited films of W(5)/$Co_{20}Fe_{60}B_{20}$(*t*)/MgO(2)/Ta(5) where *t* = 0.6 nm- 1.0 nm. All thicknesses in parenthesis are in nanometres. (bottom) The coercive fields as extracted from the hysteresis shown as a function of the thickness of the $Co_{20}Fe_{60}B_{20}$.

As can be seen all samples with ultra-thin $Co_{20}Fe_{60}B_{20}$ layers with thickness ranging from 0.6 nm to 1.0 nm have an easy axis in the out-of-plane direction. The coercive field decreases gradually as the thickness of the ferromagnet is reduced. Material systems with a smaller coercive field are suitable for field based memory devices as they exhibit the lowest energy required for magnetization reversal. The sample stack with 0.6 nm $Co_{20}Fe_{60}B_{20}$ exhibits the lowest coercive field of 5 mT. In order to further refine and tune the coercivity, the W seed layer sputter deposition power was varied from 400 W to 1500 W while keeping the thickness of the W constant. This was done so as to understand the influence of growth conditions on the magnetic properties. All thin films of W/$Co_{20}Fe_{60}B_{20}$/MgO grown with varying powers of W were magnetised in the out-of-plane direction. The coercive field was measured as a function of the applied sputter deposition power to the W target as shown in the figure below.

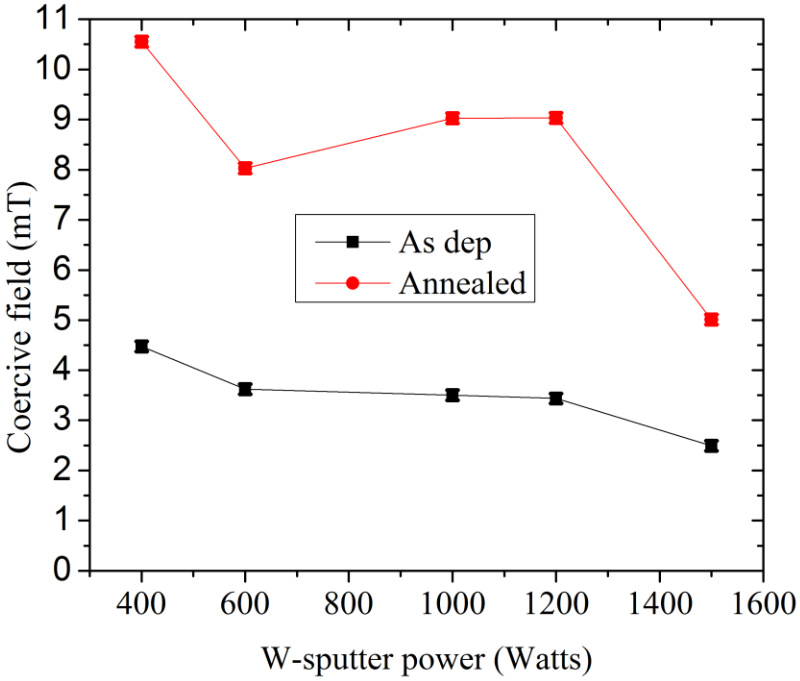

Figure 11: Variation of the coercive field as a function of the deposition power of the seed layer of tungsten for continuous films of W(5),(*P*)/$Co_{20}Fe_{60}B_{20}$(0.6)/MgO(2)/Ta(5) where *P* is the tungsten sputter power, P = 400 W- 1500 W for annealed (red) and as deposited films (black). All films are magnetised out-of-plane as measured via the MO Kerr effect (not shown). Higher powers result in a lower coercive field for both as-deposited and annealed stacks.

It can be seen that the coercive field varies; with the higher W power films exhibiting a lower coercive field. Varying the seed layer deposition conditions allows for an ever so slight variation in the interface onto which the ferromagnetic material is to be grown. Seen as the interfacial nature of this out-of-plane anisotropy, even a slight change in the deposition condition allows for tuning the switching field in the OOP direction.

An indirect evidence for film roughness is the coercive field. It has been shown that rougher films have a relatively larger coercive field due to increased pinning centres in these films [12]. Also similar coercive fields to that shown in figure 11 in the order of few mT were obtained for film stacks of Ta/CoFeB/MgO in a study by Lee *et al.* [13] showing that annealed films have a higher coercivity. The structure of the CoFeB has been shown to be strongly influenced by thermal annealing processes. The influence of sputtering power on the crystal structure and the resulting TMR is shown by Feng *et al*. [14] in which junctions of CoFeB/MgO with both top and bottom electrode separately were investigated and found that higher sputtering power leads to a modification of the CoFeB/MgO interface with a slight crystallisation of the CoFeB and larger TMR ratio. This was confirmed by cross-sectional TEM for varying power densities between 1.31-4.39 W/cm^2.

It is often difficult to provide accurate physical reasoning for effects related to process parameter modifications. The process of sputtering involves a complex series of collisions involving energy transfers and deflections between many atoms. It is difficult to model the sputtering process to obtain the dependences of sputtering process on various experimental parameters [15][9]. Moreover there are 6 interfaces each with its own roughness, thickness and density which needs to be simulated and therefore is not an easy task to obtain a suitably good fit for such films. It is worth noting here that Borodo *et al.* demonstrated that thin films of Al grown at different deposition rates exhibited different surface roughness [16]. It was found that for higher deposition rates of up to 1 nm/s to 2 nm/s the films formed outgrowths and the mean grain size increased 20-30 nm to 50-70 nm with increasing the deposition rates. The root mean squared roughness for the single layer as measured by Atomic Force Microscopy (AFM) increased to more than 3 times when the rate of deposition was increased from 0.1 nm/s to 2.0 nm/s. While studies conducted Ng *et al.* [12] on a ferromagnet, namely Permalloy, which is the workhorse of the spintronics community, show that using D.C. sputter power variations between 50 W and 250 W, a higher sputter power leads to a 40 % reduction in the film roughness and optimum film growth $Ni_{80}Fe_{20}$ on silicon substrates as measured via atomic force microscopy. However these films contain relatively simpler structures of single layers as compared to the ultra-thin multi-layered samples investigated in this work and therefore it is difficult to co-relate these findings. An important point to note here is that the degree of smoothness is modulated far more strongly via the process of annealing as evidenced by the domain structure imaging shown in figure 12 where there is a stark difference in the number of pinning sites and the domain structure for an as-deposited film and an annealed film. Similar results were found by the authors of [9]. The relative power density variations studied by [9] was 1.4 – 7.5 W/cm^2 as compared to the power density variation of 5.1 – 19.1 W/cm^2 used here.

All W/$Co_{20}Fe_{60}B_{20}$/MgO thin films where the W was grown at different powers were annealed post deposition. The coercive field of all films is almost twice the value for the as-deposited films. This may be due to the reason that in such HM/FM/oxide thin films the heavy metal layer acts as a sink for the boron[17][18]. The ferromagnetic alloy CoFeB in the as-deposited form is amorphous in nature. On annealing the alloy undergoes a chemical change and transforms from an amorphous alloy to its crystalline phase [19]. This is evidenced by Park *et al.* [20] in junctions of CoFeB/MgO/CoFeB where it was found that the CoFeB is amorphous in the as-deposited state and undergoes crystallisation on annealing as evidenced by HR-TEM imaging. The CoFeB is lattice matched to the MgO interface. This thereby also enhances the TMR from 35 % to > 100 % post annealing. The more mobile boron (as it's the lightest of elements in the alloy) present in the alloy is crucial for this transformation. Due to the large negative formation enthalpy for metal borides the HM layer absorbs the boron from the adjoining FM leading to a formation of metal borides at the interface [17]. This then leads to the crystallization of the CoFeB alloy. It has been shown that it is possible to mitigate this absorption by using metal nitrides at the interface[4][21]. Due to this phase transformation the coercive field of the now crystalline alloy is relatively higher than the as-deposited form as evidenced in figure 11.

In order to understand the effects of annealing on the domain structures, the magnetic domain structures were imaged using an *evico* wide-field Kerr microscopy. Results from these investigations are shown in figure 12.

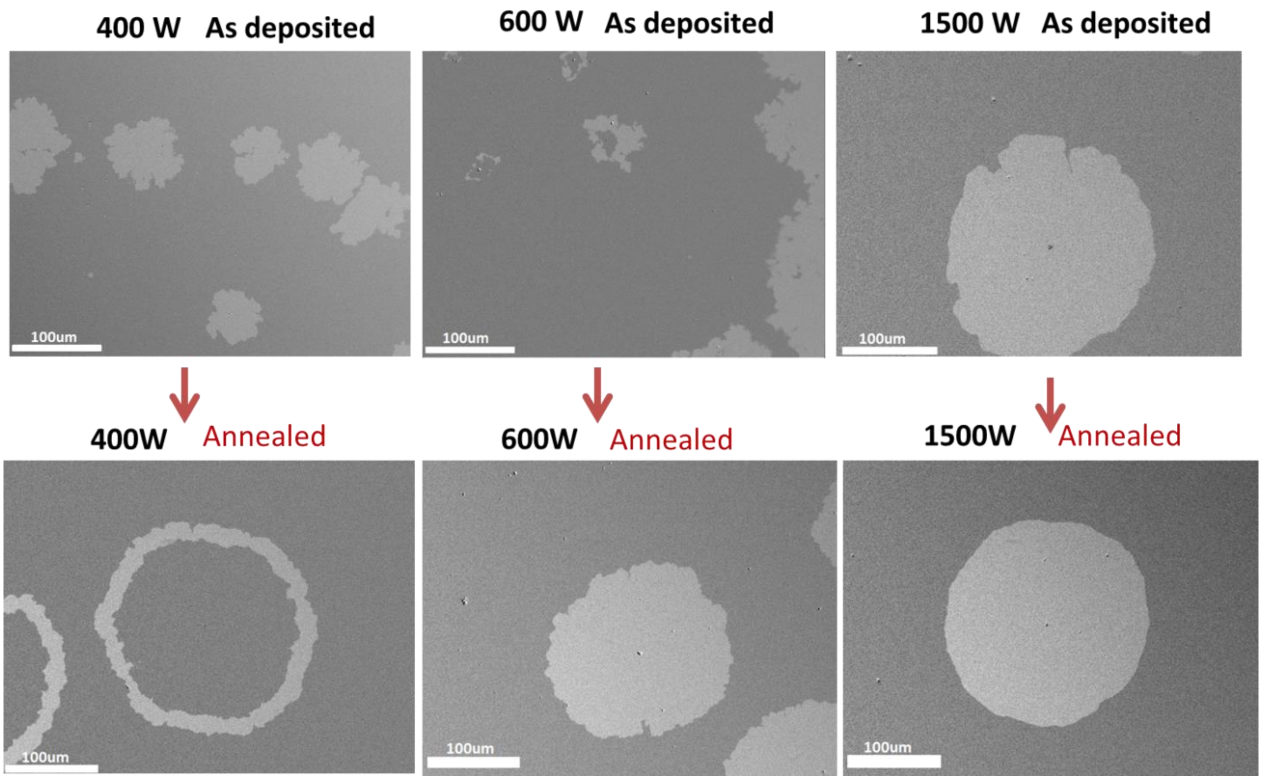

Figure 12: Domain structures as obtained using the *evico* wide-field Kerr microscope for W(5),(*P*)/Co$_{20}$Fe$_{60}$B$_{20}$(0.6)/MgO(2)/Ta(5) multilayers with various tungsten sputter powers for both as-deposited and annealed stacks. All images were obtained in difference mode as explained in chapter 3 section 3.4.2. All measurements were performed on 10×10 mm continuous thin films. Light grey contrast implies out-of-plane ⊙ magnetised and dark grey contrast signifies into the plane ⊗ .

All films exhibit out-of-plane domains as seen by the strong contrast. For low sputter power W films, multiple nucleation points for domain wall nucleation are found in proximity of each other. Moreover for the lower deposition power films, the domain structures are rougher when compared to the higher deposition power. It should be noted especially that the annealing has a strong impact not only on the coercivity but also on the domain structures as observed for the 1500 W film a smooth domain structure with very low pinning is obtained. Low pinning is crucial for the ultimate use of such layers in devices. Moreover certain techniques such as the field driven asymmetric magnetic domain expansion used to quantify the DMI require material stacks which exhibit low pinning and smooth domain structures in an out-of-plane field.

In order to understand the extent of the interfacially governed magnetic anisotropy, the capping layer as well as the seed layer thickness was modified for a given FM thickness and the PMA studied systematically. The degree of metal oxide formation at the top interface is shown to be key in achieving PMA in HM/FM/oxide thin films. This is evidenced by the out-of-plane hysteresis measurements performed as a function of MgO thickness for a W(5 nm)/$Co_{20}Fe_{60}B_{20}$(0.6 nm)/MgO(*t*) thin film as shown in figure 13. The MgO thickness was varied between 0.1 nm to 2.0 nm.

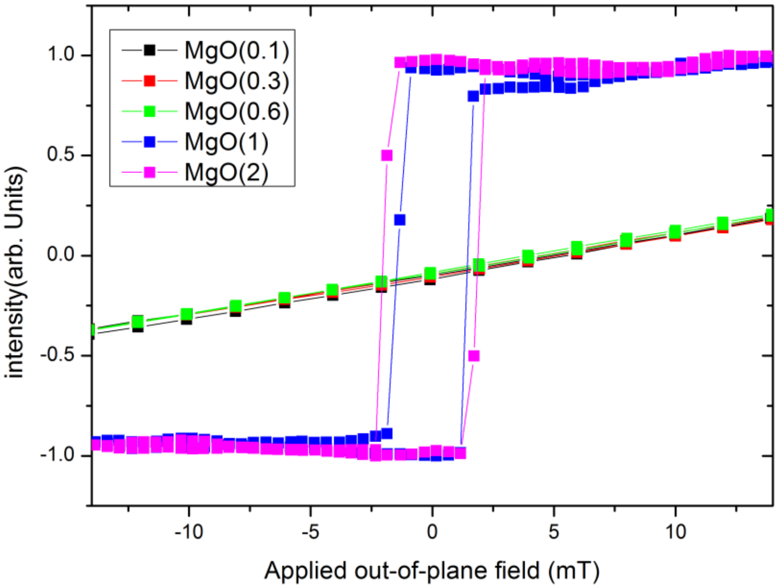

Figure 13: Out-of-plane hysteresis curves for W(5 nm)/$Co_{20}Fe_{60}B_{20}$(0.6 nm)/MgO(*t*)/Ta(5 nm) for continuous thin films measured via the MO Kerr effect for thicknesses, *t* = 0.1 nm – 2.0 nm.

For thicknesses less than 1 nm the MgO layer is not continuous and develops pin holes thereby not achieving PMA as evidenced by the lack of out-of-plane switching of the magnetisation. By performing temperature dependent measurements Ventura *et al.* [22] found a positive change in resistance with temperature which was attributed towards pinholes in 7.5 Å of MgO barriers. Moreover, pinholes have been imaged by Zhao *et al.* [23] using High Resolution (HR) cross-sectional TEM imaging during their study of failure analysis in CoFeB/MgO barriers. They have shown pinholes to be generated in such barriers with thicknesses of 8.5 Å. The MgO barrier has also been characterised using conductive atomic force microscopy which measures simultaneously the conductivity and the topography at the nanometre scale [24] by Bhutta *et al.* [25][26] and found that a closed pinhole free barrier is formed at 1 nanometre thickness. Also it was shown by authors of [25] that there is a sudden decrease in the density of pinholes between 0.6 nm and 0.8 nm. It has been shown that the origin of PMA is attributed to the hybridisation between the *2p* and the *3d* orbitals of oxygen and iron at the metal-oxide interface, respectively [27].

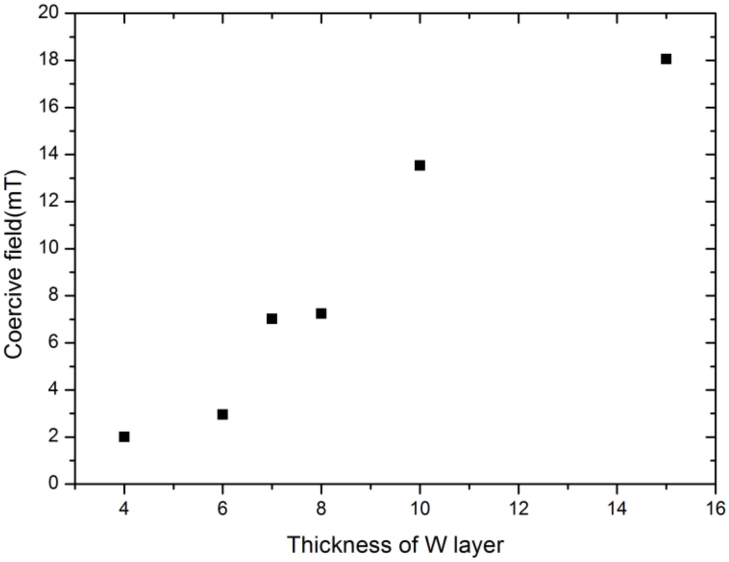

Figure 14: Modification of the coercive field as a function of the thickness of the W seed layer for multi-layered continuous thin films of W(t)/$Co_{20}Fe_{60}B_{20}$(0.6 nm)/MgO(*t*)/Ta(5 nm) with the W grown with thicknesses between 4 nm and 15 nm.

The coercivity of the PMA HM/FM/MgO need not only be modified via tuning of the top interface, but also can be modified by varying the thickness of the seed layer. As the thickness of the W seed layer is increased there is a linear increase in the coercive field as evidenced in figure 14. This may be attributed towards an increase in surface roughness above 6 nm.

In order to verify that annealing truly leads to a higher coercive field due to the diffusion of boron towards the heavy metal layer, similar experiments were performed on the same stack with Ta as a seed layer instead of W. The results for as-deposited and annealed coercive field variation as a function of varying Ta thickness are shown in figure 15.

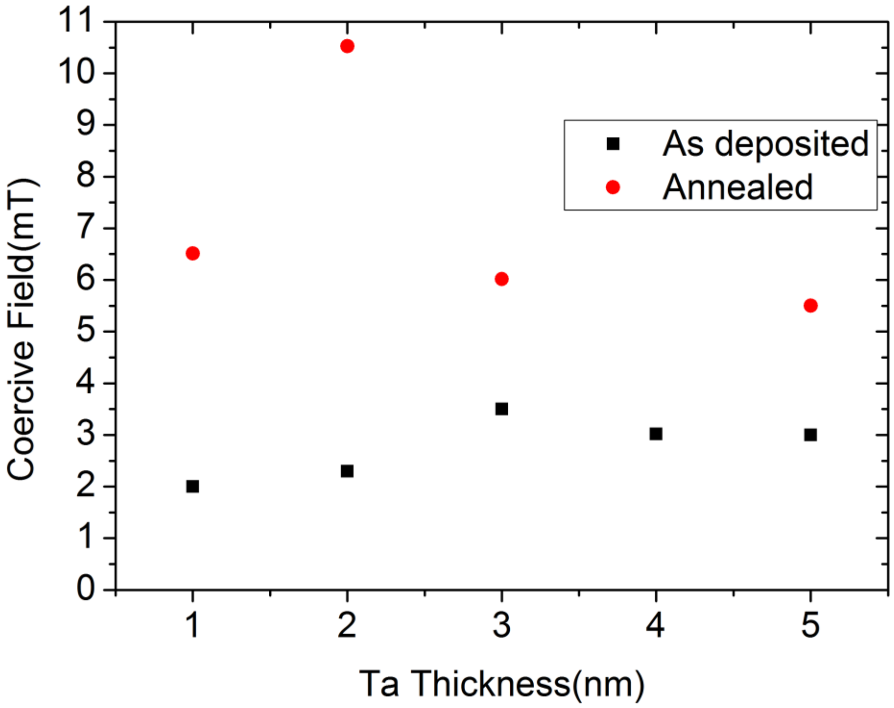

Figure 15: Variation of the coercive field as a function of the Ta thickness seed layer for both as-deposited and annealed stacks of Ta(1 nm - 5 nm)/$Co_{20}Fe_{60}B_{20}$(0.6 nm)/MgO(2)/Ta(5 nm)

It can be seen from figure 15, for a range of seed layer, Ta thicknesses the as-deposited easy axis coercive field is lower than that for the same stacks post annealing process. A higher coercivity for such PMA stacks demonstrates that the CoFeB undergoes crystallisation. Similar values for the coercive field were obtained for a Ta based magnetic tunnel junction as demonstrated in [13].

However the PMA is not independent of the FM in consideration. There needs to exist a correct combination of the FM, HM as well as the oxide. For example when $Co_{20}Fe_{60}B_{20}$ is grown using a Pt seed layer it results in an in-plane magnetised stack. PMA is not obtained for Pt/$Co_{20}Fe_{60}B_{20}$/MgO films. This can be seen from the soft, easy axis hysteresis obtained with the applied field in the in-plane direction in figure 16.

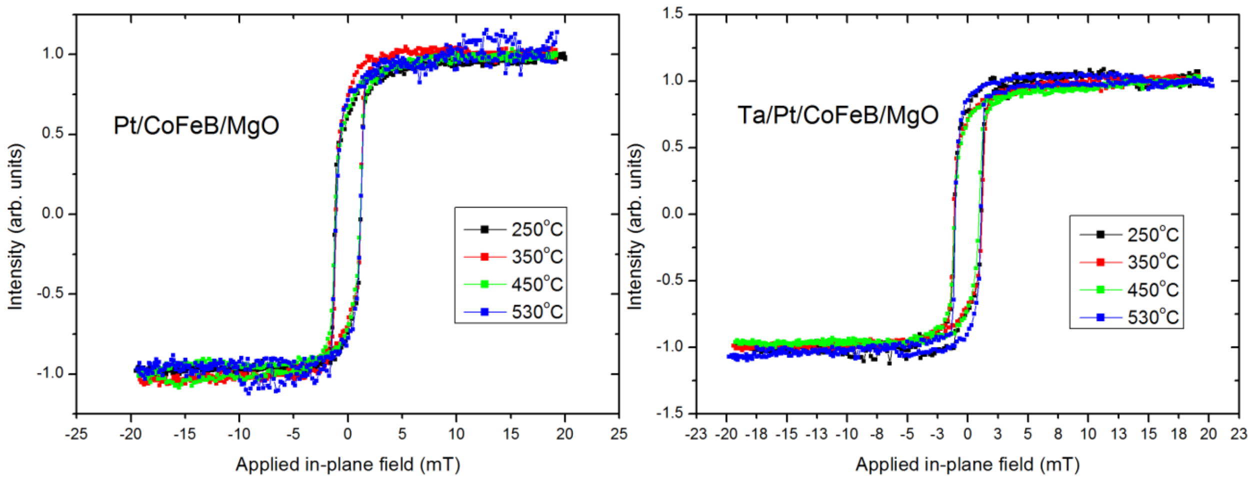

Figure 16: Easy axis hysteresis curves in the in-plane direction for continuous thin films of (left) Pt(4 nm)/$Co_{20}Fe_{60}B_{20}$(0.8 nm)/MgO(2 nm) as a function of varying annealing temperature. (Right) Easy axis hysteresis in the in-plane direction for the same film with the addition of a buffer layer, making the total film structure Ta(5 nm)/Pt(4 nm)/$Co_{20}Fe_{60}B_{20}$(0.8 nm)/MgO(2 nm) shown for various annealing temperatures (temperature set at heater). All films were capped with 2 nm Ta for oxidation protection.

Multiple thicknesses of the ferromagnet were used while always obtaining an easy axis in in-plane orientation. As can be seen from figure 16 films grown with a Pt seed and an iron rich $Co_{20}Fe_{60}B_{20}$ alloy do not result in a perpendicular magnetic anisotropy. Progressive annealing up to 530°C (heater temperature) does not have any effect on the switching field. The squareness of the hysteresis curves does not change significantly (not shown). The films remain intrinsically magnetised in the plane of the film.

This suggests that the mechanism for PMA in such films is not strictly governed by the hybridisation of the Fe *3d* and the oxygen *2p* orbitals since the top interface with the FM is identical for the W and Ta seeded CoFeB films as discussed for figure 11 and 15. Moreover, a Ta buffer was also used to improve the texturing of the Pt [28] and facilitate the growth of subsequent layers as this is assumed to enhance the PMA [29] as well as the interfacial DMI [30]. However, neither adding a buffer layer nor even annealing the stack with the Ta buffer layer resulted in any significant change in the intrinsic magnetisation in these ultra-thin films. Hence the ferromagnetic alloy itself was changed from an iron rich to a cobalt rich and the stack Pt/$Co_{60}Fe_{20}B_{20}$/MgO was tested for PMA.

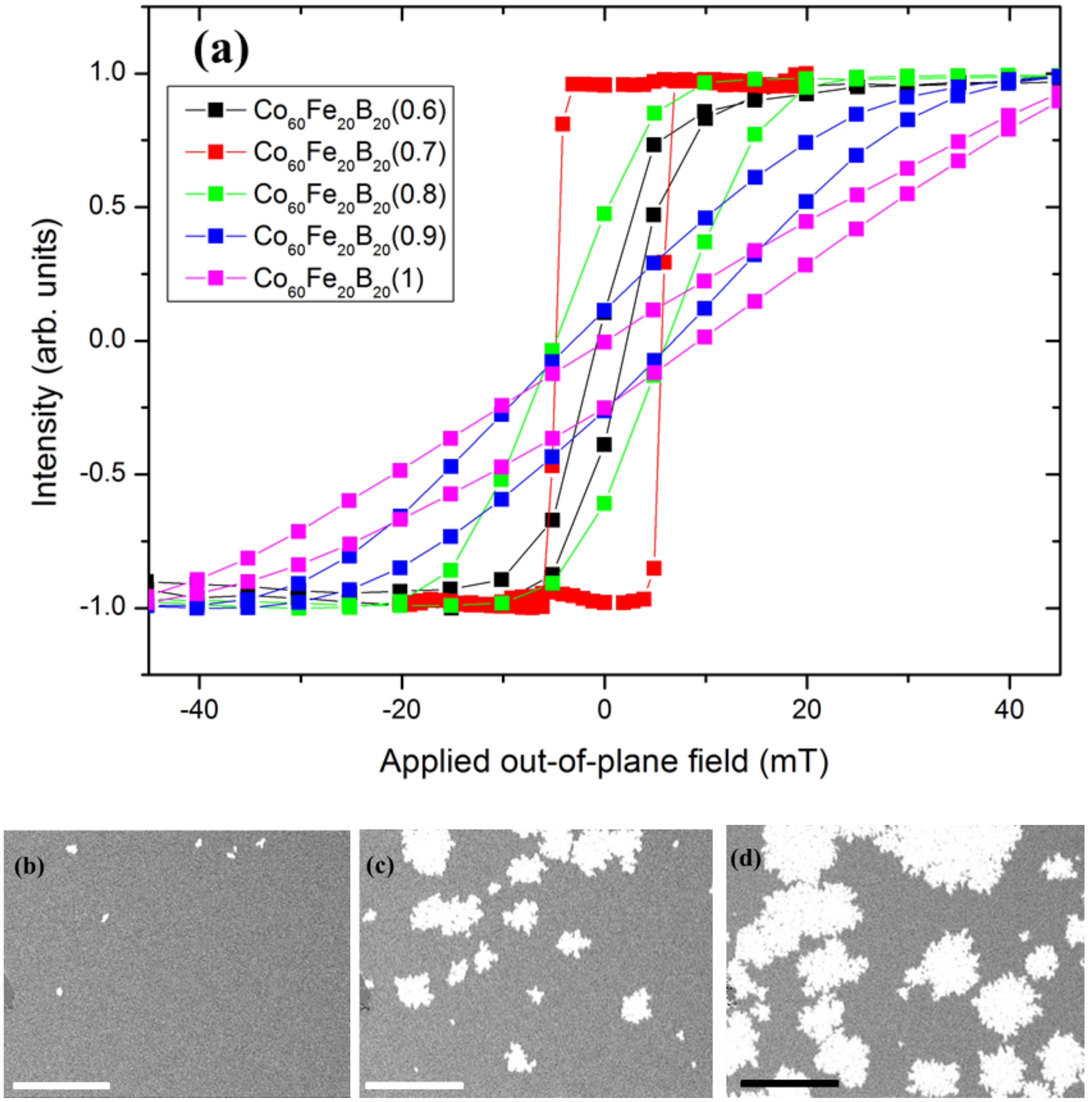

Figure 17: (a) Out-of-plane hysteresis curves determined by MOKE magnetometry for continuous thin films of Pt(5 nm)/$Co_{60}Fe_{20}B_{20}$(*t*)/MgO(2 nm)/Ta(2 nm) with thickness, *t* of $Co_{60}Fe_{20}B_{20}$ between 0.6 nm – 1.0 nm. All films were annealed at 400^{o}C (wafer temperature) in UHV with pressures $< 3\times10^{-7}$ mbar for 2 hours. The domain nucleation and propagation in the presence of out-of-plane field for a film with 0.7 nm $Co_{60}Fe_{20}B_{20}$ is shown as an example. The scale bar for (b-d) is 50 µm.

A range of thicknesses of $Co_{60}Fe_{20}B_{20}$ were grown for evaluation of the out-of-plane anisotropy with Pt as the seed layer. The out-of-plane hysteresis response of Pt/$Co_{60}Fe_{20}B_{20}$/MgO is shown in figure 17(a). The magnetisation now lies out of the plane as evidenced by the easy axis hysteresis curves as a function of $Co_{60}Fe_{20}B_{20}$ thickness. It is also evident from figure 17(a) that the lowest thickness of FM does not always result in the strongest anisotropy. It can be seen that 0.7 nm of FM has a much sharper switching as compared to 0.6 nm. This may be partly due to inhomogeneous wetting of the FM for thicknesses less than 0.7 nm. The domain structures for 0.7 nm $Co_{60}Fe_{20}B_{20}$ are shown in figure 17(b-d) as a function of field. Very strong magnetic Kerr contrast is obtained for these stacks, however, the domain structures exhibit pinning during field driven motion due to intrinsic structural defects.

Given the subtlety of the interfacial contributions to PMA it is essential to understand the contribution of each interface. Also, since annealing CoFeB leads to its crystallisation the FM in consideration was modified. Therefore thin film of Pt/Co(*t*)/Pt i.e. a symmetric stack of no alloy but 100 % Co as a ferromagnet as well as the absence of an oxide was used to test the contribution of FM-oxide interface to the PMA and to understand the contribution of the FM to the coercive field.

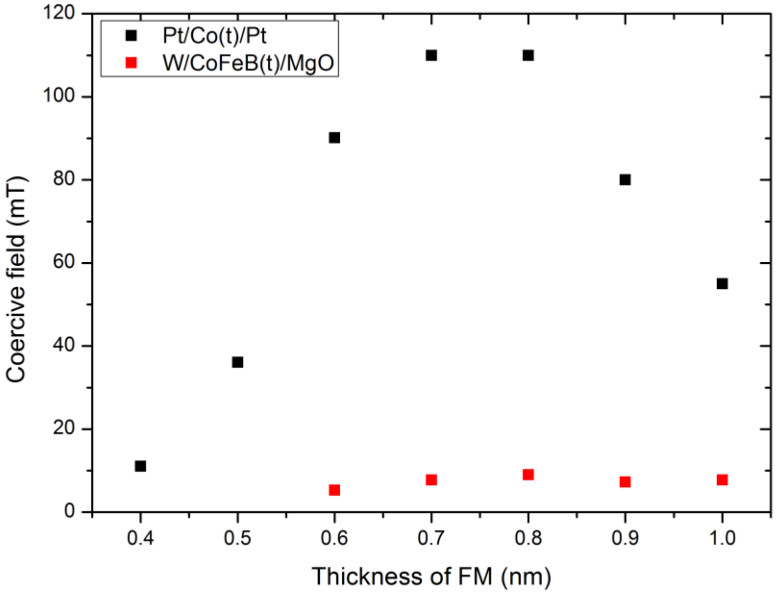

Figure 18: Relationship between the coercive field and the thickness of a ferromagnet for two stacks of continuous thin films with (black) Pt/Co/Pt symmetric interfaces and (red) W/$Co_{20}Fe_{60}B_{20}$/MgO non-symmetric interfaces.

A number of observations can be inferred from figure 18. Firstly, symmetric structures of Pt/Co/Pt which lack the presence of an FM/oxide interface results in perpendicular magnetic anisotropy in the as-deposited state. Secondly, a strong modulation of the coercive field can be achieved by tuning the thickness of the Co layer. Thirdly, when compared to a ferromagnetic alloy (CoFeB) the coercive field for Co based stacks is an order of magnitude larger.

Due to the relatively lower coercivity obtained in such FM alloys they are better suited for use in PMA devices as compared to more conventional use of Pt/Co multilayers. Since their anisotropy can be heavily influenced simply by varying the annealing temperature while keeping the thickness of the FM constant as discussed in section 4.3.2. This is a desired trait in TMR devices where not just PMA but also the Resistance Area (RA) product needs to remain low for efficient switching, and reducing the thickness of a

FM for higher PMA will increase the RA as well, due to increased surface scattering [31] . More so, the out-of-plane switching fields of such FM alloys is an order of magnitude smaller than traditional Co films. Given these reasons majority of this study was primarily focussed on FM alloys instead of pure ferromagnet.

In order to test the influence of heavy metal layer with varying SOC coupling strengths and lower electron affinity on the magnetic domain structures, a seed layer of group (X) from the periodic table was used.

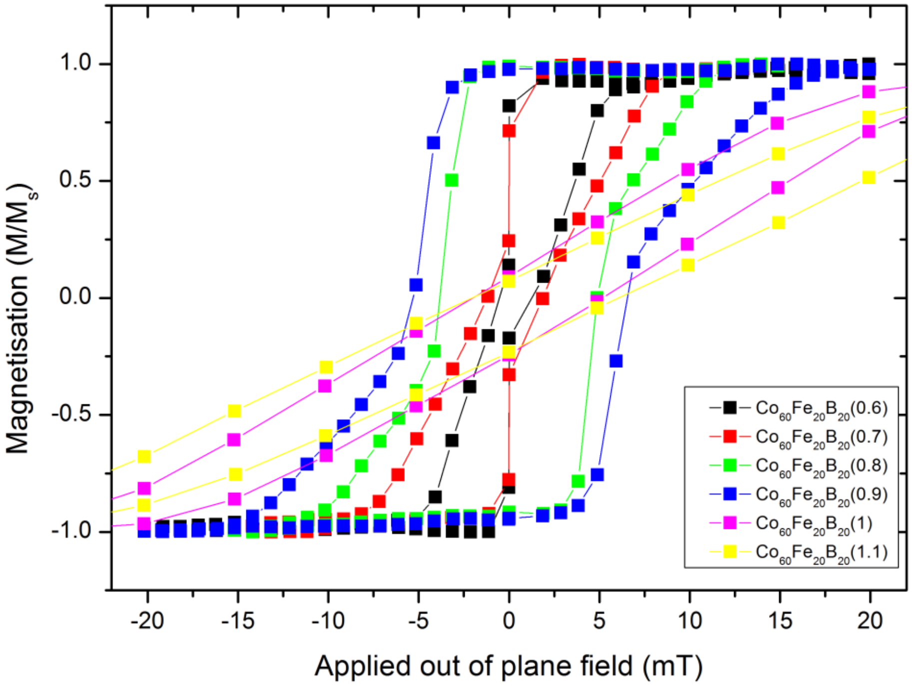

Figure 19: Out-of-plane hysteresis for continuous films of Pd(5 nm)/$Co_{60}Fe_{20}B_{20}$(*t*)/MgO(2)/Ta(5 nm). All films were annealed at 400° C (wafer temperature) for 2 hours under pressures < 3×10^{-7} mbar.

Thin films of Pd/$Co_{60}Fe_{20}B_{20}$/MgO were grown and their out-of-plane hysteresis measured. These thin films exhibit an easy axis in the out-of-plane direction for FM thicknesses from (0.6 nm to 0.9 nm) as shown in figure 19. Moreover, it is important to note here that the out-of-plane hysteresis loop exhibits two reversal events. Initially domains are nucleated at points of intrinsic defects which accounts for the sharp jump in magnetisation. The gradual increase in magnetisation is due to the expansion/propagation of the worm domain structures. This is shown as an example in figure 20(a-c).

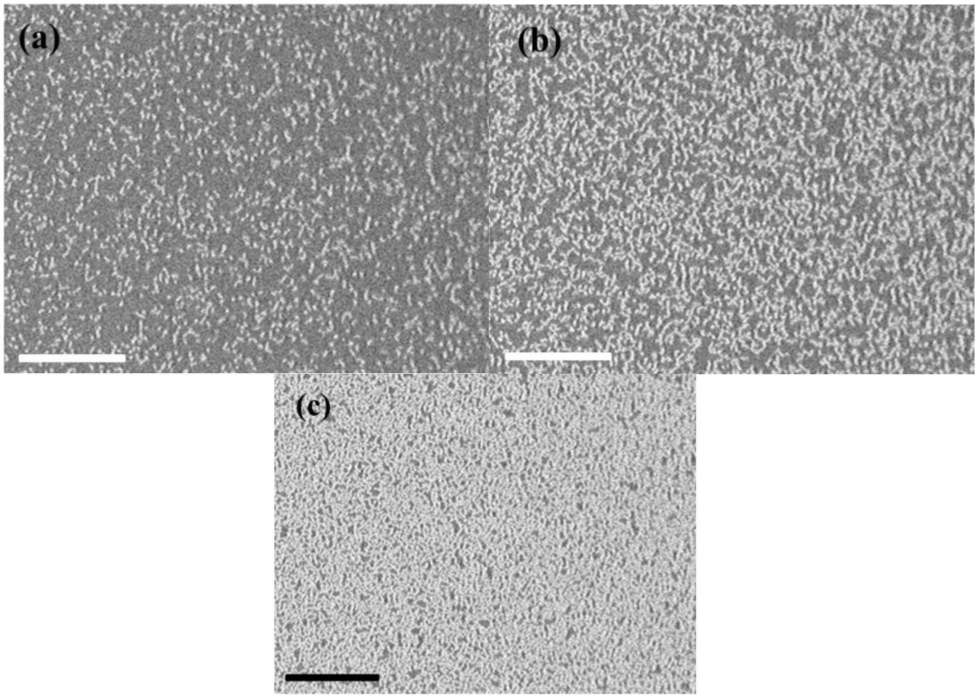

Figure 20: Magnetic domain images in the presence of a gradually increasing out-of-plane magnetic field for Pd(5 nm)/$Co_{60}Fe_{20}B_{20}$(0.7)/MgO(2)/Ta(5 nm) obtained using the *evico* wide field Kerr microscopy in the polar configuration. All images obtained are taken in differential imaging mode.

It is interesting to study such domain structures which are different from the more typical bubble domain structures obtained for a range of different seed layers and shown by different groups who have used such bubble domain structures to evaluate DMI in their systems. These worm domain structures however have been shown to give rise to skyrmions [32][33].

4.3.2 Tuning magnetic anisotropy and understanding temperature effects on PMA in multilayers

In the previous section the origin of PMA was highlighted via the use of different seed layers, and ferromagnets. In this section the magnetic properties of various magnetic multilayers along with the effects of temperature on their anisotropy are outlined. Several means of manipulating the magnetic properties (anisotropy field as well as magnetic saturation) are shown. As discussed in chapter 2, section 2.5, the Dzyaloshinskii-Moriya Interaction as well as the presence or absence of skyrmions in a given system is ultimately governed by the effective anisotropy of a material. Moreover, for existing STT-MRAM devices [34][35], as well as hard disk drives, magnetic anisotropy is the key property studied which provides an estimate of the thermal stability of the memory. Hence its method for manipulation and its tuning is a key asset required in developing new materials with higher density.

The magnetic anisotropy of thin films of W/$Co_{20}Fe_{60}B_{20}(t)$/MgO were studied as a function of thickness of the ferromagnet for both as-deposited as well as annealed thin films and is shown in figure 21.

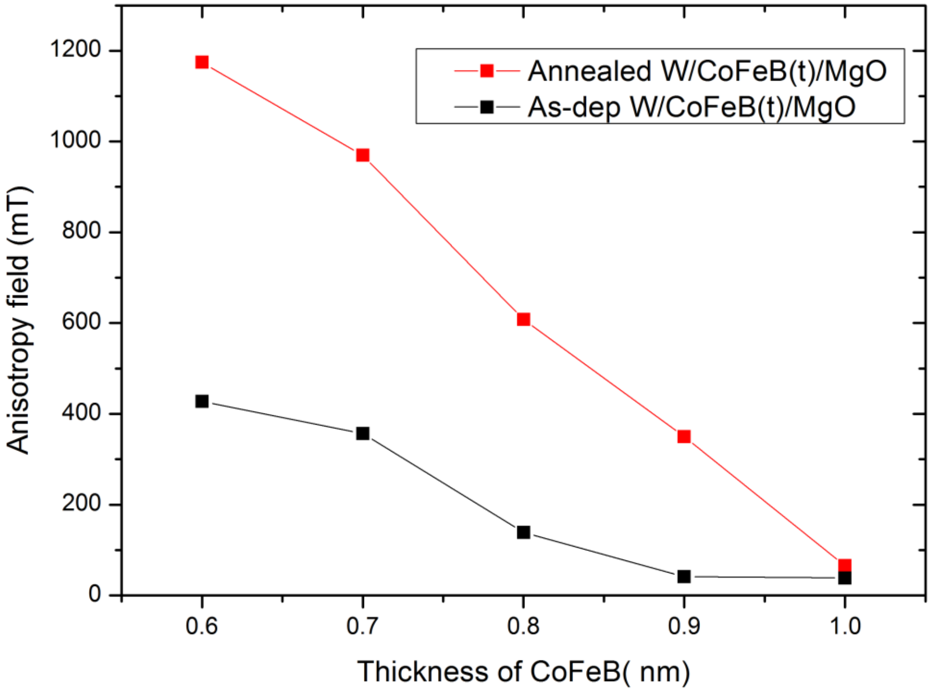

Figure 21: The variation of the anisotropy field shown as a function of the thickness of the ferromagnetic alloy as measured using the SQUID magnetometer on 10 mm × 5 mm for both as-deposited (black) and annealed (red) continuous thin films of W(5 nm)/$Co_{20}Fe_{60}B_{20}$(0.6 nm- 1.0 nm)/MgO(2 nm)/Ta(5 nm).

Both as-deposited and annealed stacks exhibit a linear increase in anisotropy field with decreasing thickness. This corroborates the fact that the PMA in such thin films is purely interfacially driven. Also there is a significant improvement in the anisotropy field with post deposition annealing as evidenced by the steeper slope in figure 21 of the annealed stacks. The higher anisotropy allows for higher density storage as the amplitude of field required for magnetisation reversal is larger, thereby allowing more bits to be stored per unit area. Therefore it is crucial to be able to generate ultra-thin thickness films; moreover as it will be demonstrated in subsequent chapters, ultra-thin films are more efficient in switching as well as the DMI scales inversely with thickness. Therefore thinner films with lower thickness of the ferromagnet are preferred. Although, there is a significant challenge in their production owing to the homogeneity of the surface and the lack of proper wetting of the surface with decreasing thicknesses.

This interfacial PMA occurs also for the Ta based thin film as evidenced by the inverse relation of the anisotropy to the thickness of $Co_{20}Fe_{60}B_{20}(t)$ shown in figure 22.

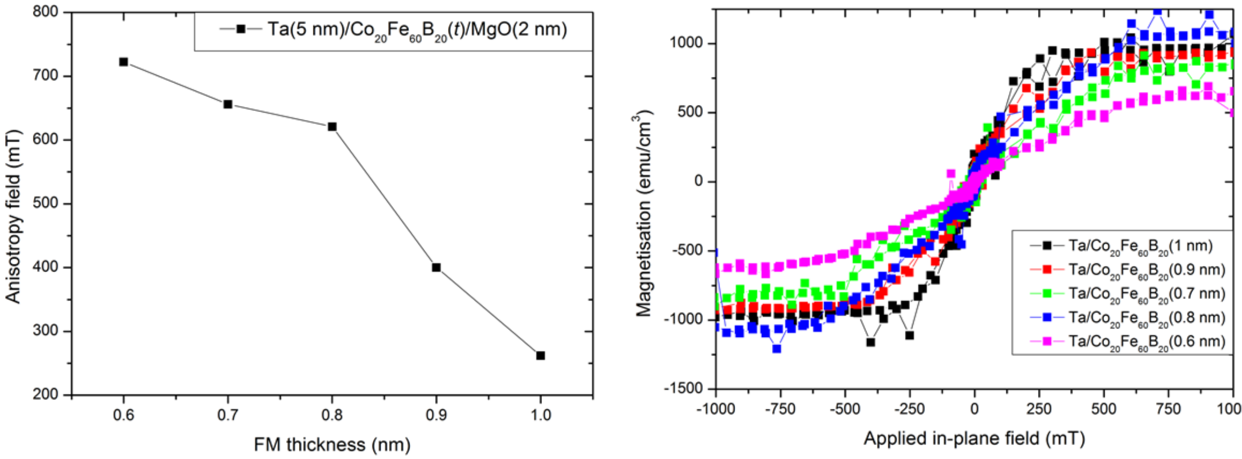

Figure 22: (Left) Variation of the anisotropy field as function of the ferromagnetic alloy thickness for as-deposited continuous thin films of Ta(5 nm)/Co$_{20}$Fe$_{60}$B$_{20}$(0.6 nm-1.0 nm)/MgO(2 nm)/Ta(5 nm) as obtained via SQUID magnetometry with sample sizes of 10 mm × 5 mm. (Right) Hard axis hysteresis curves with the field applied in the in-plane direction for as-deposited films of Ta(5 nm)/Co$_{20}$Fe$_{60}$B$_{20}$(0.6 nm-1.0 nm)/MgO(2 nm)/Ta(5 nm).

The above variation was measured for as-deposited films of Ta(5 nm)/ Co$_{20}$Fe$_{60}$B$_{20}$(t)/MgO(2 nm). It should be noted that the saturation field for a Ta based stack is larger than that of an as-deposited W based stack. Moreover, it should also be noted that for the thin 0.6 nm Co$_{20}$Fe$_{60}$B$_{20}$ there is a significant reduction in the normalised saturation magnetisation which indicates that a magnetically dead layer may have formed. The effective anisotropy energy for such films can be extracted via, $K_{eff} = \mu_0 H_K M_s/2$ and is shown in table 4.2 for (X)/Co$_{20}$Fe$_{60}$B$_{20}$(t)/MgO with X=W or Ta and t = 0.6 -1.0 nm. A dead layer ≈0.3 nm is formed at the Ta/CoFeB interface as estimated by Sinha *et al*. [4] for a Fe rich Co$_{20}$Fe$_{60}$B$_{20}$ as well as for an equal contribution Fe and Co, Co$_{40}$Fe$_{40}$B$_{20}$ shown by Jang *et al*.[36]

Seed layer	**Ferromagnet**	**Effective anisotropy (erg/cm^3)**
W	$Co_{20}Fe_{60}B_{20}$ (1 nm)	0.27×10^6
	$Co_{20}Fe_{60}B_{20}$ (0.9 nm)	0.31×10^6
	$Co_{20}Fe_{60}B_{20}$ (0.8 nm)	1.03×10^6
	$Co_{20}Fe_{60}B_{20}$ (0.7 nm)	2.65×10^6
	$Co_{20}Fe_{60}B_{20}$ (0.6 nm)	3.18×10^6
Ta	$Co_{20}Fe_{60}B_{20}$ (1 nm)	1.52×10^6
	$Co_{20}Fe_{60}B_{20}$ (0.9 nm)	2.32×10^6
	$Co_{20}Fe_{60}B_{20}$ (0.8 nm)	4.14×10^6
	$Co_{20}Fe_{60}B_{20}$ (0.7 nm)	3.41×10^6
	$Co_{20}Fe_{60}B_{20}$ (0.6 nm)	2.81×10^6

Table: 4.2: Anisotropy energies for a range of FM thicknesses grown on two separate heavy metal seed layers, W and Ta as measured on as deposited films. Complete material stack with thicknesses given in parenthesis is HM(5)/$Co_{20}Fe_{60}B_{20}$(0.6 -1.0 nm)/MgO(2 nm)/Ta(5 nm).

The values for the anisotropy energy are in the similar range as those obtained by Lee *et al*.[13]. It should be noted however, that the FM used for testing anisotropies by [13] is an alloy with equal composition of $Co_{40}Fe_{40}B_{20}$.

In order to test the variations in the anisotropy field as a function of seed layers the hysteretic response in the in-plane direction along with the variations in the anisotropy field for annealed stacks of Pd/$Co_{60}Fe_{20}B_{20}$/MgO(2) were measured and shown in figure 23.

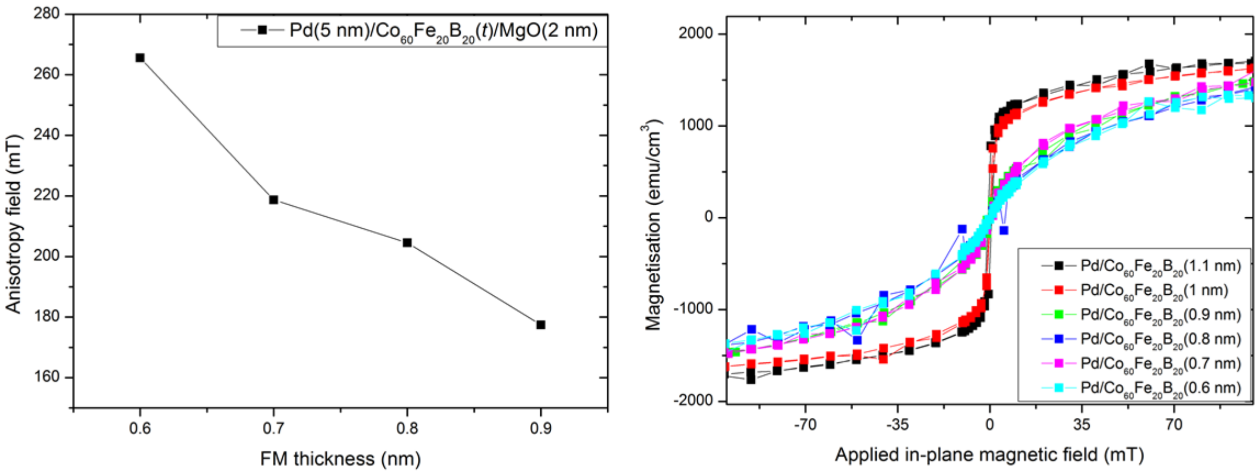

Figure 23: (Left) Anisotropy field variations as a function of thickness of ferromagnet for Pd(5 nm)/$Co_{60}Fe_{20}B_{20}$(t)/MgO(2 nm)/Ta(5 nm) along with the (right) hysteresis curves measured in the presence of an in-plane applied field using the SQUID magnetometer.

The anisotropy fields for Co rich alloys with a Pd seed are significantly lower than that of either Ta or W based stacks. This is one of the reasons for the very different chiral stripe domain structures as compared to the bubble domains observed for Ta, W and Pt based stacks. Moreover, the range of thicknesses which yield PMA is smaller compared to the Ta stacks.

Apart from tuning the anisotropy of a given material via the use of different underlayers, it is also possible to tune the anisotropy by varying the number of repetitions of a given tri-layered film. This is especially important for practical purposes of observation of sufficient magnetic contrast when studying skyrmion dynamics in such films as will be outlined in chapter 5.

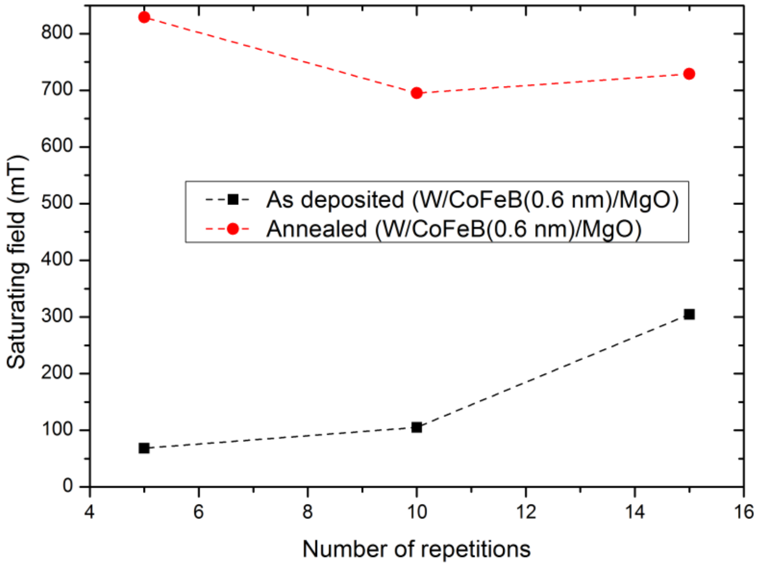

Figure 24: Modulation of the saturating field (along the in-plane hard axis direction) as a function of the number of repetitions, n of the tri-layered stack of $[W(5\ nm)/Co_{20}Fe_{60}B_{20}(0.6\ nm)/MgO(2\ nm)]_n/Ta(5\ nm)$ for both as-deposited and annealed films.

The number of repetitions n of the tri-layered stack of $[W/Co_{20}Fe_{60}B_{20}(0.6\ nm)/MgO]_n$ has a direct effect on the anisotropy of the entire multi-layered stack as is shown in figure 24. Here the PMA results from cumulative interactions from each interface of the multilayer. Moreover, for such thin films, there also exists dipolar coupling and orange peel coupling between the two ferromagnetic layers as the net thickness between the two adjoining FMs is 7 nm nominally. It should be noted, however, that this geometry of multiple tunnel barriers is not ideally suited for devices as the effective barrier thickness is greatly increased in such multi-layered stacks compared to single layered TMR junctions where only a single MgO barrier is used per cell.

Primarily both as-deposited and annealed stacks of W/$Co_{20}Fe_{60}B_{20}$/MgO exhibit out-of-plane anisotropy for varying number of repetitions. The annealed stacks showcase a slightly smaller variation in the saturating field as compared to the as-deposited stack; this may be due to the fact that annealing such multilayer stacks leads to a diffusion of the materials which affects the interfacial contributions to the PMA.

In typical SOT MRAM devices, the two major criteria for successful development are that the total resistance area product must be low and the total TMR should be high. Part of the work involved finding new materials which can be used for next generation SOT MRAM devices. Since both Ta and W exhibit strong spin-orbit coupling and PMA, co-sputtering them could lead to interesting physics and a possible alloyed material for use as a novel seed layer in MRAM. While the typical means of tuning the magnetic anisotropy in any ultra-thin film with interfacially governed PMA is to vary the ferromagnetic thickness this method also inadvertently modifies other thickness related properties [37]. Therefore it is crucial to find new material interfaces which can be used to tune the PMA irrespective of effective ferromagnetic thickness modulation. In an attempt to obtain such an interface, a compositional dependence study of the PMA was conducted. This was done by doping Ta into W and producing an alloy of WTa via co-sputter deposition. The anisotropy of WTa/$Co_{20}Fe_{60}B_{20}$/MgO was tested using the wide field MOKE microscope as well as SQUID magnetometry is shown in figure 25.

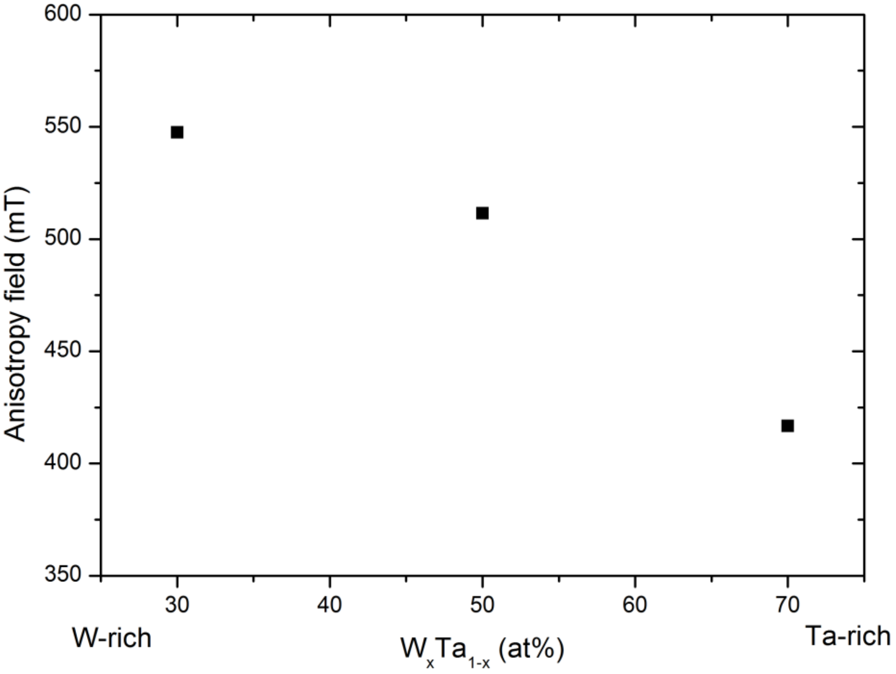

Figure 25: Modulation of the anisotropy field using heavy metal doping of the seed layer, shown here as a function of alloying of W_xTa_{1-x}. The total structure of the thin film is W_xTa_{1-x}(5 nm)/$Co_{20}Fe_{60}B_{20}$(0.6 nm)/MgO(2 nm)/Ta(5 nm).

For all compositions of the seed layer alloy the stack exhibits perpendicular magnetic anisotropy. The ferromagnetic thickness was chosen as 0.6 nm as a thinner ferromagnet would lead to a larger PMA for a given seed layer owing to its interfacial nature. Moreover, the DMI being an interfacial property would also scale inversely to the effective ferromagnetic thickness. Changing the concentration of the seed layer would allow one to identify as to why the DMI varies drastically for two neighbouring heavy metals in the periodic table. This will be discussed in the following chapter. It can be seen that the magnetic anisotropy field decreases gradually as the Ta concentration is increased. This therefore demonstrates that for a given thickness the anisotropy can be tuned by doping two different heavy metals together. More importantly, it shows that the perpendicular magnetic anisotropy depends not only on the bonding of Fe-O but on both the adjoining interfaces of a ferromagnet. It is worth mentioning here that for Ta rich alloys the coercive field for ferromagnetic thickness between 0.6 nm-0.8 nm is much lower than that for W rich.

4.4 Conclusion

In conclusion, various magnetic thin film multilayers have been studied and several means of achieving and tuning the magnetic anisotropy field, coercive field as well as the local domain structures to generate devices with low pinning and ultra-fast magnetisation dynamics have been outlined.

It has been demonstrated that perpendicular magnetic anisotropy is a subtle effect which depends very strongly on the interface quality. Magnetic stacks with Pt and Pd seed layers exhibit PMA only post annealing and not in the as-deposited form. W and Ta, however, exhibit PMA in the as-deposited form and a further enhancement of the anisotropy post annealing. Moreover the composition of the ferromagnet also plays a role in the PMA. W seeded FM alloys exhibit PMA for all three compositions of CoFeB ($Co_{20}Fe_{60}B_{20}$, $Co_{60}Fe_{20}B_{20}$ and $Co_{40}Fe_{40}B_{20}$) whereas the Pt and Pd exhibit PMA only for Co rich alloy ($Co_{60}Fe_{20}B_{20}$). Given its interfacial nature the anisotropy is primarily dominated by the total ferromagnetic thickness, however, it has been demonstrated here that it is possible to tune this anisotropy whilst keeping the ferromagnetic thickness constant. This can be done via the use of different seed layers, post deposition annealing and varying the number of repeats of a tri-layered stack. It has also been demonstrated that it is possible to tune the domain structures by varying the sputter deposition power. Also, it was shown here that for device production with respect to low pinning the ideally suited stack is the $W/Co_{20}Fe_{60}B_{20}/MgO$ trilayer with the seed layer deposited at high sputter powers. Moreover by tuning the seed layer one can obtain interesting worm like domains which can be used to generate skyrmions. Finally it has been demonstrated that it is possible to produce ultra-smooth multi-layered stacks using an industrial sputter deposition system which allows for immediate transfer of knowledge from a research lab to an industrial environment without any scalability/reliability issues which often increases significantly the time and cost between product development and deployment into the market.

The role of each interface of the ferromagnet has been outlined towards its contribution to the perpendicular magnetic anisotropy. It has been shown that given the constraints in developing a reliable SOT-MRAM device with respect to different material, magnetic and electrical properties, the PMA can be tuned in a number of ways. Understanding the generation of PMA in such ultrathin films as well as discovering various handles to tune this anisotropy will pave the way towards new materials which can ultimately be used for future memory devices.

4.5 Chapter 4- References

[1] F. Hellman, A. Hoffmann, Y. Tserkovnyak, G. S. D. Beach, E. E. Fullerton, C. Leighton, A. H. Macdonald, D. C. Ralph, D. A. Arena, H. A. Dürr, P. Fischer, and J. Grollier, "Interface-induced phenomena in magnetism," *Rev. Mod. Phys.*, vol. 89, no. June, p. 25006, 2017.

[2] A. Kobs, S. Heße, W. Kreuzpaintner, G. Winkler, D. Lott, P. Weinberger, A. Schreyer, and H. P. Oepen, "Anisotropic Interface Magnetoresistance in Pt/Co/Pt Sandwiches," *Phys. Rev. Lett.*, vol. 106, p. 217207, 2011.

[3] S. Emori, T. Nan, A. M. Belkessam, X. Wang, A. D. Matyushov, C. J. Babroski, Y. Gao, H. Lin, and N. X. Sun, "Interfacial spin-orbit torque without bulk spin-orbit coupling," *Phys. Rev. B*, vol. 93, no. 18, p. 180402R, 2016.

[4] J. Sinha, M. Hayashi, A. J. Kellock, S. Fukami, M. Yamanouchi, H. Sato, S. Ikeda, S. Mitani, S. Yang, S. S. P. Parkin, and H. Ohno, "Enhanced interface perpendicular magnetic anisotropy in Ta|CoFeB|MgO using nitrogen doped Ta underlayers," *Appl. Phys. Lett.*, vol. 102, p. 242405, Jun. 2013.

[5] M. Björck and G. Andersson, "GenX : an extensible X-ray reflectivity refinement program utilizing differential evolution," *J. Appl. Crystallogr.*, vol. 40, no. 6, pp. 1174–1178, Nov. 2007.

[6] T. P. A. Hase, B. K. Tanner, P. Ryan, C. H. Marrows, and B. J. Hickey, "Determination of the copper layer thickness in spin valves by grazing incidence x-ray fluorescence," *IEEE Trans. Magn.*, vol. 34, no. 4, pp. 4–6, 1998.

[7] Y. Khaydukov, R. Morari, O. Soltwedel, T. Keller, G. Christiani, G. Logvenov, M. Kupriyanov, A. Sidorenko, and B. Keimer, "Interfacial roughness and proximity effects in superconductor/ferromagnet CuNi/Nb heterostructures," *J. Appl. Phys.*, vol. 118, no. 21, p. 213905, 2015.

[8] "VESTA." [Online]. Available: http://jp-minerals.org/vesta/en/. [Accessed: 21-Feb-2018].

[9] B. R. Acharya, S. Prasad, N. Venkataramani, S. N. Shringi, and R. Krishnan, "The effect of deposition and annealing conditions on textured growth of sputterdeposited strontium ferrite films on different substrates," *J. Appl. Phys.*, vol. 79, no. 1, pp. 478–484, 1996.

[10] Q. Hao, W. Chen, and G. Xiao, "Beta (β) tungsten thin films: Structure , electron transport, and giant spin Hall effect," *Appl. Phys. Lett.*, vol. 106, p. 182403, 2015.

[11] J. Liu, T. Ohkubo, S. Mitani, K. Hono, and M. Hayashi, "Correlation between the spin Hall angle and the structural phases of early 5d transition metals," *Appl. Phys. Lett.*, vol. 107, no. 23, p. 232408, 2015.

[12] V. Ng, J. F. Hu, A. O. Adeyeye, J. P. Wang, and T. C. Chong, "Factors affecting surface roughness and coercivity of Ni80Fe20 thin films," *J. Appl. Phys.*, vol. 91, no. 10, pp. 7206–7208, 2002.

[13] C. Lee, L. Ye, H. Chen, and T. Wu, "The effects of deposition rate and annealing on CoFeB/MgO/CoFeB perpendicular magnetic tunnel junctions," *IEEE Trans. Magn.*, vol. 49, no. 7, pp. 4429–4432, 2013.

[14] W. Feng, C. Fowley, K. Bernert, V. Sluka, E. Kowalska, Y. Aleksandrov, J. Lindner, J. Fassbender, H. D. Gan, A. Kunz, R. Hübner, J. M. D. Coey, and A. M. Deac, "Effect of deposition conditions and annealing temperature on tunnel magnetoresistance and the structure of MgO-based double-

barrier magnetic tunnel junctions," *IEEE Trans. Magn.*, vol. 51, no. 11, p. 4400704, 2015.

[15] L. . Feldmann and J. . Mayer, *Fundamentals of surface and thin film analysis*. North-Holland, Amsterdam: Elsevier, 1986.

[16] K. Bordo and H. G. Rubahn, "Effect of deposition rate on structure and surface morphology of thin evaporated Al films on Dielectrics and Semiconductors," *Mater. Sci.*, vol. 18, no. 4, pp. 313–317, 2012.

[17] A. T. Hindmarch, V. Harnchana, A. S. Walton, A. P. Brown, R. M. D. Brydson, and C. H. Marrows, "Zirconium as a Boron Sink in Crystalline CoFeB/MgO/CoFeB Magnetic Tunnel Junctions," *Appl. Phys. Express*, vol. 4, no. 1, p. 13002, Jan. 2011.

[18] S. Mukherjee, R. Knut, S. M. Mohseni, T. N. Anh Nguyen, S. Chung, Q. Tuan Le, J. Åkerman, J. Persson, A. Sahoo, A. Hazarika, B. Pal, S. Thiess, M. Gorgoi, P. S. Anil Kumar, W. Drube, O. Karis, and D. D. Sarma, "Role of boron diffusion in CoFeB/MgO magnetic tunnel junctions," *Phys. Rev. B*, vol. 91, p. 85311, 2015.

[19] R. Lo Conte, E. Martinez, A. Hrabec, A. Lamperti, T. Schulz, L. Nasi, L. Lazzarini, R. Mantovan, F. Maccherozzi, S. S. Dhesi, B. Ocker, C. H. Marrows, T. A. Moore, and M. Kläui, "Role of B diffusion in the interfacial Dzyaloshinskii-Moriya interaction in Ta/Co20 F e60 B20/MgO nanowires," *Phys. Rev. B*, vol. 91, no. 1, p. 14433, Jan. 2015.

[20] C. Park, J.-G. Zhu, M. T. Moneck, Y. Peng, and D. E. Laughlin, "Annealing effects on structural and transport properties of rf-sputtered CoFeB⁄MgO⁄CoFeB magnetic tunnel junctions," *J. Appl. Phys.*, vol. 99, no. 8, p. 08A901, 2006.

[21] J. Sinha, M. Gruber, M. Kodzuka, T. Ohkubo, S. Mitani, K. Hono, and M. Hayashi, "Influence of boron diffusion on the perpendicular magnetic anisotropy in Ta|CoFeB|MgO ultrathin films," *J. Appl. Phys.*, vol. 117, no. 4, p. 43913, Jan. 2015.

[22] J. Ventura, J. M. Teixeira, J. P. Araujo, J. B. Sousa, P. Wisniowski, and P. P. Freitas, "Pinholes and temperature-dependent transport properties of MgO magnetic tunnel junctions," *Phys. Rev. B*, vol. 78, no. 2, p. 24403, 2008.

[23] W. Zhao, X. Zhao, B. Zhang, K. Cao, L. Wang, W. Kang, Q. Shi, M. Wang, Y. Zhang, Y. Wang, S. Peng, J. O. Klein, L. A. de Barros Naviner, and D. Ravelosona, "Failure analysis in magnetic tunnel junction nanopillar with interfacial perpendicular magnetic anisotropy," *Materials (Basel).*, vol. 9, no. 1, pp. 1–17, 2016.

[24] A. Olbrich, B. Ebersberger, C. Boit, J. Vancea, H. Hoffmann, H. Altmann, G. Gieres, and J. Wecker, "Oxide thickness mapping of ultrathin Al2O3 at nanometer scale with conducting atomic force microscopy," *Appl. Phys. Lett.*, vol. 78, no. 19, p. 2934, 2001.

[25] K. M. Bhutta, "Characterization of MgO barrier by conducting atomic force microscopy," *J. Microsc. Sci. Technol. Appl. Educ.*, vol. 3, no. 4, pp. 2022–2027, 2010.

[26] K. M. Bhutta, J. Schmalhorst, and G. Reiss, "Study of MgO tunnel barriers with conducting atomic force microscopy," *J. Magn. Magn. Mater.*, vol. 321, no. 20, pp. 3384–3390, 2009.

[27] H. X. Yang, M. Chshiev, B. Dieny, J. H. Lee, A. Manchon, and K. H. Shin, "First-principles investigation of the very large perpendicular magnetic anisotropy at Fe|MgO and Co|MgO interfaces," *Phys. Rev. B*, vol. 84, no. 5, p. 54401, 2011.

[28] S. Emori and G. S. D. Beach, "Optimization of out-of-plane magnetized Co/Pt multilayers with

resistive buffer layers," *J. Appl. Phys.*, vol. 110, no. 3, p. 33919, 2011.

[29] V. M. Parakkat, K. R. Ganesh, and P. S. Anil Kumar, "Tailoring Curie temperature and magnetic anisotropy in ultrathin Pt/Co/Pt films," *AIP Adv.*, vol. 6, no. 5, p. 56118, 2016.

[30] N.-H. Kim, D.-S. Han, J. Jung, J. Cho, J.-S. Kim, H. J. M. Swagten, and C.-Y. You, "Improvement of the interfacial Dzyaloshinskii-Moriya interaction by introducing a Ta buffer layer," *Appl. Phys. Lett.*, vol. 107, no. 14, p. 142408, Oct. 2015.

[31] M. Zhu, H. Chong, Q. B. Vu, R. Brooks, H. Stamper, and S. Bennett, "Study of CoFeB thickness and composition dependence in a modified CoFeB/MgO/CoFeB perpendicular magnetic tunnel junction," *J. Appl. Phys.*, vol. 119, p. 73907, 2016.

[32] W. Kang, Y. Huang, X. Zhang, Y. Zhou, and W. Zhao, "Skyrmion-Electronics: An Overview and Outlook," *Proc. IEEE*, vol. 104, no. 10, pp. 2040–2061, 2016.

[33] G. Finocchio, F. Büttner, R. Tomasello, M. Carpentieri, and M. Kläui, "Magnetic skyrmions: from fundamental to applications," *J. Phys. D. Appl. Phys.*, vol. 49, no. 42, p. 423001, 2016.

[34] J. S. Meena, S. M. Sze, U. Chand, and T. Tseng, "Overview of emerging nonvolatile memory technologies," *Nanoscale Res. Lett.*, vol. 9, no. 526, pp. 1–33, 2014.

[35] A. D. Kent and D. C. Worledge, "A new spin on magnetic memories.," *Nat. Nanotechnol.*, vol. 10, no. 3, pp. 187–191, Mar. 2015.

[36] S. Y. Jang, S. H. Lim, and S. R. Lee, "Magnetic dead layer in amorphous CoFeB layers with various top and bottom structures," *J. Appl. Phys.*, vol. 107, p. 09C707, 2010.

[37] B. Dieny and M. Chshiev, "Perpendicular magnetic anisotropy at transition metal/oxide interfaces and applications," *Rev. Mod. Phys.*, vol. 89, no. 2, p. 25008, 2017.

|Chapter 5

Domain wall motion, Dzyaloshinskii-Moriya Interaction and magnetic skyrmions in thin films and nano-wires

5.1 Introduction

The Dzyaloshinskii-Moriya interaction is an interesting phenomenon both from the stand point of academic research as well as from industrial output. Interfacial Dzyaloshinskii-Moriya interaction is a relatively new phenomenon [1][2] found in magnetic thin film multi-layered structures with broken inversion symmetry which contributes to an additional term in the total energy distribution governing the magnetic structures within a ferromagnet. It results in the formation of chiral magnetic structures and has recently been shown to be a key property in tuning domain wall velocities [3]. This chapter is divided into three key sections namely field driven domain wall motion, measurement of DMI and the effect of ferromagnetic composition, and finally nucleation and stabilisation of field independent room temperature skyrmions in micro-wires.

This chapter therefore focusses on understanding field driven domain wall motion in HM/FM/oxide thin films. Optimised thin films with respect to PMA as well as domain pinning are utilised to measure the interfacial Dzyaloshinskii-Moriya Interaction. Two different techniques are used to quantify the DMI systematically in a system. Furthermore, magnetic skyrmions are observed and stabilised at room temperature in novel HM/FM thin films. Later, the issues in dealing with field stabilised skyrmions and how it is possible to stabilise field free skyrmions in thin films is explained.

5.2 Field driven domain wall motion

In order to measure the Dzyaloshinskii-Moriya interaction via the asymmetric bubble expansion method as outlined in chapter 3, it is crucial to first evaluate the field driven domain wall motion in the absence of an in-plane field to understand the flow regimes experienced by a domain wall during an application of an externally applied field. Thin films with optimised magnetic properties, as demonstrated in the previous chapter are used in evaluating field based domain wall motion.

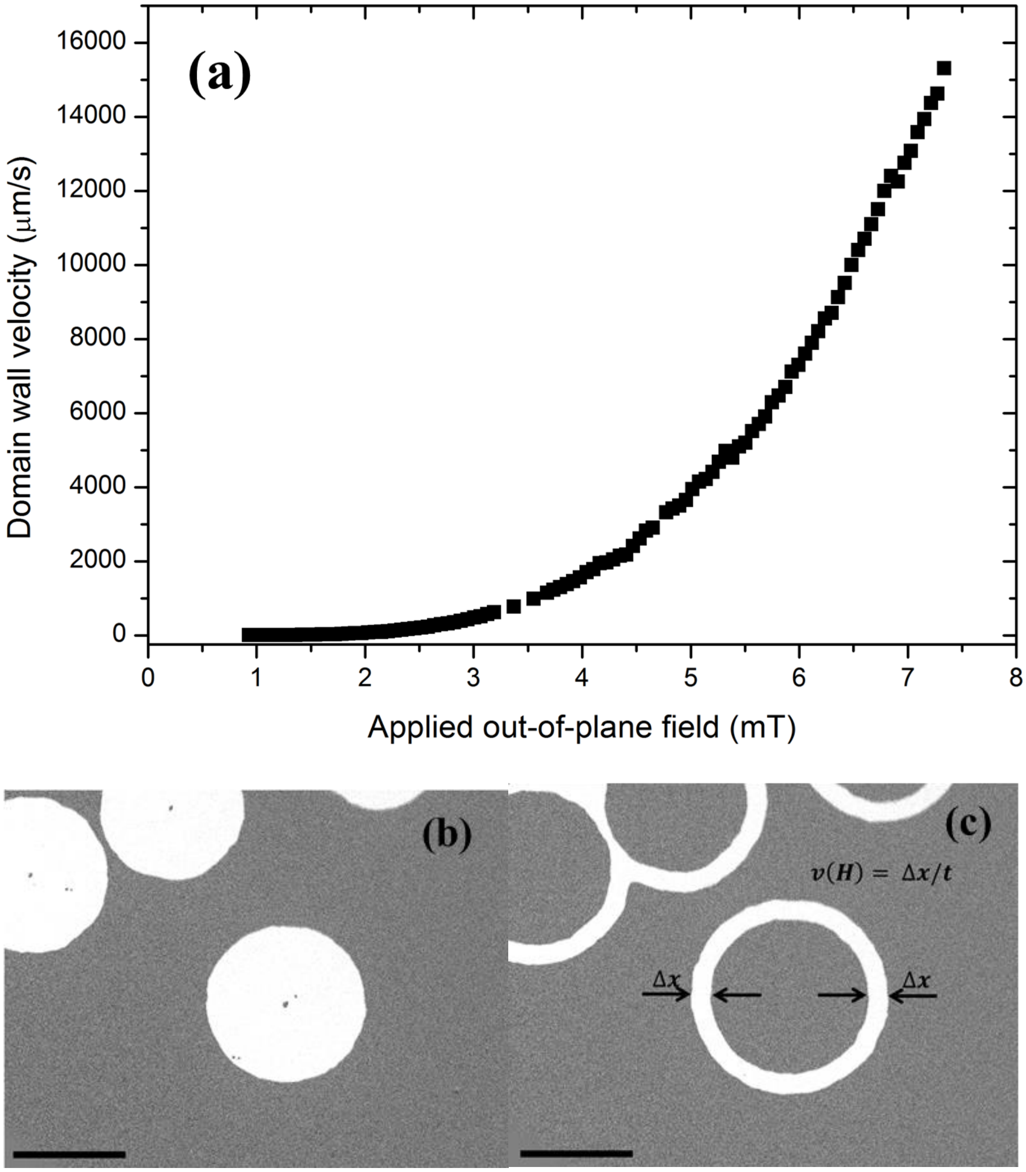

Figure 1: (a) Field driven domain wall motion for W(5 nm)/$Co_{20}Fe_{60}B_{20}$(0.6 nm)/MgO(2 nm)/Ta(5 nm) thin films post annealing at 530°C (heater temperature) measured via wide-field Kerr microscopy at room temperature as a function of out-of-plane (OOP) applied field. (b-c) Differential Kerr microscopy images obtained for out-of-plane nucleated bubble domains in W(5 nm)/$Co_{20}Fe_{60}B_{20}$(0.6 nm)/MgO(2 nm)/Ta(5 nm). Domain image taken (b) before and (c) after subtraction of the image from the preceding field step.

As shown above in figure 1(b) out-of-plane bubble domains were nucleated by applying OOP field pulses and these domains were then subsequently expanded only in the presence of an OOP field. Symmetric expansion was observed over the entire diameter of the bubble domain. After the magnetic domain was nucleated, it was used as a background image from which the image post field application is subtracted. This results in the ring shaped image of the domain as shown in figure 1(c). The domain velocity is plotted as a function of pulse amplitude of out-of-plane magnetic field. It can be seen that initially for low fields there is very little to no motion. As the field is increased the domain wall velocity gradually increases. There exist three different regimes for domain wall motion in such PMA based stacks. For a system at zero temperature, there exists a certain de-pinning force, f_{dep}, below which the elastic interface i.e. the domain wall remains pinned, at f_{dep} there is a critical transition which occurs from pinned state to de-pinning. At finite temperatures this transition region becomes smeared due to thermal activation and a finite velocity is expected for all non-zero driving forces. Therefore, domain wall motion in this creep region is dominated by thermal motion. The amount of pinning for a given material depends on its crystal structure and the defect density within the material system. As the field increases, and the driving force becomes greater than the de-pinning field, the domain wall enters into a transition region between creep and flow regime, where the wall experiences an exponential increase in velocity and finally for large fields the domain wall moves in the flow regime where it overcomes all defects and the motion is dominated purely by the driving field.

The in-plane field induced asymmetric bubble expansion method is utilised to measure the DMI in such HM/FM PMA thin films. However, this method requires that the measurement is performed in the creep regime of the domain wall motion as it has been suggested that the domain walls internal structure itself undergoes a modification at higher applied fields [4][5]. Hence, in order to verify the regime of motion for W(5 nm)/$Co_{20}Fe_{60}B_{20}$(0.6 nm)/MgO(2)/Ta(5 nm) thin films figure 1 was re-plotted to check for deviations from linearity in accordance to the creep law (chapter 2, eq. 2.19):

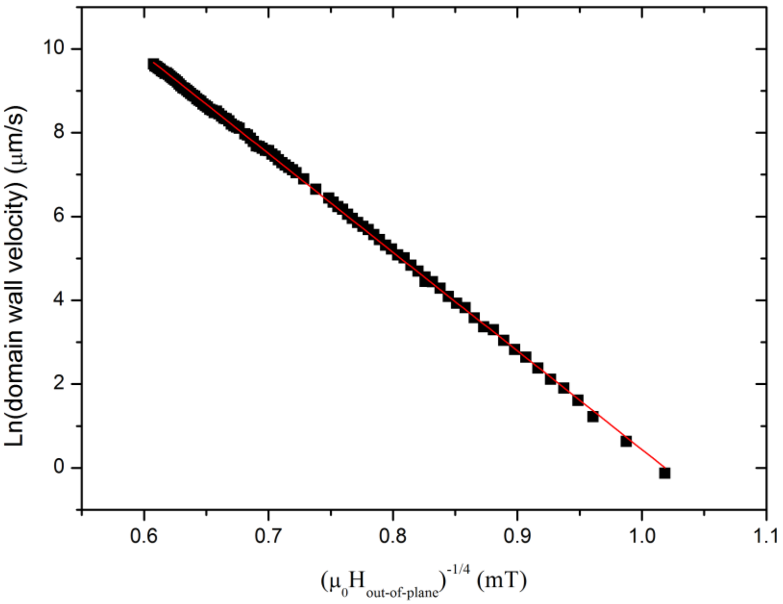

Figure 2: Natural logarithm of domain wall velocity as a function of out-of-plane field. Linear fit to the data using least squares fit yielding a slope of -23.5 ± 0.04 and an intercept of 23.9 ± 0.03 .

A linear fit was used to fit the data. As it can be seen there is no deviation from linearity which implies that for all field values for which the domain wall motion was recorded here, the wall remains in the creep regime. This therefore allows us to proceed with the DMI determination using the bubble expansion method as a viable method detailed below in section (5.2.1).

5.2.1 Measurement of the Dzyaloshinskii-Moriya Interaction

In order to develop next generation SOT-MRAM devices as well as skyrmion based memory and logic devices, it is crucial to understand the behaviour of the Dzyaloshinskii-Moriya Interaction in these ultra-thin films. Moreover, new material stacks are needed which possess the ability to stabilise skyrmions at room temperature within them. In this section two different field based methods are discussed, namely 1. Asymmetric field induced domain wall motion and 2. Magnetic domain stripe expansion used to evaluate the DMI in W/CoFeB/MgO thin films. The existence of compositional dependence of DMI is further demonstrated by varying the FM alloy composition.

There exist multiple methods found recently which have been used to study and measure the DMI in ultra-thin films [6][7]. Not all methods [8][9][10][11], can be utilised on all types of films which exhibit characteristics of interfacially driven DMI. Two methods which are widely used to study DMI and test the presence of chiral domain structures will not be used here namely 1. Current driven domain wall motion and 2. Scanning Tunnelling Microscopy (STM). However, it is important to highlight the short comings of these methods and hence the reason for their incompatibility for usage in this study.

Issues with current induced motion

Current induced domain wall motion can be used to measure the amplitude of the DMI. However, it has been shown by Emori *et* al. that in systems with a high DMI, the torque generated by the large applied currents on the Domain Wall (DW) not only rotates the DW moment but in fact tilts the entire DW line profile [12]. Also for thicker ferromagnetic systems, there is an increased current flow (due to increase in conductivity) in the FM layer which induces a higher probability for the nucleation of reverse domains during current induced domain wall experiments [13][14]. This renders DMI determination difficult. Moreover, there are theoretical studies which suggest that current induced motion can also modify the sign of the net DMI in a multi-layered stack [15][16]. Current dependent methods for the evaluation of DMI involves understanding the different components of current dependent spin torques (adiabatic, non-adiabatic, spin-Hall like and Rashba-like fields. The collective effect of these components on the motion of the domain walls remains unclear [17][18].

Issue with STM for DMI determination

Scanning tunneling microscopy was one of the first methods used to demonstrate that skyrmions can be written and destroyed deterministically [19]. However, it is not suited for the material structures studied here, as in all films studied here the FM layers are capped with at least 7 nm of material for *ex-situ* evaluation of the DMI as well as for compatibility with CMOS devices. Hence given the proximity to surface requirement by STM techniques it is not a viable means of detection of DMI in the thin film studied here.

Measurement of DMI via Bubble expansion method

Bubble expansion method was utilised to evaluate the DMI in W and Ta based HM/FM stacks [20][21]. This method is the preferred method as it avoids the complicated steps of film patterning which add to the complexity of DMI extraction due to enhanced pinning at the edges of the nanowire post processing. There are two pre-requisites to evaluate the DMI using the field driven domain wall motion.

1. The material in question must exhibit perpendicular magnetic anisotropy.
2. The degree of pinning within the material should be low and a number of spaced out nucleation sites should be present.

Both the above requirements were tuned for, as demonstrated in Chapter 4, figure 12. The material film in question must exhibit smooth domain propagation with applied field and low pinning associated with the domain wall motion. This allows for an accurate determination of the DMI, since if the domain remains largely pinned across the thin film, it can provide an overestimate of the DMI stopping field [21][13][22]. The domain wall motion in that case would be reduced in velocity not due to the intrinsic effective DMI field but possibly due to a pinning site. However, the influence of pinning strength on the local variations in DMI has not yet been quantitatively studied and is an interesting topic of discussion. Once the material stack was optimised with respect to magnetic domain structure, an out-of-plane field pulse was used to nucleate a bubble domain. This is shown in figure 3(a).

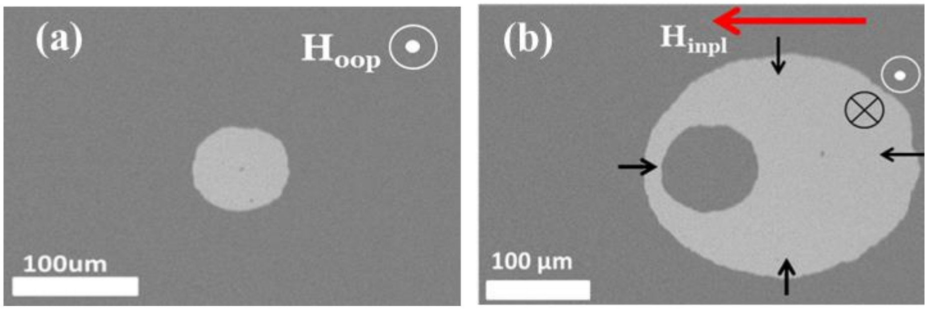

Figure 3: (a) Differential Kerr microscopy of an isometric expansion of a perpendicularly magnetised bubble domain using solely an OOP field obtained on W(5)/$Co_{20}Fe_{60}B_{20}$(0.6)/MgO(2)/Ta(5) measured at room temperature. (b) Asymmetric expansion of magnetic bubble domain obtained in the presence of both an applied in-plane and OOP field. All thicknesses in parenthesis are in nanometres.

No in-plane field is applied during the nucleation of the out-of-plane magnetised bubble domain. In order to test the presence of DMI an in-plane field needs to be applied which if there exists an intrinsic effective DMI field should lead to an asymmetric expansion of the OOP domain. This occurs due to the fact that the in-plane field lifts the degeneracy of both up-down and down-up domain walls and therefore assists in the motion of a wall of a certain chirality while it retards the other. This then manifests as an asymmetric velocity distribution. In figure 3(b) an out-of-plane field pulse was applied during the presence of an in-plane field. For the same pulse duration, this results in a faster motion for the right wall compared to the left moving wall. This is evidenced by the greater area change in the contrast image for the right moving wall compared to the left moving wall. The images before and after the application of the pulse are subtracted which results in a differential image as is shown in figure 3(b) with a darker central initial bubble nucleation.

It should be noted here, however, that in order to obtain an accurate measurement of the DMI effective field, there must be no out-of-plane component of the in-plane applied field. Else it will result in an under estimate of the effective field value. In order to ensure that the applied in-plane field has a minimal out-of-plane component, excessive care was taken by initially nucleating an out-of-plane bubble as shown in figure 4(a). Following which, a background image was taken with live image subtraction which resulted in a net zero contrast as there is no domain wall motion. With the out-of-plane coil switched off only an in-plane field was applied. If one observes a change in contrast it implies that there exists a torque driving the domain. The tilt of the applied in-plane field is adjusted to ensure no contrast is observed. This is shown in figure 4(b). This process is iterated until there is zero domain wall motion due to the presence of purely an in-plane field (i.e. via any out-of-plane component of the in-plane field). The sample alignment with the in-plane field becomes more taxing as the material system under investigation is tuned towards achieving low out-of-plane coercive fields. This implies that the material is extremely soft in its magnetic response in the out-of-plane direction. The in-plane field therefore must be aligned very carefully as even a slight component in the out-of-plane direction can lead to magnetisation reversal. While for devices and microstructures one would want to achieve magnetic films with smoother domains and lower coercive fields for faster magnetisation reversal, it is harder to obtain DMI values via the asymmetric bubble expansion technique for such films.

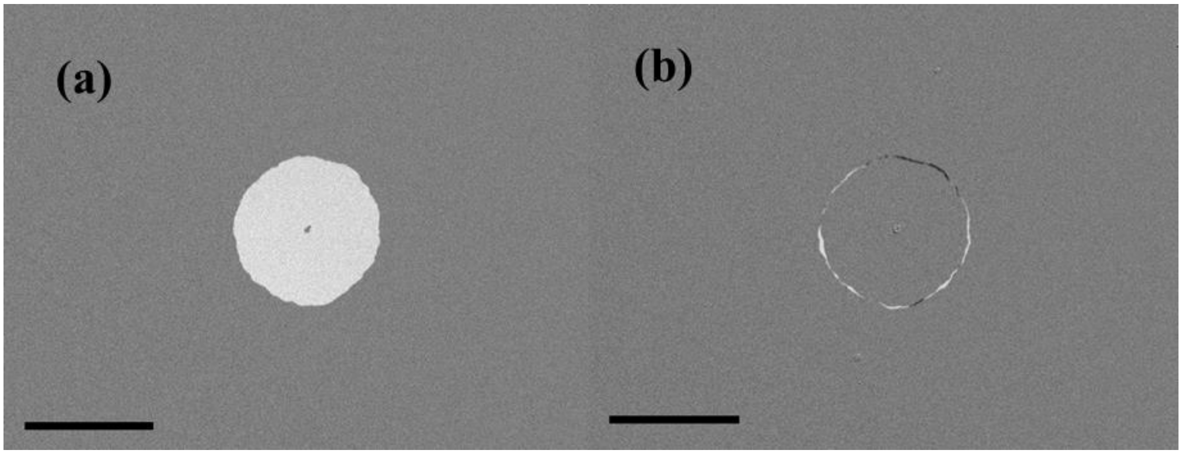

Figure 4: (a) Single OOP magnetised bubble domain obtained via pulsed reversed OOP field post saturation. (b) Slight changes in contrast obtained on application of a tilted in plane field with an OOP component proving torque for domain wall motion showcasing means for sample alignment. Images obtained via *evico* wide field Kerr microscope used in differential mode polar configuration on samples of W(5 nm)/$Co_{40}Fe_{40}B_{20}$(0.6 nm)/MgO(2 nm)/Ta(5 nm).

Post successful sample alignment, the domain wall velocity was measured as a function of applied external in-plane field for both left and right moving domain walls. For each increment in the in-plane field the out-of-plane pulse is kept constant, thereby only studying the effect of the domain wall motion due to the in-plane applied magnetic field. The domain wall velocity as measured for each of the domain wall post initial bubble nucleation is shown in figure 5.

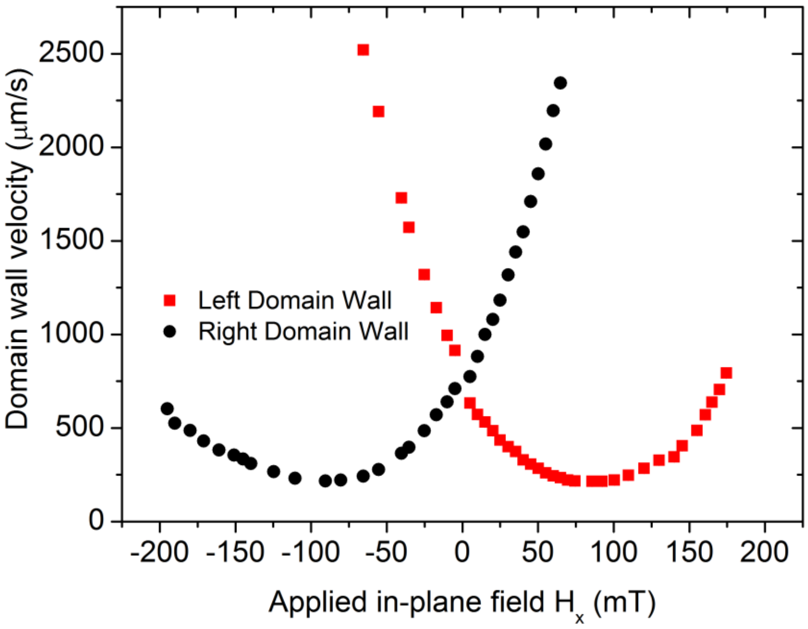

Figure 5: Magnetic domain wall velocity as a function of applied in-plane field as measured for W(5 nm)/$Co_{20}Fe_{60}B_{20}$(0.6 nm)/MgO(2 nm)/Ta(5 nm) sample using the domain images obtained via magnetic Kerr microscopy for both left and right moving magnetic domains.

It should be noted that the sample was saturated and the domain wall re-nucleated for every in-plane field step. This is required as post in-plane field application causes the magnetic bubble to deform to an asymmetric state which cannot be used further as an initial domain state.

The in-plane field at which the domain wall velocity exhibits a minimum is used as the effective DMI field in the calculation of the DMI value since at this field the internal DMI field and the applied in-plane field cancel out. It can be seen from figure 5 that even at H_{min} = 93 mT, the velocity of the domain wall is not zero. This is due to the application of a finite out-of-plane field pulse. Also clearly evidenced is that for a given in-plane field direction the left and right moving domain walls experience very different velocities as seen from figure 5. The magnetic anisotropy was measured in order to obtain the domain wall width, post which the DMI was calculated by using the measured effective DMI field as shown by

$$\mu_0 H_{DMI} = \frac{D}{\Delta M_s} \tag{5.1}$$

where H_{DMI} ,Δ,M_s and D are the effective in-plane DMI field, the domain wall width, the saturation magnetisation and the DMI constant for a given thin film.

The resulting interfacial DMI was calculated to be (0.63 ± 0.05) mJm^{-2} with an effective DMI field of 93 mT [23]. Similar material stacks of W/$Co_{20}Fe_{60}B_{20}$/MgO have been investigated by R. Soucaille *et al.*

[17] and the DMI value reported is (0.23 ± 0.03) mJm^{-2}. The value calculated in this work is twice of what is obtained by [17]. However, it is important to note that the DMI scales at the atomic level [2] and even slight changes or variations in the interfacial quality can result in a significantly different DMI value. Moreover, the ferromagnetic thickness used in [17] is *nominally* 1.7 times thicker than that used in this work. This may account for the smaller DMI value, given that DMI scales inversely with the thickness of FM. More importantly, the W thickness as used by the authors of [17] is only 2 nm as compared to ours which is 5 nm. Thinner W films might imply partial inhomogeneity which might contribute to the lowering of the DMI, as well as higher pinning of the domain wall as seen in figure 1 from [17]. Moreover it has been shown that in fact there is indeed also a strong dependence of the DMI on the thickness of not only the ferromagnet but also the seed layer as seen by S. Tacchi *et* al [1] where the DMI is shown to undergo a sharp rise with increasing heavy metal thickness and saturate at approximately 3 nm. It is important to note here that the effective measured DMI is the sum of the DMI at the W/CoFeB interface and the CoFeB/MgO interface [24]. It is expected that the net contribution to the total DMI from the MgO interface would be rather low compared to the W interface; given the fact that MgO has a low spin-orbit coupling. However, recently it has been shown by A. Cao *et al.* [25] that it is indeed possible to tune the DMI significantly by variations in the MgO thickness with a 6× enhancement of interfacial DMI for only a $\approx$ 0.6 nm change in MgO thickness. First principle calculations, using Density Functional Theory (DFT) have shown that the interfacial oxidation is associated with the large charge transfer and the large electric field which compensates for the low spin-orbit coupling of the MgO [26].

Nevertheless there have been a number of reports which show significantly different amplitude and even sign of the DMI coefficient. Therefore, it is crucial to identify independent means of measuring DMI in films grown in the same laboratory. Moreover, given the relatively large value of D obtained for W/$Co_{20}Fe_{60}B_{20}$/MgO films it indicates towards the possibility of the existence of skyrmions in this system. Hence in order to obtain magnetic domain information at a smaller length scale and to check the presence of magnetic skyrmions, thin films of W/$Co_{20}Fe_{60}B_{20}$/MgO were grown on a transmittive SiN membrane substrate using magnetron sputtering as shown in chapter 2.

In order to confirm that the substrate does not contribute to any variations in the anisotropy, two samples of [W(5 nm)/$Co_{20}Fe_{60}B_{20}$(0.6 nm)/MgO(2 nm)]$_{15}$/Ta(5 nm) were deposited during the same deposition cycle on two different substrates namely SiO and SiN and the magnetisation of both was measured via SQUID magnetometry as shown in figure 6.

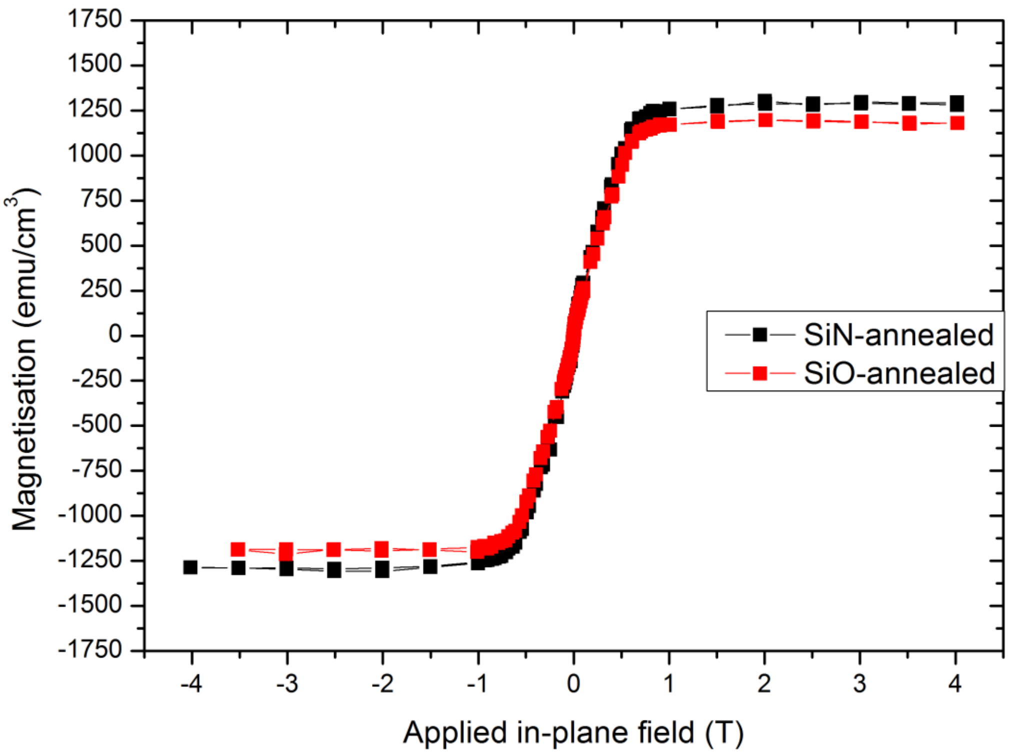

Figure 6: Hard axis, in-plane hysteresis curves for $[W(5)/Co_{20}Fe_{60}B(0.6)/MgO(2)]_{15}/Ta(5)$ thin films deposited on two substrates, SiN (black) and SiO_2 (red) during the same deposition as measured via SQUID magnetometry. All thicknesses in parenthesis are in nanometres. 1 $emu/cm^3 = 10^3$ A/m.

Since both the thin films were deposited together it eliminates systematic variations in thin film properties due to the deposition process. As measured on the SQUID magnetometer they yield very similar magnetic response indicated by the nearly overlapping hysteresis curves. This implies that SiN and SiO_2 are comparative substrates with respect to the magnetic properties of the films grown on them.

Post magnetic characterisation the continuous films were patterned into microwires of 1.4 µm × 5.0 µm. The samples were patterned by K. Litzius using electron beam lithography. Scanning Transmission X-ray Microscopy (STXM) measurements were performed at the BESSY II synchrotron in Berlin at the MAXYMUS [27] end station and the Swiss Light Source (SLS), ‘PolLux’ on $W/Co_{20}Fe_{60}B_{20}/MgO$ multilayers. The STXM measurements were performed along with K. Litzius and K. Richter. The assistance on the operation of the STXM microscope from the beam line scientist M. Weigand and S. Finizio is gratefully acknowledged. X-ray Magnetic Circular Dichroism (XMCD) [28] was used for element specific measurements and observation of domain structures shown in figure 7. STXM XMCD images of stripe domains were obtained for $[W/Co_{20}Fe_{60}B_{20}/MgO]_{15}/Ta$. The X-ray energy was tuned to the Fe absorption edge, and the measurement was performed in the out-of-plane geometry.

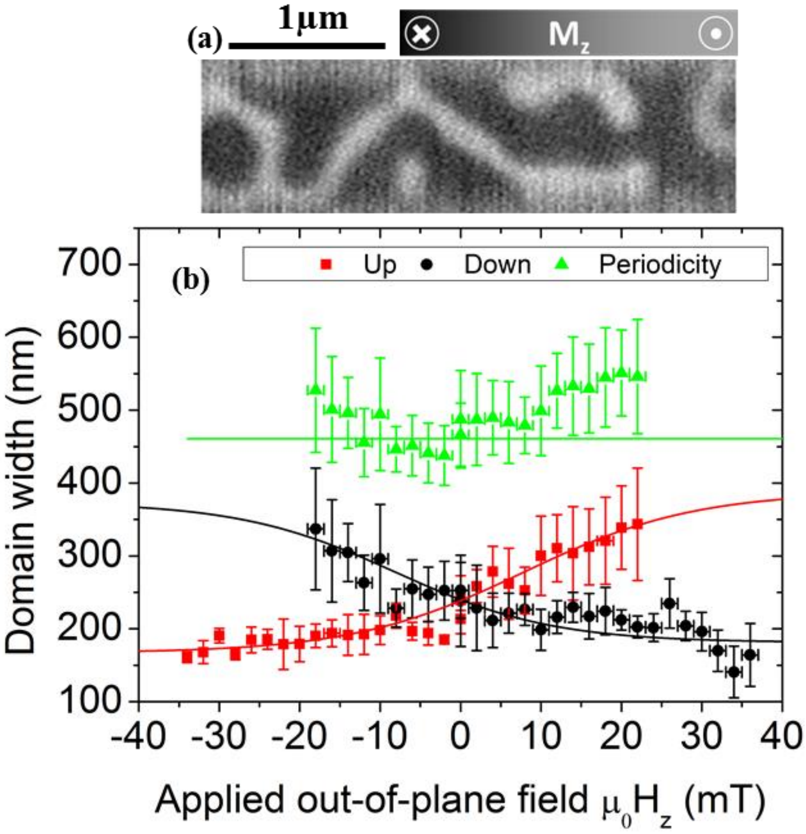

Figure 7: (a) Scanning Transmission X-ray Microscopy with XMCD imaging of worm-like magnetic domains obtained in [W(5 nm)/$Co_{20}Fe_{60}B_{20}$(0.6 nm)/MgO(2 nm)]/Ta(5 nm) for wires of dimensions 1.4 μm × 5.0 μm. Image was obtained while X-ray wavelength tuned to the Fe- absorption edge and with sample in the perpendicular orientation to incoming X-rays. Sensitivity is therefore limited to out-of-plane magnetisation. (b) Stripe domain widths measured as a function of applied out-of-plane field for both up and down magnetised domains with the periodicity fitted around $H_z = 0$ mT.

The film was initially saturated in the out-of-plane direction by applying a field of 50 mT. The domain stripe width was measured as a function of the OOP field as shown in figure 7. The applied field was then gradually reduced. As the field is increased further in the negative direction the stripe width of the up polarity (red curve) increases until a point in field where the sample achieves saturation. The domain width at the maximum field value at which the worm domains exist can be used to determine the DMI energy [29]. The domain width is also measured for the domains with down polarity along with the periodicity of the domains as a function of applied field as shown in figure 7(b) which together are used to calculate the DMI. A hysteretic response curve is obtained by studying the field evolution of the width of the stripe domains. This hysteresis loop can be fitted using the function $w(H) = a \cdot \tanh(\delta \cdot H + \phi) + d$. Here (H) is the domain width as a function of external field, δ is the inverse loop width, ϕ is the phase offset, a is the amplitude and d is the domain width at zero field [30]. At high fields the stripe domains of opposite polarities (black and white contrast) corresponding to up and down magnetisation orientation approach a terminal domain width before the sample attains saturation. This terminal width can be extracted from $w_{term}= |d - a|$ which results in a value of w_{term}= (172 ± 24) nm. The average periodicity was calculated from the measured sample periodicity as a function of OOP field and found to be w_{aver}= (461 ± 10) nm. In order to obtain an accurate estimate of the DMI it is important to take into account the stray field contributions to the stripe domain phase in a multi-layered thin film. The exact analytical energy expressions are defined in [31] which take into account the domain wall periodicity to calculate the DMI. The expressions for the stray field associated with the volume charges inside an isolated domain wall was obtained by Büttner *et al.* [32]. The value of DMI can be computed by numerical minimisation of the total effective energy density with respect to domain wall width and domain width of the multilayer film as derived theoretically by I. Lemesh *et al*. [31]

$$\mathcal{E}^{\infty,N}_{tot,eff} = \frac{1}{w}\left[\frac{2A'}{\Delta} + 2K'_u\Delta - \pi D'\right] + C + \mathcal{E}d,s + \mathcal{E}d,v \quad (5.2)$$

where the surface and volume stray field energies are defined as

$$\mathcal{E}_{d,s} = \chi \sum_{n=1,3,5..}^{\infty} \frac{1}{\left[\sinh\left(\frac{\pi^2 n\Delta}{2w}\right)\right]^2} \frac{1-e^{-\upsilon}}{n} \quad (5.3)$$

$$\mathcal{E}_{d,v} = \chi \sum_{n=1,3,5..}^{\infty} \frac{1}{\left[\cosh\left(\frac{\pi^2 n\Delta}{2w}\right)\right]^2} \frac{e^{-\upsilon}+\upsilon-1}{n} \quad (5.4)$$

and the effective constants are defined as: $A' = fA$, $D' = fD$, $M_s' = fM_s$, $K_u' = K_u f - \frac{\mu_o M_s^2}{2}(f - f^2)$, $C = \frac{\mu_o M_s^2}{2}(f - f^2)$, the constants in eqs. (5.2-5.3) are defined as $\chi = \frac{\pi\mu_o M_s^2 \Delta^2}{w\lambda}$ and $\upsilon = \pi n\lambda/w$ where f is the scaling factor given by the ratio of thickness of a single FM layer thickness to the multilayer periodicity, λ is the product of multilayer periodicity and the number of layer repeats and K_u is the uniaxial anisotropy.

The theoretical description of the volume and stray field contributions to the energy of a domain wall in single domain systems, stripe domain phase as well as an extension to multi-layered thin films is detailed in [31], the derivation of which is out of the scope of this work. Numerical calculations as well as the derivation of the analytical energy expression shown in eqs (5.2)-(5.4) were not developed by the author. I. Lemesh is acknowledged in providing theoretical calculations of the DMI via the stripe annihilation.

The value of D as calculated via the energy minimisation outlined above yielded $D = (0.73 \pm 0.5)$ mJ/m^2 which is in line with the value obtained using the bubble expansion technique. This therefore allows for an independent method of the evaluation of the DMI coefficient. It should be noted, however, that the errors estimated for the bubble expansion and the stripe annihilation method are different. This is because for the bubble expansion measurements, magnetic domains which showed no significant pinning but smooth elliptic expansion were used. The total error here is governed by the minimum velocity determination. However for wires, all stripe domains over the entire wire width were considered and used in the evaluation of the stripe widths. This included regions with pinning sites which dominates the DMI error. Each method therefore has its advantages as well as short comings. The bubble expansion lacks the requirement of having to pattern the films into micro-wires, and therefore removes complications which arise due to pinning at the wire edges etc. The stripe annihilation method, however, allows for a more direct determination of DMI by calculating it directly from the total energy of a Néel wall, whereas the bubble expansion technique one infers the DMI value as the actual measured quantity is the DMI effective field. The most direct means, however, of determining the interfacial DMI of a system is by directly observing the degree of tilt towards a Néel ordering of the actual domain wall itself. However, this is not feasible given that the small domain wall width (6 nm) of our investigated system is well below the current resolution of synchrotron X-ray microscopy techniques (20 nm).

5.2.2 Ferromagnetic compositional dependence of DMI

Given the strong implications of DMI in HM/FM thin films with respect to the production of more efficient storage devices, it crucial to find novel methods which can be used to tune the DMI independent of varying FM thickness. One of the methods explored here is the tuning of the DMI by varying the compositions of the active FM layer. Moreover, such a FM dependence study has not yet been undertaken hence it allows for a deeper understanding of the interfacial origin of DMI.

In order to study the FM compositional dependence of DMI, three different alloy compositions of CoFeB were used namely, $Co_{20}Fe_{60}B_{20}$, $Co_{60}Fe_{20}B_{20}$, $Co_{40}Fe_{40}B_{20}$. Thin films of W(5 nm)/CoFeB(0.6 nm)/MgO(2 nm)/Ta(5 nm) were grown using each of the mentioned compositions of CoFeB with the same thickness.

The DMI for each of these three compositions was evaluated using the field driven magnetic domain expansion described in section 5.2.1. It can be seen from the figure 8(a-b) that there is a significant variation in the measured DMI effective field.

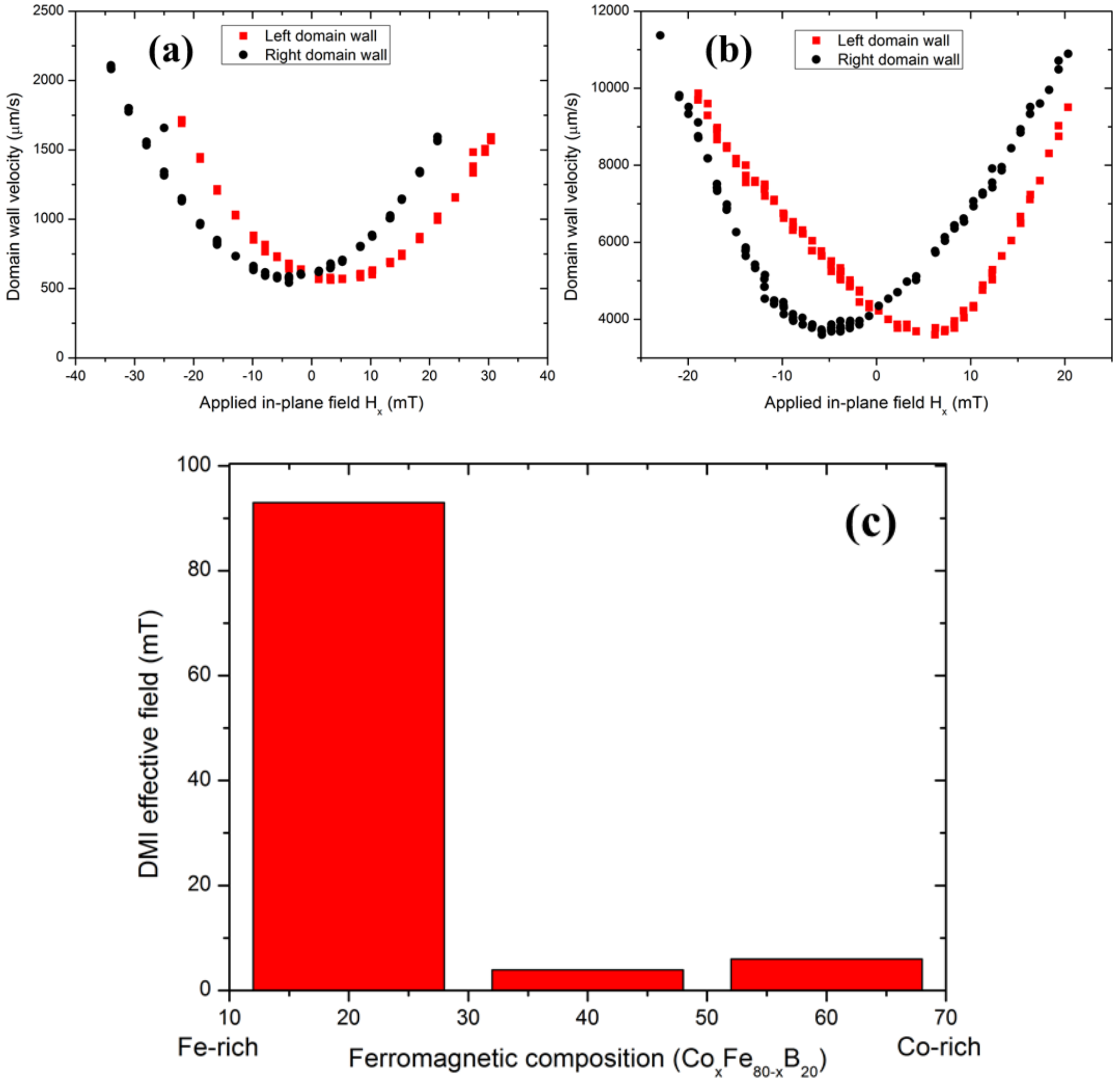

Figure 8: Domain wall velocity as measured for (a) W(5 nm)/$Co_{40}Fe_{40}B_{20}$(0.6 nm)/MgO(2 nm) and (b) W(5 nm)/$Co_{60}Fe_{20}B_{20}$(0.6 nm)/MgO(2 nm) as a function of in-plane applied field using asymmetric field dependent magnetic domain expansion technique. Both measurements were performed on 10×10 mm films grown on SiO_2 substrates measured using differential imaging on an *evico* wide field Kerr microscope. (c) dependence of the effective DMI as a function of the ferromagnetic composition for a 0.6 nm of CoFeB in a trilayer of W/$Co_xFe_{80-x}B_{20}$/MgO.

For the Co-rich CoFeB alloy as well as the equally distributed Co and Fe alloy the DMI is significantly lower than when compared to the Fe- rich alloy. All samples were grown with the same seed and cap layers which were grown using identical growth recipes, the sputtering gas pressure as well as the sputter power was kept the same during the growth of all seed and cap layers for all three FM alloy stacks. This highlights the subtlety of this interfacial effect. All stacks underwent the exact same annealing process as well, which is likely to introduce material changes at the interface. Due to the large negative formation enthalpy for metal borides, the heavy metal layer acts as a sink for the boron, thereby modifying the bottom interface [33]. The degree of boron diffusion however, is expected to be different across the three different FM compositions since the boron mobility would be affected by the variations in the alloy composition of Fe and Co. For an Fe-rich alloy of CoFeB it is known that the Fe-rich composition has the higher crystallinity (from the relatively higher TMR ratio's for Fe-rich CoFeB [34][35], as well as cross-sectional TEM studies[36]). The top interface's contribution to the net DMI would be the most in the case of the Fe-rich CoFeB as a result of the clean interface comprising of the Fe-O bond formation. Further HR-TEM studies would be required, especially in-situ measurements, to understand the exact nature of the chemical bonding occurring at this ultra-thin interface. It should be noted here that DFT calculations were not performed in this study to extract the interfacial contributions to the DMI.

The precise alloy composition variation for a given interface is not yet studied. However it was shown by A. Soumyanarayanan *et al.* that by tuning each interface separately in films of Ir/Fe/Co/Pt by changing the thickness of each ferromagnet individually the additive nature of the DMI [24] can be exploited to obtain a collectively large value of 2.25 mJ/m^2 for 0.4 nm of Fe and 0.4 nm of Co [37]. Similar technique has been envisaged by Woo *et al.* [38] for the enhancement of Spin-Orbit Torque in a trilayer of Pt/Co/Ta in which the torque on the acting ferromagnet is generated from both the interfaces.

The significantly larger DMI obtained for the Fe- rich $Co_{20}Fe_{60}B_{20}$ alloy compelled one to explore the capability of such a material to exhibit room temperature skyrmions. This is tested in the following section.

5.3 Designing skyrmion devices using thin film optimisation

It has been shown theoretically that skyrmions can exhibit high speeds at low threshold current density's and manoeuvre around defects [39]. Majority of the skyrmion structures studied until now were performed in bulk films with B20 structures in which the crystal symmetry breaks not at the surface but in the bulk [40][41][42]. However, only a few studies have been performed on ultra-thin films [24][29].

In order to study the existence of skyrmions in W/$Co_{20}Fe_{60}B_{20}$/MgO multilayers, thin films grown on transmittive SiN membranes were patterned into micro-wires using electron-beam lithography and structured into devices with Au contact on each end of the narrow wire for current injection. Such W based thin films post material optimisation and quantification of DMI were used to test for the presence of skyrmions. In order to nucleate skyrmions from the stripe domain phase and move them, current pulses of 5 ns with an amplitude of 3.9×10^{11} Am^{-2} were applied to the microwire as shown in figure 9. This resulted in the transformation of the stripe domains into Néel skyrmions in the magnetic wires as previously shown in [29].

In figure 9 the nucleation and current induced propagation of room temperature skyrmions in W/$Co_{20}Fe_{60}B_{20}$/MgO micro-wires is demonstrated. Multiple skyrmions of few 100 nm diameter are nucleated in this racetrack device. In order to test the skyrmion motion, forward and reverse current pulses were applied within the micro-wires, this is shown in figure (b) and figure (c).

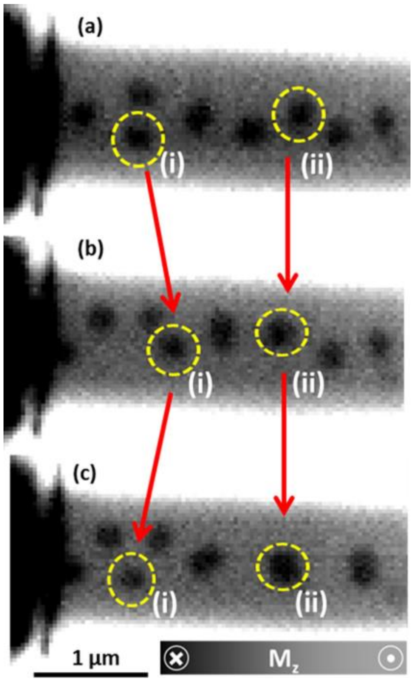

Figure 9: Room temperature skyrmions nucleated in a 1.4 µm × 5.0 µm micro-wire of $[W(5\ nm)/Co_{20}Fe_{60}B_{20}(0.8\ nm)/MgO(2\ nm)]_{10}/Ta(5\ nm)$ (a). Subsequently nucleated skyrmions are moved forwards and backwards by applying current pulses with opposite polarity (b)-(c). Highlighted skyrmion (i) is moved forward (current applied along the wire from left to right) and backward (reversed polarity). Skyrmion (ii) is an example of a pinned skyrmion that does not move at this current density. All images were obtained using Fe absorption edge for maximum contrast via STXM with XMCD technique.

It can be seen as an example that skyrmion (i) in image (b) and (c) moves in accordance to the pulse direction, forwards and backwards, respectively. Skyrmion (ii) however, is pinned in its original location (a) and does not move, irrespective to the pulse direction. The direction of motion with respect to the current direction indicates here that the DMI for such a stack is positive and that the sense of rotation for the spins is right handed [29]. The skyrmions are observed to move against the electron flow and show generally a regular circular shape in line with the low pinning deduced from the domain wall motion experiments. It has therefore been demonstrated that it is possible to stabilise skyrmions at room temperature in W/$Co_{20}Fe_{60}B_{20}$/MgO multilayers. However, one of the biggest issue with using materials which exhibit RT skyrmions for memory devices is that they require an extremely large out-of-plane field to stabilize the structures. The field evolution of the skyrmion for W/$Co_{20}Fe_{60}B_{20}$/MgO multilayers is shown in the figure 10. Similar fields of 20 mT were used for Pt/$Co_{60}Fe_{20}B_{20}$/MgO multilayers by Woo *et al.* to stabilize skyrmions in their samples [43].

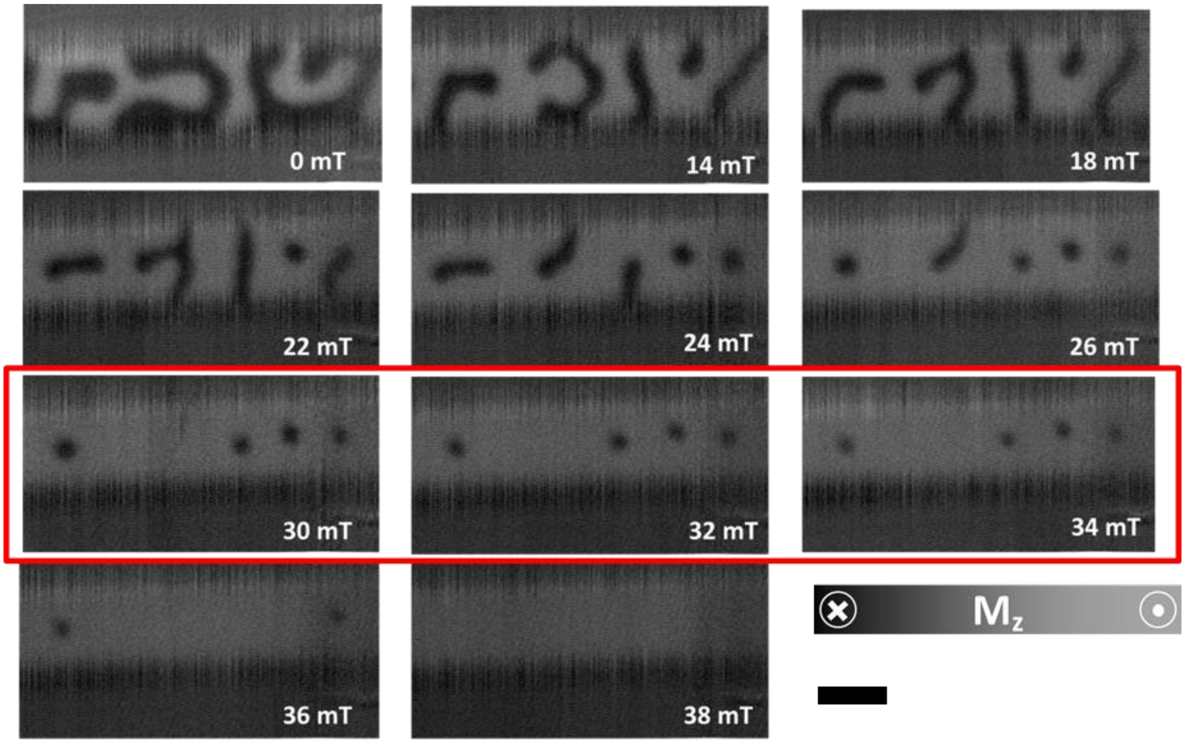

Figure 10: STXM microscopy imaging with X-ray energies tuned to Fe absorption edge showing magnetic domain stripe evolution as a function of out-of-plane applied field. Room temperature skyrmion structures stabilized in the presence of a constant out-of-plane field highlighted (red). Scale bar included in the figure is 1 µm.

This issue with regard to a constant out-of-plane field required in the process of skyrmion nucleation for a range of different material stacks investigated in the literature has not been highlighted significantly even though this poses a significant obstacle in the realization of such a skyrmionic based memory device. It can be seen from figure 10, that fields of the order of 30 mT are required to stabilize skyrmions. The current induced skyrmion motion shown in figure 9 is also performed in the presence of an external out-of -plane applied field.

In order to find stable conditions for skyrmion nucleation another material stack was made use of which was developed during the course of this study namely Ta/$Co_{20}Fe_{60}B_{20}$/MgO as discussed in chapter 4. It has been shown that such a stack exhibits PMA. Moreover, multiple studies have shown that CoFeB on a Ta seed exhibits a low DMI of the order of 0.06 mJm^{-2}, but also very low pinning in domain wall motion experiments [10][44][45]. As it has been shown in a recent study on Ta/CoFeB/MgO layers that slight modifications of the interface by the insertion of Au, Pd or Pt can have a strong influence on a DMI, PMA and the Spin-Hall switching current efficiency [46]. Bommanaboyena *et al.* have found that the DMI parameter is reduced by 50% by the insertion of Au and 35% by the insertion of Pd at the bottom interface between Ta and CoFeB. The PMA as well is reduced by an order of magnitude on the insertion of only 0.2 nm of Pd, thereby implying towards the subtlety of these interfacial effects. A modified stack is therefore utilised with the top interface engineered to change the anisotropy very slightly. It has also been shown recently [47] that it is feasible to stabilize micron sized skyrmions in Ta based stacks with a modified top interface. Authors of [47] have utilised a naturally oxidised TaO_x as the top interface as their metal oxide for inducing PMA along with a Ta seed, resulting in the total material stack of Ta/$Co_{20}Fe_{60}B_{20}$/TaO_x. A similar stack is adopted here with a modification of the top interface. Through the use of a very slow growth rate an ultra-thin dusting layer of Ta was deposited between the $Co_{20}Fe_{60}B_{20}$ and the MgO layers. This was done so as to alter the interface, the thin Ta layer deposited is designed to oxidise on deposition of MgO which then would modify the interface to a TaO_x interface as compared to an MgO interface. The creation of such an interface ensures the sustainability of the entire material stack over extended periods of time. Since MgO is hygroscopic, it is also capped with a thick 5 nm of Ta. Only an ultra-thin layer of Ta dusting layer is required as a thicker layer will result in a total loss of PMA and render the material stack not useful for device production. This thin Ta interface results in a weaker anisotropy as compared to when only MgO is used at the interface without the Ta dusting layer. This is due to the fact that the TaO_x formation introduces disorder in the system and reduces the homogeneity of the interface. Thicknesses of 0.7 to 1.1 nm of $Co_{20}Fe_{60}B_{20}$ were used with 0.08 nm of dusting layer of Ta to check for skyrmions. The Ta dusting layer was varied from 0.07 to 0.1 nm in steps of 0.01 nm grown on a 1 nm $Co_{20}Fe_{60}B_{20}$. A thicker $Co_{20}Fe_{60}B_{20}$ was chosen for two reasons. Firstly, given the inverse thickness relation [7] to the DMI a 1 nm relatively thick $Co_{20}Fe_{60}B_{20}$ would have a lower DMI and therefore allow for skyrmions if present to be observable and within resolution using lab based techniques such as the MOKE microscopy. Skyrmions of large sizes are not the first choice for high density storage, they are however very useful in studying the dynamics and the effects of current induced motion on skyrmions. Secondly, given the ultra-thin dusting layer, it is important to have a continuous film as a base. In this regard, a thicker film is more reasonable as it allows for a better wetting than a thinner film. This results in the optimised material stack of Ta(5 nm)/$Co_{20}Fe_{60}B_{20}$(1 nm)/Ta(0.08 nm)/MgO(2)/Ta(5 nm).

The material stack was then annealed at 250 °C for 1h in UHV environment using the substrate heater in the *Singulus Rotaris deposition tool* as described in chapter 3. MOKE microscopy was used to check for domain structures as well as obtaining hysteresis curves. Out-of-plane hysteresis curves for the above mentioned stack is shown below in figure 11. It can be seen that the sample exhibits a gradual switching of the magnetisation in the out-of-plane direction.

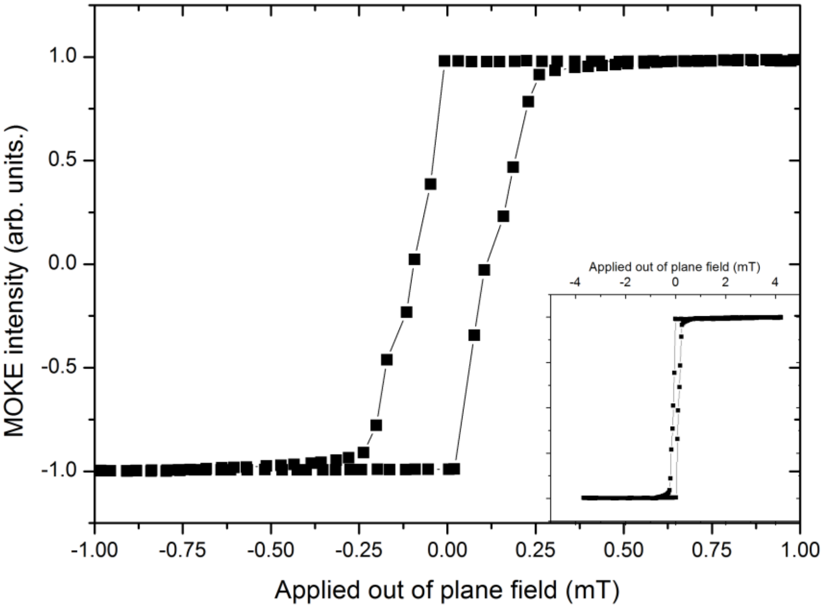

Figure 11: Out of plane hysteresis curve for Ta(5 nm)/$Co_{20}Fe_{60}B_{20}$(1 nm)/Ta(0.08 nm)/MgO(2)/Ta(5 nm). Sample exhibiting easy axis hysteresis in the OOP direction with a two-step reversal process. Inset showing higher field zoomed-out hysteresis curve showing extremely low coercive fields as measured using MO Kerr effect.

A stripe domain phase is obtained under the presence of a low out-of-plane field shown in figure 12. Extremely low pinning is observed for the said material stack, this is evidenced by the thermally activated motion/growth of the stripe domains even in the absence of an external change of field. The domain is initially nucleated in a region with slight surface variations in anisotropy due to an underlying defect. The subsequent domain motion and growth occurs randomly from all regions of the initially nucleated stripe. The magnetic stripe domain nucleation, propagation, expansion and saturation are shown below in figure 12 as individual frames during the motion of the domain wall.

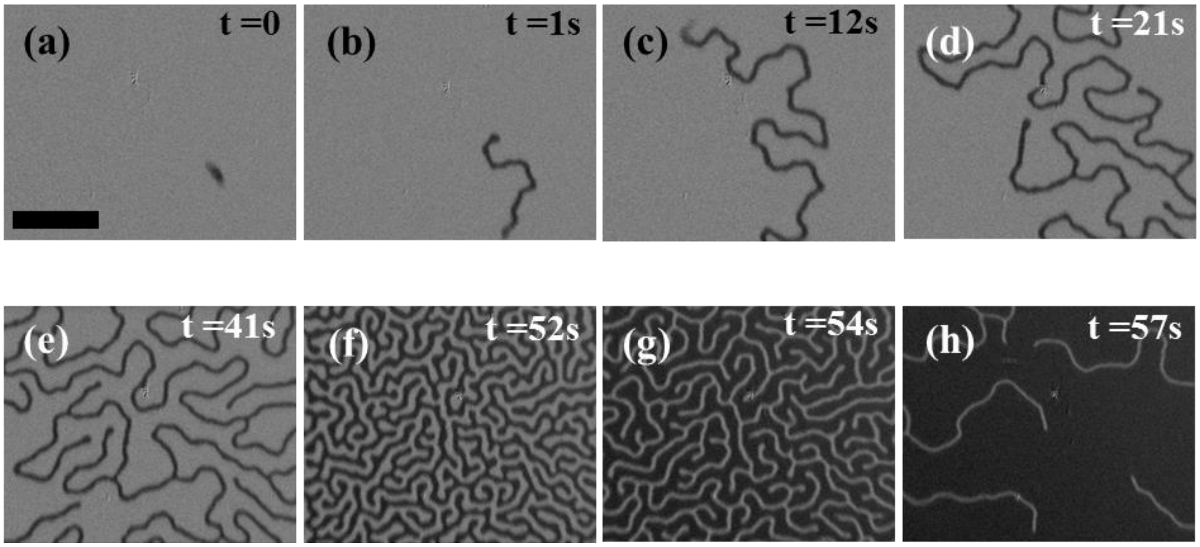

Figure 12: (a-e) Magneto-Optical Kerr microscopy images of a 10 × 10 mm Ta(5 nm)/$Co_{20}Fe_{60}B_{20}$(1 nm)/Ta(0.08 nm)/MgO(2)/Ta(5 nm) ultra-thin film exhibiting the thermally activated magnetic domain evolution random walk motion of domains expansion occurring isotropically due to low pinning. (f) Domain structure settles into a stripe domain phase of defined width on application of a small magnetic field of approx. 0.3 mT in the OOP direction. (g-h) Domain expansion as a result of increasing OOP field leading to sample saturation. No in-plane field was applied during this process. The scale bar for (a-h) as indicated in (a) is 50 µm.

The magnetic domain structure obtained for Ta/$Co_{20}Fe_{60}B_{20}$/Ta/MgO is not bubble like as observed for thin films of the same stack without the Ta dusting layer, implying that the dusting layer modifies the surface structure and the underlying anisotropy of the ferromagnet. As it can be seen from figure 12(b)-(e), the magnetic stripes expand in the absence of any magnetic field, i.e. the domain expansion post nucleation that occurs is thermally driven. Moreover, the domain expansion occurs not only from the leading edge of the stripe but also from the entire length of the stripe. New domains are formed depending on local variations in anisotropy and competition with the thermal energy barrier. Exceptionally smooth propagation of domains are observed in this system which suggests very low pinning, and a low magnetically damped system. A very small out-of-plane field of 3 Oe is applied which when gradually is increased causes the domain structure to move from a striped phase to a saturated state.

Given that there exists a Ta layer between the ferromagnet and the oxide layer, the magnetic anisotropy of such a trilayer is not as strong. Hence to test the influence of an in-plane field on the domain structure, polar MOKE microscopy was used to image magnetic domains in the presence of an in-plane field. Magnetic domains do indeed appear in the presence of an in-plane field. However, since the magnetisation of the sample is out-of-plane the magnetic domains do not undergo expansion like in the case of out-of-plane field application but instead the nucleated stripes expand along the direction of the field to form elongated stripes. As the field is reduced and switched off the stripe domains collapse into skyrmion-like domain structure resulting in a 2D lattice structure as shown in figure 13. These bubble skyrmion structures are comparable in their diameter to those obtained by the authors in [47]. However, unlike [47] these structures are zero-field stabilised entities. This allows them to be suitably used in real world devices as storage elements. In order to further reduce the size of the skyrmions in these stacks further material engineering would be required which is beyond the scope of this work.

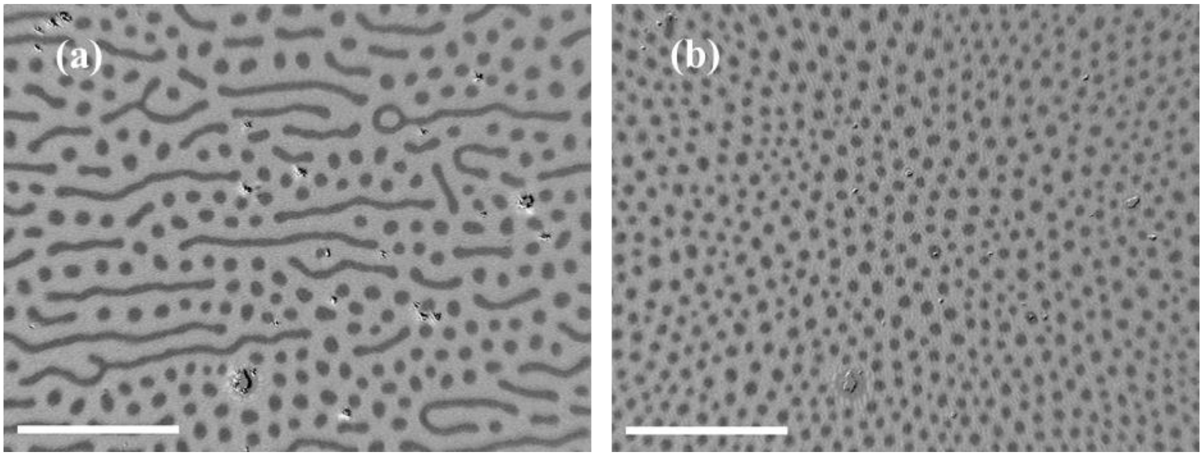

Figure 13: (a) Stripe and bubble skyrmion mixed phase domain structure obtained on reduction of in-plane fields from saturation. (b) complete coverage of bubble skyrmions and disappearance of stripes on switching off of magnetic field. Both images obtained on 10 mm × 10 mm un-patterned samples of Ta(5 nm)/$Co_{20}Fe_{60}B_{20}$(1 nm)/Ta(0.08 nm)/MgO(2)/Ta(5 nm) via wide field Kerr microscopy demonstrating the stabilisation of zero-field skyrmion entities at room temperature. The scale bar in (a) and (b) is 50 μm.

It is worth noting that the skyrmions obtained in the Ta-seeded stacks are much larger in diameter compared to those obtained in the W-seeded stacks. This depends strongly on the relative DMI and the anisotropy for a given material. In order to understand the magnetic anisotropy and the influence of annealing temperature of the same, thin films of Ta/$Co_{20}Fe_{60}B_{20}$/Ta/MgO were scribed into 10 × 5 mm pieces and SQUID magnetometry was performed on them.

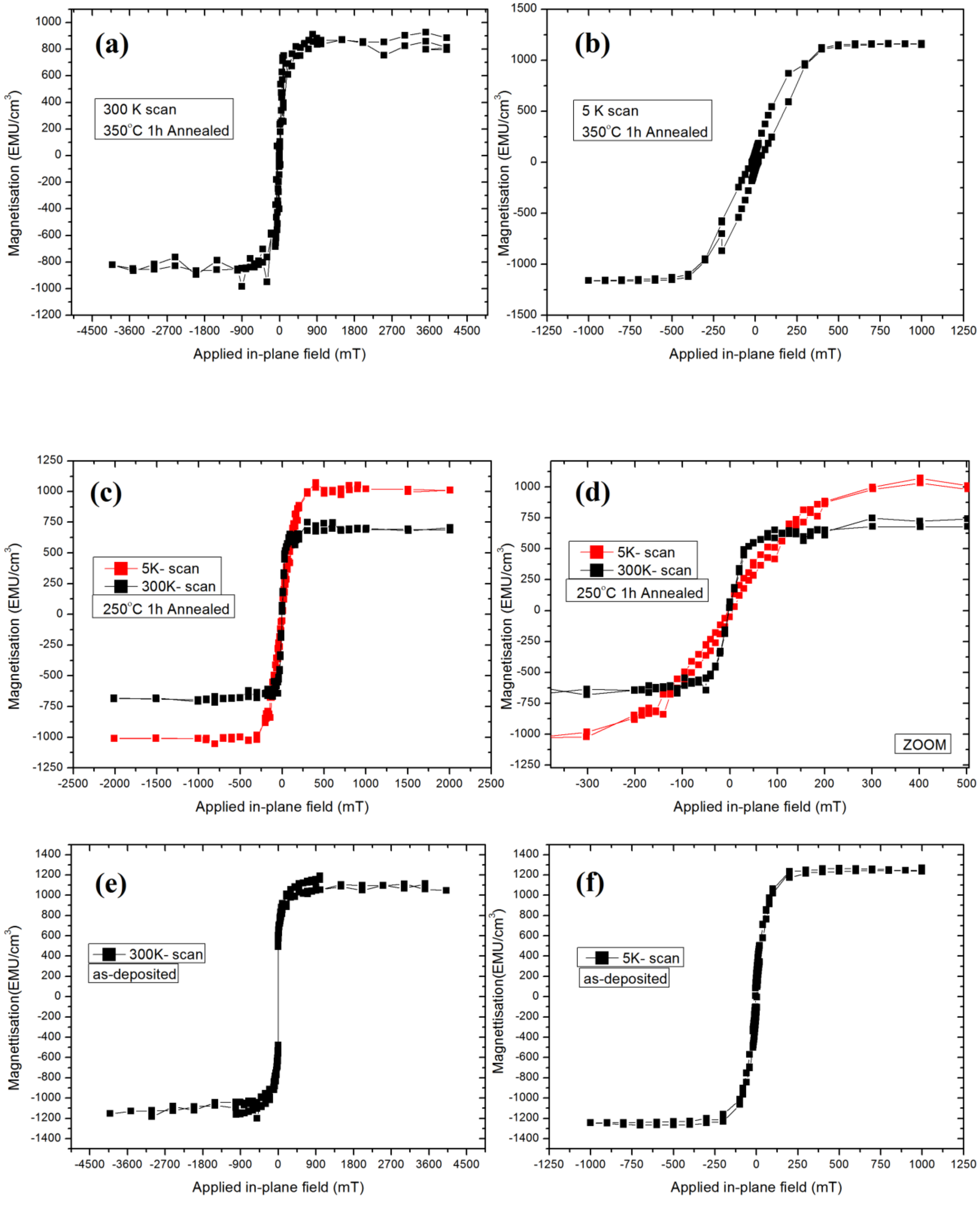

Figure 14: Magnetic anisotropy dependence of 10 mm x 5 mm thin films of Ta(5 nm)/$Co_{20}Fe_{60}B_{20}$(1 nm)/Ta(0.08 nm)/MgO(2)/Ta(5 nm) measured as a function of varying annealing temperatures via SQUID magnetometry at both 5 K and 300 K. All scans were performed with the applied magnetic field along the plane of the sample surface.

As it can be seen in figure 14, initially for the as-deposited state the thin films of Ta/$Co_{20}Fe_{60}B_{20}$/Ta/MgO/Ta are magnetised along the easy axis, in the plane of the film as seen from the sharp switching of the magnetisation at low fields. The film is magnetised in-plane when measured at room temperature, however, low temperature scans suggest a partial hard axis alignment in the plane of the film. However, for when the film is annealed at 250 °C for 1h and the SQUID magnetometry measured, the annealed film exhibits a hard axis in the in-plane direction at both room temperature and at low temperature (5 K). The anisotropy field at room temperature is lower than that measured at 5 K. Anisotropy fields of less than 90 mT were obtained at 300 K. The perpendicular magnetic anisotropy is however lost when the thin film is annealed at an elevated temperature of 350 °C for 1h.

Therefore annealing and more importantly temperature at which the annealing of the thin film is performed has a strong influence on the anisotropy of the ferromagnet. Care was taken to ensure than the sample is not displaced in the sample holder between temperature scans, i.e. the 300 K and the 5 K scan were done in a single mounting session of the sample. This therefore removes any possible contributions in the variations of anisotropy due to sample misalignment with the field between temperature scans. This suggests that an internal structural modification occurs at low temperatures which influences the anisotropy field. The material stacks investigated and observed to exhibit zero-field stabilised bubble skyrmions as shown in figure 13 are annealed at 250 °C for 1h and exhibit a weak out-of-plane anisotropy. Hence given the low annealing temperatures of these films they are ideally suited for use in memory devices since the low temperature required is compatible with CMOS device processing which is necessary in on-die memories.

In order to study their viability in a device these films of Ta/$Co_{20}Fe_{60}B_{20}$/Ta/MgO were patterned into micro-wires to study current induced dynamics [30][29][47]. As can be seen in the figure 15 these skyrmions of the order of few 10’s µm were optimised for nucleation in microwires. Current was injected via contact pads (not seen) and the skyrmions are seen to move along the direction of the current. Four different skyrmions were nucleated as an example of bits of information stored on a track.

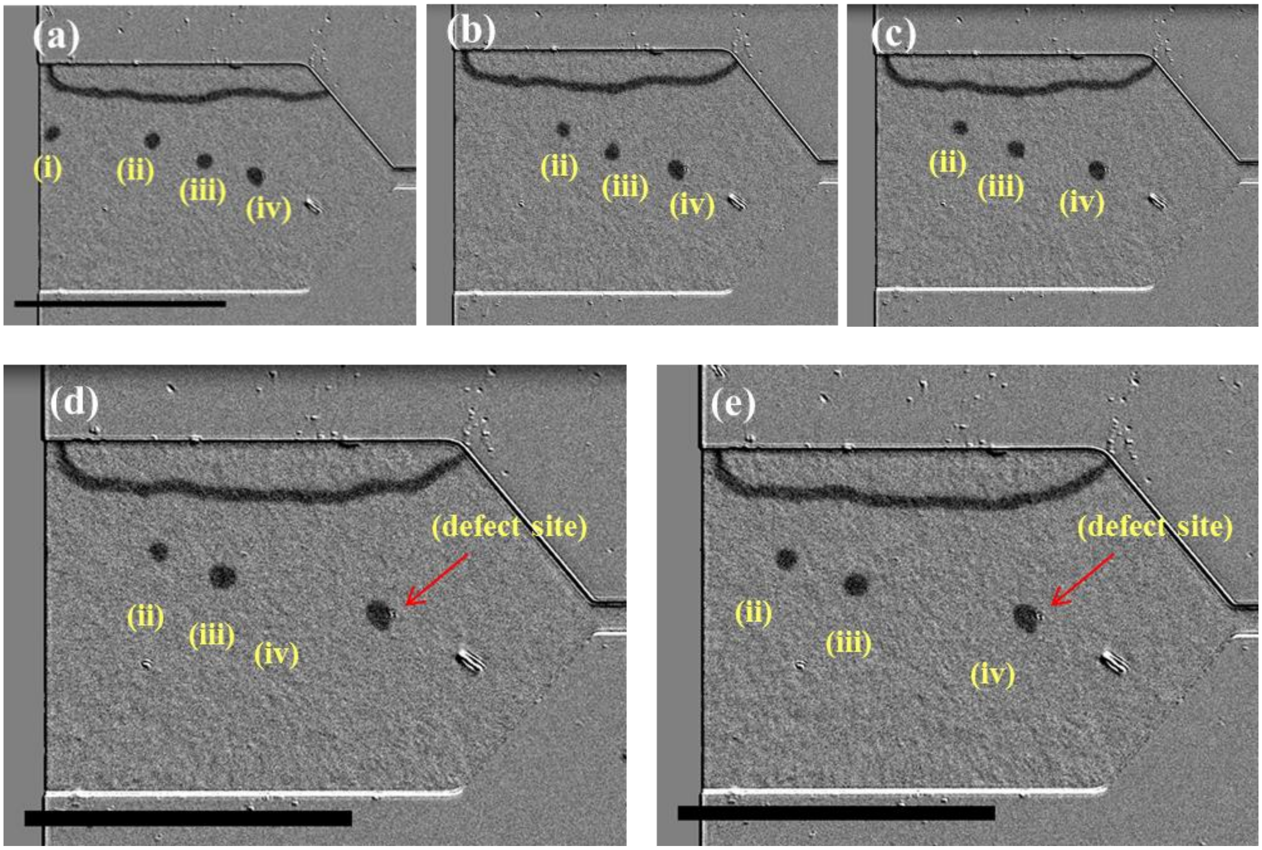

Figure 15: Kerr microscopy images of Ta(5 nm)/Co$_{20}$Fe$_{60}$B$_{20}$(1 nm)/Ta(0.08 nm)/MgO(2)/Ta(5 nm) patterned microwires exhibiting magnetic bubble skyrmions and their motion in the presence of an applied current (electron flow left to right). Each image (a-e) obtained after consecutive current pulses with a single pulse per burst. Highlighted skyrmion (iv) is pinned at a local defect present in the microwire, site of pinning indicated. The scale bar shown is 50 μm. Current induced measurements were performed along with J. Zázvorka using the Kerr microscope.

Quasi-static wide field Kerr microscopy images were obtained after applying single current pulses of 3.94×10^9 A/m^2 with a pulse width of 50 ms in the microwire to detect skyrmion motion. Post application of the first current pulse skyrmion (i) has moved out of the magnetic wire as seen in figure 15(a), while (ii) and (iii) are displaced towards the left of the wire. Subsequent motion of skyrmions (ii) and (iii) is observed for successive pulses. The current pulse amplitude was kept constant along with the duration of the pulse which was also constant. However, it should be noted that there is no motion observed for skyrmion (iv). This skyrmion remains pinned due to a visible surface defect and is not displaced during the pulsing. The defect is highlighted in a zoomed in view shown in figure 15 (d-e). This implies that further optimisation is required with respect to the patterning of the wire as the material itself exhibits exceptionally low pinning in the full film form. Nevertheless, it has been demonstrated that the magnetic properties of the thin film are strongly influenced by the addition of an ultra-thin dusting layer of Ta between the FM and oxide. Moreover, room temperature stable bubble skyrmions with a sizable diameter have been discovered. This is very useful and convenient for studying skyrmion dynamics and pinning properties using in-house experimental apparatus instead of using synchrotron facilities. If the skyrmion diameter is too small one would require specialised X-ray microscopy techniques which are not always accessible on a daily basis. Hence these Ta seeded samples serve as a bed for further research allowing one to tune skyrmion size and study skyrmion dynamics.

5.4 Conclusion

In conclusion field induced domain wall motion for thin films of (*X= W, Ta)/FM/oxide* has been studied. Thin films of W(5 nm)/$Co_{20}Fe_{60}B_{20}$(0.6 nm)/MgO(2 nm) were used to study domain propagation in the presence of an out-of-plane field. It was shown that such films exhibit field induced domain wall motion in accordance with the creep law while yielding the creep exponent, $\mu = 0.25$. Optimised thin films with respect to magnetic domain structures and coercivity, of W(5 nm)/$Co_{20}Fe_{60}B_{20}$(0.6 nm)/MgO(2 nm)/ Ta(5 nm) were then used to measure the Dzyaloshinskii-Moriya Interaction. Two different *field-based methods* were used to obtain the DMI in this film namely the field-induced asymmetric magnetic domain expansion technique and the field induced magnetic stripe annihilation method. Both these techniques utilised only magnetic field as the sole method to manipulate the energy of the domains and cause them to undergo motion. The DMI as measured via the asymmetric expansion and stripe annihilation methods were (0.63 ± 0.05) mJm^{-2} and (0.73 ± 0.5) mJm^{-2} respectively. The key difference between the two techniques is that for the asymmetric expansion the DMI obtained is an inferred value from the effective DMI field of the sample whereas for the stripe annihilation method the stripe widths and periodicity are used directly in the calculation of the DMI energy. Furthermore, a strong ferromagnetic compositional dependence of the DMI was found in which exactly the same stack with respect to thickness was studied while varying the CoFe composition of the ferromagnet. It was found that for films with W as the seed layer, the largest DMI is obtained in films with an Fe-rich $Co_{20}Fe_{60}B_{20}$. The DMI field for Fe-rich $Co_{20}Fe_{60}B_{20}$ was found to be 93 mT. Given the large DMI and the structural inversion asymmetry thin films of W/$Co_{20}Fe_{60}B_{20}$ were tested as a viable candidate to exhibit skyrmions. These were patterned into microwires and room temperature skyrmions were stabilised in these W/$Co_{20}Fe_{60}B_{20}$ thin films successfully.

In order to remove the requirement of fields for stabilizing skyrmions and to generate room temperature field independent skyrmions, the interface between the FM and the MgO was modified. A thin dusting layer of Ta was included in the material stack of Ta(5 nm)/$Co_{20}Fe_{60}B_{20}$(0.6 nm)/MgO(2 nm). Thin films of Ta(5 nm)/$Co_{20}Fe_{60}B_{20}$(0.6 nm)/Ta(0.08 nm)/MgO(2 nm) were shown to exhibit magnetic stripes domains with exceptionally low pinning. Domain wall motion in such a film was thermally driven. The magnetic anisotropy and the hysteretic response to field was studied in this stack as a function of annealing temperatures for both at 5 K and at 300 K. It was found that the material stack has a very strong dependence of anisotropy on annealing temperature. Thin films annealed at 250 °C exhibit weak out-of-plane anisotropy at room temperature. Zero-field magnetic skyrmion-bubbles were stabilised in full films of diameters of few 10’s micrometre. Finally, these skyrmions were nucleated and stabilised in a micro-wire and shown to be able to be displaced in the presence of an applied current hence demonstrating their viability to be used as storage elements in next generation magnetic media.

5.5 Chapter 5- References

[1] S. Tacchi, R. E. Troncoso, M. Ahlberg, G. Gubbiotti, M. Madami, J. Åkerman, and P. Landeros, "Interfacial Dzyaloshinskii-Moriya Interaction in Pt/CoFeB Films: Effect of the Heavy-Metal Thickness," *Phys. Rev. Lett.*, vol. 118, no. 14, p. 147201, 2017.

[2] H. Yang, A. Thiaville, S. Rohart, A. Fert, and M. Chshiev, "Anatomy of Dzyaloshinskii-Moriya Interaction at Co/Pt Interfaces.," *Phys. Rev. Lett.*, vol. 115, no. 26, p. 267210, Dec. 2015.

[3] F. Ajejas, V. Křižáková, D. De Souza Chaves, J. Vogel, P. Perna, R. Guerrero, A. Gudin, J. Camarero, and S. Pizzini, "Tuning domain wall velocity with Dzyaloshinskii-Moriya interaction," *Appl. Phys. Lett.*, vol. 111, no. 20, p. 202402, 2017.

[4] S. A. Nasseri, S. Moretti, E. Martinez, C. Serpico, and G. Durin, "Collective coordinate models of domain wall motion in perpendicularly magnetized systems under the spin hall effect and longitudinal fields," *J. Magn. Magn. Mater.*, vol. 426, no. October 2016, pp. 195–201, 2017.

[5] S. Nasseri, E. Martinez, and G. Durin, "Effect of canting in the domains on magnetic domain wall motion," in *2017 IEEE International Magnetics Conference (INTERMAG)*, 2017, p. 1.

[6] D. Han, N. Kim, J. Kim, Y. Yin, J. Koo, J. Cho, S. Lee, M. Kläui, H. J. M. Swagten, B. Koopmans, and C. You, "Asymmetric Hysteresis for Probing Dzyaloshinskii − Moriya Interaction," *Nano Lett.*, vol. 16, no. 7, pp. 4438–4446, 2016.

[7] J. Cho, N.-H. Kim, S. Lee, J.-S. Kim, R. Lavrijsen, A. Solignac, Y. Yin, D.-S. Han, N. J. J. van Hoof, H. J. M. Swagten, B. Koopmans, and C.-Y. You, "Thickness dependence of the interfacial Dzyaloshinskii–Moriya interaction in inversion symmetry broken systems," *Nat. Commun.*, vol. 6, no. May, p. 7635, 2015.

[8] E. C. Corredor, S. Kuhrau, F. Kloodt-twesten, R. Frömter, and H. P. Oepen, "SEMPA investigation of the Dzyaloshinskii-Moriya interaction in the single , ideally grown Co / Pt (111) interface," *Phys. Rev. B*, vol. 96, p. 60410, 2017.

[9] M. J. Benitez, A. Hrabec, A. P. Mihai, T. A. Moore, G. Burnell, D. McGrouther, C. H. Marrows, and S. McVitie, "Magnetic microscopy and topological stability of homochiral Néel domain walls in a Pt/Co/AlOx trilayer.," *Nat. Commun.*, vol. 6, p. 8957, 2015.

[10] J.-P. Tetienne, T. Hingant, L. J. Martínez, S. Rohart, A. Thiaville, L. Herrera Diez, K. Garcia, J.-P. Adam, J.-V. Kim, J.-F. Roch, I. M. Miron, G. Gaudin, L. Vila, B. Ocker, D. Ravelosona, and V. Jacques, "The nature of domain walls in ultrathin ferromagnets revealed by scanning nanomagnetometry," *Nat. Commun.*, vol. 6, p. 6733, 2015.

[11] K. Ryu, L. Thomas, S. Yang, and S. Parkin, "Chiral spin torque at magnetic domain walls," *Nat. Nanotechnol.*, vol. 8, no. June, pp. 527–533, 2013.

[12] S. Emori, E. Martinez, K.-J. Lee, H.-W. Lee, U. Bauer, S.-M. Ahn, P. Agrawal, D. C. Bono, and G. S. D. Beach, "Spin Hall torque magnetometry of Dzyaloshinskii domain walls," *Phys. Rev. B*, vol. 90, no. 18, p. 184427, Nov. 2014.

[13] R. Lo Conte, G. V Karnad, E. Martinez, K. Lee, N.-H. Kim, D. Han, J.-S. Kim, S. Prenzel, T. Schulz, C.-Y. You, H. J. M. Swagten, and M. Kläui, "Ferromagnetic layer thickness dependence of the Dzyaloshinskii-Moriya interaction and spin-orbit torques in Pt\Co\AlOx," *AIP Adv.*, vol. 7, no. 6, p. 65317, 2017.

[14] R. Lo Conte, G. V Karnad, E. Martinez, K. Lee, N.-H. Kim, D. Han, J.-S. Kim, S. Prenzel, T. Schulz, C.-Y. You, H. J. M. Swagten, and M. Kläui, "[Supplementary Material] Ferromagnetic layer thickness dependence of the Dzyaloshinskii-Moriya interaction and spin-orbit torques in Pt\Co\AlOx," *AIP Adv. Adv.*, vol. 7, no. 6, p. 65317, 2017.

[15] F. Freimuth, S. Blügel, and Y. Mokrousov, "Relation of the Dzyaloshinskii-Moriya interaction to spin currents and to the spin-orbit field," *Phys. Rev. B*, vol. 96, p. 54403, 2017.

[16] J. Hanke, F. Freimuth, S. Blügel, and Y. Mokrousov, "Higher-dimensional Wannier Interpolation for the Modern Theory of the Dzyaloshinskii – Moriya Interaction : Application to Co-based Trilayers," *J. Phys. Soc. Japan*, vol. 87, p. 41010, 2018.

[17] R. Soucaille, M. Belmeguenai, J. Torrejon, J. V. Kim, T. Devolder, Y. Roussigne, S. M. Cherif, A. A. Stashkevich, M. Hayashi, and J.-P. Adam, "Probing the Dzyaloshinskii-Moriya interaction in CoFeB ultrathin films using domain wall creep and Brillouin light spectroscopy," *Phys. Rev. B*, vol. 94, no. 10, p. 104431, 2016.

[18] K. Obata and G. Tatara, "Current-induced domain wall motion in Rashba spin-orbit system," *Phys. Rev. B*, vol. 77, no. 21, p. 214429, Jun. 2008.

[19] N. Romming, C. Hanneken, M. Menzel, J. E. Bickel, B. Wolter, K. V Bergmann, A. Kubetzka, and R. Wiesendanger, "Writing and Deleting Single Magnetic Skyrmions," *Science*, vol. 341, no. August, pp. 636–639, 2013.

[20] S.-G. Je, D.-H. Kim, S.-C. Yoo, B.-C. Min, K.-J. Lee, and S.-B. Choe, "Asymmetric magnetic domain-wall motion by the Dzyaloshinskii-Moriya interaction," *Phys. Rev. B*, vol. 88, no. 21, p. 214401, Dec. 2013.

[21] A. Hrabec, N. A. Porter, A. Wells, M. J. Benitez, G. Burnell, S. McVitie, D. McGrouther, T. A. Moore, and C. H. Marrows, "Measuring and tailoring the Dzyaloshinskii-Moriya interaction in perpendicularly magnetized thin films," *Phys. Rev. B*, vol. 90, no. 2, p. 20402, Jul. 2014.

[22] R. Lo Conte, E. Martinez, A. Hrabec, A. Lamperti, T. Schulz, L. Nasi, L. Lazzarini, R. Mantovan, F. Maccherozzi, S. S. Dhesi, B. Ocker, C. H. Marrows, T. A. Moore, and M. Kläui, "Role of B diffusion in the interfacial Dzyaloshinskii-Moriya interaction in Ta/Co20 F e60 B20/MgO nanowires," *Phys. Rev. B*, vol. 91, no. 1, p. 14433, Jan. 2015.

[23] S. Jaiswal, K. Litzius, I. Lemesh, F. Büttner, S. Finizio, J. Raabe, M. Weigand, K. Lee, J. Langer, B. Ocker, G. Jakob, G. S. D. Beach, and M. Kläui, "Investigation of the Dzyaloshinskii-Moriya interaction and room temperature skyrmions in W/CoFeB/MgO thin films and microwires," *Appl. Phys. Lett.*, vol. 111, p. 22409, 2017.

[24] C. Moreau-Luchaire, C. Moutafis, N. Reyren, J. Sampaio, C. A. F. Vaz, N. Van Horne, K. Bouzehouane, K. Garcia, C. Deranlot, P. Warnicke, P. Wohlhüter, J.-M. George, M. Weigand, J. Raabe, V. Cros, and A. Fert, "Additive interfacial chiral interaction in multilayers for stabilization of small individual skyrmions at room temperature," *Nat. Nanotechnol.*, vol. 11, no. May, pp. 444–449, 2016.

[25] A. Cao, X. Zhang, B. Koopmans, S. Peng, Y. Zhang, Z. Wang, S. Yan, H. Yang, and W. Zhao, "Tuning the Dzyaloshinskii-Moriya Interaction in Pt/Co/MgO heterostructures through MgO thickness," *ArXiv e-printsArXiv e-prints*, no. arXiv:1710.09051v1, 2017.

[26] O. Boulle, J. Vogel, H. Yang, S. Pizzini, D. de S. Chaves, A. Locatelli, T. O. Menteş, A. Sala, L. D. Buda-Prejbeanu, O. Klein, M. Belmeguenai, Y. Roussigné, A. Stashkevich, S. M. Chérif, L. Aballe,

M. Foerster, M. Chshiev, S. Auffret, I. M. Miron, and G. Gaudin, "Room temperature chiral magnetic skyrmion in ultrathin magnetic nanostructures," *Nat. Nanotechnol.*, vol. 11, no. May, pp. 449–454, 2016.

[27] D. Nolle, M. Weigand, P. Audehm, E. Goering, U. Wiesemann, C. Wolter, E. Nolle, and G. Schütz, "Note: Unique characterization possibilities in the ultra high vacuum scanning transmission x-ray microscope (UHV-STXM) 'MAXYMUS' using a rotatable permanent magnetic field up to 0.22 T," *Rev. Sci. Instrum.*, vol. 83, no. 4, p. 46112, 2012.

[28] G. Schütz, W. Wagner, W. Wilhelm, P. Kienle, R. Zeller, R. Frahm, and G. Materlik, "Absorption of Circularly Polarized X-Rays in Iron," *Phys. Rev. Lett.*, vol. 58, no. 7, pp. 737–740, 1987.

[29] S. Woo, K. Litzius, B. Krüger, M.-Y. Im, L. Caretta, K. Richter, M. Mann, A. Krone, R. M. Reeve, M. Weigand, P. Agrawal, I. Lemesh, M.-A. Mawass, P. Fischer, M. Kläui, and G. S. D. Beach, "Observation of room-temperature magnetic skyrmions and their current-driven dynamics in ultrathin metallic ferromagnets.," *Nat. Mater.*, vol. 15, no. Febuary, pp. 501–506, Feb. 2016.

[30] K. Litzius, I. Lemesh, B. Krüger, P. Bassirian, L. Caretta, K. Richter, F. Büttner, J. Förster, R. M. Reeve, M. Weigand, I. Bykova, H. Stoll, G. Schütz, G. S. D. Beach, and M. Kläui, "Skyrmion Hall Effect Revealed by Direct Time-Resolved X-Ray Microscopy," *Nat. Phys.*, vol. 13, no. December, pp. 170–175, 2016.

[31] I. Lemesh, F. Büttner, and G. S. D. Beach, "Accurate model of the stripe domain phase of perpendicularly magnetized multilayers," *Phys. Rev. B*, vol. 95, p. 174423, 2017.

[32] F. Büttner, B. Krüger, S. Eisebitt, and M. Kläui, "Accurate calculation of the transverse anisotropy of a magnetic domain wall in perpendicularly magnetized multilayers," *Phys. Rev. B*, vol. 92, no. 5, p. 54408, 2015.

[33] A. T. Hindmarch, V. Harnchana, A. S. Walton, A. P. Brown, R. M. D. Brydson, and C. H. Marrows, "Zirconium as a Boron Sink in Crystalline CoFeB/MgO/CoFeB Magnetic Tunnel Junctions," *Appl. Phys. Express*, vol. 4, no. 1, p. 13002, Jan. 2011.

[34] M. Zhu, H. Chong, Q. B. Vu, R. Brooks, H. Stamper, and S. Bennett, "Study of CoFeB thickness and composition dependence in a modified CoFeB/MgO/CoFeB perpendicular magnetic tunnel junction," *J. Appl. Phys.*, vol. 119, p. 73907, 2016.

[35] S. Ikeda, J. Hayakawa, Y. Ashizawa, Y. M. Lee, K. Miura, H. Hasegawa, M. Tsunoda, F. Matsukura, and H. Ohno, "Tunnel magnetoresistance of 604% at 300 K by suppression of Ta diffusion in CoFeB/MgO/CoFeB pseudo-spin-valves annealed at high temperature," *Appl. Phys. Lett.*, vol. 93, no. 8, p. 82508, 2008.

[36] J. Hayakawa, S. Ikeda, F. Matsukura, H. Takahashi, and H. Ohno, "Dependence of giant tunnel magnetoresistance of sputtered CoFeB/MgO/CoFeB magnetic tunnel junctions on MgO barrier thickness and annealing temperature," *Jpn. J. Appl. Phys.*, vol. 44, pp. L587–L589, Apr. 2005.

[37] A. Soumyanarayanan, M. Raju, A. L. G. Oyarce, A. K. C. Tan, M. Y. Im, A. P. Petrovic, P. Ho, K. H. Khoo, M. Tran, C. K. Gan, F. Ernult, and C. Panagopoulos, "Tunable room-temperature magnetic skyrmions in Ir/Fe/Co/Pt multilayers," *Nat. Mater.*, vol. 16, no. 9, pp. 898–904, 2017.

[38] S. Woo, M. Mann, A. J. Tan, L. Caretta, and G. S. D. Beach, "Enhanced spin-orbit torques in Pt/Co/Ta heterostructures," *Appl. Phys. Lett.*, vol. 105, no. 21, p. 212404, Nov. 2014.

[39] A. Fert, V. Cros, and J. Sampaio, "Skyrmions on the track," *Nat. Nanotechnol.*, vol. 8, no. 3, pp.

152–156, 2013.

[40] Y. Iguchi, S. Uemura, K. Ueno, and Y. Onose, “Nonreciprocal magnon propagation in a noncentrosymmetric ferromagnet LiFe5O8,” *Phys. Rev. B*, vol. 92, no. 18, p. 184419, 2015.

[41] S. Seki, X. Z. Yu, S. Ishiwata, and Y. Tokura, “Observation of skyrmions in a multiferroic material,” *Science*, vol. 336, no. 6078, pp. 198–201, 2012.

[42] X. Z. Yu, N. Kanazawa, Y. Onose, K. Kimoto, W. Z. Zhang, S. Ishiwata, Y. Matsui, and Y. Tokura, “Near room-temperature formation of a skyrmion crystal in thin-films of the helimagnet FeGe.,” *Nat. Mater.*, vol. 10, no. February, pp. 106–109, 2011.

[43] S. Woo, K. Litzius, B. Krüger, M.-Y. Im, L. Caretta, K. Richter, M. Mann, A. Krone, R. M. Reeve, M. Weigand, P. Agrawal, I. Lemesh, M.-A. Mawass, P. Fischer, M. Kläui, and G. S. D. Beach, “[Supplementary material] Observation of room-temperature magnetic skyrmions and their current-driven dynamics in ultrathin metallic ferromagnets.,” *Nat. Mater.*, vol. 15, no. Febuary, pp. 501–506, Feb. 2016.

[44] R. A. Khan, P. M. Shepley, A. Hrabec, A. W. J. Wells, B. Ocker, C. H. Marrows, and T. A. Moore, “Effect of annealing on the interfacial Dzyaloshinskii-Moriya interaction in Ta/CoFeB/MgO trilayers,” *Appl. Phys. Lett.*, vol. 109, p. 132404, 2016.

[45] C. Burrowes, N. Vernier, J.-P. Adam, L. H. Diez, K. Garcia, I. Barisic, G. Agnus, S. Eimer, J. Kim, A. Lamperti, R. Mantovan, B. Ockert, E. E. Fullerton, and D. Ravelosona, “Low depinning fields in Ta-CoFeB-MgO ultrathin films with perpendicular magnetic anisotropy,” *Appl. Phys. Lett.*, vol. 103, p. 182401, 2013.

[46] S. P. Bommanaboyena and M. Meinert, “Tuning the perpendicular magnetic anisotropy , spin Hall switching current density , and domain wall velocity by submonolayer insertion in Ta/CoFeB/MgO heterostructures,” *Appl. Phys. Lett.*, vol. 111, p. 42407, 2017.

[47] W. Jiang, P. Upadhyaya, W. Zhang, G. Yu, M. B. Jungfleisch, F. Y. Fradin, J. E. Pearson, Y. Tserkovnyak, K. L. Wang, O. Heinonen, S. G. E. Velthuis, and A. Hoffmann, “Blowing magnetic skyrmion bubbles,” *Science*, vol. 349, no. 6245, pp. 283–286, 2015.

|Chapter 6

Conclusion and future outlook

The interfacial effects in ultra-thin material stacks have only just been broached and there remain a lot of possible explanations which are yet to be strengthened. There exist a multitude of phenomena at the interface which are yet to be understood completely. A deeper and more thorough evaluation of such interfacial phenomenon can be understood by obtaining information pertaining to the structural changes which occur at this ultra-thin interface. More often than not what is needed is *in-situ* measurements of the structure i.e. during the growth processes subtle changes which are being introduced at for example the HM and FM interface need to be studied to understand the over-arching effect it has on the various different transport and magnetic interfacial phenomena.

In conclusion, during the course of this study multiple thin film structures of the form corresponding to HM/FM/MgO were studied where the HM= W, Ta, Pd, Pt and W_xTa_{1-x}; FM= $Co_{20}Fe_{60}B_{20}$, $Co_{60}Fe_{20}B_{20}$, $Co_{40}Fe_{40}B_{20}$ and Co to investigate the interfacial phenomenon namely perpendicular magnetic anisotropy and the interfacial Dzyaloshinskii-Moriya Interaction arising in such systems lacking structural symmetry. Both PMA and DMI have been shown to be crucial for generation of future non-volatile magnetic memory devices.

The domain morphology in thin films of W/CoFeB/MgO was studied using Magneto-Optical Kerr Microscopy. It was shown that the domain structures and the resulting pinning in the presence of applied out-of-plane magnetic field can be tuned by the varying the growth conditions used to grow the tungsten seed layer. A higher sputter power of 1500 W was shown to promote a smoother film growth. W/CoFeB/MgO was grown to be magnetised in the out-of-plane direction. Post deposition annealing exhibited an increase in the coercive field (× 2) for all $Co_{20}Fe_{60}B_{20}$ thicknesses. This can be attributed to the thermally induced crystallisation of the as-deposited CoFeB alloy. The HM acts as a "sink" for the boron due to its large negative formation enthalpy for metal borides. Similar behaviour was observed for thin films of Ta/CoFeB/MgO. The coercive field of the FM as a function of different seed layer as well as different FM compositions was tested. A highly tunable coercive field with respect to the thickness of the Co layer was found in symmetric films of Pt/Co/Pt whereas extremely low coercivity < 1 mT was obtained for films with CoFeB as the ferromagnetic material. Moreover, apart from the seed layer, the sputter deposition power of the seed layer was shown to also be able to influence the coercivity of the resulting stack. Perpendicular magnetic anisotropy cannot be simply achieved by heat treatment of the HM/FM material stack via annealing but the composition of the FM also plays a role in obtaining PMA. Pt/$Co_{20}Fe_{60}B_{20}$/MgO was in-plane post annealing however when the Fe-rich alloy is replaced by the Co-rich alloy the material stack is magnetised in the out-of-plane direction. PMA is truly an interfacial driven phenomena in such HM/FM stacks as evidenced in chapter 4 by the narrow thickness range of the FM over which the samples were magnetised in the out-of-plane direction. The magnetic anisotropy measurements clearly show an inverse thickness relationship with the FM thus highlighting the subtle interfacially driven phenomenon that is PMA, obtaining anisotropies of 1 T for such HM/FM structures. The top interface of the FM is equally important in generating out-of-plane magnetised films with ferromagnetic alloys. MgO when grown below a critical thickness of 1 nm does not result in PMA. Almost 3 times larger magnetic anisotropy is obtained for films with a Ta underlayer as compared to a Pd underlayer. Moreover the resulting domain pattern is also vastly influenced by the seed layer as one can obtain worm like structures for a range of FM thicknesses with a Pd underlayer.

Post optimization of magnetic anisotropy and domain structures, the Dzyaloshinskii-Moriya interaction was investigated in W/CoFeB/MgO thin films. Two separate field driven techniques were utilised namely, asymmetric magnetic domain expansion and field driven domain strip annihilation. Asymmetric expansion of the magnetic bubble was observed which established the presence of DMI in such material stacks. The DMI values obtained using the two techniques were (0.63 ± 0.05) mJm^{-2} and (0.73 ± 0.5) mJm^{-2} respectively. The ferromagnetic compositional dependence on the effective DMI was studied by varying the CoFe content for the same nominal thickness. This allowed to for an additional handle to tune the DMI. Fe-rich CoFeB exhibited the largest DMI. Scanning Transmission X-ray microscopy was used to study the presence of skyrmions in W/$Co_{20}Fe_{60}B_{20}$/MgO. Room temperature stable skyrmions were nucleated in W/$Co_{20}Fe_{60}B_{20}$/MgO micro-wires patterned from films grown on SiN membranes. Current induced motion was obtained for such skyrmions along a track using current densities of 3.9×10^{11} Am^{-2}. The skyrmions were observed to move against electron flow. However such skyrmions are not viable for device production as a constant perpendicular field of 30 mT were required to stabilise them. Material stacks comprising of Ta/$Co_{20}Fe_{60}B_{20}$/MgO with an ultra-thin dusting layer of Ta between the FM and oxide was used to tune the PMA. Zero field stable skyrmions with a few tens of micrometre diameter were nucleated in thin films of Ta/CoFeB/Ta/MgO and tested for current induced motion in a magnetic nanowire.

Experiments conducted and the results obtained here only serve as a seed for further research into the Dzyaloshinskii-Moriya Interaction as well as skyrmion dynamics. There are a number of further studies which can be undertaken, some of which are outlined as follows.

A study involving the role of boron and its influence on the Dzyaloshinskii-Moriya Interaction. For a given heavy metal for example and a set ferromagnetic thickness, the degree of boron within the alloy should determine its crystallization on annealing the material stack at a set temperature. The interface would therefore be modified giving rise to a possible modulation of the DMI via boron doping. Another way in which material engineering maybe used to extend the study conducted here is by varying the Fe concentration in CoFeB alloy. As it has been shown that a Fe-rich $Co_{20}Fe_{60}B_{20}$ exhibits a large DMI with a W see layer therefore a material stack of the form W/Fe(t)/MgO can be studied which in principle should have a larger DMI. Another key property which could lead to the fortification of skyrmions in devices is its life time and resistance to thermal fluctuations. For example studying temperature dependence of skyrmions motion and understanding the influence of temperature on DMI are two possible avenues which can shed light towards the viability of skyrmions in devices.

In a structure of the form HM_1/FM/HM_2 where the DMI at the bottom interface (HM_1/FM) is opposite to that at the top interface (FM/HM_2) such that it leads to a net enhancement of DMI, can be modified by the introduction of an ultra-thin non-heavy metal species such as Cu between HM_1/FM. By measuring the DMI in stacks with varying thickness of Cu, one can establish the individual contribution of each interface towards the net DMI.

A direct extension to the already studied WTa alloy seed layer in this work would be to test the influence of DMI as a function of HM doping as both W and Ta have the same sign of the DMI but different magnitudes one would expect a linear increase in effective DMI as the doping is changed from a Ta rich to W rich seed layer.

The outlooks mentioned above are only a few examples of the studies which can be undertaken. There are a vast number of magnetic phenomena at the interface which are yet to be explored in totality. In the years to come the complexities various interfaces will be made clearer by the extension of existing technology. This can be used as a tool for the experimental physicist to extend ones conceptual understanding of the mysteries governing the interface. It can pave the road towards the future of both device developments in terms of skyrmionic based memory, as well as enrich the understanding of the physics phenomena occurring at the interface. The story has only just begun to unfold.

|Appendix A:

Methods

Here, the details for the setting up of the X-ray measurements and the SQUID magnetometry experiments along with the procedures used for obtained the results are elaborated.

A.1 Protocol of X-ray measurement

In order to obtain X-ray reflection/diffraction data, it is required that the optical set-up for the X-ray diffractometer is aligned properly. Failure to do could cause damage to the equipment as well as result in inaccurate measurements. Here the procedure used for alignment of the sample prior to structural characterisation is detailed.

The X-ray generators are powered up to 40 mA and 40 kV. The first step of alignment is to position the detector in line with the source of the X-rays. With the attenuator set to maximum attenuation a two-theta de-coupled scan is performed. This fixes the sample stage and only moves the detector over a small angular displacement with respect to the source. This then aligns the detector with the source in the absence of the sample. The detector displacement (2ϴ) is not tied to any other motor hence it is decoupled from the sample stage motor as opposed to the 2ϴ-ω scan discussed later which is a combination motion. A misaligned detector scan is shown in figure 1(a) along with the scan taken after alignment in figure 1(b).

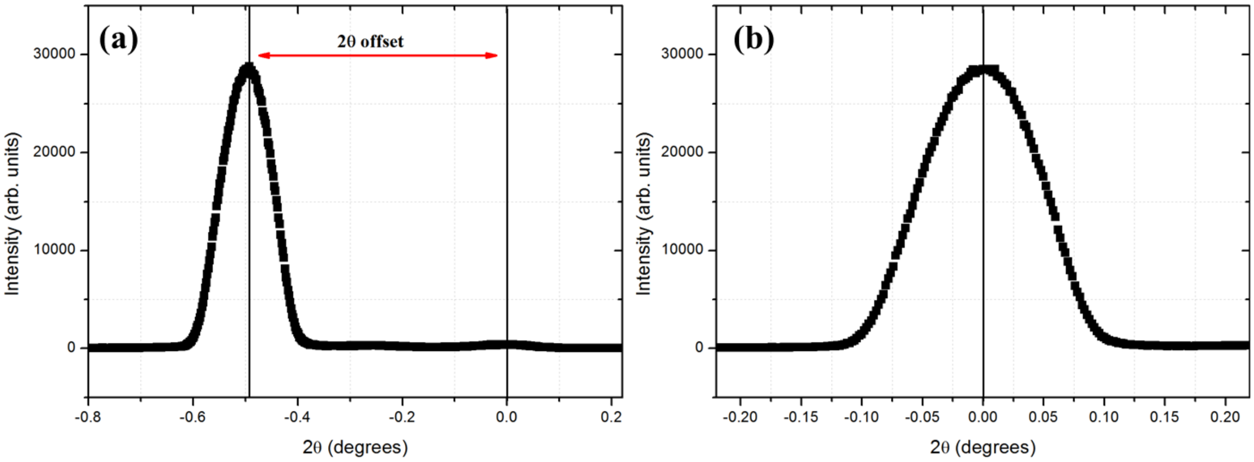

Figure 1: (a) A 2Ө sweep of the detector across the source without the sample, showing the offset present at the detector angle during alignment scans for X-ray reflectometry. (b) The same scan of the detector after re-adjustment of the detector-zero position and removal of the offset showing the source and detector centred at 0°.

If the detector is partially not aligned it can result in a reduction in the total intensity which can have an impact when studying low intensity diffraction or high angle reflectometry which would provide an over estimate of the roughness due to non-visible fringes. However if the detector is completely misaligned as seen in figure 1(a) it will not be possible to perform structural characterisation of the sample.

Once the detector is aligned, the sample is mounted on the holder and needs to be aligned with the X-ray optics. The sample here is part of the optical geometry. Hence a z-axis scan is performed. This scan moves the sample in the path of the X-ray beam and is shown in figure 2.

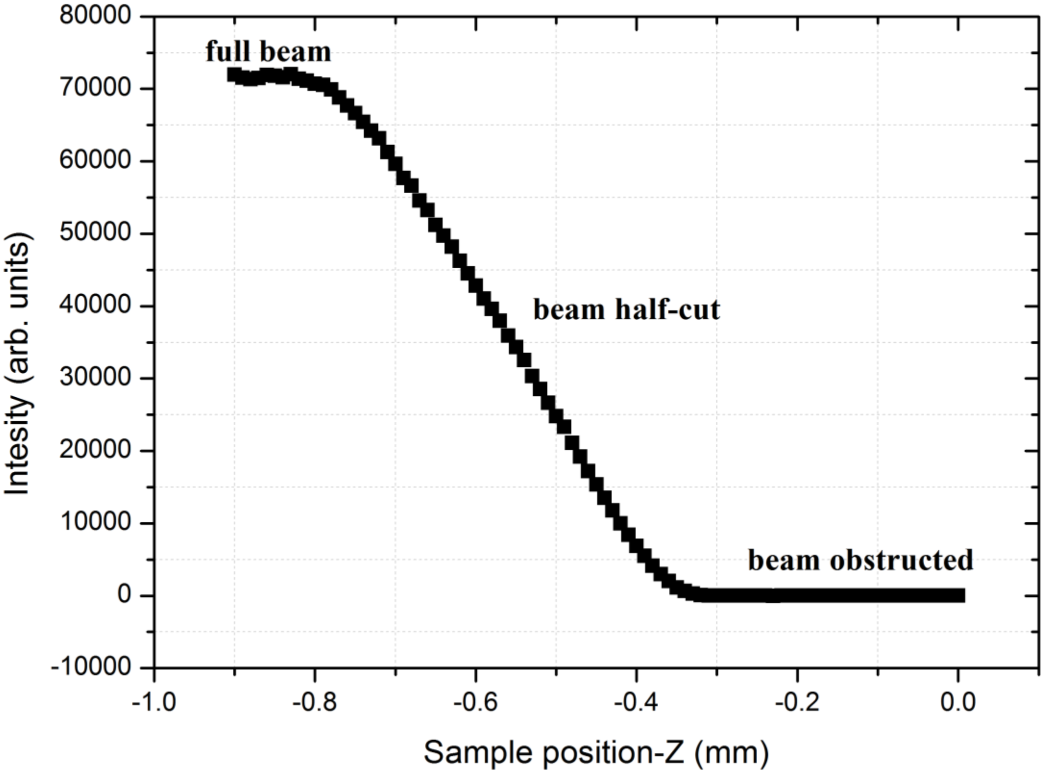

Figure 2: Alignment scan with the sample moved inwards into the path of the beam and intersecting the X-rays path between the source and the detector. The sample is positioned such that it intersects half the beam width.

The sample is positioned such that it is in the middle of the beam path with respect to its thickness. The structural information obtained about any given sample is obtained from the total surface area probed by the X-ray beam. In order to ensure that the sample is centred in the line of the X-ray beam an x-axis scan is performed which moves the sample vertically into the path of the beam as shown in figure 3.

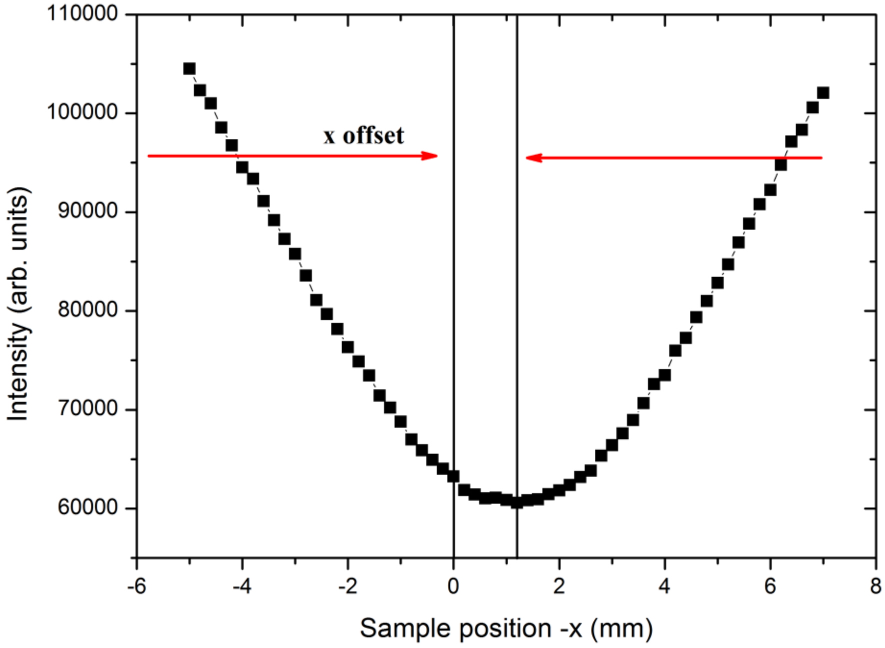

Figure 3: Sample alignment scan for vertical adjustment of the sample. The sample is moved across the entire height of the beam from out of the beam (maximum intensity) to in-line with the beam (minimum intensity) and again past the beam (max. intensity). The sample is placed at the min. of intensity where it is completely in-line with the X-ray beam.

As can be seen from figure 3, the collimated incoming X-rays decrease in intensity as the sample is moved towards the centre of the X-ray beam. The minimum in the X-ray intensity is obtained when the sample is placed in the centre of the X-ray beam.

Now that the sample is centred in-line with the X-ray intensity care should be taken to remove any tilt in the sample mounting. Therefore in order to ensure that the sample is flat and that there is no angular displacement due to sample mounting a zeta axis scan is performed in which the sample is rocked at a specular reflection peak. The detector is placed at $2\theta = 1°$ and $\omega = 0.5°$. Depending on the roughness of the sample these values need to be adjusted in order to obtain a peak with sufficient intensity. Choosing too large a value for 2θ and ω will not result in any reflection peak as the Kiessig fringes decay rapidly with increasing 2θ. An example correction zeta scan is shown in figure 4.

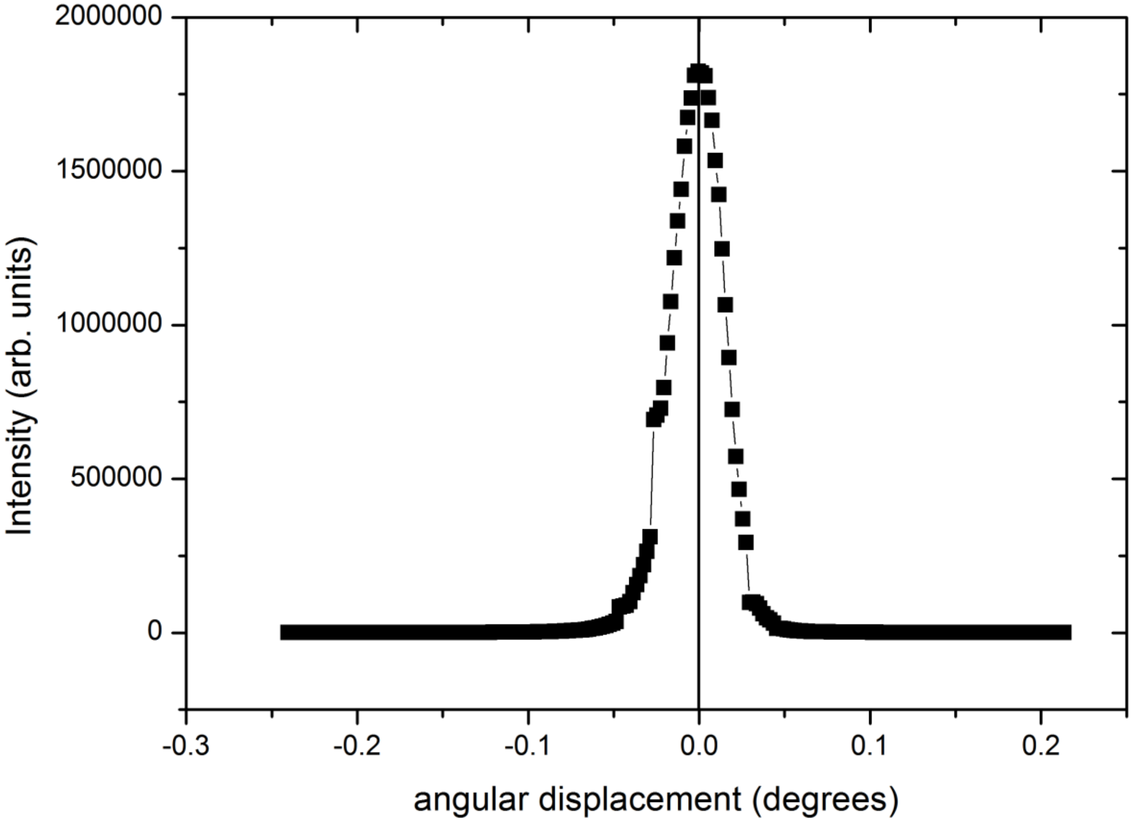

Figure 4: Sample tilt alignment (zeta) scan to remove sample tilt on the sample stage. Small angular displacement of sample stage for a fixed detector with the sample obstructing the detector giving zero intensity and strong peak for when the zeta is aligned.

Once the sample is aligned one obtains a centred zeta-axis scan with the centre of the beam intensity occurring at 0° offset. The sudden rise in intensity at -0.02° is due to the change in the detector attenuation during the scan. All reflectometry of samples shown in chapter 4 were measured with 2θ values $\geq 0.3°$ such that the detector is not saturated with full beam.

Post sample tilt alignment structural characterisation of X-ray reflectometry was performed, the results of which are shown in chapter 4.

A.2 Protocol of sample alignment and SQUID measurement technique

In order to obtain in-plane hysteresis measurements the sample was scribed using a diamond scribe into 10 × 5 mm^2 and inserted into the sample holder as shown in figure 5:

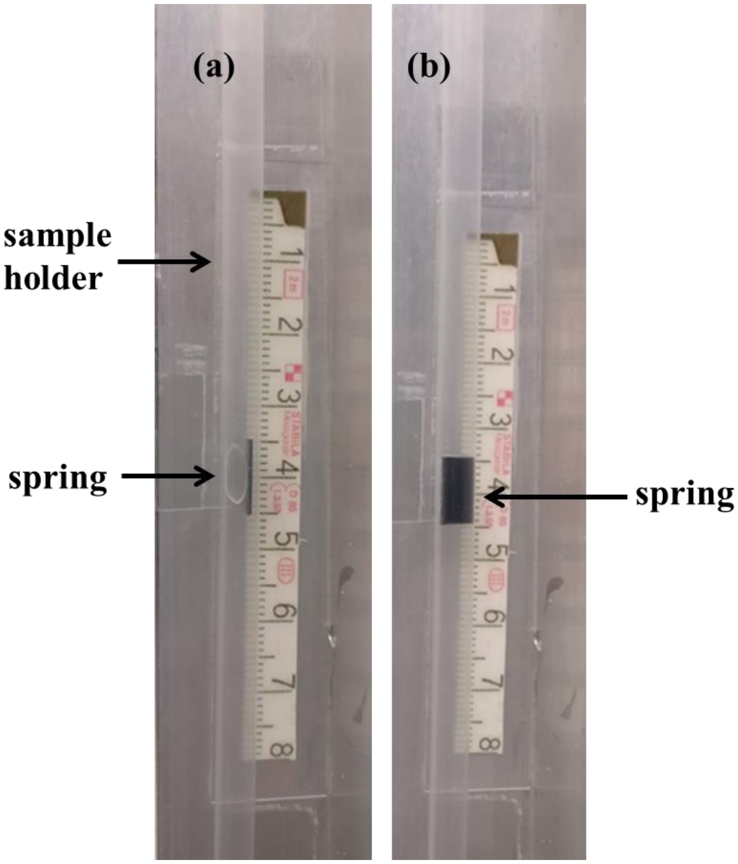

Figure 5: (a) side view (b) front view of sample rod along with sample holder and a spring suspension used to hold the sample in place before inserting inside the SQUID magnetometer.

The holder was loaded on the sample rod and inserted into the SQUID. It is then required to align the sample within the superconducting coils such that one obtains an accurate signal from the sample. Therefore a centring of the sample was performed by moving the sample gradually through the two detection coils in order to sense the signal. The magnetic sample generates a stray field around it which can be used in the alignment process. If the moment is weak and the stray field generated is too low an external field can be applied during the alignment process. To enhance the signal a small field was applied, given the diamagnetic contribution scales linearly with field the larger the field the stronger the signal. In order to better understand sample mounting and sample insertion into chamber see [1][2]. A D.C. centering scan was performed and the sample position was fixed at the centre of the two coils. Following this, hysteresis curves were measured by sweeping fields with varying step sizes from +4 T to -4 T. Larger fields were used to remove diamagnetic contributions as highlighted in the section below.

Method to extract ferromagnetic contribution

All samples studied here were grown on CMOS compatible SiO_2 substrates. In order to obtain true magnetisation data it is necessary to remove any diamagnetic contributions from the sample stack. This is crucial when measuring thin films comprising of multilayers in which one or more layers are non-ferromagnetic. Since the majority of sample comprises of (≈ 0.5 mm) Si substrate and only ≈ 0.6 nm of ferromagnetic material the signal measured by the SQUID at high fields shows a strong diamagnetic contribution which needs to be subtracted in order to obtain the ferromagnetic contribution. The measured hysteresis curve for such a sample is shown in figure 6.

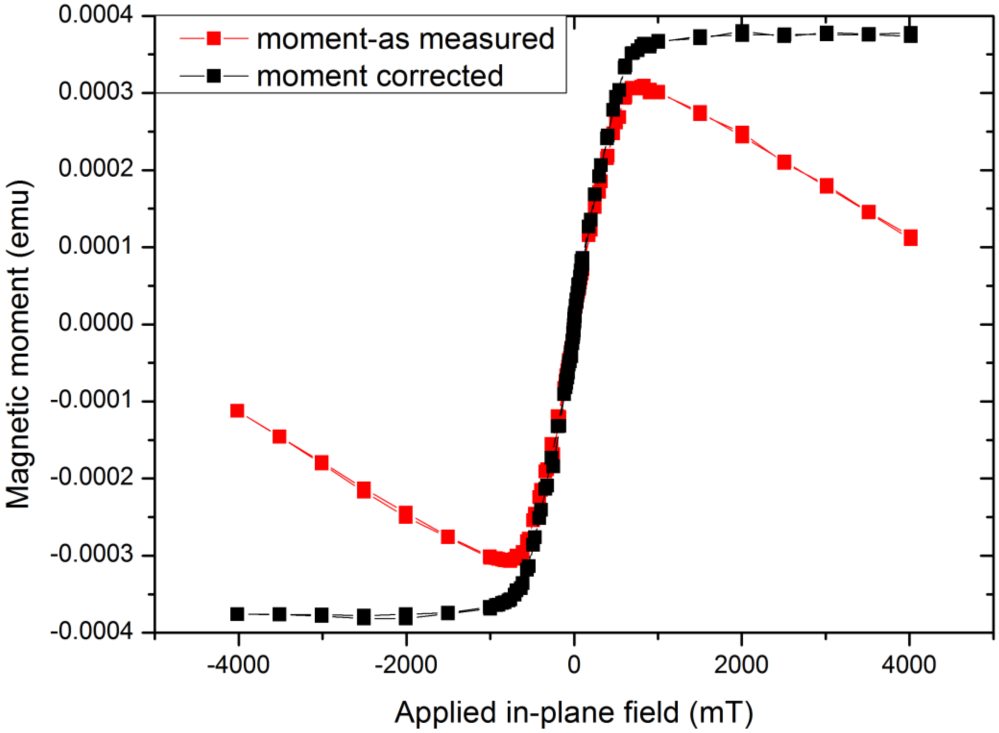

Figure 6: Magnetisation response of a ferromagnetic sample as obtained from the SQUID magnetometer (shown in red) along with the corrected hysteresis curve obtained post removal of background substrate signal.

To obtain this, the slope of the as-measured data shown in figure 6 was calculated for both positive and negative magnetic fields, this was then subtracted to obtain the corrected magnetisation. Ideally the sample holder as described earlier must also be measured without the sample in place, to obtain the background noise. However the diamagnetic contributions from the sample holder are often small compared to the largely ferromagnetic dominated signal. The actual value of magnetisation is then calculated by using the now corrected moment for high fields and by measuring the surface area using the image processing software, ImageJ® along with the calibrated thickness to obtain magnetisation per cubic centimetre. There exist other methods of obtaining magnetisation per cubic centimetre. This is done by weighing the substrate prior to deposition and then again post deposition with the deposited film. The total volume is then estimated using, $V = \frac{Mass}{Density}$. However this relies on using bulk values for densities of sputtered thin films which might not always be the same.

A.3 Sample temperature during annealing

The annealing of the thin films studied in this work was performed in-situ using a two intertwined SiC heaters placed below the sample plate. The wafer was placed on the sample holder and therefore there is a difference in the temperature experienced by the wafer as compared to the temperature at the heater. This was calibrated using thermos-couples placed on the wafer stage by the research team at Singulus Technologies AG. The difference in temperature at the heater and that at the wafer was recorded and is shown in figure 7. This temperature difference in annealing is very important especially for testing and comparison of data from films grown in other laboratories.

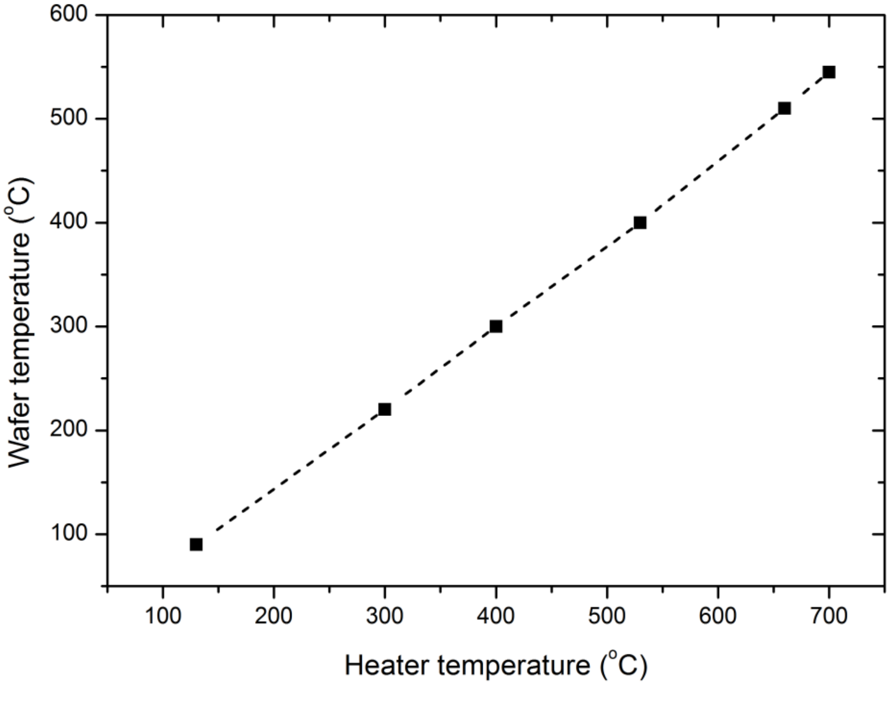

Figure 7: Temperature obtained at sample as a function of set temperature at heater. Heater calibration was obtained on the Singulus *Rotaris* and the data was provided by Mr. Karl-Heinz Schuller whose support is greatly acknowledged.

A.4 Appendix- References:

[1] QuantumDesign, “Sample Mounting Considerations,” 2000. [Online]. Available: https://www.qdusa.com/sitedocs/appNotes/mpms/1014-201.pdf. [Accessed: 10-Jan-2018].

[2] QuantumDesign, “Connecting a Straw Adapter to the Standard Transport Rod.” [Online]. Available: https://www.qdusa.com/sitedocs/appNotes/mpms/1014-819.pdf. [Accessed: 10-Jan-2018].

List of publications

Efficient metallic spintronic emitters of ultrabroadband terahertz radiation- Nature Photonics 10, 483–488 (2016)
T. Seifert, **S. Jaiswal**, U. Martens, J. Hannegan, L. Braun, P. Maldonado, F. Freimuth, A. Kronenberg, J. Henrizi, I. Radu, E. Beaurepaire, Y. Mokrousov, P. M. Oppeneer, M. Jourdan, G. Jakob, D. Turchinovich, L. M. Hayden, M. Wolf, M. Münzenberg, M. Kläui & T. Kampfrath

Magnetization switching behaviour with competing anisotropies in epitaxial Co_3FeN/MnN exchange-coupled bilayers- Phys. Rev. B 94, 184412 (2016)
T. Hajiri, T. Yoshida, **S. Jaiswal**, M. Filianina, B. Borie, H. Asano, H. Zabel, and M. Kläui

Ultrabroadband single-cycle terahertz pulses with peak fields of 300 kV cm^{-1} from a metallic spintronic emitter- Appl. Phys. Lett. 110, 252402 (2017)
T. Seifert, **S. Jaiswal**, M. Sajadi, G. Jakob, S. Winner, M. Wolf, M. Kläui, and T. Kampfrath

Investigation of the Dzyaloshinskii-Moriya interaction and room temperature skyrmions in W/CoFeB/MgO thin films and microwires- Appl. Phys. Lett. 111, 022409 (2017)
S. Jaiswal, K. Litzius, I. Lemesh, F. Büttner, S. Finizio, J. Raabe, M. Weigand, K. Lee, J. Langer, B. Ocker, G. Jakob, G. S. D. Beach, and M. Kläui

Electric field controlled domain wall dynamics and magnetic easy axis switching in liquid gated CoFeB/MgO films- Journal of Appl. Phys., 122, 133907 (2017)
Y.T. Liu, S.Ono, G. Agnus, J. –P. Adams, **S. Jaiswal**, J. Langer, B. Ocker, D. Ravelosona, L.H. Diez

45° sign switching of effective exchange bias due to competing anisotropies in fully epitaxial Co_3FeN/MnN bilayers- J. Phys.: Condens. Matter, 30, 015806 (2017)
T. Hajiri, T. Yoshida, M. Filianina, **S. Jaiswal**, B. Borie, H. Asano, H. Zabel, and M. Kläui

Study of interfacial perpendicular magnetic anisotropy, domain structures and skyrmion phase diagram in thin film multilayers and microwires- (Manuscript in Preparation)
S. Jaiswal, G. Jakob, J. Langer, B. Ocker, M. Kläui